Wake CFD Validation Reports

CLEW Inc.

Table of contents

1 Wake CFD Validation Reports 3

Wake CFD Validation Reports 4
1.1 How to Read These Reports . . . 4
1.2 Verification and Validation Cases . . . 4

I Introduction 5

Case Directory 6
How Cases Are Classified . . . 6
Verification . . . 7
DBNS . . . 7
PBNS . . . 7
FR . . . 7
Validation . . . 7
DBNS . . . 7
PBNS . . . 7
FR . . . 8

II Flat Plate Boundary Layer 9

2 Flat Plate Boundary Layer 10

3 2D Laminar Flat-Plate Boundary Layer — Blasius & Pohlhausen Verification 12
3.1 Run Provenance and Artifacts . . . 12
3.1.1 Downloadable Files . . . 12
3.2 Verification Objective . . . 12
3.3 Reference Solution and Data . . . 13
3.3.1 Analytical Solution . . . 13
3.4 Simulation Conditions . . . 13
3.5 Mesh . . . 14
3.6 Boundary and Initial Conditions . . . 15
3.7 Numerical Methods . . . 16
3.7.1 Numerical Schemes Compared . . . 16
3.8 Results . . . 16
3.8.1 Scheme comparison . . . 16
3.8.2 Closer Look: Roe Without Low-Mach Preconditioning . . . 21
3.9 Conclusions and Applicable Scope . . . 25
3.10 References . . . 26

4 2D Turbulent Flat-Plate Boundary Layer — NASA TMR SA Verification 27
4.1 Run Provenance and Artifacts . . . 27
4.1.1 Downloadable Files . . . 27
4.2 Verification Objective . . . 28
4.3 Reference Solution and Data . . . 28
4.4 Simulation Conditions . . . 28
4.5 Mesh . . . 29
4.6 Boundary and Initial Conditions . . . 29
4.7 Numerical Methods . . . 30
4.8 Results . . . 31
4.8.1 Convergence History . . . 31
4.8.2 Grid Convergence . . . 34
4.8.3 Difference between the gradient methods . . . 37
4.8.4 Observed order of convergence . . . 38
4.8.5 Detailed Comparison . . . 39
4.9 Conclusions and Applicable Scope . . . 45
4.10 References . . . 46

5 2D Turbulent Flat-Plate Boundary Layer — NASA TMR SST Verification 47
5.1 Run Provenance and Artifacts . . . 47
5.1.1 Downloadable Files . . . 47
5.2 Verification Objective . . . 48
5.3 Reference Solution and Data . . . 48
5.4 Simulation Conditions . . . 48
5.5 Mesh . . . 49
5.6 Boundary and Initial Conditions . . . 50
5.7 Numerical Methods . . . 50
5.8 Results . . . 52
5.8.1 Convergence History . . . 52
5.8.2 Grid Convergence . . . 55
5.8.3 Difference between the gradient methods . . . 58
5.8.4 Detailed Comparison . . . 59
5.9 Conclusions and Applicable Scope . . . 66
5.10 References . . . 66

6 2D Turbulent Flat-Plate Boundary Layer, M=2 and M=5 — NASA TMR SA Verification 67
6.1 Run Provenance and Artifacts . . . 67
6.1.1 Downloadable Files . . . 67
6.2 Verification Objective . . . 67
6.3 Reference Solution and Data . . . 68
6.3.1 Analytical Solution . . . 68
6.3.2 Numerical Reference . . . 68
6.4 Simulation Conditions . . . 68
6.5 Mesh . . . 69
6.6 Boundary and Initial Conditions . . . 70
6.7 Numerical Methods . . . 71
6.8 Results . . . 72
6.8.1 Convergence History . . . 72

6.8.2 Skin Friction . . . 76
6.8.3 Law of the Wall . . . 82
6.9 Conclusions and Applicable Scope . . . 85
6.10 References . . . 86

7 3D Laminar Flat-Plate Boundary Layer — PBNS Blasius Verification 87
7.1 Run Provenance and Artifacts . . . 87
7.1.1 Downloadable Files . . . 87
7.2 Verification Objective . . . 87
7.3 Reference Solution and Data . . . 88
7.3.1 Analytical Solution . . . 88
7.4 Simulation Conditions . . . 88
7.5 Mesh . . . 89
7.6 Boundary and Initial Conditions . . . 90
7.7 Numerical Methods . . . 91
7.8 Results . . . 91
7.9 Conclusions and Applicable Scope . . . 93
7.10 References . . . 93

8 2D Laminar Flat-Plate Boundary Layer — FR Blasius Verification 94
8.1 Run Provenance and Artifacts . . . 94
8.1.1 Downloadable Files . . . 94
8.2 Verification Objective . . . 94
8.3 Reference Solution and Data . . . 95
8.3.1 Analytical Solution . . . 95
8.4 Simulation Conditions . . . 95
8.5 Mesh . . . 96
8.6 Boundary and Initial Conditions . . . 96
8.7 Numerical Methods . . . 96
8.8 Results . . . 97
8.9 Conclusions and Applicable Scope . . . 99
8.10 References . . . 99

III Shock & Expansion Flows 100

9 Supersonic Wedge — Oblique-Shock Verification 101
9.1 Run Provenance and Artifacts . . . 101
9.1.1 Downloadable Files . . . 101
9.2 Verification Objective . . . 101
9.3 Reference Solution and Data . . . 102
9.3.1 Analytical Solution . . . 102
9.4 Simulation Conditions . . . 102
9.5 Mesh . . . 102
9.6 Boundary and Initial Conditions . . . 103
9.7 Numerical Methods . . . 103
9.8 Results . . . 104
9.9 Conclusions and Applicable Scope . . . 105

9.10 References . . . 105

10 Forward-Facing Step — Supersonic Shock-System Verification **106**
10.1 Run Provenance and Artifacts . . . 106
10.1.1 Downloadable Files . . . 106
10.2 Verification Objective . . . 106
10.3 Reference Solution and Data . . . 107
10.3.1 Numerical Reference . . . 107
10.4 Simulation Conditions . . . 107
10.5 Mesh . . . 107
10.6 Boundary and Initial Conditions . . . 107
10.7 Numerical Methods . . . 107
10.8 Results . . . 108
10.9 Conclusions and Applicable Scope . . . 109
10.10References . . . 109

11 Prandtl-Meyer Expansion Fan — Isentropic Verification **110**
11.1 Run Provenance and Artifacts . . . 110
11.1.1 Downloadable Files . . . 110
11.2 Verification Objective . . . 110
11.3 Reference Solution and Data . . . 111
11.4 Simulation Conditions . . . 111
11.5 Mesh . . . 111
11.6 Boundary and Initial Conditions . . . 112
11.7 Numerical Methods . . . 112
11.8 Results . . . 112
11.9 Conclusions and Applicable Scope . . . 114
11.10References . . . 114

IV Heat Transfer **115**

12 Conjugate Heat Transfer — Flat Plate Verification **116**
12.1 Run Provenance and Artifacts . . . 116
12.1.1 Downloadable Files . . . 116
12.2 Verification Objective . . . 116
12.3 Reference Solution and Data . . . 117
12.4 Simulation Conditions . . . 117
12.5 Mesh . . . 119
12.6 Boundary and Initial Conditions . . . 119
12.7 Numerical Methods . . . 119
12.8 Results . . . 119
12.9 Conclusions and Applicable Scope . . . 121
12.10References . . . 122

V Shear Flows & Jets 123

13 2D Planar Mixing Layer — SA/SST Validation 124
13.1 Run Provenance and Artifacts . . . 124
13.1.1 Downloadable Files . . . 124
13.2 Validation Objective . . . 124
13.3 Reference Solution and Data . . . 125
13.4 Simulation Conditions . . . 125
13.5 Mesh . . . 126
13.6 Boundary and Initial Conditions . . . 127
13.7 Numerical Methods . . . 128
13.8 Results . . . 128
13.9 Conclusions and Applicable Scope . . . 131
13.10 References . . . 131

14 2D Coflowing Jet — NASA TMR SA Verification 132
14.1 Run Provenance and Artifacts . . . 132
14.1.1 Downloadable Files . . . 132
14.2 Verification Objective . . . 132
14.3 Reference Solution and Data . . . 133
14.4 Simulation Conditions . . . 133
14.5 Mesh . . . 133
14.6 Boundary and Initial Conditions . . . 134
14.7 Numerical Methods . . . 135
14.8 Results . . . 135
14.8.1 Grid Convergence . . . 135
14.8.2 Detailed Comparison on the Finest Grid . . . 140
14.9 Conclusions and Applicable Scope . . . 143
14.10 References . . . 143

VI Vortex Shedding 144

15 Laminar Cylinder Vortex Shedding — Strouhal/CD/CL Validation 145
15.1 Run Provenance and Artifacts . . . 145
15.1.1 Downloadable Files . . . 145
15.2 Validation Objective . . . 145
15.3 Reference Solution and Data . . . 146
15.4 Simulation Conditions . . . 146
15.5 Mesh . . . 146
15.6 Boundary and Initial Conditions . . . 147
15.7 Numerical Methods . . . 147
15.8 Results . . . 147
15.9 Conclusions and Applicable Scope . . . 151
15.10 References . . . 152

16 Laminar Cylinder Vortex Shedding — Time Integration and Precision Comparison 153
16.1 Run Provenance and Artifacts . . . 153
16.1.1 Downloadable Files . . . 153

16.2 Verification Objective . . . 154
16.3 Reference Solution and Data . . . 154
16.3.1 Numerical Reference . . . 154
16.4 Simulation Conditions . . . 154
16.5 Mesh . . . 155
16.6 Boundary and Initial Conditions . . . 155
16.7 Numerical Methods . . . 155
16.8 Results . . . 155
16.8.1 Convergence to the reference solution . . . 155
16.8.2 Order of accuracy . . . 158
16.8.3 FP64 versus FP32 . . . 159
16.9 Conclusions and Applicable Scope . . . 161
16.10References . . . 162

17 Laminar Cylinder Vortex Shedding — Explicit Classical RK4 163
17.1 Run Provenance and Artifacts . . . 163
17.1.1 Downloadable Files . . . 163
17.2 Validation Objective . . . 164
17.3 Reference Solution and Data . . . 164
17.4 Simulation Conditions . . . 164
17.5 Mesh . . . 165
17.6 Boundary and Initial Conditions . . . 166
17.7 Numerical Methods . . . 166
17.8 Results . . . 166
17.8.1 Drag Decomposition . . . 169
17.8.2 Development History . . . 171
17.8.3 Flow Field . . . 172
17.8.4 Readout Methodology . . . 173
17.8.5 Readout window . . . 173
17.8.6 Frequency estimation . . . 174
17.9 Conclusions and Applicable Scope . . . 174
17.10References . . . 175

18 Laminar Cylinder Vortex Shedding — PBNS Strouhal/CD/CL Validation 176
18.1 Run Provenance and Artifacts . . . 176
18.1.1 Downloadable Files . . . 176
18.2 Validation Objective . . . 176
18.3 Reference Solution and Data . . . 177
18.3.1 Experimental Data . . . 177
18.4 Simulation Conditions . . . 177
18.5 Mesh . . . 178
18.6 Boundary and Initial Conditions . . . 179
18.7 Numerical Methods . . . 179
18.8 Results . . . 182
18.8.1 Development of the Shedding . . . 182
18.8.2 Readout Window . . . 183
18.8.3 Comparison with Literature . . . 183
18.8.4 Pressure and Friction Drag . . . 184

18.8.5 Flow Field . . . 185
18.9 Conclusions and Applicable Scope . . . 185
18.10References . . . 186

VII Airfoils & Wings **187**

19 2D Transonic Airfoil — RAE2822 RANS Validation **188**
19.1 Run Provenance and Artifacts . . . 188
19.1.1 Downloadable Files . . . 188
19.2 Validation Objective . . . 188
19.3 Reference Solution and Data . . . 189
19.4 Simulation Conditions . . . 189
19.5 Mesh . . . 189
19.6 Boundary and Initial Conditions . . . 191
19.7 Numerical Methods . . . 191
19.8 Results . . . 192
19.8.1 Key Results . . . 192
19.8.2 Comparisons for Scheme Selection . . . 195
19.9 Conclusions and Applicable Scope . . . 202
19.10References . . . 203

20 2D NACA0012 Airfoil — SA RANS Polar Validation **204**
20.1 Run Provenance and Artifacts . . . 204
20.1.1 Downloadable Files . . . 204
20.2 Validation Objective . . . 204
20.3 Reference Solution and Data . . . 205
20.4 Simulation Conditions . . . 205
20.5 Mesh . . . 205
20.6 Boundary and Initial Conditions . . . 206
20.7 Numerical Methods . . . 206
20.8 Results . . . 206
20.8.1 Linear Range (−10° to 10°) . . . 206
20.8.2 Near and Beyond Stall (11° to 19°) . . . 210
20.8.3 Convergence History . . . 213
20.9 Conclusions and Applicable Scope . . . 216
20.10References . . . 216

21 2D Airfoil Near-Wake — NASA TMR SA and SST Verification **217**
21.1 Run Provenance and Artifacts . . . 217
21.1.1 Downloadable Files . . . 217
21.2 Verification Objective . . . 218
21.3 Reference Solution and Data . . . 218
21.3.1 Numerical Reference . . . 218
21.3.2 Experimental Data . . . 218
21.4 Simulation Conditions . . . 219
21.5 Mesh . . . 219
21.6 Boundary and Initial Conditions . . . 219

21.7 Numerical Methods . . . 220
21.8 Results . . . 220
21.8.1 Iteration Counts and Termination . . . 220
21.8.2 Force Coefficients . . . 221
21.8.3 Near-Wake Profiles . . . 225
21.9 Conclusions and Applicable Scope . . . 236
21.10References . . . 236

22 3D Transonic Wing — ONERA M6 RANS Validation 237
22.1 Run Provenance and Artifacts . . . 237
22.1.1 Downloadable Files . . . 237
22.2 Validation Objective . . . 237
22.3 Reference Solution and Data . . . 238
22.4 Simulation Conditions . . . 238
22.5 Mesh . . . 238
22.6 Boundary and Initial Conditions . . . 239
22.7 Numerical Methods . . . 239
22.8 Results . . . 240
22.8.1 Key Results . . . 240
22.8.2 Comparison with Experiment and NASA WIND-US . . . 242
22.8.3 Comparisons for Scheme Selection . . . 243
22.9 Conclusions and Applicable Scope . . . 243
22.10References . . . 243

23 CRM DPW-5 Wing–Body — SA Grid-Convergence Verification 244
23.1 Run Provenance and Artifacts . . . 244
23.1.1 Downloadable Files . . . 244
23.2 Verification Objective . . . 245
23.3 Reference Solution and Data . . . 245
23.4 Simulation Conditions . . . 245
23.5 Mesh . . . 245
23.6 Boundary and Initial Conditions . . . 246
23.7 Numerical Methods . . . 246
23.8 Results . . . 248
23.8.1 Surface contours: hex L3 SA . . . 249
23.9 Conclusions and Applicable Scope . . . 249
23.10References . . . 251

24 3D High-Lift Trap Wing — HiLiftPW-1 Configuration 1 Validation 252
24.1 Run Provenance and Artifacts . . . 252
24.1.1 Downloadable Files . . . 252
24.2 Validation Objective . . . 252
24.3 Reference Solution and Data . . . 253
24.4 Simulation Conditions . . . 253
24.5 Mesh . . . 254
24.6 Boundary and Initial Conditions . . . 254
24.6.1 Initial field and procedure . . . 255
24.7 Numerical Methods . . . 255

24.8 Results . . . 255
24.8.1 Forces and Moment . . . 255
24.8.2 Surface pressure . . . 258
24.8.3 Is the Stall Found? . . . 263
24.8.4 Convergence History . . . 268
24.9 Conclusions and Applicable Scope . . . 271
24.10References . . . 271

VIIIAxisymmetric Bodies **272**

25 3D Sphere Bow Shock — Stand-off Distance Validation **273**
25.1 Run Provenance and Artifacts . . . 273
25.1.1 Downloadable Files . . . 273
25.2 Validation Objective . . . 273
25.3 Reference Solution and Data . . . 274
25.4 Simulation Conditions . . . 274
25.5 Mesh . . . 275
25.6 Boundary and Initial Conditions . . . 275
25.7 Numerical Methods . . . 275
25.8 Results . . . 275
25.9 Conclusions and Applicable Scope . . . 278
25.10References . . . 278

26 Secant-Ogive-Cylinder — Static and Magnus Aerodynamic Coefficients **279**
26.1 Run Provenance and Artifacts . . . 279
26.1.1 Downloadable Files . . . 279
26.2 Validation Objective . . . 279
26.3 Reference Solution and Data . . . 280
26.4 Simulation Conditions . . . 280
26.5 Mesh . . . 282
26.6 Boundary and Initial Conditions . . . 282
26.7 Numerical Methods . . . 282
26.8 Results . . . 282
26.8.1 Static Coefficients . . . 282
26.8.2 Magnus Coefficients . . . 284
26.9 Conclusions and Applicable Scope . . . 287
26.10References . . . 287

IX Internal Flow **288**

27 3D Supersonic Square Duct — SA-QCR2000 Secondary-Flow Validation **289**
27.1 Run Provenance and Artifacts . . . 289
27.1.1 Downloadable Files . . . 289
27.2 Validation Objective . . . 289
27.3 Reference Solution and Data . . . 290
27.4 Simulation Conditions . . . 290
27.5 Mesh . . . 292

27.6 Boundary and Initial Conditions 292
27.7 Numerical Methods 292
27.8 Results 293
27.8.1 Secondary-Flow Signature (SA vs. SA-QCR2000) 293
27.8.2 Comparison Against Experiment and Reference Codes (medium grid) 296
27.9 Conclusions and Applicable Scope 298
27.10References 298

1 Wake CFD Validation Reports

Wake CFD Validation Reports

This site publishes verification and validation results for Wake CFD. Each report records the simulation conditions, reference data, results, and error metrics so that engineers can assess its applicable scope.

The primary published engineering track is density-based Navier–Stokes (DBNS), especially external aerodynamics. Pressure-based Navier–Stokes (PBNS) and Flux Reconstruction (FR) are in development. Their reports show results for specific conditions, not production readiness across those solver paths.

Wake CFD baseline version: `0.23.0`.

1.1 How to Read These Reports

Each report provides the following information:

- **Objective and reference solution**: the physical phenomenon and published reference data being compared
- **Simulation setup**: geometry, mesh, flow conditions, and turbulence and numerical models
- **Results and comparison**: key distributions, integral quantities, time histories, and error metrics
- **Reproducibility information**: the input configuration and execution environment used

1.2 Verification and Validation Cases

For external aerodynamics, start with the SA flat-plate grid study, the RAE2822 transonic airfoil, the NACA0012 SA polar, the ONERA M6 wing, and the CRM DPW-5 SA mesh study. The HiLiftPW-1 Trap Wing adds a high-lift comparison; its report states where the computed stall remains unresolved.

The full directory also covers shocks and expansion fans, unsteady cylinder shedding, shear flows and jets, conjugate heat transfer, corner secondary flow, and static/Magnus coefficients. Each case describes what its comparison establishes and what remains outside its tested range.

Browse the case directory

Part I

Introduction

Case Directory

This section collects the verification and validation cases. Each case includes its run provenance, conditions, results, and comparison data.

The left sidebar groups cases by **physical case type** (flat plate, cylinder, airfoils, …) for browsing. This page instead groups them by **verification vs. validation** — see below — since that distinction matters for interpreting a result but isn't what most readers browse by first.

How Cases Are Classified

Verification and validation answer different questions, and this report keeps them apart. The test is simply **what the result is compared against**.

	Verification	Validation
Question	Are the equations solved correctly?	Are the correct equations solved?
Compared against	Exact or analytical solutions, published results from other codes (code-to-code), grid convergence, agreement between independent schemes	**Experimental data**, or a correlation fitted to experimental data

Two consequences worth stating explicitly:

- **The institution is not the criterion; the nature of the reference is.** The Turbulent Flat-Plate Boundary Layer case uses NASA TMR material, but it is compared against CFL3D and FUN3D *computations*, so it is verification rather than validation.
- **Verification precedes validation.** Where numerical error has not been bounded, close agreement with an experiment can be error cancellation rather than physical accuracy. Each case states what it actually established.

Within each category, cases are grouped by solver: **DBNS** (density-based Navier–Stokes), **PBNS** (pressure-based Navier–Stokes), or **FR** (Flux Reconstruction, high-order).

PBNS and FR are in development. Their published cases document specific verified or validated conditions; they do not establish production readiness across the broader solver paths.

Verification

- Flat Plate Boundary Layer — Laminar & Turbulent, All Solver Tracks

DBNS

- 2D Laminar Flat-Plate Boundary Layer — Blasius & Pohlhausen Verification
- 2D Turbulent Flat-Plate Boundary Layer — NASA TMR SA Verification
- 2D Turbulent Flat-Plate Boundary Layer — NASA TMR SST Verification
- 2D Turbulent Flat-Plate Boundary Layer, M=2 and M=5 — NASA TMR SA Verification
- Supersonic Wedge — Oblique-Shock Verification
- Forward-Facing Step — Supersonic Shock-System Verification
- 2D Coflowing Jet — NASA TMR SA Verification
- Laminar Cylinder Vortex Shedding — Time Integration and Precision Comparison
- Conjugate Heat Transfer — Flat Plate Verification
- Prandtl-Meyer Expansion Fan — Isentropic Verification
- CRM DPW-5 Wing–Body — SA Grid-Convergence Verification
- 2D Airfoil Near-Wake — NASA TMR SA and SST Verification

PBNS

- 3D Laminar Flat-Plate Boundary Layer — PBNS Blasius Verification

FR

- 2D Laminar Flat-Plate Boundary Layer — FR Blasius Verification

Validation

DBNS

- Laminar Cylinder Vortex Shedding — Explicit Classical RK4
- 2D Transonic Airfoil — RAE2822 RANS Validation
- 2D Planar Mixing Layer — SA/SST Validation
- 3D Supersonic Square Duct — SA-QCR2000 Secondary-Flow Validation
- 2D NACA0012 Airfoil — SA RANS Polar Validation
- 3D Sphere Bow Shock — Stand-off Distance Validation
- Secant-Ogive-Cylinder — Static and Magnus Aerodynamic Coefficients
- 3D Transonic Wing — ONERA M6 RANS Validation
- 3D High-Lift Trap Wing — HiLiftPW-1 Configuration 1 Validation

PBNS

- Laminar Cylinder Vortex Shedding — PBNS Strouhal/CD/CL Validation

FR

- Laminar Cylinder Vortex Shedding — Strouhal/CD/CL Validation

Part II

Flat Plate Boundary Layer

2 Flat Plate Boundary Layer

Laminar and turbulent flat-plate boundary-layer verification, across solver tracks

The flat plate is Wake CFD's baseline boundary-layer verification geometry — the same physical setup family (Blasius/Pohlhausen similarity for laminar flow, NASA TMR for turbulent SA/SST) is run across solver tracks so results can be compared directly, independent of laminar/turbulent regime.

Solver	Regime	Case	Compared against
DBNS	Laminar	2D Laminar Flat-Plate Boundary Layer — Blasius & Pohlhausen Verification	Blasius/Pohlhausen similarity solutions
DBNS	Turbulent (SA)	2D Turbulent Flat-Plate Boundary Layer — NASA TMR SA Verification	NASA TMR (CFL3D/FUN3D)
DBNS	Turbulent (SST)	2D Turbulent Flat-Plate Boundary Layer — NASA TMR SST Verification	NASA TMR (CFL3D/FUN3D)
DBNS	Turbulent (SA), M=2 and M=5	2D Turbulent Flat-Plate Boundary Layer, M=2 and M=5 — NASA TMR SA Verification	van Driest II / I theory, CFL3D SA (NASA TMR)
PBNS	Laminar	3D Laminar Flat-Plate Boundary Layer — PBNS Blasius Verification	Blasius similarity solution
FR	Laminar	2D Laminar Flat-Plate Boundary Layer — FR Blasius Verification	Blasius similarity solution

All six published cases are **verification** cases (see How Cases Are Classified): each compares against a computed reference — an exact similarity solution, or independent CFD codes, or van

Driest theory — rather than experimental data.

3 2D Laminar Flat-Plate Boundary Layer — Blasius & Pohlhausen Verification

Verification of velocity profiles, wall friction, and wall heat transfer against the exact Blasius and Pohlhausen similarity solutions, across seven convective schemes

3.1 Run Provenance and Artifacts

Item	Value
Wake CFD baseline version	`0.22.0`
Solver	DBNS
Compute device	CPU
Parallel execution	1 MPI rank
Arithmetic precision	FP64
Run date	2026-09-20

> **Note**
>
> Results depend on the solver build that produced them. Read every figure in this report together with the version and date above — re-running the same input on a later build may give different numbers.

3.1.1 Downloadable Files

Not available: input decks and result files have not yet been published for this case.

3.2 Verification Objective

This case simulates the boundary layer over a two-dimensional laminar flat plate and compares the computed result with the Blasius (velocity) and Pohlhausen (heat transfer) similarity solutions. It verifies Wake CFD implementation accuracy for:

- no-slip wall boundary conditions, both adiabatic-equivalent (Blasius) and isothermal (Pohlhausen)

- self-similarity of laminar boundary-layer velocity and temperature profiles
- variation of the local skin-friction coefficient (`Cf`) and local Nusselt number (`Nu_x`)
- low-Mach behavior of DBNS numerical fluxes, across seven convective schemes: five schemes with all-speed/low-Mach treatment (`AUSM+up`, `AUSM+up2`, `SLAU`, `SLAU2`, `Roe-Turkel`) and two reference schemes without explicit low-Mach correction (`Roe`, `JST`)

Because the laminar flat-plate flow has zero pressure gradient and well-known analytical solutions for both the velocity and thermal boundary layers, it is a useful reference case for checking viscous-wall treatment, low-Mach schemes, numerical diffusion, and wall heat-flux computation together.

3.3 Reference Solution and Data

3.3.1 Analytical Solution

Let `x` be the distance from the leading edge, `y` the wall-normal distance, `U_inf` the freestream velocity, and `nu` the kinematic viscosity. The following nondimensional quantities are used:

$$Re_x = \frac{U_\infty x}{\nu}, \qquad \eta = y\sqrt{\frac{U_\infty}{\nu x}}.$$

The Blasius solution is expressed as `u/U_inf = f'(eta)`, with the primary comparison values:

$$\delta_{99} \approx 4.91\sqrt{\frac{\nu x}{U_\infty}}, \qquad C_f(x) = \frac{0.664}{\sqrt{Re_x}}.$$

When velocity profiles at several `x/L` locations are plotted against `eta`, they should collapse onto a single curve.

For the thermal boundary layer, with an isothermal wall at temperature `T_wall` different from the freestream temperature `T_inf`, the Pohlhausen solution gives the local Nusselt number:

$$Nu_x = \theta'(0)\sqrt{Re_x}, \qquad \theta'(0) = 0.295635 \text{ for } Pr = 0.72,$$

where `Pr` is the Prandtl number. This case uses `T_wall=327.38 K` and `T_inf=297.62 K` with air (`Pr 0.72`).

3.4 Simulation Conditions

Item	Setting
Dimension	2D
Domain	`x=[0, 0.762] m`, `y=[0, 0.1524] m`
Flat plate	`x=[0.1524, 0.4572] m`, `L=0.3048 m`
Analysis	Steady, compressible DBNS, laminar Navier–Stokes
Target Reynolds number	`Re_L=1.0×10^5`

Item	Setting
Mach conditions	`0.1`, `0.05`, `0.0144`
Wall	no-slip, isothermal, `T_wall=327.38 K`
Freestream temperature	`T_inf=297.62 K` (`Pr 0.72`)

To compare numerical behavior at low Mach numbers, viscosity was adjusted while keeping `Re_L` constant. Therefore, the Mach conditions do not all represent the same physical air experiment. `M=0.0144` is a low-speed condition close to physical air viscosity; `M=0.1` and `M=0.05` compare low-Mach numerical behavior at the same Reynolds number.

3.5 Mesh

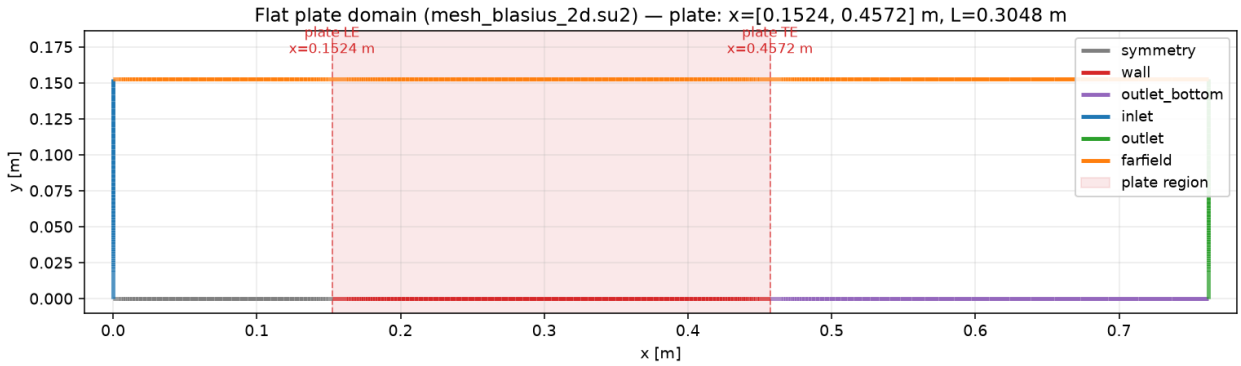


Figure 3.1: Domain for laminar flat-plate flow simulation

The computational domain consists of buffer regions upstream and downstream of the plate and a boundary-layer resolution region around it. The leading edge, trailing edge, and near-wall region are refined to capture boundary-layer velocity gradients and wall shear.

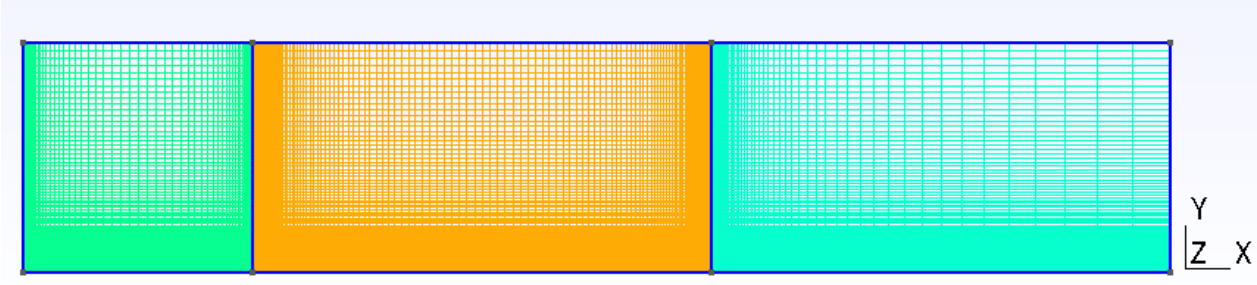


Figure 3.2: Full 2D flat-plate mesh

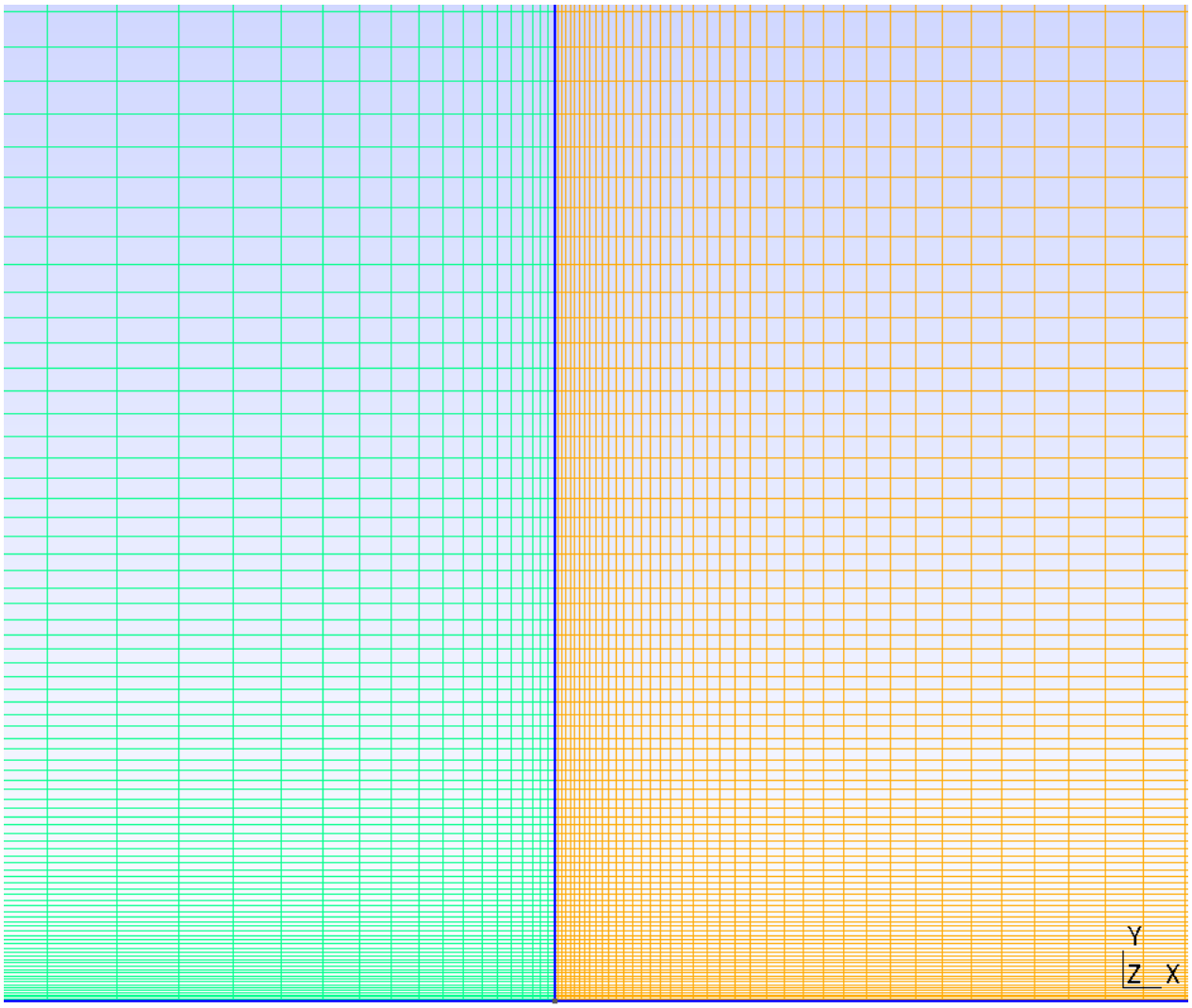


Figure 3.3: Mesh near the flat-plate leading edge

3.6 Boundary and Initial Conditions

Boundary	Segment	Type	Setting
Wall	Plate segment	`wall`	no-slip, isothermal
Symmetry plane	Bottom upstream of plate	`symmetry`	—
Bottom outlet	Bottom downstream of plate	`outlet_bottom`	—
Inlet	Left	`inlet`	—
Outlet	Right	`outlet`	—
Farfield	Top	`farfield`	—

Not reported: the source record does not specify the initial field for this steady-state calculation.

3.7 Numerical Methods

Item	Setting
Analysis	Steady, compressible DBNS, laminar Navier–Stokes
Convective schemes	`AUSM+up`, `AUSM+up2`, `SLAU`, `SLAU2`, `Roe-Turkel`, `Roe`, `JST` (compared below)
Spatial accuracy	Second order, Venkatakrishnan limiter
Time integration	Euler implicit (steady solution)
CFL	Adaptive, `1 → 100`
Convergence criterion	Cauchy-window monitor on the total streamwise force coefficient `CFx` (`eps=1e-5` over a `1000`-iteration window)

For the general input structure and boundary-condition definitions, see the CLI and **Domain and Boundary Conditions** sections of the public Wake CFD documentation.

3.7.1 Numerical Schemes Compared

Seven DBNS convective schemes were run at each of the three Mach numbers (21 cases total): five schemes designed for accuracy across a wide Mach range (`AUSM+up`, `AUSM+up2`, `SLAU`, `SLAU2`, `Roe-Turkel`, the last using a Turkel low-Mach preconditioner), and two reference schemes with no explicit low-Mach treatment (`Roe`, `JST`), included specifically to probe where low-Mach accuracy actually breaks down.

3.8 Results

3.8.1 Scheme comparison

Method	Low-Mach treatment	Result summary (`M=0.1` → `0.0144`)
AUSM+up, AUSM+up2, SLAU, SLAU2	All-speed flux formulation	Close to Blasius/Pohlhausen at every Mach; no degradation
Roe-Turkel	Turkel preconditioner	Close to Blasius/Pohlhausen at every Mach; converges in roughly 1/3–1/4 the iterations of the other schemes
Roe	None	Close to Blasius/Pohlhausen at every Mach — comparable to the all-speed group in this case
JST	None	Visibly degrades as Mach decreases; used here as the low-Mach control case

These results do not imply that a particular flux scheme is superior for every problem; they show the applicable range of the numerical methods in Wake CFD for this specific flat-plate boundary layer, mesh, and Reynolds number. In particular, `Roe` remaining accurate down to `M=0.0144` without explicit preconditioning is a case- and mesh-specific observation here, not a general claim about the scheme — see **Conclusions** below.

The comparison below aggregates all seven schemes at each Mach number. Two whole-plate metrics summarize accuracy at a glance: the mean ratio of computed skin friction to the Blasius reference, `Cf/Cf_Blasius`, and the mean ratio of computed local Nusselt number to the Pohlhausen reference, `Nu_x/Nu_x,Pohlhausen`, both averaged over `x/L=0.03-0.95` (both are unweighted point-wise means, not force-integrated coefficients; ratios near 1.00 indicate agreement).

Scheme	`M`	Velocity RMS (`x/L=.25,.50,.75`)	`Cf/Cf_Blasius`	`Nu_x/Nu_x,Pohlhausen`
AUSM+up2	0.1 / 0.05 / 0.0144	0.7–1.1% at all three	1.02–1.03	0.98 → 1.00
AUSM+up	0.1 / 0.05 / 0.0144	0.7–1.1% at all three	1.02–1.03	0.98 → 1.00
SLAU2	0.1 / 0.05 / 0.0144	0.7–1.1% at all three	1.02–1.03	0.98 → 1.00
SLAU	0.1 / 0.05 / 0.0144	0.7–1.1% at all three	1.02–1.03	0.98 → 1.00
Roe-Turkel	0.1 / 0.05 / 0.0144	0.7–1.0% at all three	1.02	0.98 → 1.00
Roe	0.1 / 0.05 / 0.0144	0.7–1.1% at all three	1.02	0.98 → 1.01
JST	0.1 / 0.05 / 0.0144	1.0–1.2% → 2.2–3.3%	1.09 → 1.16	0.99 → 1.02

For all seven schemes, `Nu_x` moves monotonically closer to the Pohlhausen value as `M` decreases (from roughly −2% at `M=0.1` to within +0.5% at `M=0.0144`); this trend is consistent with a compressible, ideal-gas isothermal-wall coupling that vanishes as `M→0`, since the analytical Pohlhausen solution assumes constant properties. Six of the seven schemes hold their velocity/`Cf` accuracy essentially flat across the whole Mach range; only `JST` shows a clear, monotonic degradation, concentrated in the second half of the plate where the boundary layer is thinnest and wall-normal gradients are largest.

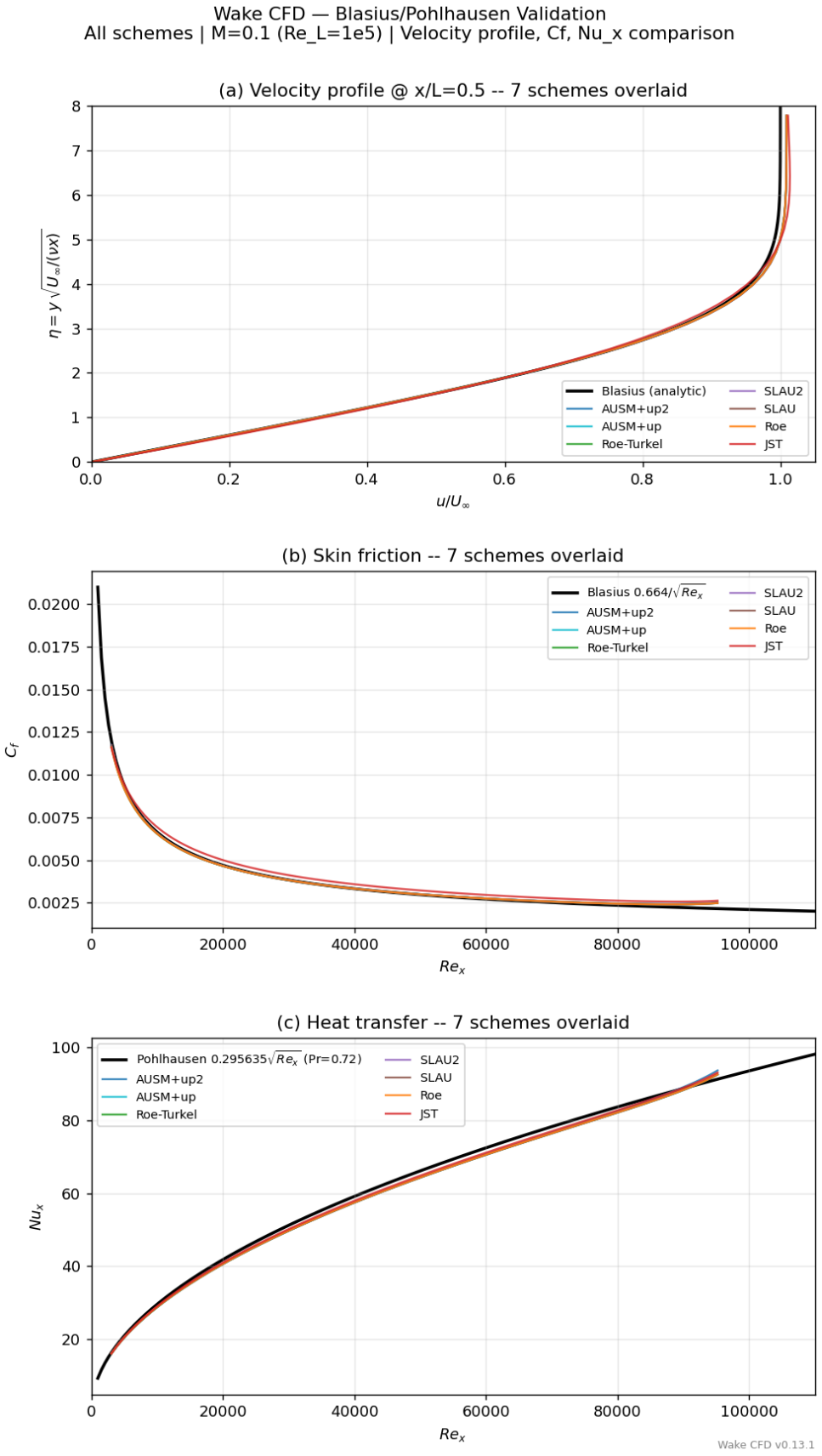


Figure 3.4: All seven schemes, M=0.1: velocity profile (x/L=0.5), skin friction, and Nusselt number

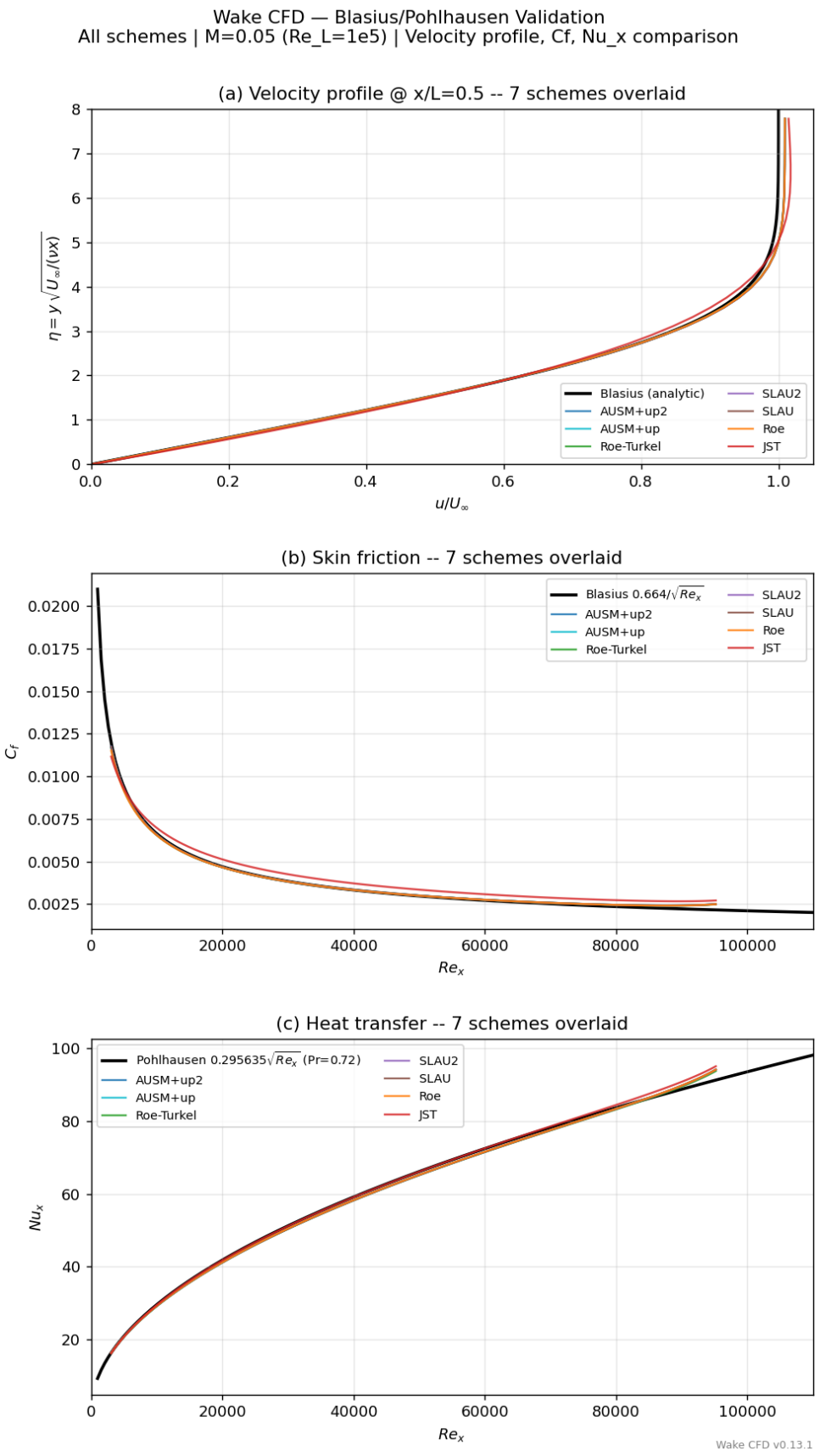


Figure 3.5: All seven schemes, M=0.05: velocity profile (x/L=0.5), skin friction, and Nusselt number

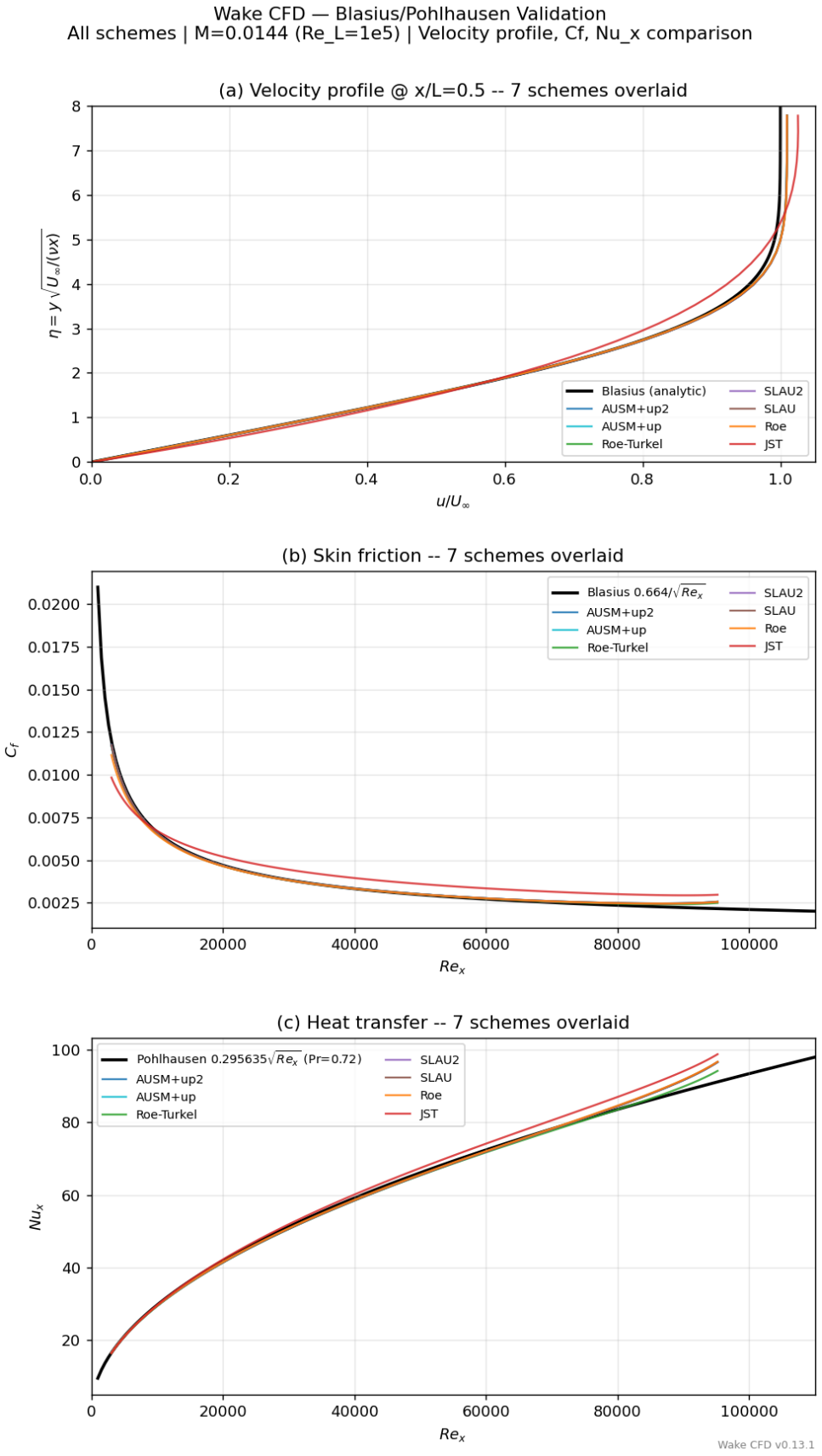


Figure 3.6: All seven schemes, M=0.0144: velocity profile (x/L=0.5), skin friction, and Nusselt number

At M=0.1 all seven curves are essentially indistinguishable. As Mach decreases, JST (shown in red) separates visibly from the rest, while the five all-speed schemes and Roe remain clustered on the reference curves even at M=0.0144.

3.8.2 Closer Look: Roe Without Low-Mach Preconditioning

Roe is highlighted separately because, unlike JST, it was not expected to hold its accuracy at low Mach without an explicit correction (compare Roe-Turkel, which adds a Turkel preconditioner to the same base scheme). The station-by-station detail below is the same comparison used to build the summary table above, shown per Mach with all three stations (x/L=0.25, 0.50, 0.75) instead of the single-station overlay.

M	Velocity RMS (x/L=.25,.50,.75)	99() (x/L=.25,.50,.75)	Cf/Cf_Blasius	Nu_x/Nu_x,Pohlhausen
0.1	0.68%, 0.67%, 0.96%	4.71, 4.61, 4.49	1.021	0.981
0.05	0.70%, 0.70%, 0.99%	4.70, 4.60, 4.49	1.021	0.995
0.0144	0.78%, 0.72%, 1.06%	4.71, 4.59, 4.47	1.022	1.005

(The Blasius reference value of 99() is approximately 4.9.)

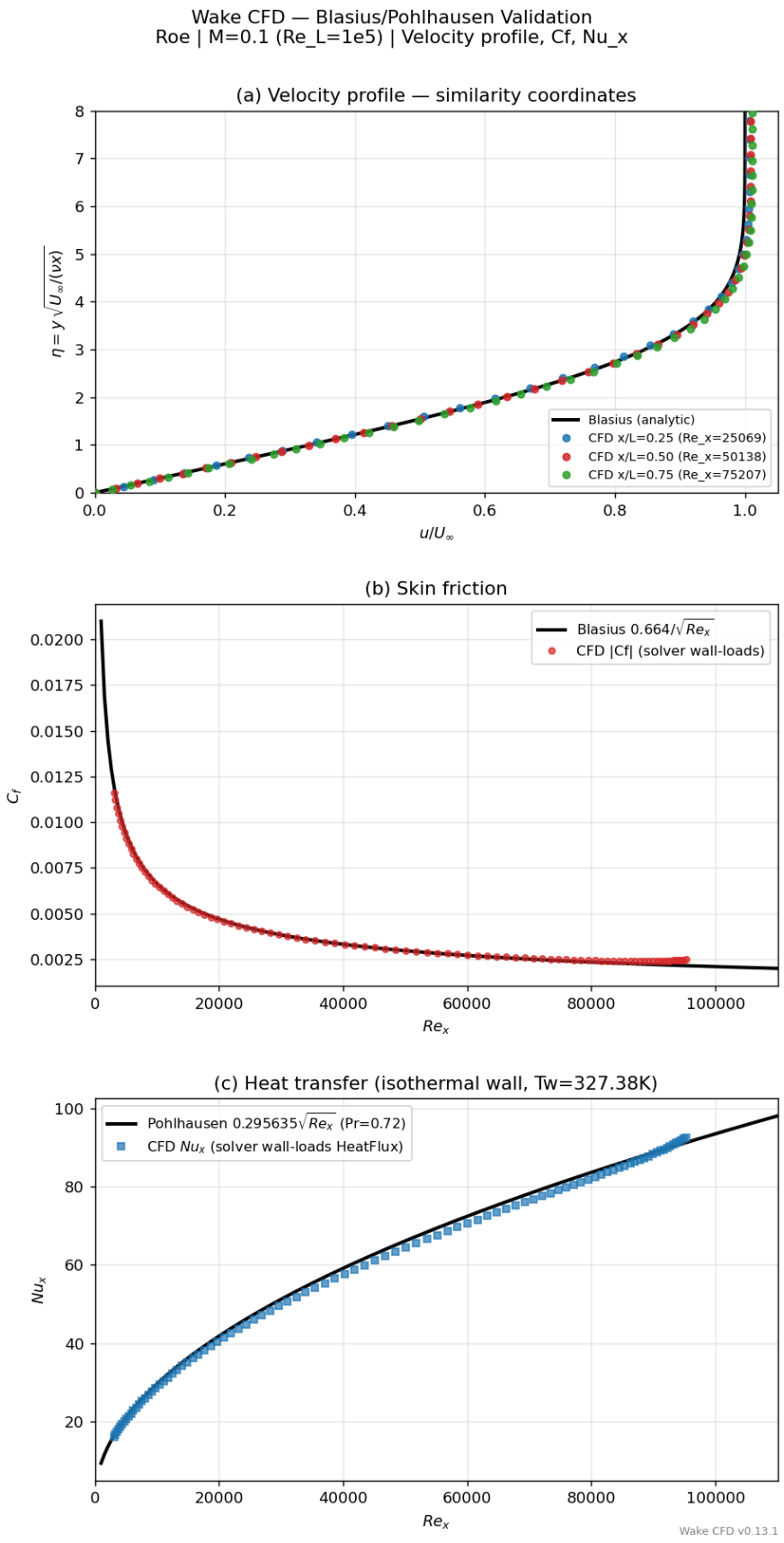


Figure 3.7: Roe, M=0.1: velocity profiles at three stations, skin friction, and Nusselt number

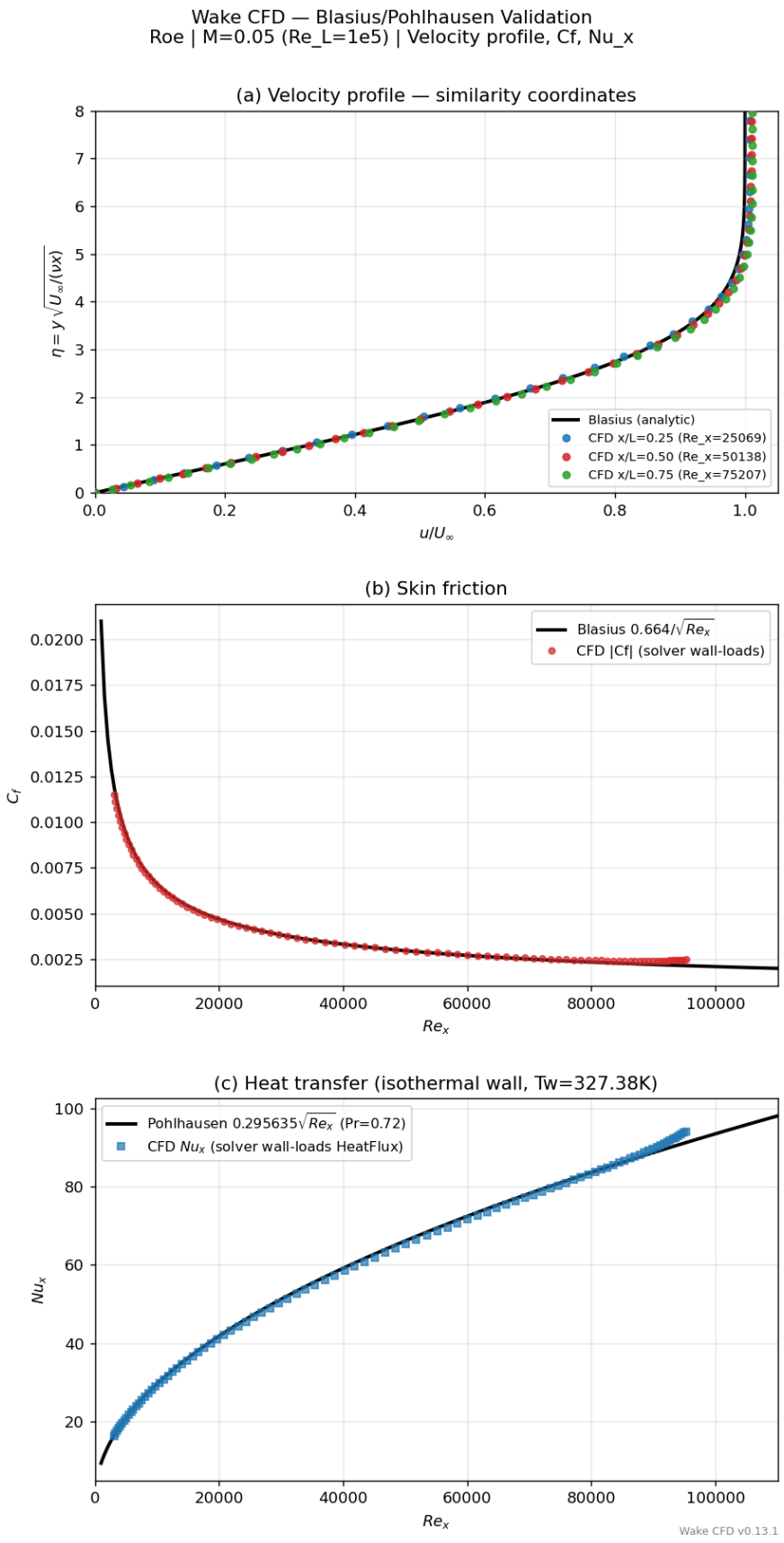


Figure 3.8: Roe, M=0.05: velocity profiles at three stations, skin friction, and Nusselt number

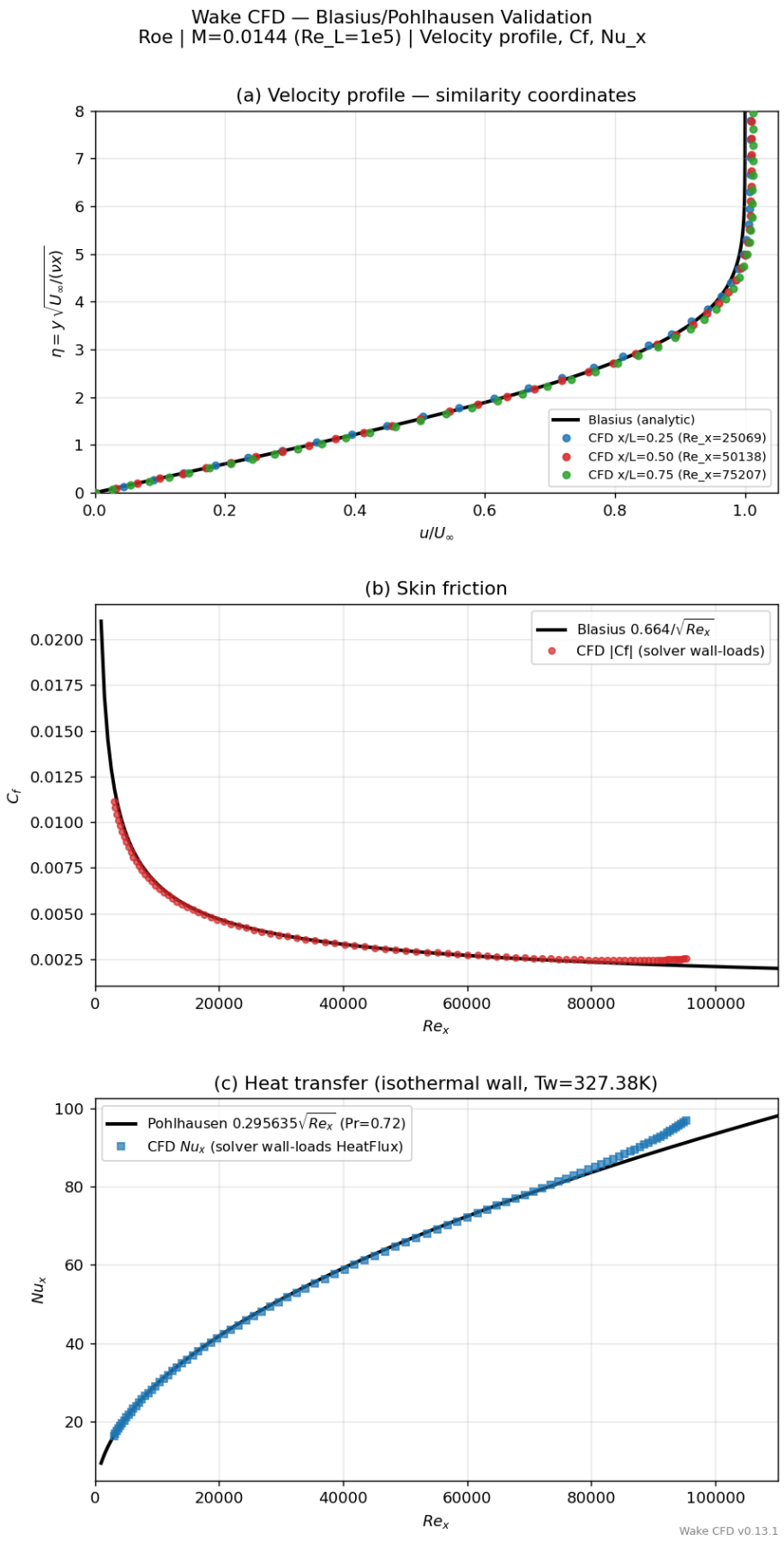


Figure 3.9: Roe, M=0.0144: velocity profiles at three stations, skin friction, and Nusselt number

For qualitative reference, the two contour plots below (`M=0.1`) show the velocity and temperature fields near the leading edge, illustrating the developing momentum and thermal boundary layers on the isothermal wall.

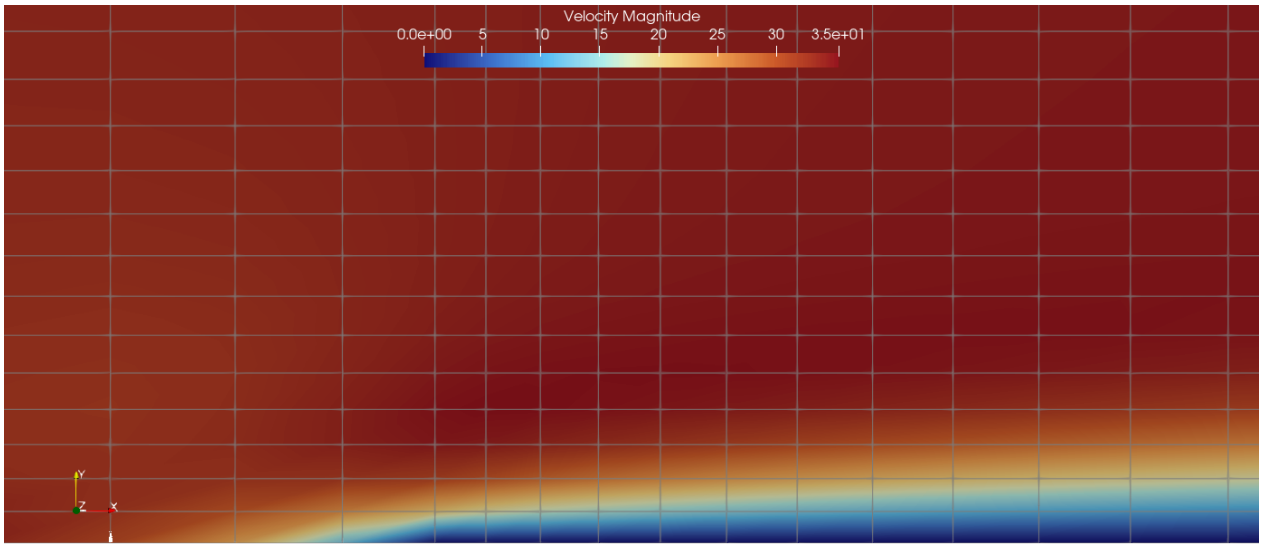


Figure 3.10: Roe, M=0.1: velocity-magnitude contour near the leading edge

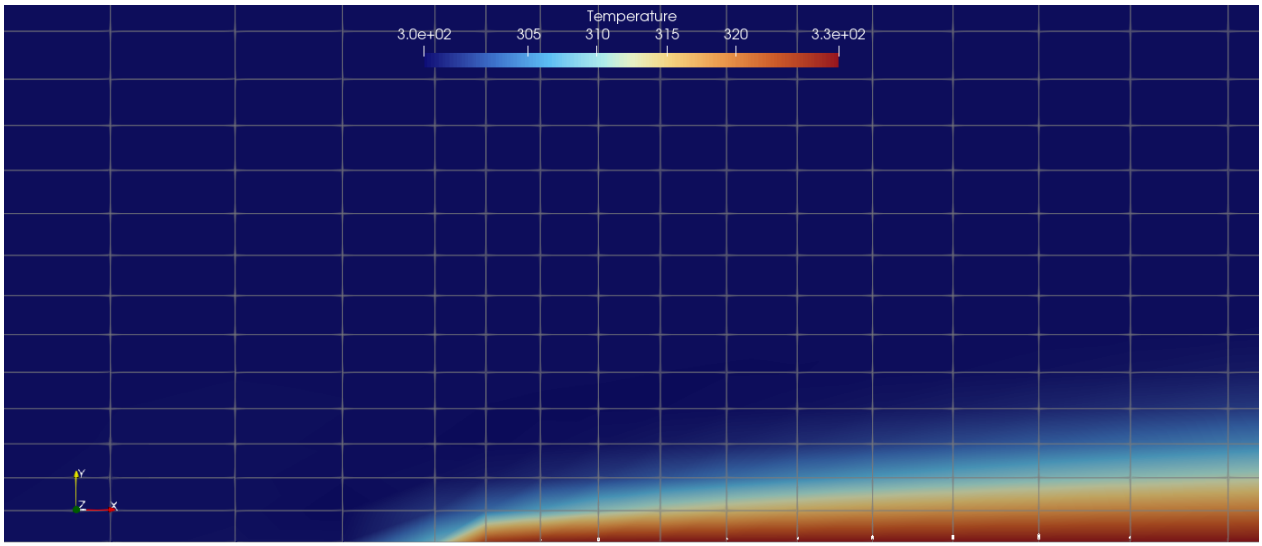


Figure 3.11: Roe, M=0.1: temperature contour near the leading edge

3.9 Conclusions and Applicable Scope

- The five all-speed schemes (`AUSM+up`, `AUSM+up2`, `SLAU`, `SLAU2`, `Roe-Turkel`) agree well with both the Blasius velocity profile and the Pohlhausen heat-transfer solution from `M=0.1` down to `M=0.0144`, and are essentially indistinguishable from one another on this case.

- `Roe-Turkel` reaches its converged state in roughly 1/3–1/4 the iterations of the other six schemes at the same Mach numbers; its practical advantage here is convergence speed rather than accuracy.
- `JST`, run without low-Mach correction as a control case, shows the expected monotonic loss of accuracy as Mach decreases, confirming that some form of low-Mach treatment is needed for schemes of this type on this problem.
- `Roe`, also run without explicit low-Mach correction, unexpectedly remained close to the all-speed group down to `M=0.0144` on this mesh and Reynolds number. This should not be read as a general claim that `Roe` does not need low-Mach treatment — it has not been checked at other mesh densities, Reynolds numbers, or geometries, and is reported here as an observation specific to this case.
- These results apply only to a 2D, steady, laminar flat-plate boundary layer at `Re_L=1×10^5`. They cannot be generalized to turbulence, pressure gradients, curved surfaces, separation, transition, or other Reynolds numbers.
- Follow-on validation should vary mesh resolution, Reynolds number, and wall-temperature ratio independently to check whether the `Roe`/`JST` split observed here persists.

This case does not establish absolute accuracy of the Wake CFD solver. It defines minimum applicable numerical-analysis conditions for a low-Mach viscous-wall problem, with and without wall heat transfer, with zero pressure gradient on a two-dimensional geometry.

3.10 References

- Blasius, H., "Grenzschichten in Flüssigkeiten mit kleiner Reibung," *Zeitschrift für Mathematik und Physik*, 56, 1908, pp. 1–37.
- Pohlhausen, E., "Der Wärmeaustausch zwischen festen Körpern und Flüssigkeiten mit kleiner Reibung und kleiner Wärmeleitung," *Zeitschrift für Angewandte Mathematik und Mechanik*, 1, 1921, pp. 115–121.
- White, F.M., *Viscous Fluid Flow*, 3rd ed., McGraw-Hill, 2006 (Blasius and Pohlhausen similarity solutions, Chapter 4).

4 2D Turbulent Flat-Plate Boundary Layer — NASA TMR SA Verification

Code-to-code verification of wall friction, eddy viscosity, and grid convergence for the Spalart–Allmaras model (against CFL3D/FUN3D)

4.1 Run Provenance and Artifacts

Item	Value
Wake CFD baseline version	`0.23.0`
Solver	DBNS
Compute device	CPU
Parallel execution	8 MPI ranks
Arithmetic precision	Mixed tier
Run date	2026-10-15

> **Note**
>
> Results depend on the solver build that produced them. Read every figure in this report together with the version and date above — re-running the same input on a later build may give different numbers.
> All ten runs (five meshes × two gradient methods) used the same input apart from the mesh and the gradient method. Eight of them ran on `0.21.2` from start to end; the two `545×385` runs ended on `0.21.4`.

4.1.1 Downloadable Files

Not available: standalone input decks and solver result files have not yet been published for download.

4.2 Verification Objective

This case simulates a turbulent boundary layer over a flat plate with zero pressure gradient using the Spalart–Allmaras (SA) model. It compares Wake CFD results with the meshes, conditions, and reference data published by the NASA Turbulence Modeling Resource (TMR). The TMR flat-plate case is a standard benchmark that provides grid-convergence results from two mature, independent RANS codes, CFL3D and FUN3D, on the same mesh family. It verifies Wake CFD for:

- skin-friction coefficient (`Cf`) and eddy-viscosity (`mu_t`) prediction with the SA turbulence model
- the direction and rate of convergence toward the reference as the mesh is refined
- the effect of the gradient method (Green–Gauss versus weighted least squares) on the result and on its convergence with the mesh
- reproduction of the law of the wall in wall coordinates (`u+` versus `y+`)
- behavior of wind-tunnel total-pressure inlet and outlet boundaries (`pressure_inlet`/`pressure_outlet`)

4.3 Reference Solution and Data

The NASA TMR flat-plate case is a zero-pressure-gradient (ZPG) flat plate at `Mach=0.2` and `Re_L=5×10^6`, with `L=1 m`. It defines a five-level grid-convergence family from `35×25` to `545×385`; all five levels were run in Wake CFD, each with two gradient methods. TMR publishes numerical grid-convergence data from CFL3D (structured, cell-centered) and FUN3D (unstructured, node-centered), enabling direct comparison on the same meshes and stations.

Item	Setting
References	CFL3D (cell-centered) and FUN3D (node-centered), published by NASA TMR

4.4 Simulation Conditions

Item	Setting
Dimension	3D (one-cell spanwise extrusion; effectively 2D flow)
Geometry	ZPG flat plate, `x=[0, 2] m` (leading edge `x=0`, reference length `L=1 m`)
Analysis	Steady, compressible DBNS, RANS (Spalart–Allmaras)
Mach	`0.2`
`Re_L`	`5×10^6`
Reference quantities	Reference area `2`, as in the CFL3D (`SREF`) and FUN3D (`area_reference`) inputs; with it `C_D` is the plate's streamwise force coefficient

4.5 Mesh

The meshes are the grids distributed by the NASA Turbulence Modeling Resource, used as distributed (the one-cell spanwise extrusion of the 2D grid family), without modification.

Mesh	Streamwise × wall-normal	Node count (including spanwise extrusion)
Coarsest	35 × 25	1,750
Coarse	69 × 49	6,762
Medium	137 × 97	26,578
Fine	273 × 193	105,378
Finest	545 × 385	419,650

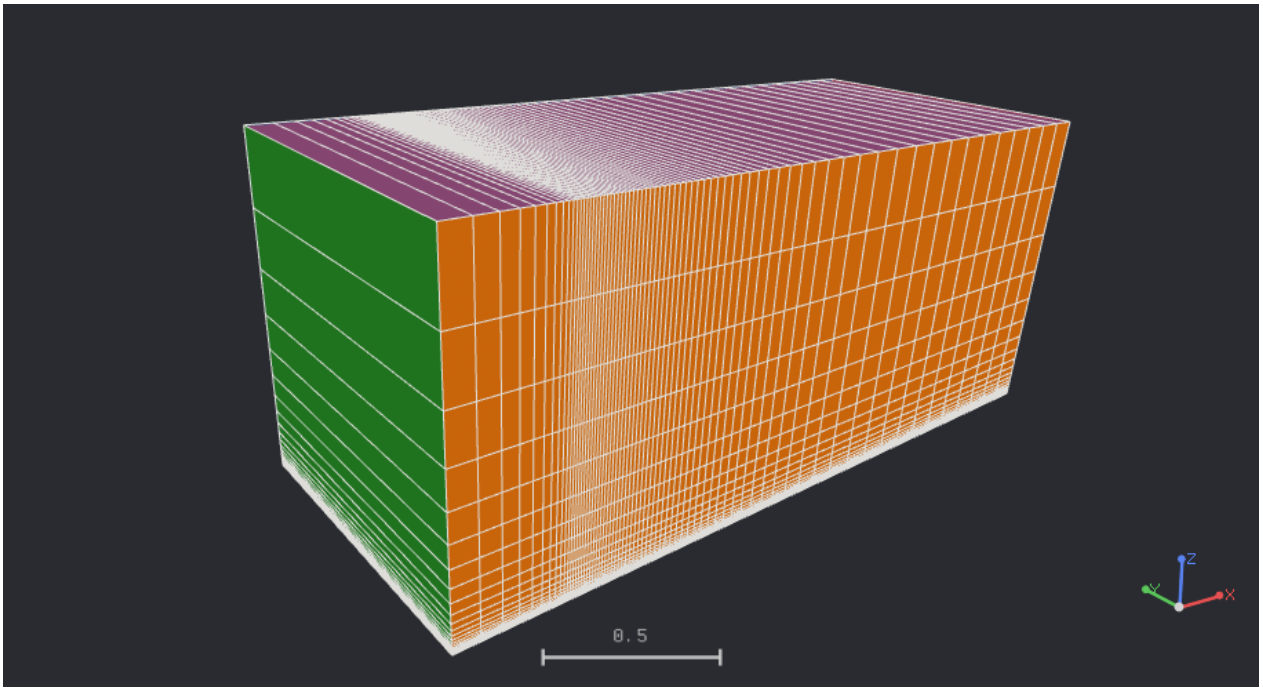


Figure 4.1: The `69×49` mesh in three dimensions — one cell in the spanwise direction; the plate is the bottom face, the upstream inlet is on the left, and the colors distinguish boundary groups

4.6 Boundary and Initial Conditions

Using a uniform `farfield` condition on the boundary-layer exit plane produces a near-wall pressure gradient. Therefore, a wind-tunnel-style domain uses the `pressure_inlet/pressure_outlet` combination. For the general definition of each boundary condition, see **Domain and Boundary Conditions** in the public Wake CFD documentation.

Boundary	Segment	Type	Setting
Wall	Plate, `x [0,2]`	`wall`	no-slip, adiabatic
Symmetry plane	Upstream slip segment + spanwise front/rear faces	`symmetry`	—
Inlet	Upstream	`pressure_inlet`	Total pressure `104190.6 Pa`, total temperature `302.4 K`, freestream `nu_tilde/nu = 3`
Outlet	Downstream	`pressure_outlet`	Back pressure `101325 Pa`
Farfield	Top	`farfield`	`Mach 0.2`, `101325 Pa`, `300 K`, freestream `nu_tilde/nu = 3`

Initial field: Not reported.

4.7 Numerical Methods

Item	Setting
Convergence criterion	Force-based — the drag and normal force coefficients each changing by less than `1×10` over 1,000 iterations. The `545×385` runs used a drag-only criterion (change below `1×10` over 1,000 iterations) and ended on an iteration cap and a manual stop, respectively, before it was met (see *Convergence History*)
Turbulence model	SA (Spalart–Allmaras) with the `ft2` term, `Pr_t = 0.9`
Convective scheme	Roe, no limiter, entropy fix off, `umuscl_kappa = 0.5`
Gradient method	Green–Gauss (`gg`) and weighted least squares (`wls`), each run on all five meshes (the selected method is also used for the viscous stresses and the SA terms)
Time integration	Euler implicit; FGMRES with DILU preconditioning (flow and turbulence)
CFL	Adaptive, `5 → 100` (reached `100` within about 20 iterations on all ten runs and stayed there)
Gas model	Ideal gas, `gamma = 1.4`, Sutherland viscosity (`S = 110.4 K`, reference viscosity set so that `Re_L = 5×10^6`), constant Prandtl number `0.72`

Note

Assumptions and differences from the references.

- The TMR page and the CFL3D/FUN3D inputs specify only the reference temperature (`540 °R = 300 K`) and leave the viscosity law and the laminar Prandtl number to the codes' defaults. Sutherland viscosity with `Pr = 0.72` was assumed to match those defaults; this was not isolated, but the finest-mesh differences below are small.
- The reference inputs differ from each other in the reconstruction setting: the CFL3D input uses `RKAP0 = 0.33333` (`kappa = 1/3`), while FUN3D's 2013 input uses `kappa_umuscl = 0.5`. Wake CFD was run with `umuscl_kappa = 0.5`.
- The TMR page states that both reference codes advected the turbulence variable with first-order upwinding. Wake CFD also advects the turbulence variables with a first-order scheme, so this matches.
- The TMR reference is the standard SA model (`SA`, with the `ft2` term); the page notes that `SA-noft2` gives essentially identical results for this case. The `ft2` term was enabled in these runs.

For the general input structure and turbulence-model settings, see the CLI and **Model Configuration** sections of the public Wake CFD documentation.

4.8 Results

4.8.1 Convergence History

Eight of the ten runs converged by the force-based criterion. The iteration counts (Green–Gauss / weighted least squares) were 1,882 / 1,900 on `35×25`, 2,797 / 2,787 on `69×49`, 4,485 / 4,479 on `137×97`, and 7,729 / 7,726 on `273×193`. The two `545×385` runs did not end on the criterion and are described below (19,999 / 18,320 iterations in total, about 22.7 and 20.3 hours on 8 CPU cores).

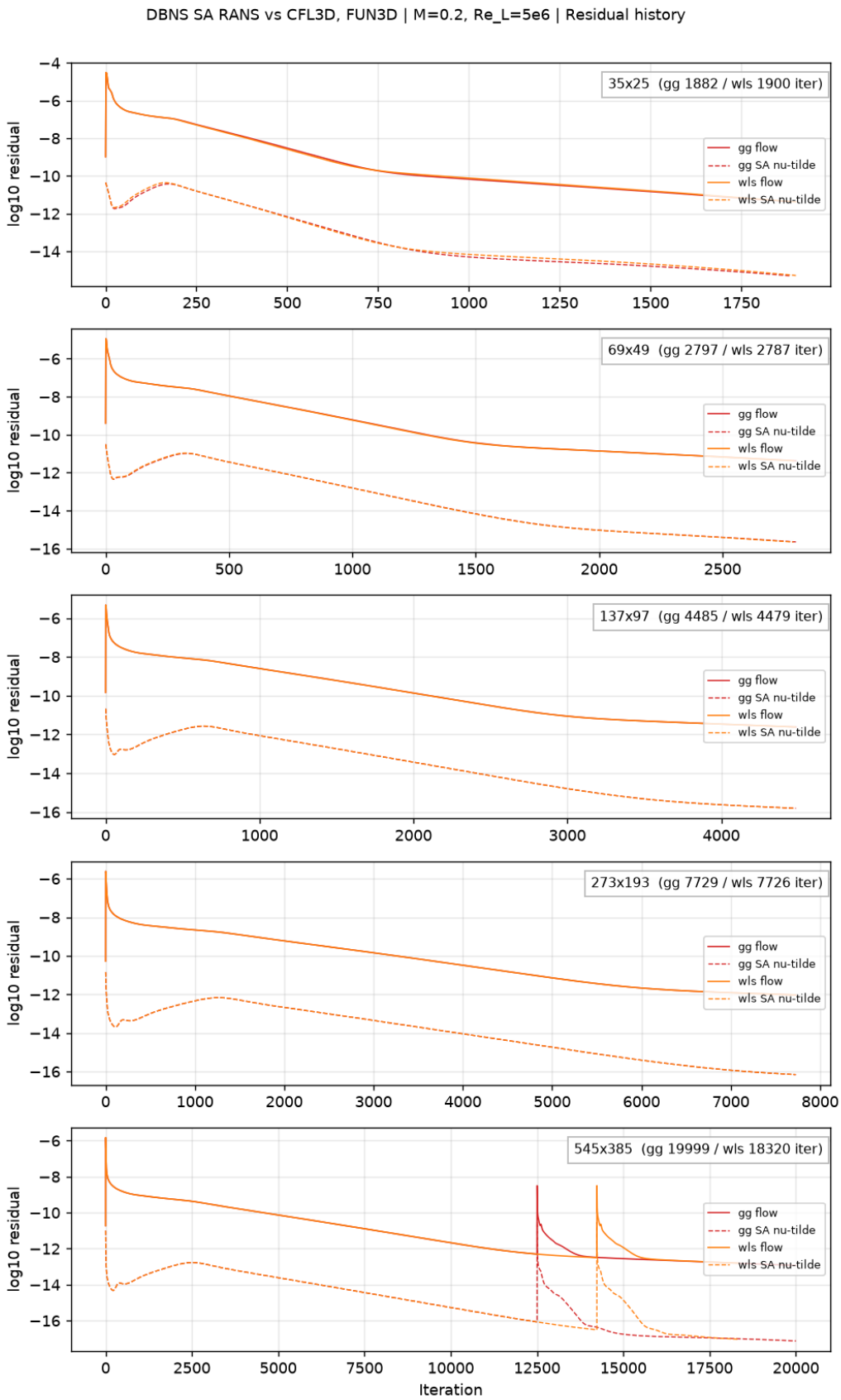


Figure 4.2: Residual history — absolute flow residual and SA `nu_tilde` residual, Green–Gauss and weighted least squares on each mesh

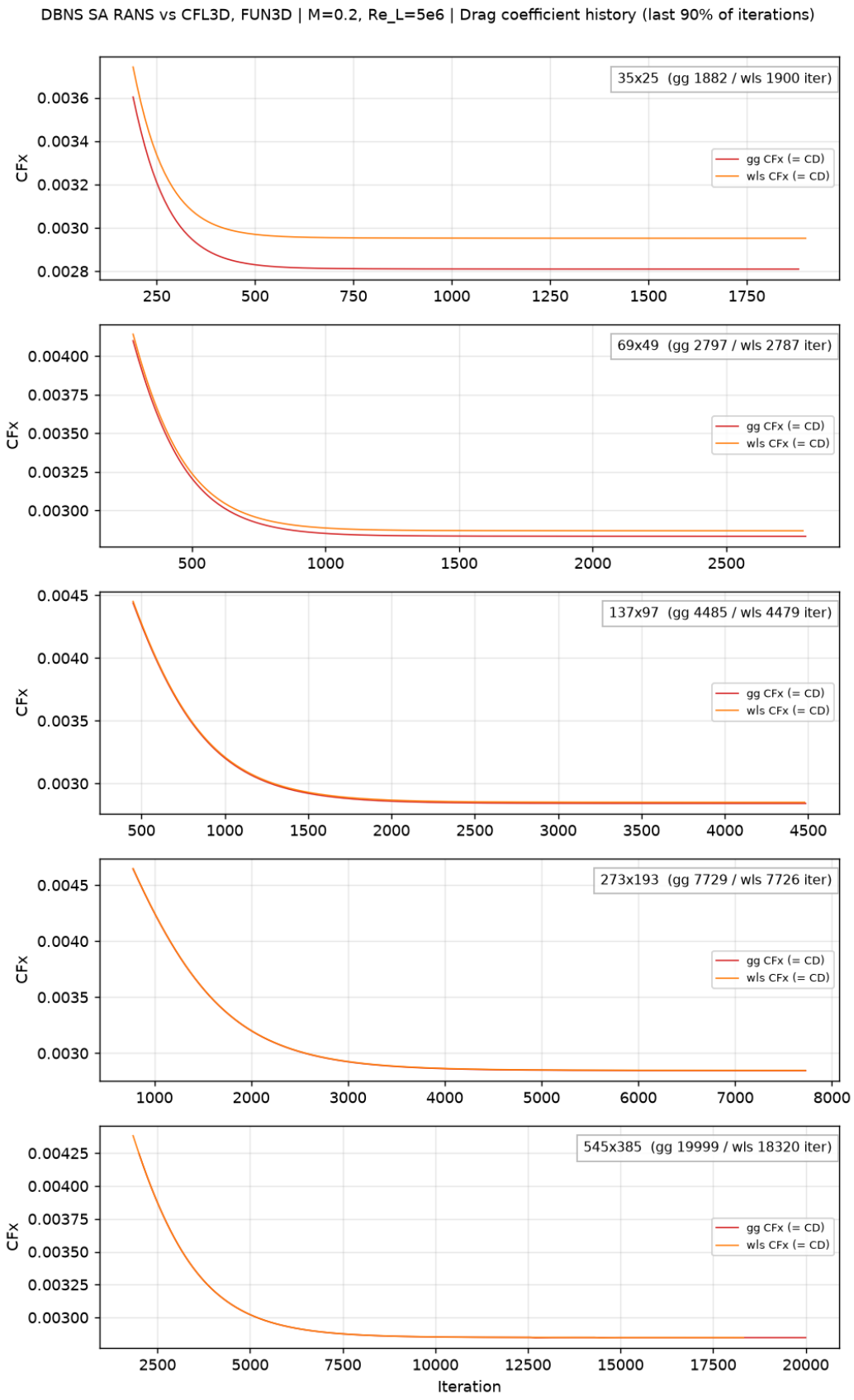


Figure 4.3: Drag-coefficient history on the five meshes (last 90% of the iterations)

The flow residual at termination was between `-11.4` and `-12.9` log10 (the termination criterion is force-based, not residual-based). The two gradient methods give residual and drag histories that are nearly indistinguishable on the three finest meshes.

The two `545×385` runs were stopped before reaching the criterion — the Green–Gauss run at the iteration cap (19,999) and the weighted-least-squares run manually at iteration 18,320. They are slightly less converged than the other eight: the drag coefficient was still drifting by about `0.002%` per 1,000 iterations, more than an order of magnitude below the mesh-to-mesh differences and the offsets from the references discussed below. Because the two ended at different iteration counts, the `C_D` difference between the methods on this mesh carries an uncertainty of order `5×10` (at a common iteration, 18,320, it is `5.4×10`).

4.8.2 Grid Convergence

The results were compared directly at the same mesh and station (`x=0.970084`) as the CFL3D/FUN3D data published by TMR.

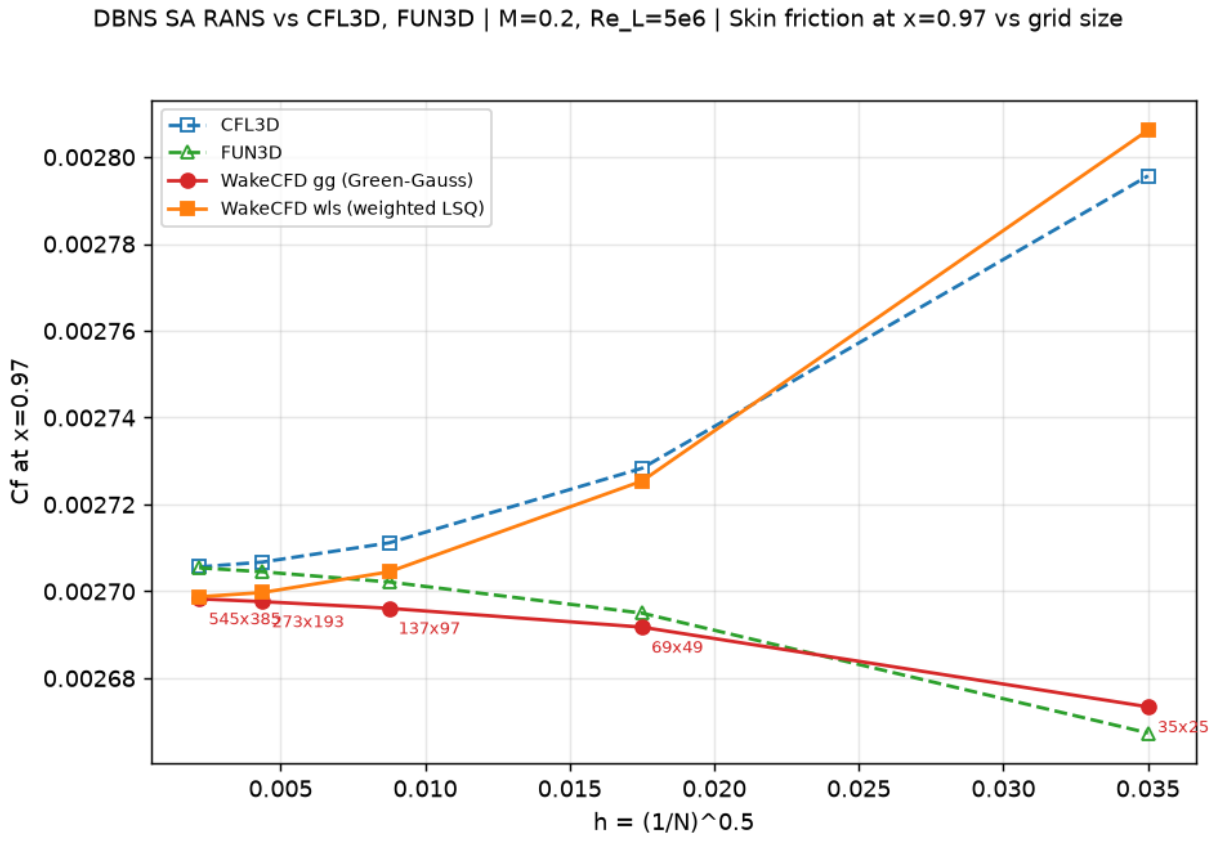


Figure 4.4: Grid convergence of `Cf(x=0.97)` — five Wake CFD points versus five CFL3D/FUN3D grid levels

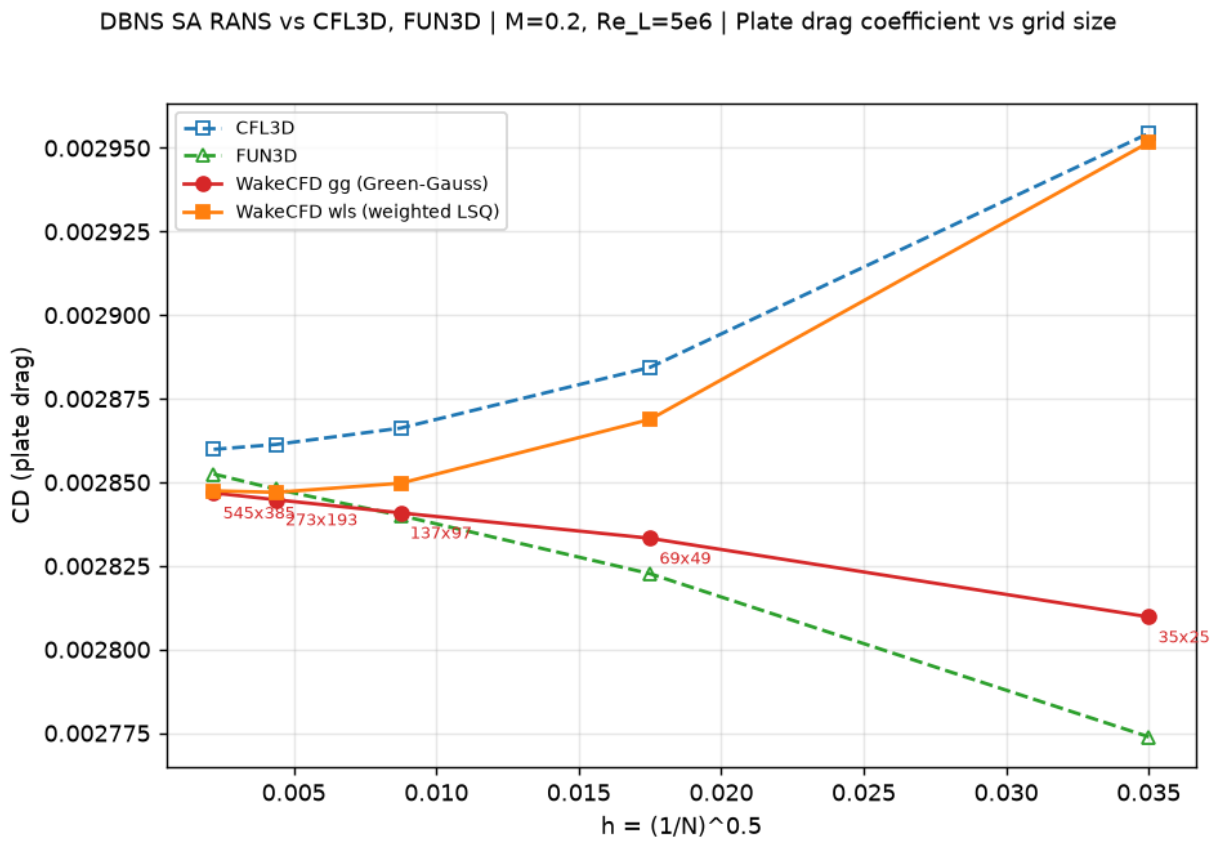


Figure 4.5: Grid convergence of the plate drag coefficient `C_D`

Both gradient methods are shown with the reference data. `Cf` is the skin-friction coefficient at `x=0.97` and `C_D` is the plate drag coefficient.

Skin-friction coefficient at `x=0.97`:

Mesh	Wall `y+` (0.97)	`Cf` gg	`Cf` wls	CFL3D	FUN3D
35×25	1.51	0.002673	0.002806	0.002796	0.002667
69×49	0.74	0.002692	0.002725	0.002728	0.002695
137×97	0.37	0.002696	0.002704	0.002711	0.002702
273×193	0.18	0.002698	0.002700	0.002707	0.002704
545×385	**0.09**	**0.002698**	**0.002699**	**0.002706**	**0.002705**

Plate drag coefficient:

Mesh	`C_D` gg	`C_D` wls	CFL3D	FUN3D
35×25	0.002810	0.002952	0.002954	0.002774
69×49	0.002833	0.002869	0.002884	0.002823
137×97	0.002841	0.002850	0.002866	0.002840
273×193	0.002845	0.002847	0.002861	0.002848

Mesh	C_D gg	C_D wls	CFL3D	FUN3D
545×385	**0.002847**	**0.002847**	**0.002860**	**0.002852**

Difference of Wake CFD relative to each reference code, on the same mesh:

Mesh	Method	Cf vs. FUN3D	Cf vs. CFL3D	C_D vs. FUN3D	C_D vs. CFL3D
35×25	gg	+0.23%	−4.37%	+1.29%	−4.90%
35×25	wls	+5.20%	+0.38%	+6.41%	−0.09%
69×49	gg	−0.12%	−1.34%	+0.38%	−1.77%
69×49	wls	+1.13%	−0.11%	+1.64%	−0.54%
137×97	gg	−0.22%	−0.56%	+0.03%	−0.89%
137×97	wls	+0.09%	−0.25%	+0.34%	−0.58%
273×193	gg	−0.25%	−0.34%	−0.11%	−0.58%
273×193	wls	−0.18%	−0.26%	−0.03%	−0.50%
545×385	gg	**−0.26%**	**−0.27%**	**−0.20%**	**−0.46%**
545×385	wls	**−0.25%**	**−0.25%**	**−0.18%**	**−0.43%**

- **On the finest mesh the two gradient methods give the same result** (C_D 28.47 counts for both and Cf 26.98 / 26.99 counts of 1×10) and agree with both references within 0.46% (C_D) and 0.27% (Cf).
- **On coarse meshes the result depends strongly on the gradient method.** At 35×25 the weighted-least-squares result is close to CFL3D (C_D −0.09%) and the Green–Gauss result is close to FUN3D (C_D +1.29%). The two references differ from each other by 6.5% in C_D there. The reason was not isolated; it is not a property of node-centered versus cell-centered discretization, since both Wake CFD runs use the same discretization apart from the gradient.
- **A systematic offset of about −0.25% in Cf relative to both references remains on the finest meshes** for both gradient methods, and it does not shrink with refinement (Green–Gauss: −0.25% at 273×193 and −0.26% at 545×385). The two reference codes agree with each other to within 0.01% on the finest mesh, so this is not scatter between codes, and a discretization error would decrease with refinement. This points to a difference in setting or model between the Wake CFD runs and the references rather than a mesh effect. Candidates are the viscosity law (assumed, see above), umuscl_kappa, and the way Cf is extracted at the station; none has been isolated. The corresponding C_D difference is −0.20% (Green–Gauss) and −0.18% (weighted least squares) relative to FUN3D. The drift left at the end of the runs (about 0.002% per 1,000 iterations) is well below this offset.

4.8.3 Difference between the gradient methods

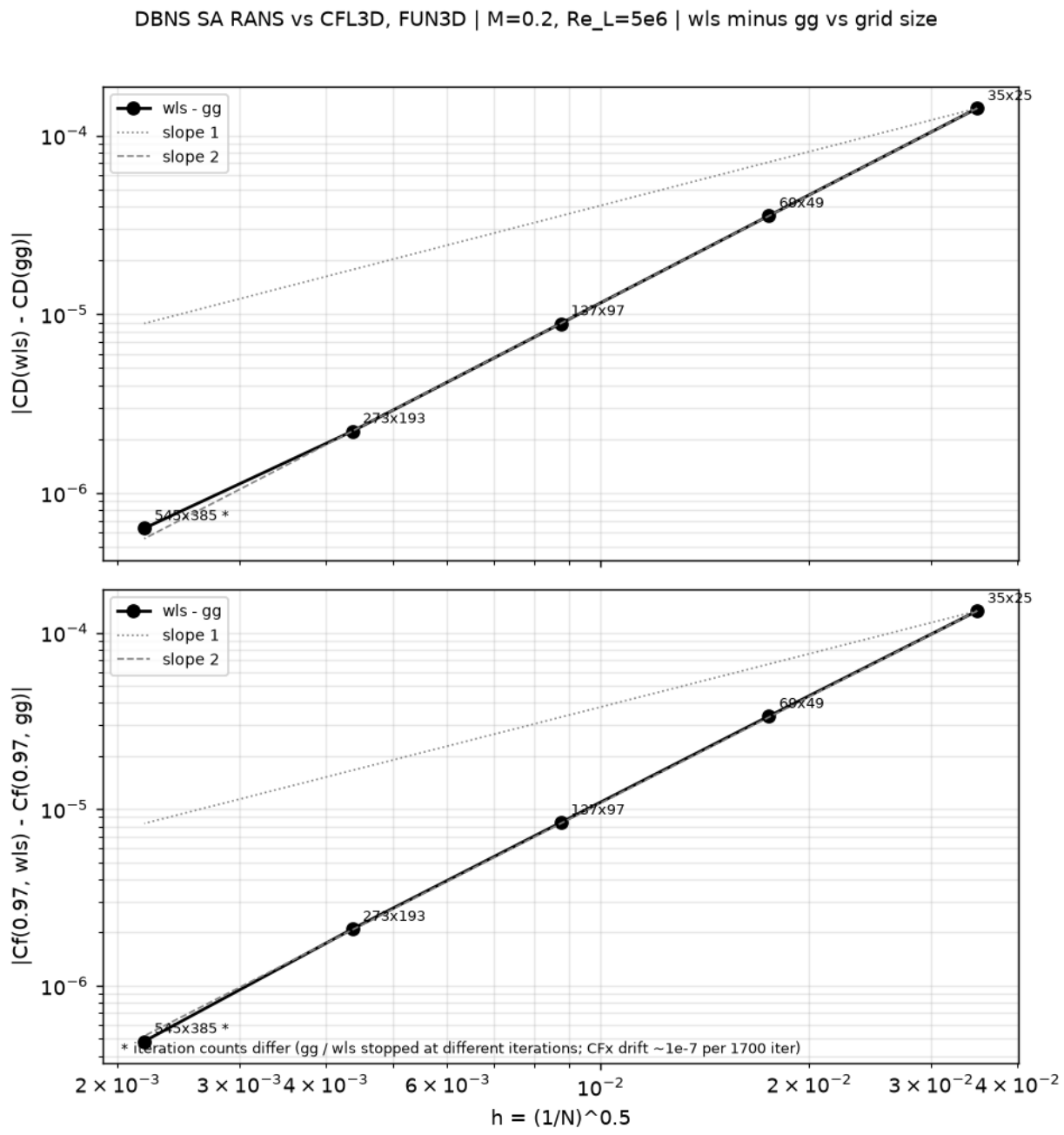


Figure 4.6: Difference between the weighted-least-squares and Green–Gauss results versus mesh size

The difference between the two methods drops by a factor of about four ($\mathtt{h}^2$) at each refinement:

Mesh	wls − gg, `C_D`	wls − gg, `Cf` (0.97)
35×25	1.419e-4	1.328e-4

Mesh	wls − gg, C_D	wls − gg, Cf (0.97)
69×49	3.557e-5	3.365e-5
137×97	8.868e-6	8.395e-6
273×193	2.215e-6	2.097e-6
545×385 (*)	6.3e-7	4.8e-7

(*) The two runs ended at different iteration counts (gg 19,999, wls 18,320), which adds an uncertainty of order 5×10 per 1,000 iterations. At the common iteration 18,320 the C_D difference is 5.4e-7. An h^2 extrapolation from the 273×193 row gives about 5.5e-7 (C_D) and 5.2e-7 (Cf).

Both methods therefore converge to the same solution, and the difference between them is a second-order term. All five points lie close to the slope-two line, including the 545×385 point, whose value carries an uncertainty of a few 10 from the residual drift (see *Convergence History*).

4.8.4 Observed order of convergence

The observed order p = log2(Δ_k / Δ_{k+1}) is computed from the changes Δ between successive meshes (each step halves the mesh spacing, so p = 2 means the change drops by a factor of four). The three values per row come from the three consecutive pairs of steps: 35→69→137, 69→137→273, and 137→273→545.

Code	Quantity	p
CFL3D	C_D	1.95 / 1.89 / 1.75
CFL3D	Cf (0.97)	1.97 / 1.96 / 1.98
FUN3D	C_D	1.49 / 1.14 / 0.80
FUN3D	Cf (0.97)	1.94 / 1.62 / 1.34
Wake CFD, gg	C_D	1.63 / 0.95 / 0.95 †
Wake CFD, gg	Cf (0.97)	2.08 / 1.50 / 1.28 †
Wake CFD, wls	C_D	2.12 / 2.81 / — ‡
Wake CFD, wls	Cf (0.97)	1.95 / 2.13 / 2.28

† The last value uses the 545×385 Green–Gauss run, which still drifts by about 0.0006 counts of 1×10 per 1,000 iterations (about 3% of the last C_D change), so digits beyond the first decimal are not reliable.

‡ The C_D change from 273×193 to 545×385 is +0.004 counts, with the opposite sign to the previous step, so p cannot be computed; it is of the same size as the residual drift.

CFL3D converges at second order throughout. The weighted-least-squares results behave like CFL3D over the first two steps (about second order) and the Cf values stay near second order on the finest step (the C_D step is within the noise). The Green–Gauss results and FUN3D both fall below second order on the fine meshes (about first order for C_D, between first and second for Cf). Both gradient methods use the same umuscl_kappa = 0.5 (CFL3D uses 1/3), so that setting alone cannot explain the lower order of the Green–Gauss results. The gradient method is a candidate, but this has not been tested directly. Because the order is below two for some codes, the finest-mesh values are not extrapolated with an h^2 law; the 545×385 values are the best available estimate of the grid-converged result rather than an extrapolated limit.

4.8.5 Detailed Comparison

The profiles below show the Wake CFD results (Green–Gauss and weighted least squares) against the CFL3D and FUN3D references (finest reference meshes). The profile figures use the `545×385` mesh.

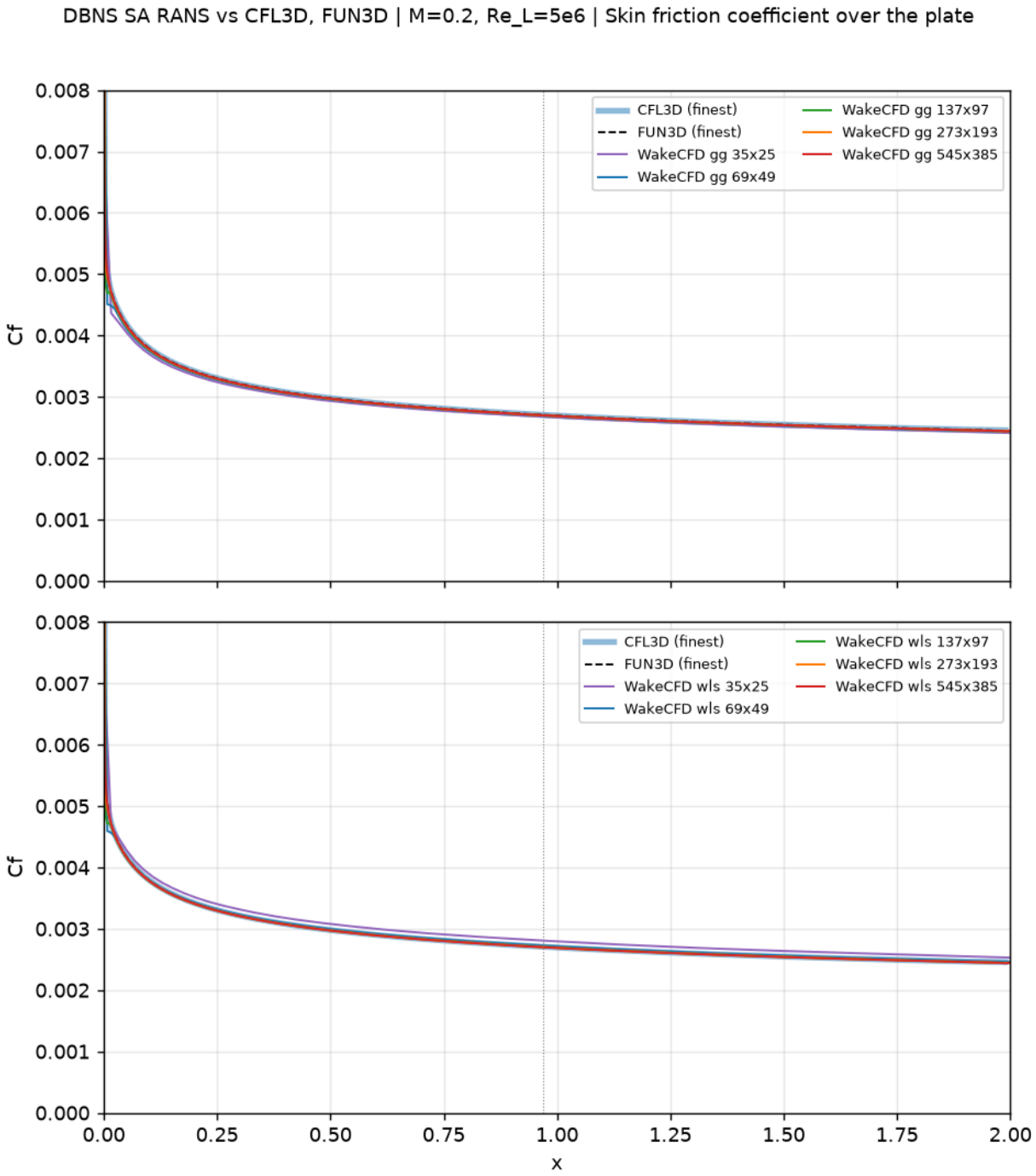


Figure 4.7: `Cf(x)` over the full plate on all five meshes for both gradient methods, against CFL3D and FUN3D

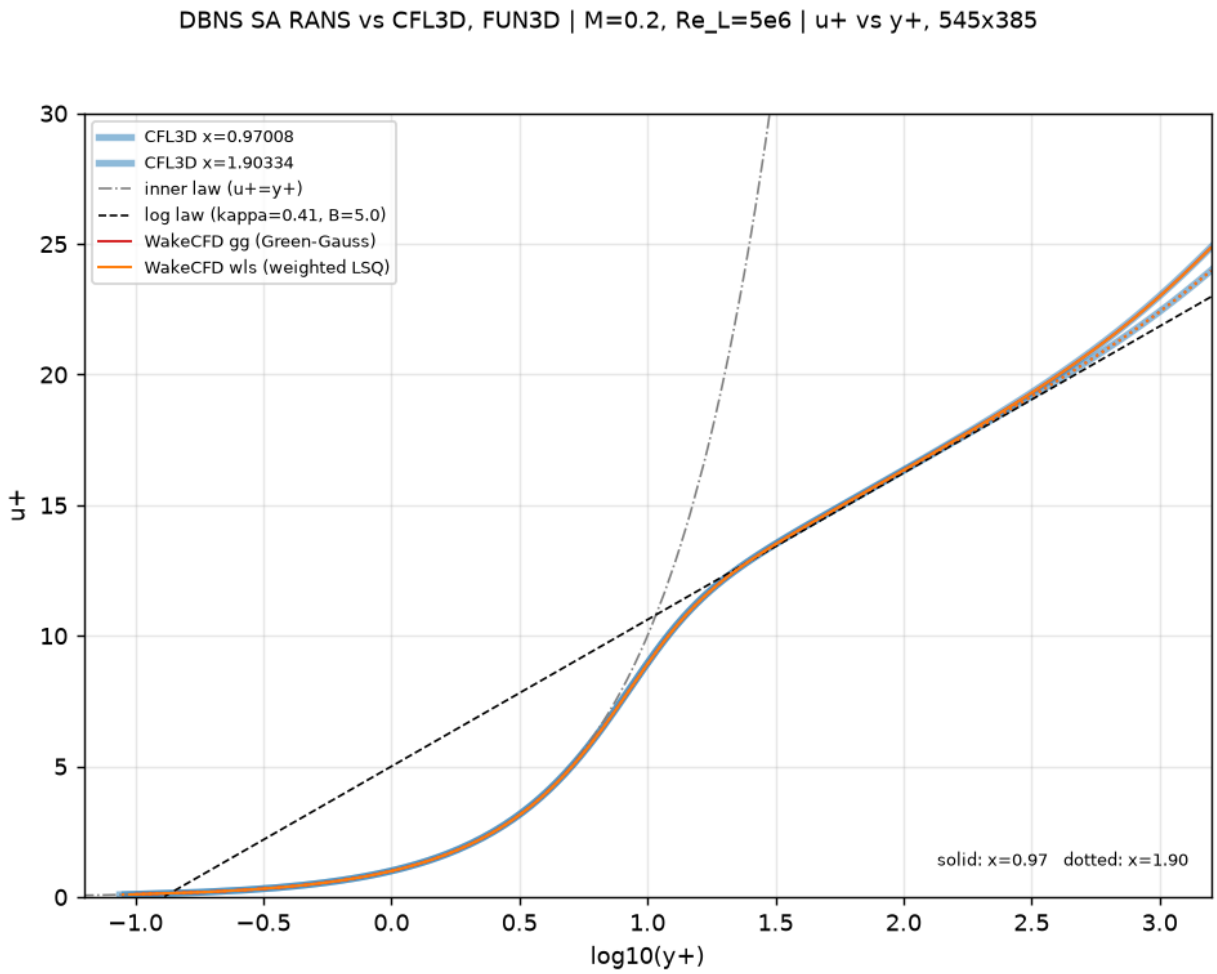


Figure 4.8: u+ versus y+ at x=0.97 (solid) and x=1.90 (dotted) against the law of the wall

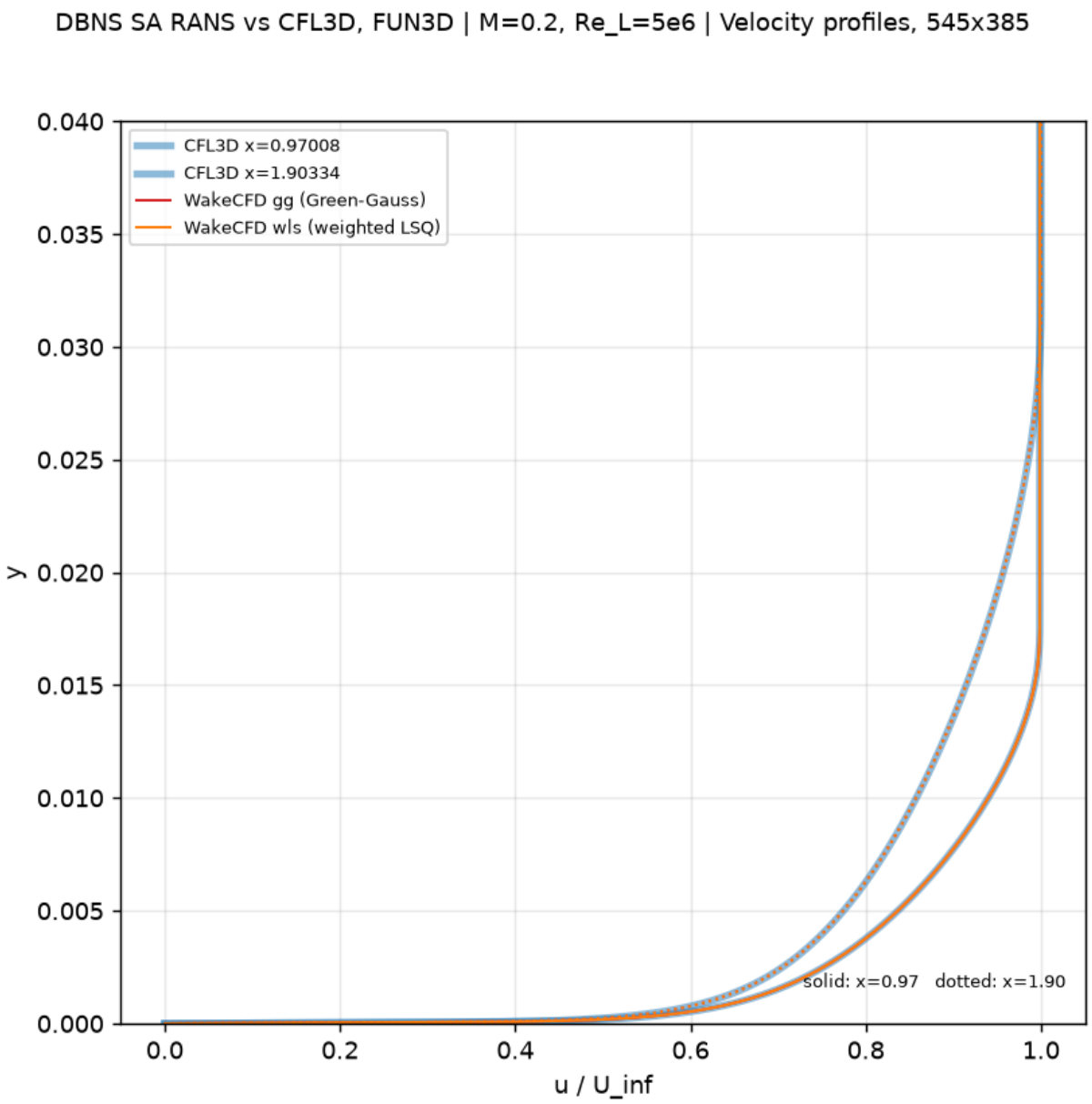


Figure 4.9: Velocity profiles `u/U_inf` versus height at x=0.97 and x=1.90

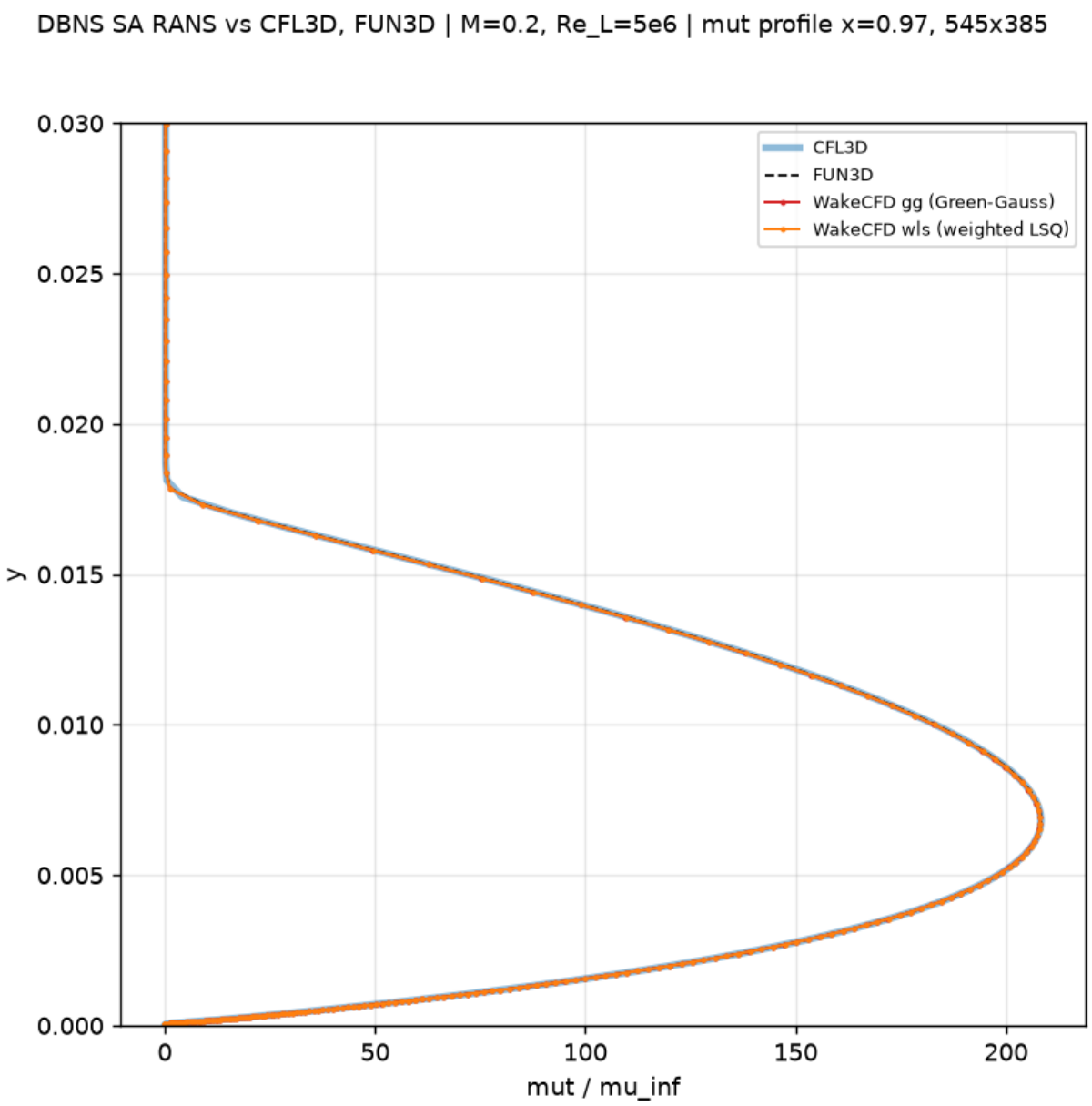


Figure 4.10: Eddy-viscosity-ratio profile at x=0.97

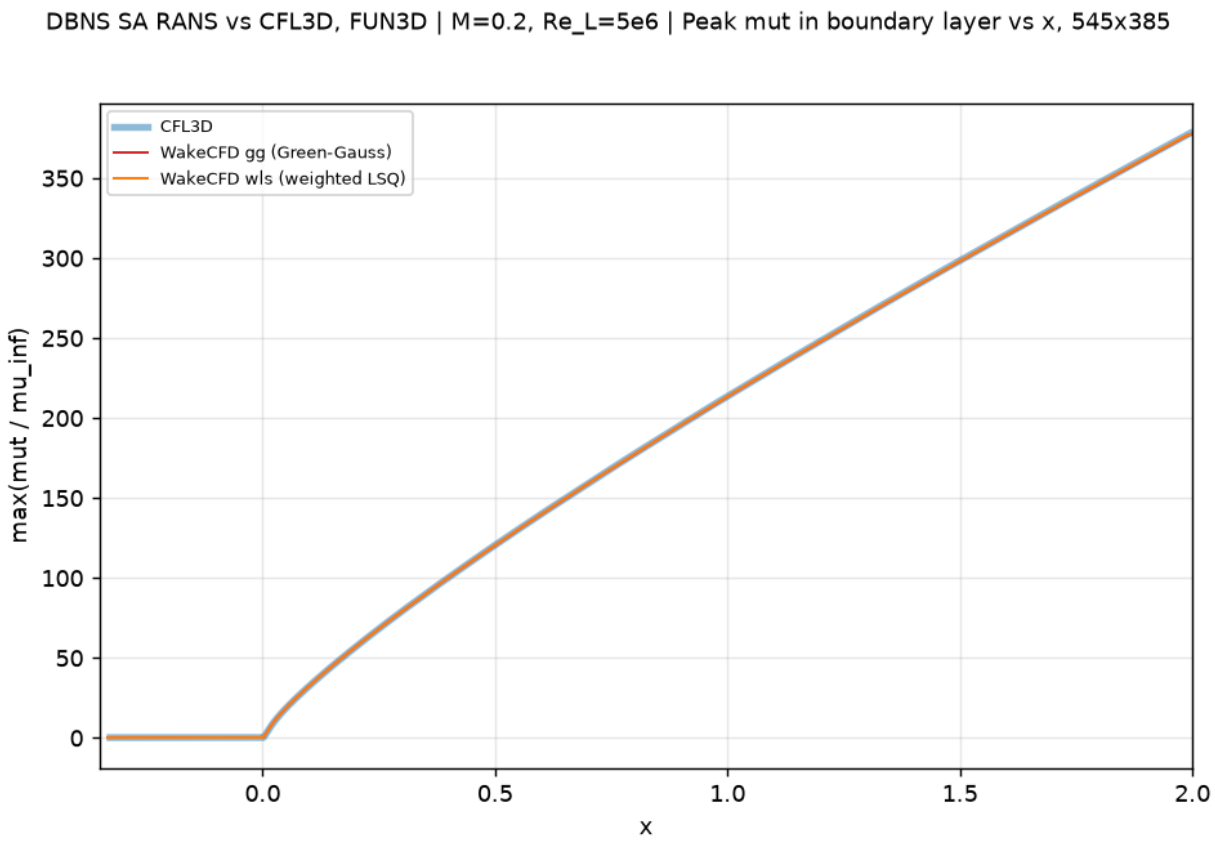


Figure 4.11: Maximum eddy-viscosity ratio in the boundary layer along the plate

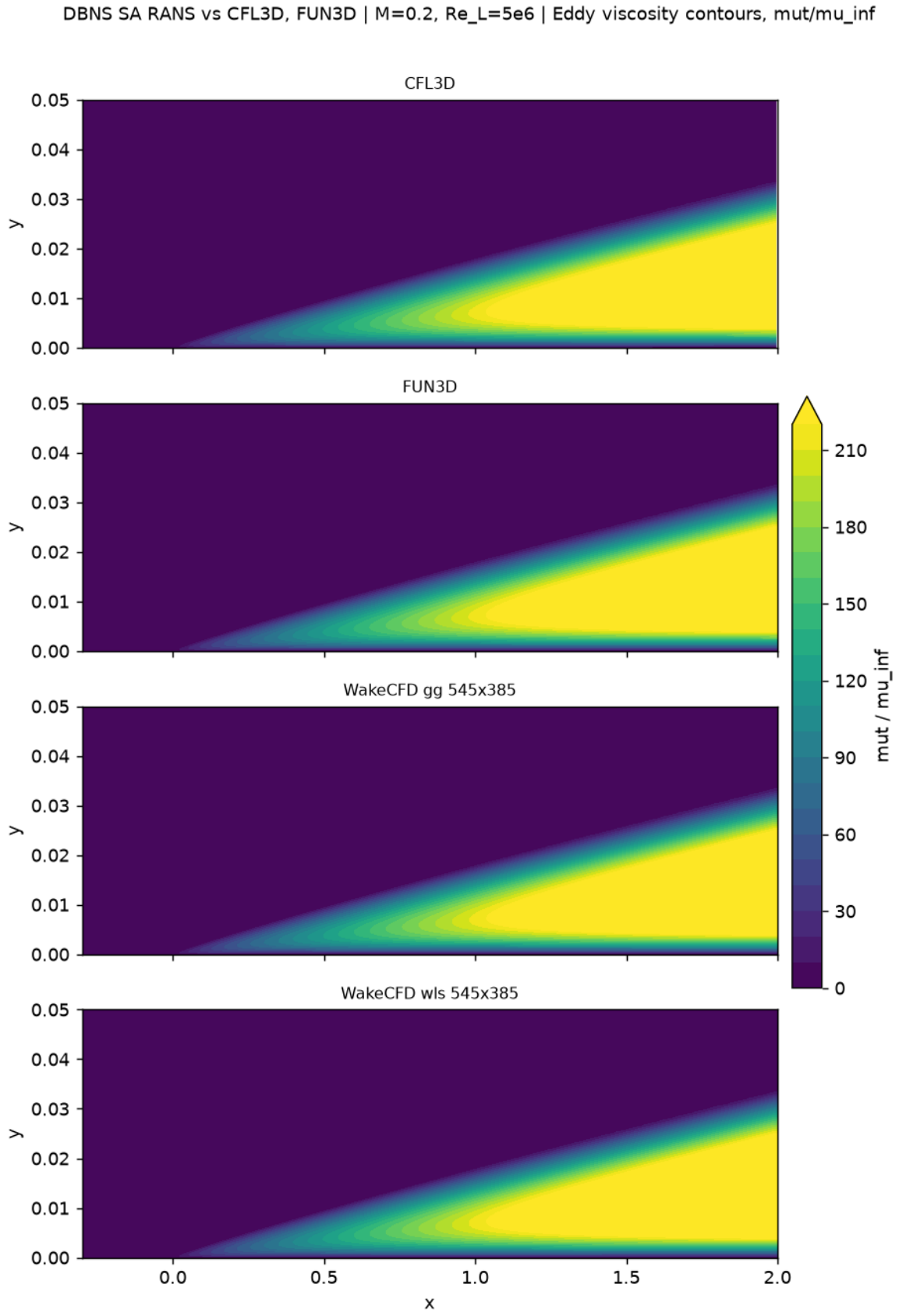


Figure 4.12: Eddy-viscosity-ratio contours — CFL3D, FUN3D, and Wake CFD (both gradient methods) on the `545×385` mesh

Mesh	Max `mu_t/mu_inf` (0.97) gg / wls	Outer `u+` plateau (0.97) gg / wls
35×25	203.7 / 228.7	27.21 / 26.55
69×49	206.3 / 212.4	27.10 / 26.93
137×97	208.2 / 209.6	27.07 / 27.03
273×193	208.1 / 208.4	27.06 / 27.05
545×385	**208.1 / 208.1**	**27.05 / 27.05**
CFL3D (545×385)	208.3	27.05
FUN3D (545×385)	208.3	—
Finest-grid difference (vs. CFL3D / FUN3D)	−0.12% / −0.13% (gg), −0.08% / −0.09% (wls)	0.00%

On the finest meshes the peak eddy-viscosity ratio at `x=0.97` is within 0.15% of the references for both gradient methods (Green–Gauss from `137×97`, weighted least squares from `273×193`), while the coarsest meshes deviate (−2.2% for Green–Gauss and +9.8% for weighted least squares at `35×25`). The profile, the peak distribution along the plate, and the contours agree with both references. The `u+` versus `y+` curves follow the law of the wall through the viscous sublayer, the log region, and the outer plateau. The curves were compared visually; only the tabulated quantities above were quantified. The `Cf` offset of about −0.25% discussed above is not visible in these profile comparisons.

4.9 Conclusions and Applicable Scope

- The SA turbulence-model implementation agrees with the official NASA TMR references (CFL3D and FUN3D) on the finest mesh within 0.46% for `C_D` and 0.27% for `Cf`, for both gradient methods, and within 0.15% for the peak eddy-viscosity ratio.
- The full five-level grid-convergence family defined by TMR was run with both Green–Gauss and weighted-least-squares gradients. The two methods converge to the same solution, and the difference between them decreases as h^2. On coarse meshes the choice of method changes `C_D` by up to 5% at `35×25` and 1.3% at `69×49`, so the method matters for coarse-mesh accuracy but not for the converged result.
- A systematic difference of about −0.25% in `Cf` relative to both references remains for both gradient methods and does not shrink with refinement, so it is not a mesh effect. Its cause is not identified; candidates are the viscosity law, `umuscl_kappa`, and the extraction of `Cf` at the station.
- The observed order of convergence of the weighted-least-squares `Cf` is close to two on all three steps, while the Green–Gauss results and FUN3D fall below second order on the fine meshes (Green–Gauss about first order for `C_D`). The cause of the lower order is not identified. The `545×385` runs ended on an iteration cap / manual stop with a small residual drift, so the finest-mesh values should be read as converged to within the differences in the tables above, not as extrapolated limits.
- These results apply to a two-dimensional, zero-pressure-gradient flat plate at one subsonic condition (`M=0.2`). They cannot be generalized to pressure gradients, separation, transition, curved surfaces, or strong compressibility effects.

- Follow-on validation should isolate the settings behind the remaining `Cf` offset, compare other RANS models (such as SST), and extend to pressure-gradient and fully three-dimensional geometries.

This case shows that Wake CFD's SA turbulence-model implementation achieves accuracy comparable with mature reference codes for a subsonic flat-plate boundary layer without a pressure gradient. It establishes a minimum validation baseline for this range of conditions rather than an absolute accuracy guarantee.

4.10 References

- NASA Turbulence Modeling Resource: 2D Flat Plate Validation Case
- NASA Turbulence Modeling Resource: SA results for the 2D flat plate

5 2D Turbulent Flat-Plate Boundary Layer — NASA TMR SST Verification

Code-to-code verification of wall friction, eddy viscosity, and grid convergence for the Menter SST (k-) model (against CFL3D/FUN3D)

5.1 Run Provenance and Artifacts

Item	Value
Wake CFD baseline version	`0.22.0`
Solver	DBNS
Compute device	CPU
Parallel execution	8 MPI ranks
Arithmetic precision	Mixed tier
Run date	2026-10-20

> **Note**
>
> Results depend on the solver build that produced them. Read every figure in this report together with the version and date above — re-running the same input on a later build may give different numbers.
> All ten runs (five meshes × two gradient methods) used the same input apart from the mesh, the gradient method, and the turbulence pseudo-time-step reduction listed under *Numerical Methods*. The first nine runs used version `0.21.4`; the `545×385` weighted-least-squares run was made later on version `0.21.5`, so the two `545×385` runs are not from the same build. The sibling SA case (case-02) was run on version `0.21.2`.

5.1.1 Downloadable Files

Not available: standalone input decks and solver result files have not yet been published for download.

5.2 Verification Objective

This case simulates a turbulent boundary layer over a flat plate with zero pressure gradient using the Menter Shear-Stress-Transport (SST, k-) model. It reuses the mesh family, boundary conditions, and numerical method of the SA flat-plate verification case and compares Wake CFD SST results with the meshes, conditions, and reference data published by the NASA Turbulence Modeling Resource (TMR). It verifies Wake CFD for:

- skin-friction coefficient (`Cf`) and eddy-viscosity (`mu_t`) prediction with the SST turbulence model
- the direction and rate of convergence toward the CFL3D/FUN3D references as the mesh is refined
- the effect of the gradient method (Green–Gauss versus weighted least squares) on the result and on its convergence with the mesh
- turbulent-kinetic-energy (`k`) and specific-dissipation-rate (`omega`) profile agreement in the boundary layer

5.3 Reference Solution and Data

The NASA TMR flat-plate case is a zero-pressure-gradient (ZPG) flat plate at `Mach=0.2` and `Re_L=5×10^6`, with `L=1 m`. It defines a five-level grid-convergence family from `35×25` to `545×385`; all five levels were run in Wake CFD, each with two gradient methods. TMR publishes SST grid-convergence data from CFL3D (structured, cell-centered) and FUN3D (unstructured, node-centered) on the same mesh family, enabling direct comparison at matching mesh levels and stations. The TMR reference model is **SST-Vm** (vorticity-based production, without the second production term); TMR states that SST, SST-V, and SST-Vm give nearly identical results for this flat plate.

Item	Setting
References	CFL3D (cell-centered) and FUN3D (node-centered) SST-Vm results, published by NASA TMR

5.4 Simulation Conditions

Item	Setting
Dimension	3D (one-cell spanwise extrusion; effectively 2D flow)
Geometry	ZPG flat plate, `x=[0, 2] m` (leading edge `x=0`, reference length `L=1 m`)
Analysis	Steady, compressible DBNS, RANS (Menter SST, k- , 2003 variant, log- formulation)
Mach	`0.2`
`Re_L`	`5×10^6`

Item	Setting
Reference quantities	Reference area `2`, as in the CFL3D and FUN3D inputs; with it `C_D` is the plate's streamwise force coefficient

5.5 Mesh

The meshes are the grids distributed by the NASA Turbulence Modeling Resource, used as distributed (the one-cell spanwise extrusion of the 2D grid family), without modification.

Mesh	Streamwise × wall-normal	Node count (including spanwise extrusion)
Coarsest	35 × 25	1,750
Coarse	69 × 49	6,762
Medium	137 × 97	26,578
Fine	273 × 193	105,378
Finest	545 × 385	419,650

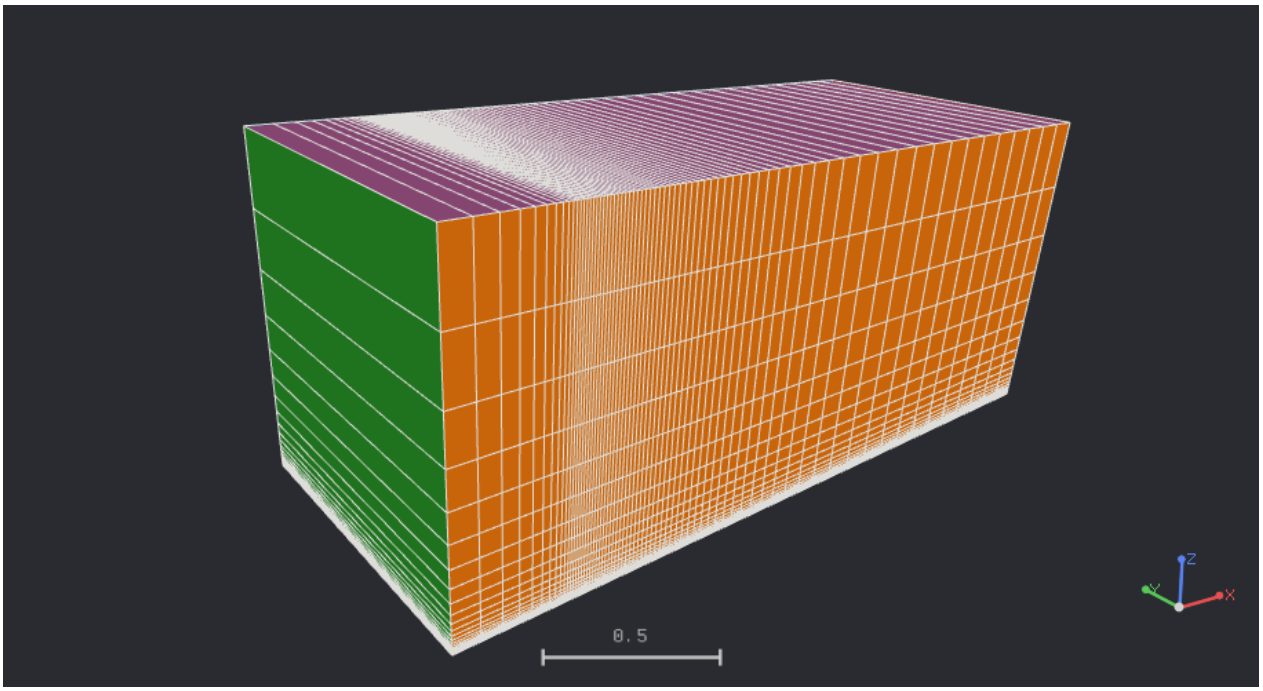


Figure 5.1: The `69×49` mesh in three dimensions — one cell in the spanwise direction; the plate is the bottom face, the upstream inlet is on the left, and the colors distinguish boundary groups

5.6 Boundary and Initial Conditions

Using a uniform `farfield` condition on the boundary-layer exit plane produces a near-wall pressure gradient. Therefore, a wind-tunnel-style domain uses the `pressure_inlet/pressure_outlet` combination. For the general definition of each boundary condition, see **Domain and Boundary Conditions** in the public Wake CFD documentation.

Boundary	Segment	Type	Setting
Wall	Plate, `x [0,2]`	`wall`	no-slip, adiabatic
Symmetry plane	Upstream slip segment + spanwise front/rear faces	`symmetry`	—
Inlet	Upstream	`pressure_inlet`	Total pressure `104190.6 Pa`, total temperature `302.4 K`, freestream turbulence as below
Outlet	Downstream	`pressure_outlet`	Back pressure `101325 Pa`
Farfield	Top	`farfield`	`Mach 0.2`, `101325 Pa`, `300 K`, freestream turbulence as below

The freestream turbulence follows the TMR SST definition: `k = 9×10  aω²` (1.088×10^{3} m²/s²) and `mu_t/mu = 0.009` (`omega = 8713 1/s`), set through a turbulence intensity of `3.873×10` and an eddy-viscosity ratio of `0.009` on the inlet and farfield. The solver log of these runs was not checked for the resulting `k` and `omega` values; the agreement of the `k` and `omega` profiles outside the boundary layer with the references (see *Detailed Comparison*) is the indirect check.

Initial field: Not reported.

5.7 Numerical Methods

Item	Setting
Convergence criterion	Force-based — the drag and normal force coefficients each changing by less than `1×10` over 1,000 iterations
Turbulence model	SST (Menter k- , 2003 variant), vorticity-based production (to match SST-Vm), `Pr_t = 0.9`
Convective scheme	Roe, no limiter, entropy fix off, `umuscl_kappa = 0.5`
Gradient method	Green–Gauss (`gg`) and weighted least squares (`wls`), each run on all five meshes (the selected method is also used for the viscous stresses and the turbulence terms)

Item	Setting
Time integration	Euler implicit; FGMRES with DILU preconditioning (flow and turbulence)
CFL	Adaptive, `5 → 100` (reached `100` within about 30 iterations on all ten runs and stayed there)
Gas model	Ideal gas, `gamma = 1.4`, Sutherland viscosity (`S = 110.4 K`, reference viscosity set so that `Re_L = 5×10^6`), constant Prandtl number `0.72`

> **Note**
>
> **Assumptions and differences from the references.**
>
> - The TMR page and the CFL3D/FUN3D inputs specify only the reference temperature and leave the viscosity law and the laminar Prandtl number to the codes' defaults. Sutherland viscosity with `Pr = 0.72` was assumed to match those defaults; this was not isolated.
> - The reference inputs differ from each other in the reconstruction setting: CFL3D uses `kappa = 1/3`, FUN3D uses `umuscl = 0.5`. Wake CFD was run with `umuscl_kappa = 0.5`.
> - The TMR page states that both reference codes advected the turbulence variables with first-order upwinding. Wake CFD also advects the turbulence variables with a first-order scheme, so this matches.
> - The production term of the Wake CFD runs is vorticity-based, matching SST-Vm. The effect of using the strain-rate form instead was not tested.
> - The pseudo-time step of the turbulence equations was reduced on the two finest meshes: by a factor `0.5` on `273×193` and `0.25` on `545×385` (both gradient methods); the three coarser meshes use no reduction (the solver default). These factors are inherited from earlier SST work on an older solver version and were not re-examined with the current build; they are not expected to change the converged solution, but this was not tested, and the mesh-to-mesh comparison therefore mixes three settings. The `545×385` runs were not repeated with the default.
> - **No turbulence seeding was applied.** Earlier SST investigations (older solver versions) found that on very fine meshes this flow can also converge to a spuriously re-laminarized solution when started from a very low freestream turbulence level. The input deck of these runs contained an initial-turbulence setting intended to guard against this, but the solver does not apply it with the initialization mode used, so every run started from the freestream turbulence values above. No run re-laminarized, including the two `545×385` runs, the mesh level where the effect was seen before.

For the general input structure and turbulence-model settings, see the CLI and **Model Configuration** sections of the public Wake CFD documentation.

5.8 Results

5.8.1 Convergence History

All ten runs converged by the force-based criterion. The iteration counts (Green–Gauss / weighted least squares) were 1,820 / 1,832 on `35×25`, 2,664 / 2,651 on `69×49`, 4,402 / 4,398 on `137×97`, 7,013 / 7,016 on `273×193`, and 15,852 / 15,849 on `545×385` (about 1.8 hours each on 8 CPU cores for `273×193`, and 17.6 / 16.0 hours for `545×385`).

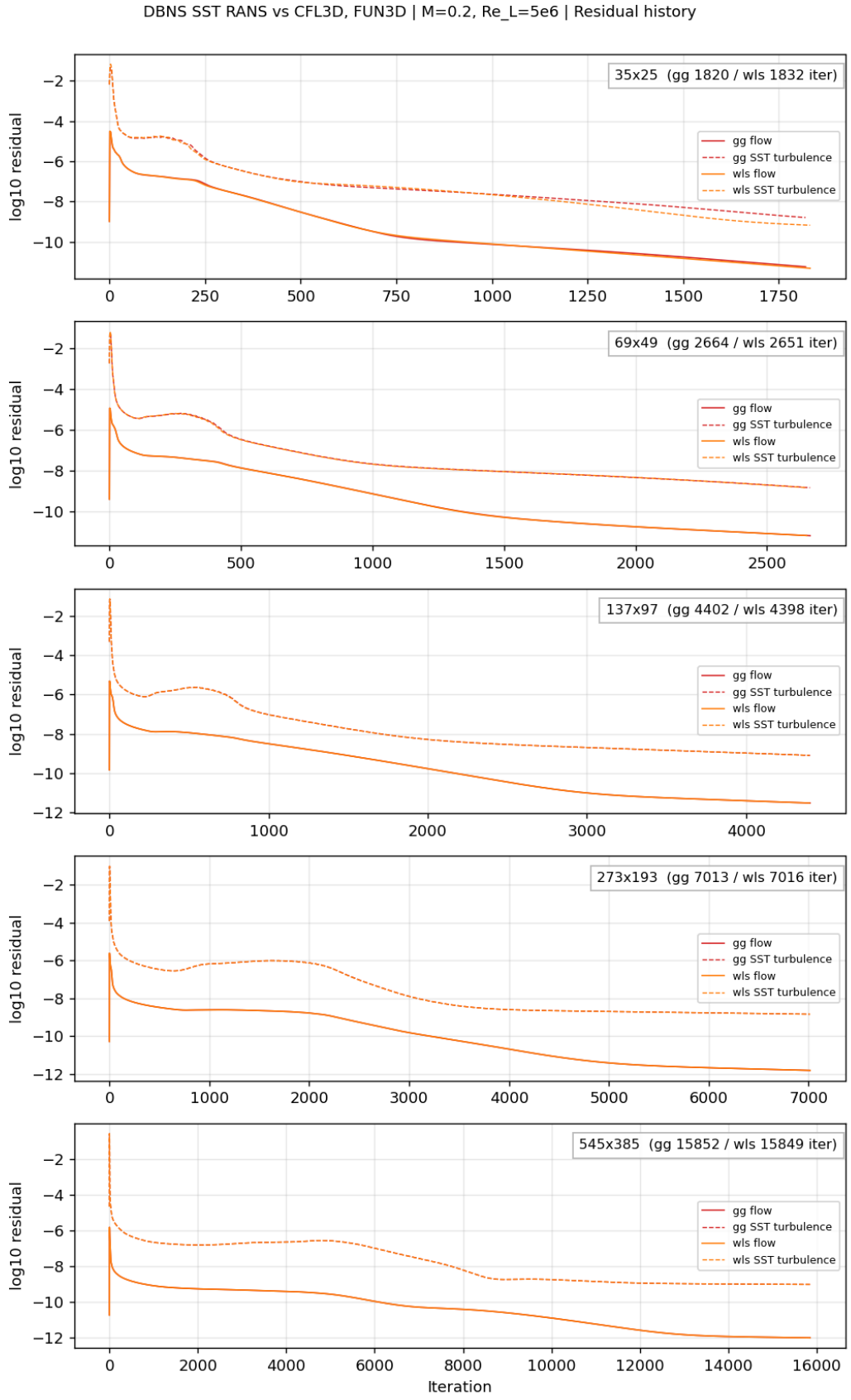


Figure 5.2: Residual history — absolute flow residual and SST turbulence residual, Green–Gauss and weighted least squares on each mesh

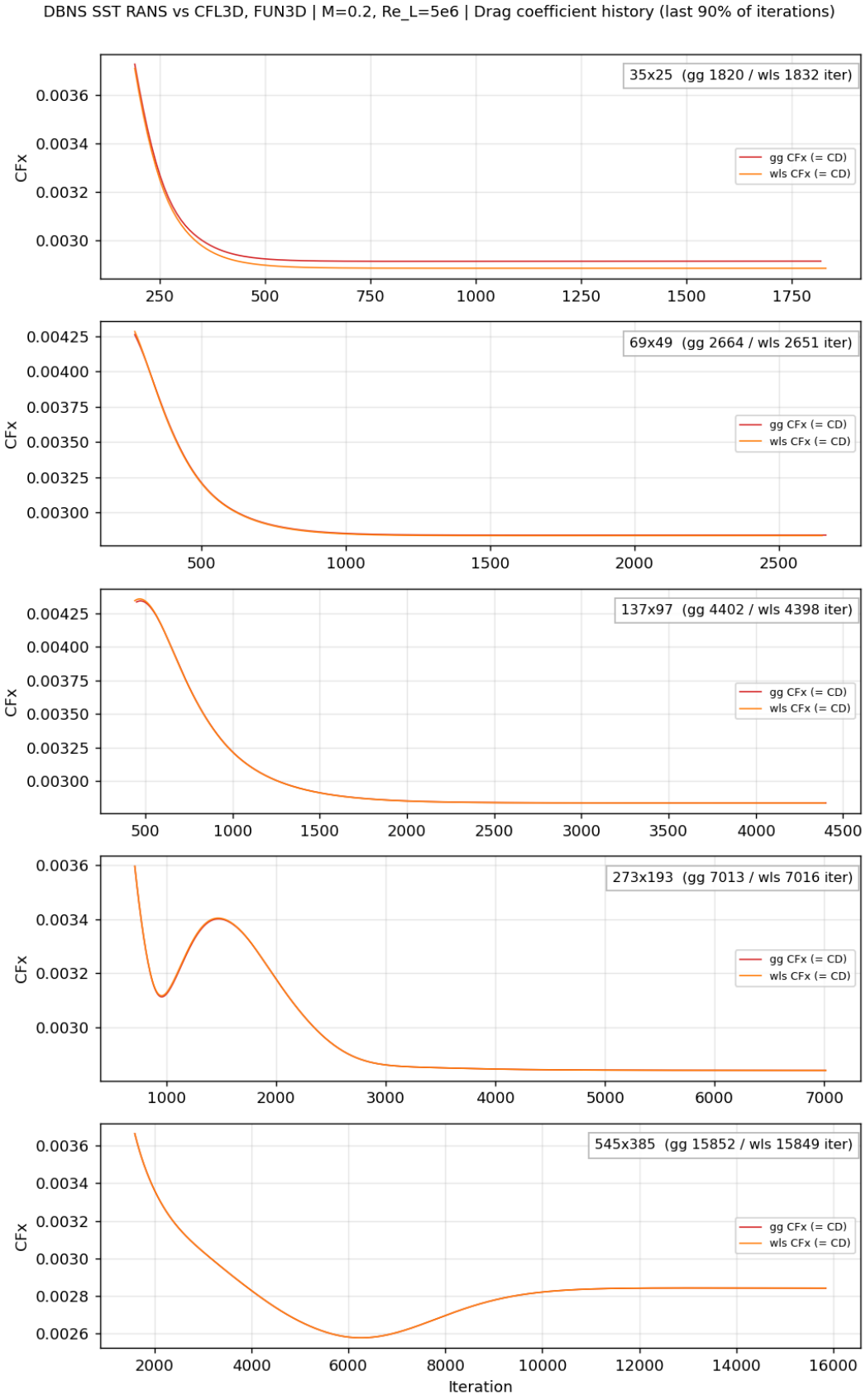


Figure 5.3: Drag-coefficient history on the five meshes (last 90% of the iterations)

The flow residual at termination was between `-11.2` and `-12.0` log10 (the termination criterion is force-based, not residual-based). **The SST turbulence residual levels off between `-8.8` and `-9.2` log10 and does not decrease further** (on `545×385` it ends at `-9.0`), unlike the Spalart–Allmaras residual in case-02. The drag coefficient is settled at termination (variation below `7×10` over the last 1,000 iterations on every run, `3×10` on `545×385`), so this does not affect the results reported here; the cause of the plateau was not investigated. The two gradient methods give residual and drag histories that are nearly indistinguishable except on the coarsest mesh.

5.8.2 Grid Convergence

The results were compared directly at the same mesh and station (`x=0.970084`) as the CFL3D/FUN3D data published by TMR.

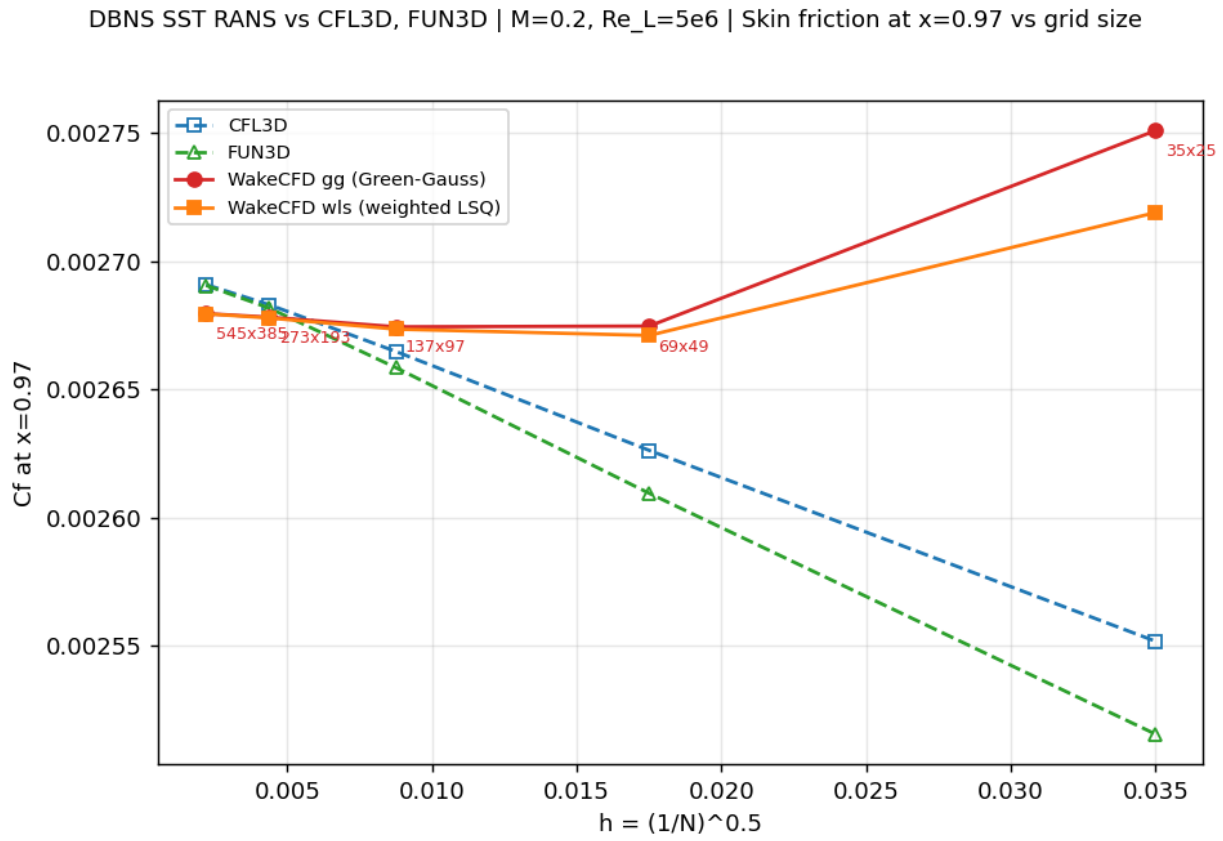


Figure 5.4: Grid convergence of `Cf(x=0.97)` — five Wake CFD points versus five CFL3D/FUN3D grid levels

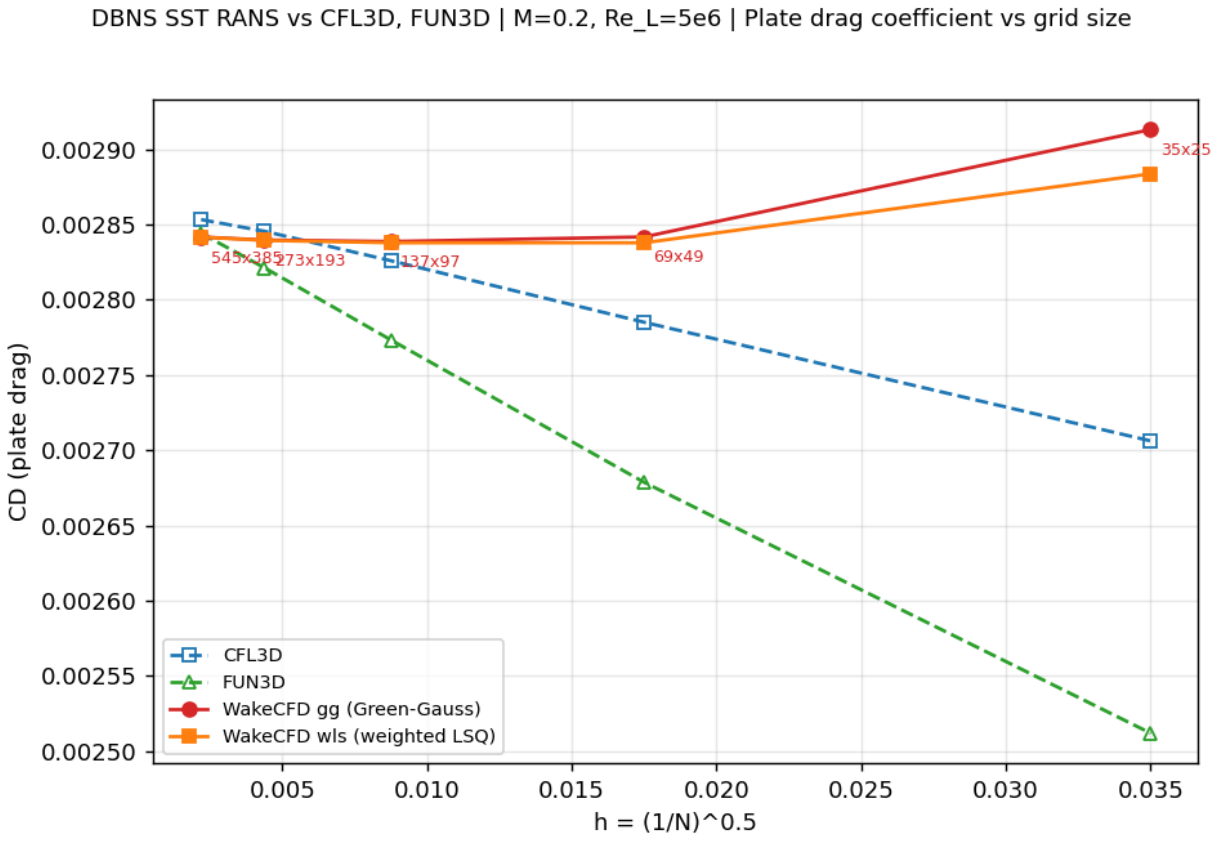


Figure 5.5: Grid convergence of the plate drag coefficient `C_D`

Both gradient methods are shown with the reference data. `Cf` is the skin-friction coefficient at `x=0.97` and `C_D` is the plate drag coefficient.

Skin-friction coefficient at `x=0.97`:

Mesh	`Cf` gg	`Cf` wls	CFL3D	FUN3D
35×25	0.002751	0.002719	0.002552	0.002516
69×49	0.002675	0.002671	0.002626	0.002610
137×97	0.002674	0.002673	0.002665	0.002658
273×193	0.002678	0.002678	0.002683	0.002682
545×385	0.002680	0.002679	0.002691	0.002691

Plate drag coefficient:

Mesh	`C_D` gg	`C_D` wls	CFL3D	FUN3D
35×25	0.002913	0.002884	0.002706	0.002512
69×49	0.002842	0.002838	0.002785	0.002679
137×97	0.002839	0.002838	0.002826	0.002773
273×193	0.002840	0.002839	0.002846	0.002821

Mesh	C_D gg	C_D wls	CFL3D	FUN3D
545×385	0.002842	0.002842	0.002853	0.002844

Difference of Wake CFD relative to each reference code, on the same mesh:

Mesh	Method	Cf vs. FUN3D	Cf vs. CFL3D	C_D vs. FUN3D	C_D vs. CFL3D
35×25	gg	+9.35%	+7.80%	+15.97%	+7.65%
35×25	wls	+8.08%	+6.55%	+14.80%	+6.56%
69×49	gg	+2.50%	+1.84%	+6.09%	+2.04%
69×49	wls	+2.36%	+1.71%	+5.94%	+1.90%
137×97	gg	+0.60%	+0.36%	+2.36%	+0.45%
137×97	wls	+0.57%	+0.33%	+2.33%	+0.42%
273×193	gg	−0.13%	−0.18%	+0.65%	−0.21%
273×193	wls	−0.14%	−0.19%	+0.64%	−0.21%
545×385	gg	−0.41%	−0.42%	−0.08%	−0.41%
545×385	wls	−0.41%	−0.42%	−0.09%	−0.41%

- **Wake CFD results are nearly independent of the mesh from 69×49 on**, while the reference codes keep rising toward their finest-mesh values. Wake CFD C_D stays between 0.002838 and 0.002842 from 69×49 to 545×385, and Cf stays within 1×10 of 0.002675. On the coarsest meshes Wake CFD is therefore above the references (up to +16% in C_D), it falls within 0.7% of both references at 273×193, and it ends below both at 545×385.
- **A small systematic offset to the references remains on the finest mesh.** At 545×385 the Wake CFD Cf is lower than CFL3D by 0.42% (both gradient methods) and than FUN3D by 0.41%; C_D is lower than CFL3D by 0.41% and than FUN3D by 0.08% / 0.09% (gg / wls). From 273×193 to 545×385 the Wake CFD Cf changed by only +1.4×10 (gg) / +1.7×10 (wls), so the offset is not shrinking with mesh refinement in this range. The sibling SA case shows a Cf offset of about −0.25%; whether the two share a cause was not investigated. The 273×193 agreement reported earlier was a crossing of a flat curve and a still-rising reference, not a converged match.
- The change of the Wake CFD results between successive meshes is not monotonic (for example, Green–Gauss C_D decreases from 69×49 to 137×97 and increases from 137×97 to 545×385), and each change is larger than the settling noise of the termination criterion (about 3×10). The observed order of convergence therefore cannot be computed from these five meshes; the solution has either not entered the asymptotic range or other error terms are superimposed. This is not resolved. The turbulence pseudo-time-step reduction differs between 273×193 and 545×385 (see *Numerical Methods*), which may contribute; this was not isolated.

5.8.3 Difference between the gradient methods

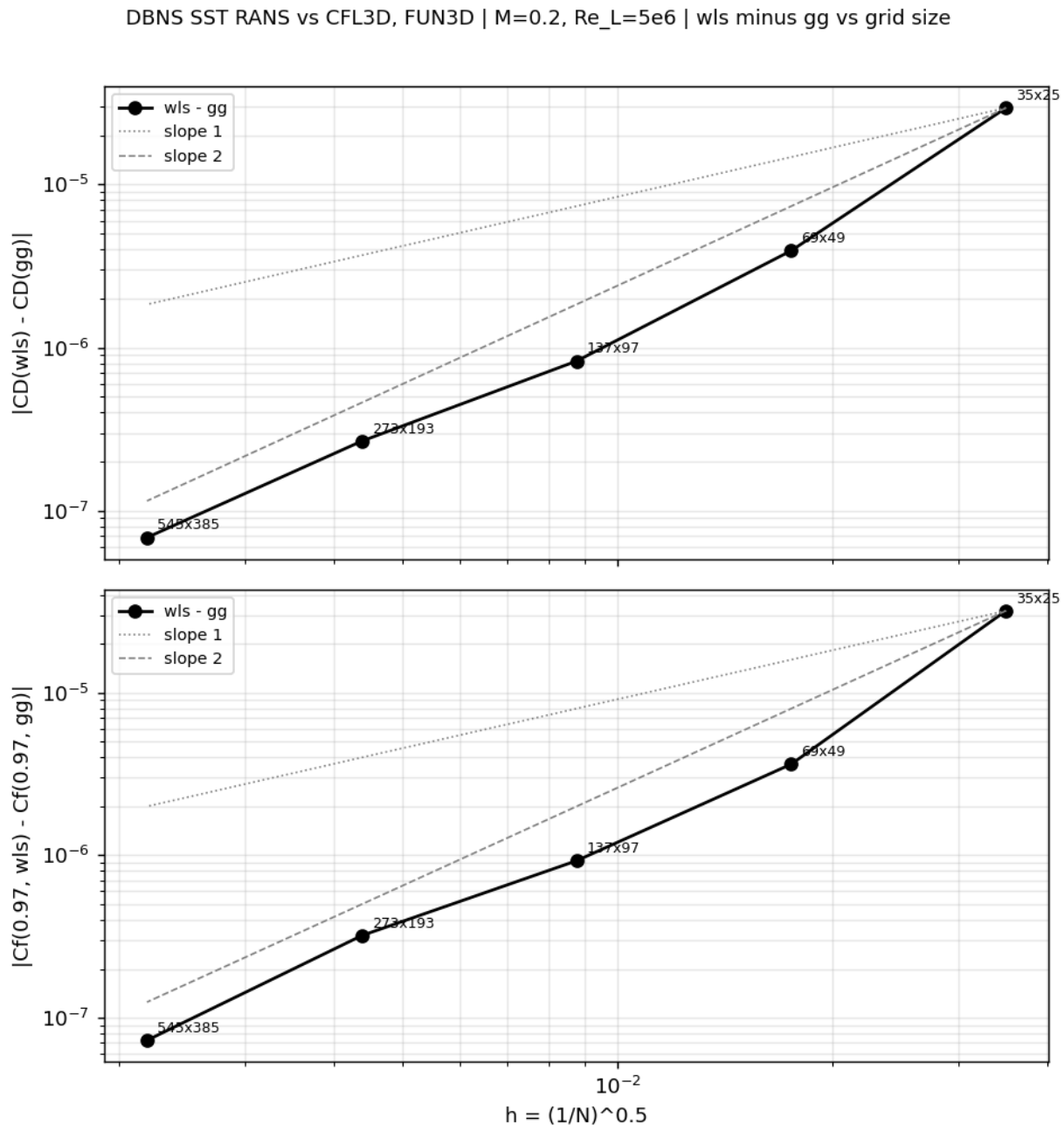


Figure 5.6: Difference between the weighted-least-squares and Green–Gauss results versus mesh size

Mesh	wls − gg, `C_D`	wls − gg, `Cf` (0.97)	Reduction from previous mesh (`C_D` / `Cf`)
35×25	−2.942e-5	−3.196e-5	—

Mesh	wls − gg, C_D	wls − gg, Cf (0.97)	Reduction from previous mesh (C_D / Cf)
69×49	−3.927e-6	−3.637e-6	÷7.5 / ÷8.8
137×97	−8.264e-7	−9.249e-7	÷4.8 / ÷3.9
273×193	−2.671e-7	−3.204e-7	÷3.1 / ÷2.9
545×385	−6.857e-8	−7.262e-8	÷3.9 / ÷4.4

The two methods approach the same solution: the difference decreases at every refinement and is about 0.002% of C_D on 545×385. Unlike the SA case, where the difference dropped by exactly a factor of four (h^2) at each step, the reduction here fell from 7.5 to 3.1 before returning to 3.9 (C_D) and 4.4 (Cf) on the last step, and the sign is opposite (weighted least squares is below Green–Gauss). The reason for the slower reduction on the 273×193 step was not identified. The two 545×385 runs were made on different solver builds (see *Run Provenance*) and the finest two meshes use different turbulence pseudo-time-step reductions, so neither the return to about four nor the earlier slowdown can be attributed to the gradient methods alone.

5.8.4 Detailed Comparison

The profiles below show the Wake CFD results (Green–Gauss and weighted least squares) against the CFL3D and FUN3D references (finest reference meshes). The profile figures use the 545×385 mesh, the finest mesh run.

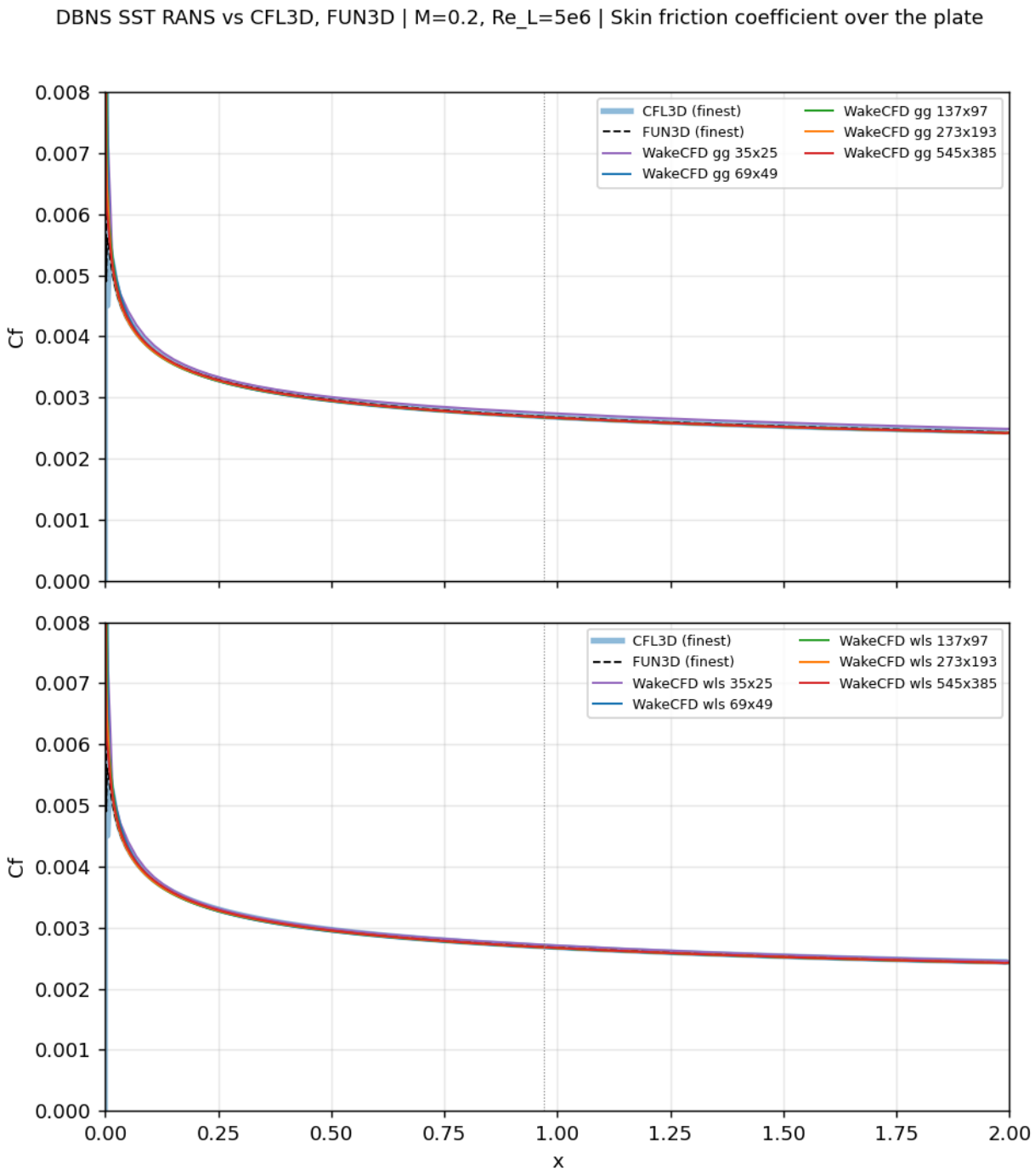


Figure 5.7: `Cf(x)` over the full plate on all five meshes for both gradient methods, against CFL3D and FUN3D

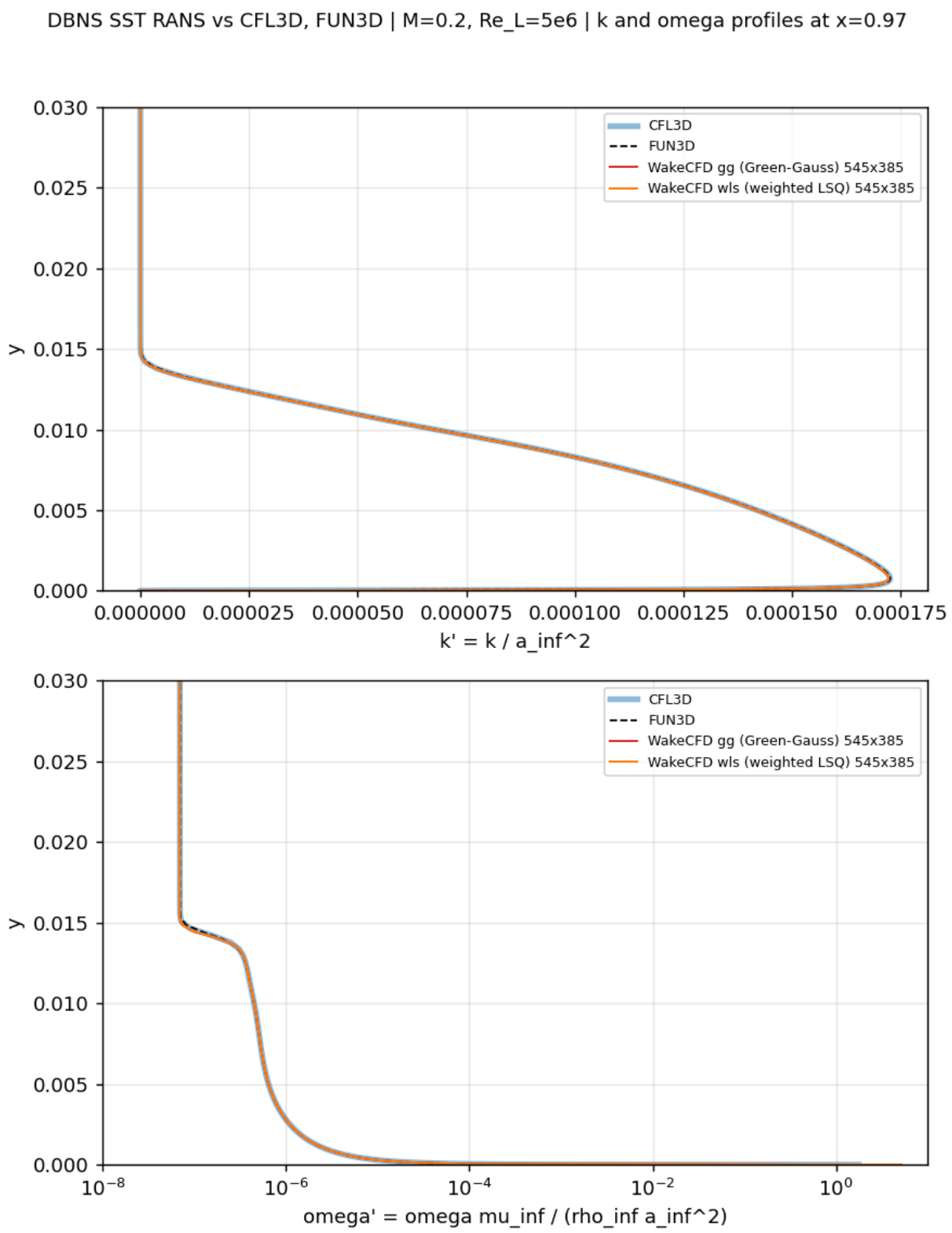


Figure 5.8: Turbulent kinetic energy `k'` and specific dissipation rate `omega'` at x=0.97, in the TMR non-dimensionalization

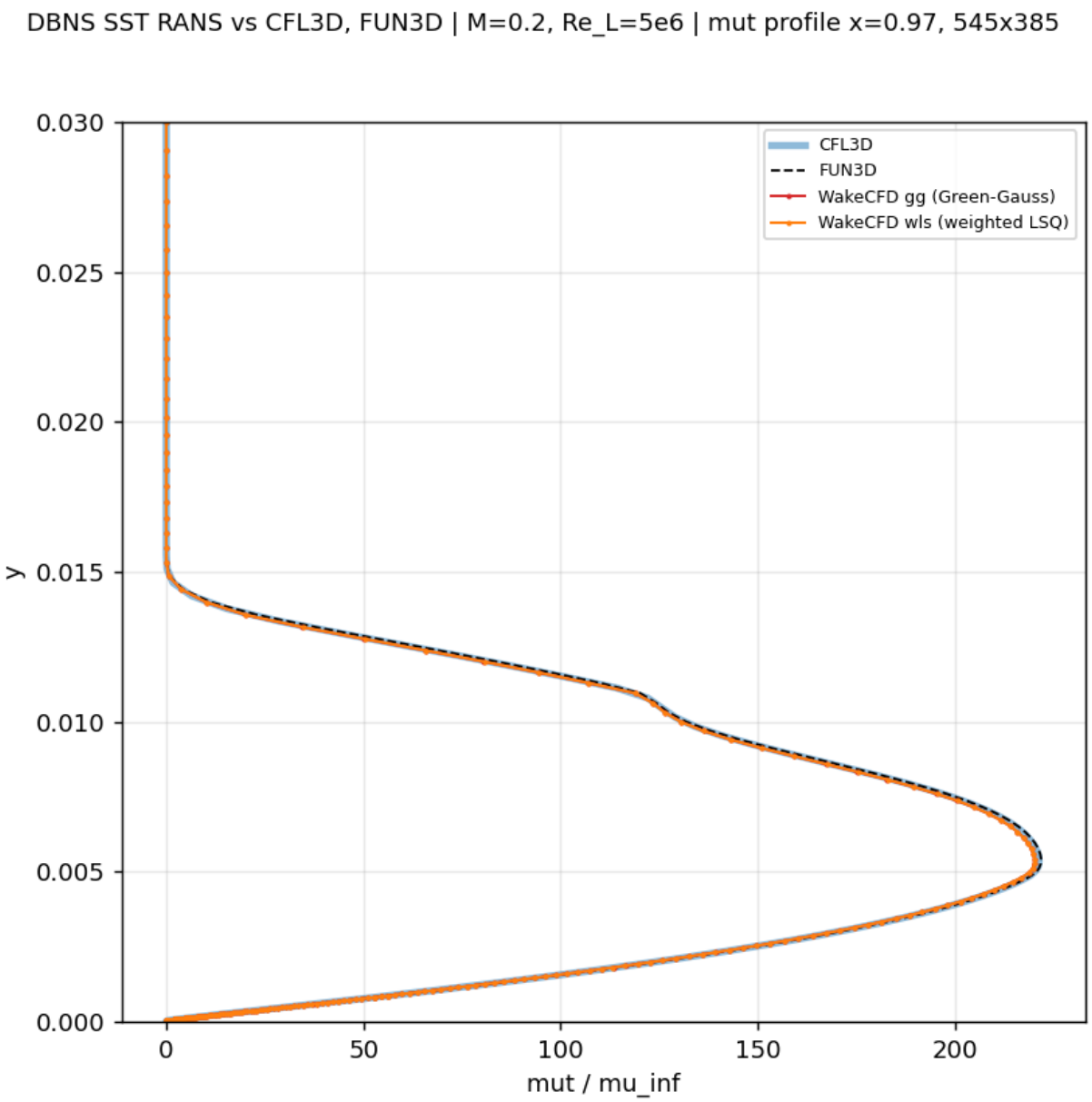


Figure 5.9: Eddy-viscosity-ratio profile at x=0.97

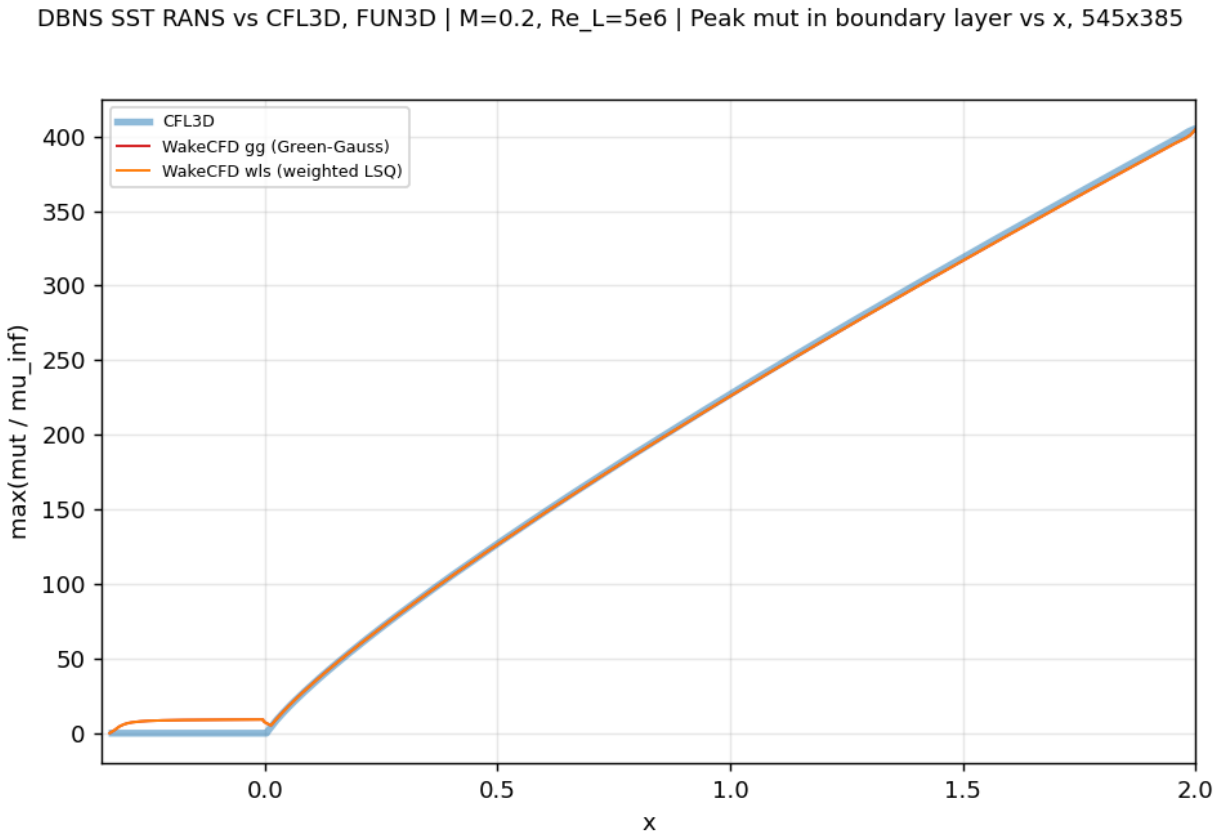


Figure 5.10: Maximum eddy-viscosity ratio in the boundary layer along the plate

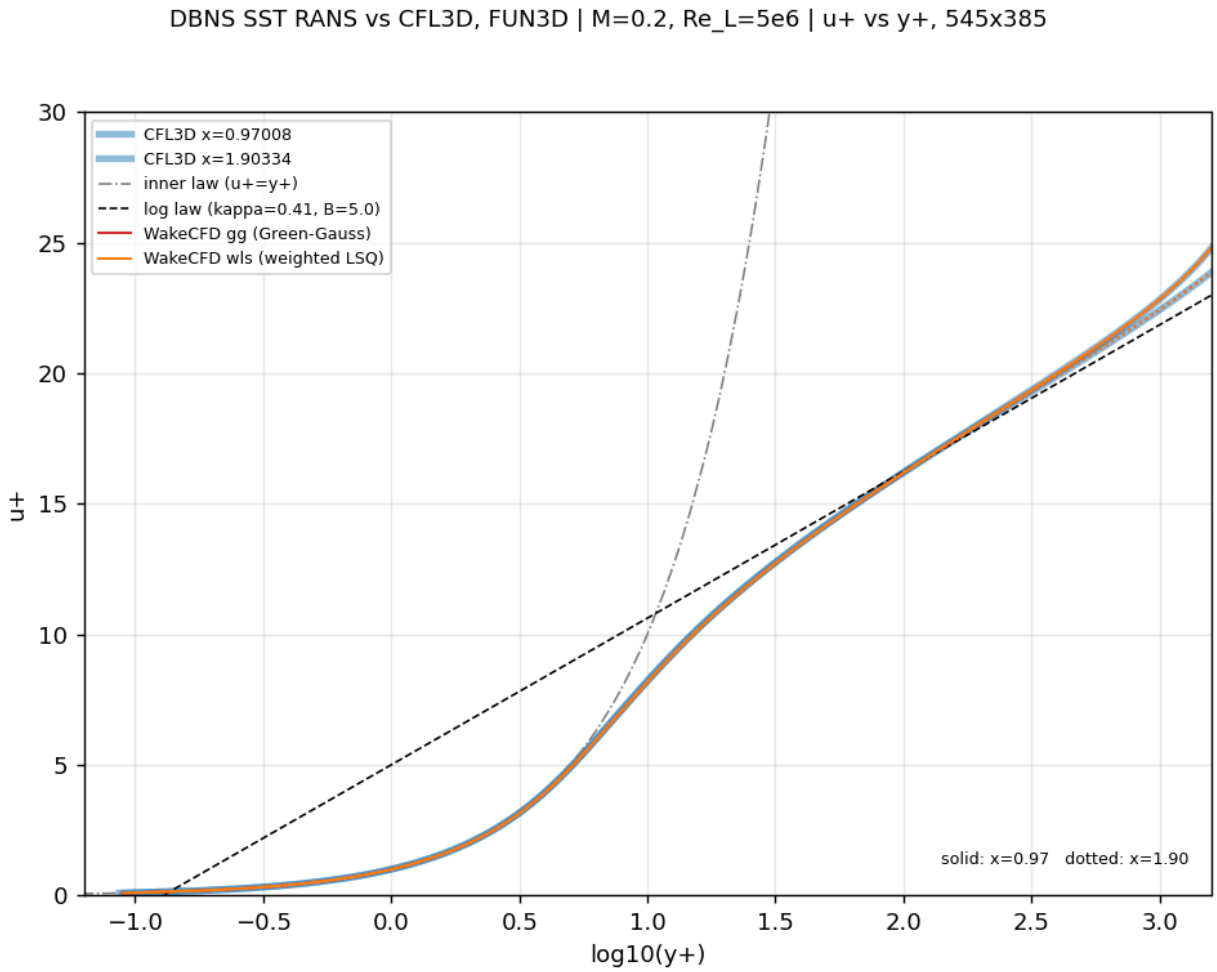


Figure 5.11: u+ versus y+ at x=0.97 (solid) and x=1.90 (dotted) against the law of the wall

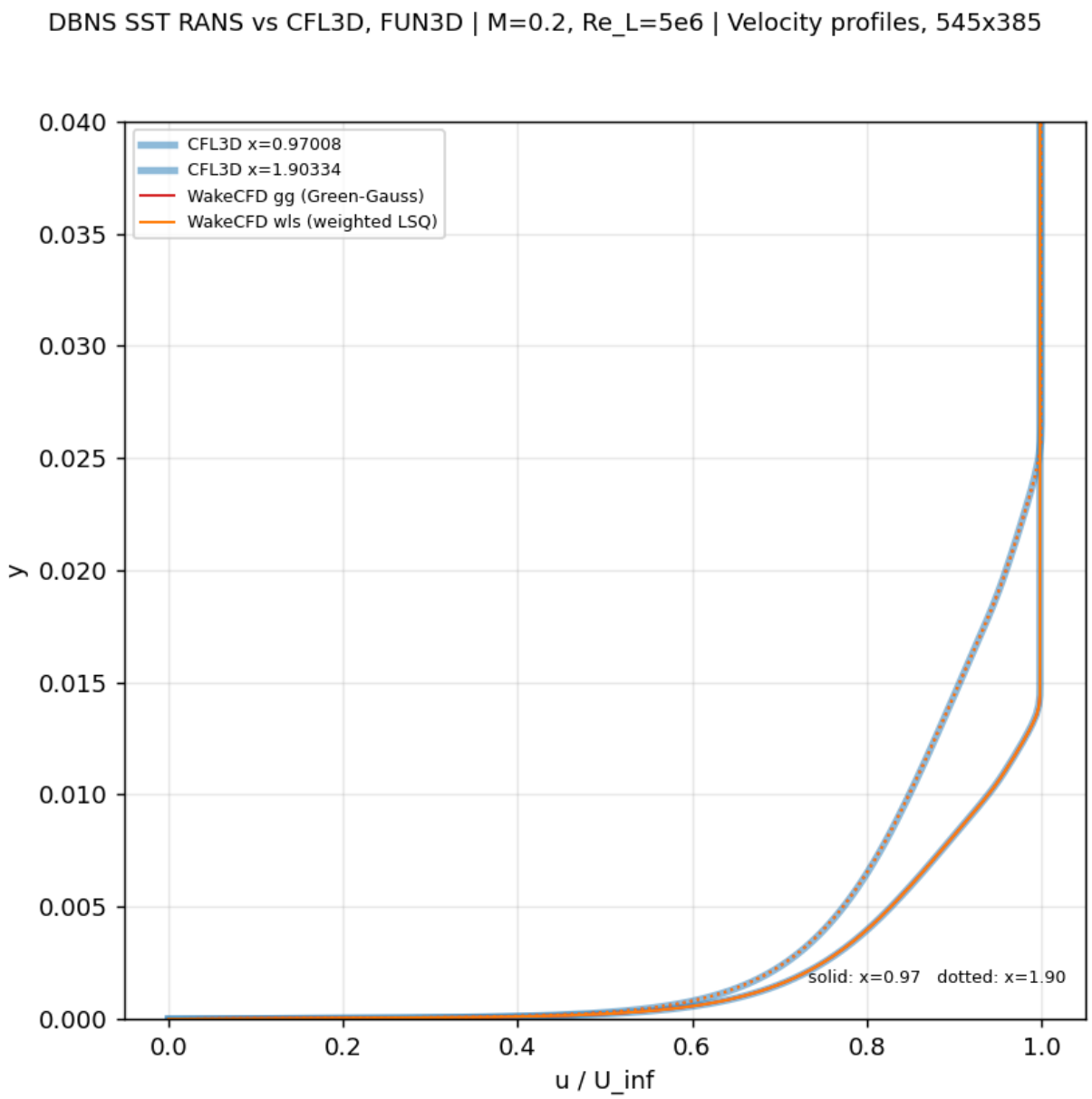


Figure 5.12: Velocity profiles `u/U_inf` versus height at x=0.97 and x=1.90

`k'` and `omega'` are k/a_∞^2 and $\omega\, \mu_\infty/(\rho_\infty a_\infty^2)$, with $a_\infty = 347.7$ m/s. On the 545×385 mesh, the `Cf(x)` distribution, the `k'` and `omega'` profiles (across eight decades on the log axis for `omega'`), the velocity profiles, and `u+` versus `y+` coincide with the references within the width of the lines, and the two gradient methods cannot be told apart. These comparisons are visual.

The maximum eddy-viscosity ratio at `x=0.97` on 545×385 is `220.21` (gg) and `220.25` (wls), against `221.41` (CFL3D) and `221.92` (FUN3D), i.e. 0.54% / 0.52% lower than CFL3D and 0.77% / 0.75% lower than FUN3D. On 273×193 the values were `220.41` and `220.53` (0.45% / 0.40% below CFL3D), so the peak did not move toward the references with mesh refinement; the reason was not investigated. The Wake CFD values are cell-center values on the mesh's own points.

5.9 Conclusions and Applicable Scope

- On the same mesh, the SST turbulence-model implementation agrees with the NASA TMR references (CFL3D and FUN3D) on `Cf` within 0.2% and on `C_D` within 0.7% at `273×193`, and on `Cf` within 0.42% and on `C_D` within 0.41% (CFL3D) at the finest mesh `545×385`, for both gradient methods. The Wake CFD results are lower than the references by that margin on the finest mesh.
- Wake CFD results change by less than 0.2% in `C_D` from `69×49` to `545×385`, while the references keep rising; a `Cf` offset of about −0.4% relative to the references remains on the finest mesh and does not shrink with refinement in the range run. The observed order of convergence cannot be established from the five meshes.
- The Green–Gauss and weighted-least-squares gradients approach the same solution; their difference falls to about 0.002% of `C_D` at `545×385`, with a reduction per refinement that is irregular (7.5, 4.8, 3.1, then about four).
- `k`, `omega`, velocity, and `u+` profiles agree with the references; the peak eddy-viscosity ratio is 0.5% to 0.8% lower on the finest mesh.
- The two finest meshes were run with a reduced turbulence pseudo-time step (`0.5` and `0.25`) and the two `545×385` runs used different solver builds; neither was tested for an effect on the results, so the finest-mesh comparison carries those caveats.
- No run re-laminarized, although no turbulence seeding was applied (see *Numerical Methods*), including on the finest mesh. Cases with a similarly quiescent freestream turbulence level and fine near-wall resolution should still be checked.
- These results apply to a two-dimensional, zero-pressure-gradient flat plate at one subsonic condition (`M=0.2`). They cannot be generalized to pressure gradients, separation, transition, curved surfaces, or strong compressibility effects.

This case shows that Wake CFD's SST turbulence-model implementation reproduces the wall friction and the boundary-layer profiles of mature reference codes for a subsonic flat-plate boundary layer without a pressure gradient to within the stated differences. It establishes a minimum validation baseline for this range of conditions rather than an absolute accuracy guarantee.

5.10 References

- NASA Turbulence Modeling Resource: 2D Flat Plate Validation Case
- NASA Turbulence Modeling Resource: SST results for the 2D flat plate
- Wake CFD SA Flat-Plate Verification — sibling case, same mesh/BC/numerics

6 2D Turbulent Flat-Plate Boundary Layer, M=2 and M=5 — NASA TMR SA Verification

Skin friction versus Re_ and the law of the wall for the Spalart–Allmaras model on a cooled supersonic/hypersonic flat plate (against van Driest theory and CFL3D)

6.1 Run Provenance and Artifacts

Item	Value
Wake CFD baseline version	`0.23.0`
Solver	DBNS
Compute device	CPU
Parallel execution	8 MPI ranks
Arithmetic precision	Mixed
Run date	2026-10-18

> **Note**
>
> Results depend on the solver build that produced them. Read every figure in this report together with the version and date above — re-running the same input on a later build may give different numbers.
> All twenty runs (four conditions × five meshes) used the same input apart from the mesh, the freestream and wall-temperature values, and the iteration cap.

6.1.1 Downloadable Files

Not available: standalone input decks and solver result files have not yet been published for download.

6.2 Verification Objective

This case simulates a zero-pressure-gradient turbulent boundary layer on an isothermal flat plate at supersonic and hypersonic Mach numbers with the Spalart–Allmaras (SA) model. It follows the

high-Mach flat-plate case of the NASA Turbulence Modeling Resource (TMR), which uses the same mesh family as the low-speed flat-plate case (case 02) but adds compressibility, a real Sutherland viscosity, and a cooled wall. It verifies Wake CFD for:

- the skin-friction coefficient `Cf` as a function of the momentum-thickness Reynolds number `Re_θ`, against van Driest II theory and the CFL3D SA result published by TMR
- the direction and size of the change in `Cf` as the mesh is refined, at four Mach number / wall-temperature conditions
- the near-wall velocity profile in wall coordinates (`u+` versus `y+`)

The TMR page treats this case as a comparison with theory rather than with other codes, and compares only the fully turbulent region of the plate. This report follows that: the primary quantity is the error in `Cf` against theory at `Re_θ = 10,000`, and the CFL3D SA result is shown as a second reference.

6.3 Reference Solution and Data

6.3.1 Analytical Solution

The reference curves are those published by TMR: the skin friction from van Driest II theory (`Cf` versus `Re_θ`) and the law of the wall from van Driest I theory (`u+` versus `y+`), each given per condition. TMR states that the theory is applicable to the fully turbulent region only, and compares `Cf` over `4000 < Re_θ < 13000` and `u+` at `Re_θ = 10,000`.

6.3.2 Numerical Reference

TMR also publishes a CFL3D SA result on the `545×385` mesh for each condition. The CFL3D data cover only `Re_θ 4,000` to `14,000`, as distributed. TMR describes such code results as representative rather than definitive, so they are shown for context and the theory is the reference for the error figures. CFL3D and FUN3D use a freestream `nu_tilde/nu = 3` for SA; the same value was used here.

6.4 Simulation Conditions

Four conditions were run. The freestream temperature is `Tω = 300 K` and the unit Reynolds number is `Re = 1.5×10^7 /m` for all four.

Condition (label in figures)	Mach	`Tw/Tω`	`Tw`	`ω` [kg/m³]	`pω` [Pa]	`Uω` [m/s]
M=2, Tw/Tinf=1.712	2	1.712	513.6 K	0.398722	34,335.92	694.44
M=5, Tw/Tinf=1.090	5	1.090	327.0 K	0.159489	13,734.37	1736.09

Condition (label in figures)	Mach	Tw/T∞	Tw	∞ [kg/m³]	p∞ [Pa]	U∞ [m/s]
M=5, Tw/Tinf=2.725	5	2.725	817.5 K	0.159489	13,734.37	1736.09
M=5, Tw/Tinf=5.45	5	5.45	1635.0 K	0.159489	13,734.37	1736.09

Item	Setting
Dimension	3D (one-cell spanwise extrusion; effectively 2D flow)
Geometry	Flat plate, `x = [0, 2] m`, leading edge at `x = 0`
Analysis	Steady, compressible DBNS, RANS (Spalart–Allmaras)
Gas model	Ideal gas (`R = 287.05 J/(kg·K)`, `  = 1.4`), Sutherland viscosity (`_ref = 1.716×10  Pa·s`, `T_ref = 273.15 K`, `S = 110.4 K`), constant Prandtl number `0.72`
Wall	No-slip, isothermal at `Tw` above

For `M = 5`, the adiabatic wall temperature is about `5.45 T∞`, so the three `M = 5` conditions have `Tw/Taw  0.2`, `0.5`, and `1.0`. TMR notes that the strongly cooled `Tw/T∞ = 1.09` condition is more sensitive to the mesh than the others.

6.5 Mesh

The meshes are the grids distributed by TMR for the flat-plate cases (the same family as case 02), used as distributed, with one cell in the spanwise direction. The `y+` values are the wall values reported by the solver at the end of the run.

Mesh	Streamwise × wall-normal	Node count (including spanwise extrusion)
Coarsest	35 × 25	1,750
Coarse	69 × 49	6,762
Medium	137 × 97	26,578
Fine	273 × 193	105,378
Finest	545 × 385	419,650

First-cell wall `y+` (average over the plate):

Condition	35×25	545×385
M=2, Tw/Tinf=1.712	2.13	0.13
M=5, Tw/Tinf=1.090	2.87	0.20
M=5, Tw/Tinf=2.725	1.02	0.06
M=5, Tw/Tinf=5.45	0.45	0.03

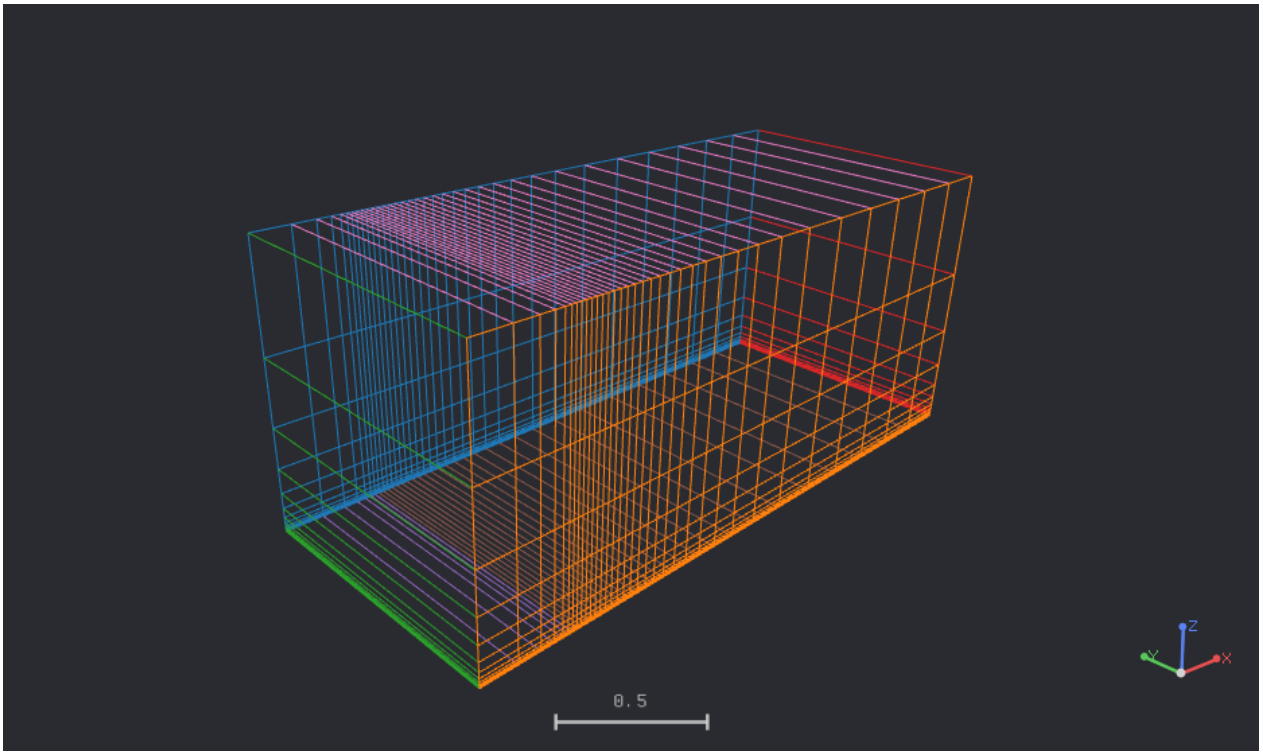


Figure 6.1: The `35×25` mesh in three dimensions — one cell in the spanwise direction; the plate is the bottom face, the upstream inlet is on the left, and the colors distinguish boundary groups

6.6 Boundary and Initial Conditions

Boundary	Segment	Type	Setting
Wall	Plate, `x [0,2]`	`wall`	no-slip, isothermal at `Tw` (see conditions)
Symmetry plane	Upstream slip segment + spanwise front/rear faces	`symmetry`	—
Inlet	Upstream	`farfield`	freestream Mach, `pω`, `Tω`, flow in `+x`, freestream `nu_tilde/nu = 3`

Boundary	Segment	Type	Setting
Outlet	Downstream	`pressure_outlet`	supersonic outlet, back pressure p_∞
Farfield	Top	`farfield`	same as inlet

Initial field: uniform freestream (Mach, pressure, temperature, flow in `+x`). The initial turbulence value is the solver default.

6.7 Numerical Methods

Item	Setting
Turbulence model	SA-neg variant with the `ft2` term, `Pr_t = 0.9`
Convective scheme	Roe, second-order reconstruction with no limiter, U-MUSCL `kappa = 0`, entropy fix off (all solver defaults; the reconstruction gradient is the same Green–Gauss gradient)
Gradient method	Green–Gauss
Time integration	Euler implicit; FGMRES (error `0.01`, at most 15 iterations) with SGS preconditioning for the flow equations (2 sweeps, = 0.9)
CFL	Constant, 50 on all runs. The three `545×385 M = 5` runs were continued from the iteration-8,000 state with CFL 100 up to iteration 16,000
Convergence criterion	Absolute flow residual `−12` (log10), or a 12-order reduction from the initial residual
Iteration cap	`M = 2`: 8,000 (`35×25`, `69×49`), 40,000 (`137×97`, `273×193`), 60,000 (`545×385`); `M = 5`: 8,000 on all meshes, 16,000 for the `545×385` runs as described above
Wall treatment	Solver default (`automatic`); no alternative was compared

> **Note**
>
> **Assumptions and differences from the references.**
>
> - The TMR reference is the standard SA model; the SA-neg variant used here is the same where `nu_tilde` is non-negative. The effect of the variant was not isolated.
> - CFL3D and FUN3D advect the turbulence variable with first-order upwinding, as stated by TMR. Wake CFD advects the turbulence variable with a first-order scheme in the build used (`0.21.5`), so this matches.
> - The CFL value was chosen to make the runs converge in a practical number of iterations; at `CFL 5` the `M = 5` runs stalled on the fine meshes. Converged solutions did not depend

on the CFL value in a check on the 137×97 mesh (CFL 20 and 50 gave the same Cf at Re_ = 10,000).

6.8 Results

6.8.1 Convergence History

Iterations to termination, and the final absolute flow residual (log10) for the runs that ended on the iteration cap:

Condition	35×25	69×49	137×97	273×193	545×385
M=2, Tw/Tinf=1.712	718	718	2,214	8,008	28,530
M=5, Tw/Tinf=1.090	418	718	2,619	8,000 (−10.59)	16,000 (−9.72)
M=5, Tw/Tinf=2.725	432	620	2,225	8,000 (−11.82)	16,000 (−10.67)
M=5, Tw/Tinf=5.45	626	619	1,917	6,357	16,000 (−11.69)

Fifteen of the twenty runs reached the residual criterion of −12. Five ended on the iteration cap with a residual between −9.7 and −11.8, still decreasing: the 273×193 runs of M=5, Tw/Tinf=1.090 and 2.725, and the three 545×385 M = 5 runs. The criterion was not met in these five, and they are treated as converged for this comparison: on 545×385 the Cf at Re_ = 10,000 differs from the 273×193 value by 0.6 percentage points of the theory value or less (table below), so the mesh trend is not changed by these runs ending short of the criterion, as far as this comparison shows. A longer run was not made to confirm that the Cf values no longer change.

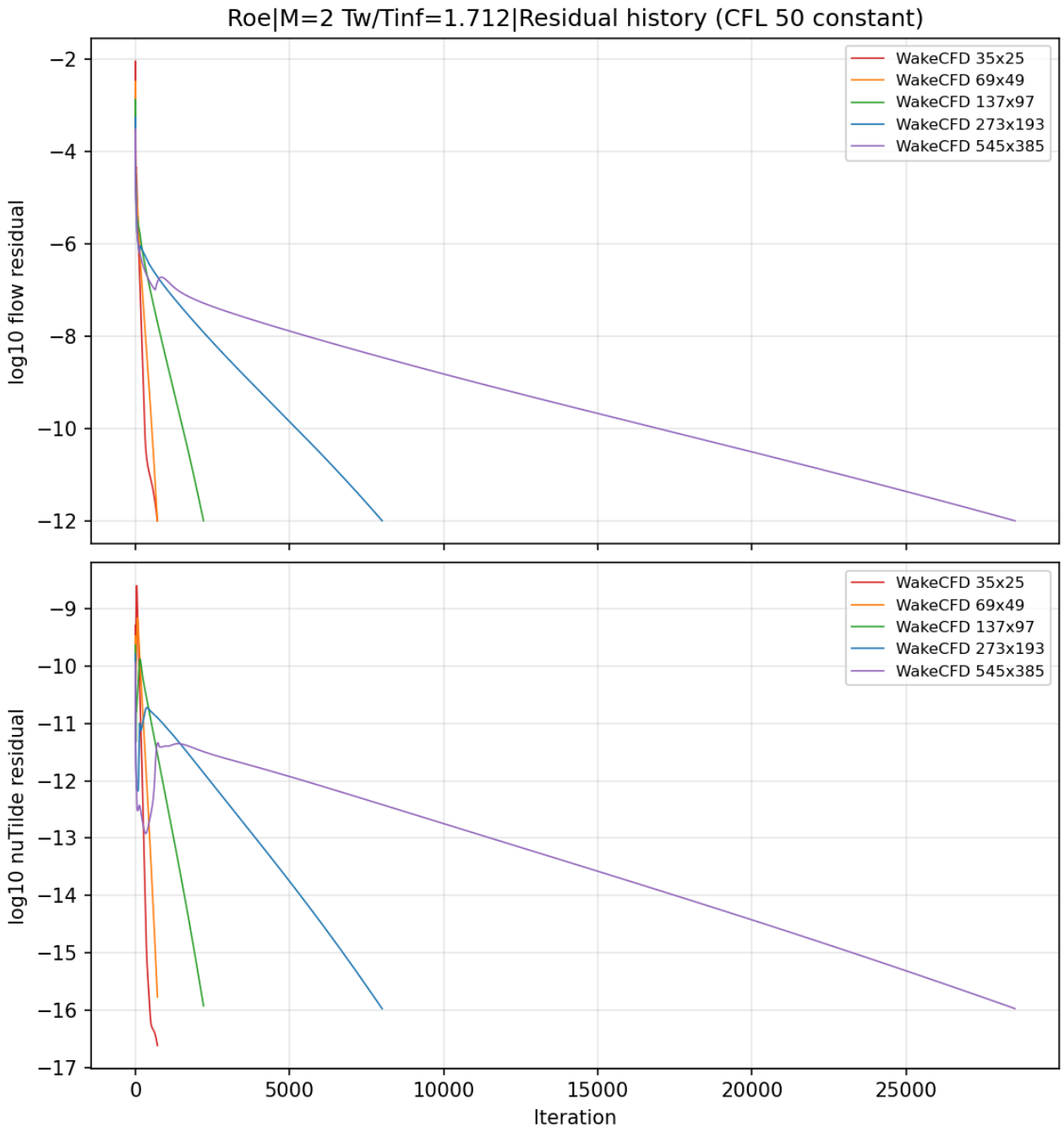


Figure 6.2: Residual history of the flow and `nu_tilde` residuals on the five meshes — M=2, Tw/Tinf=1.712

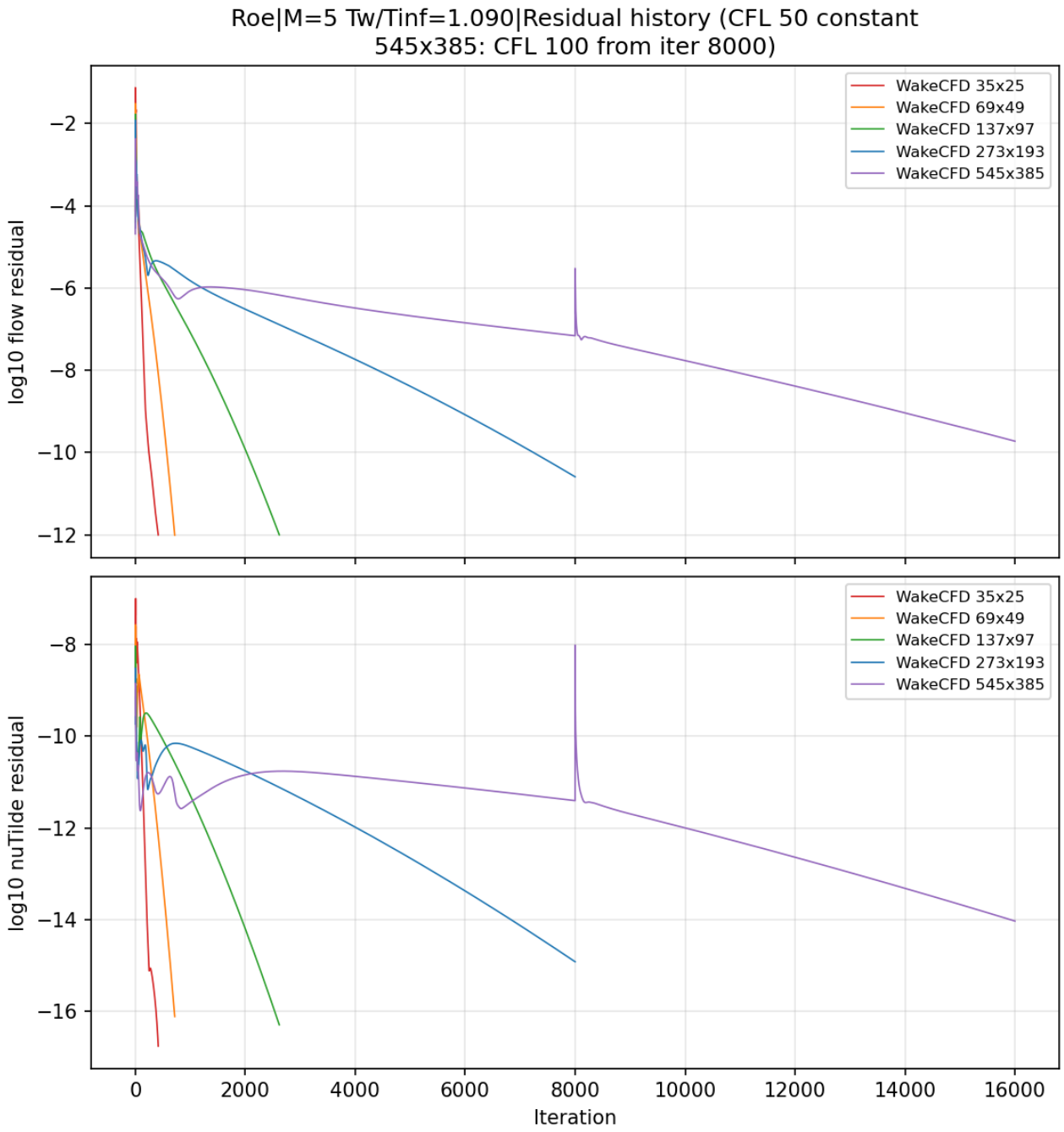


Figure 6.3: Residual history — M=5, Tw/Tinf=1.090

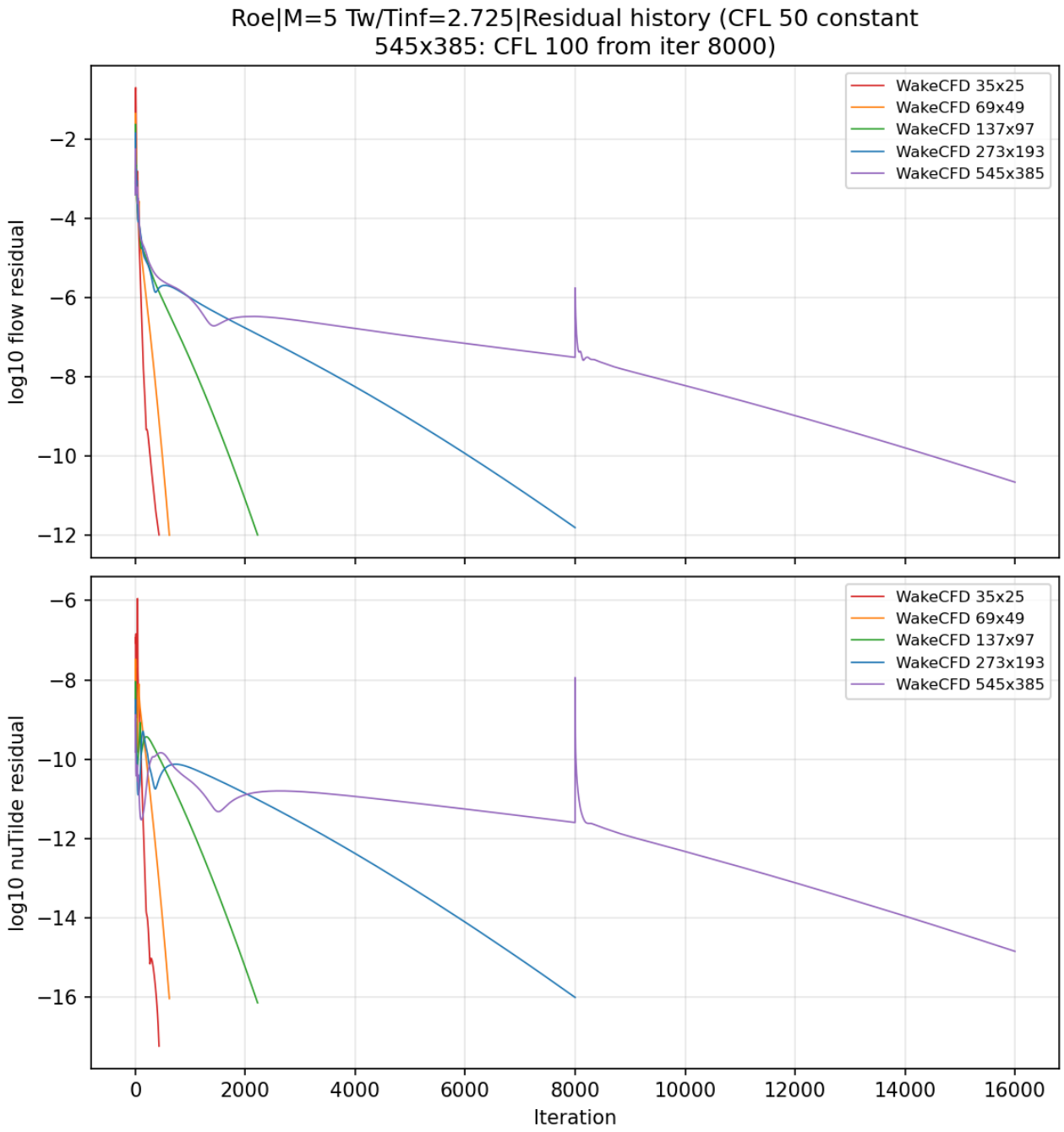


Figure 6.4: Residual history — M=5, Tw/Tinf=2.725

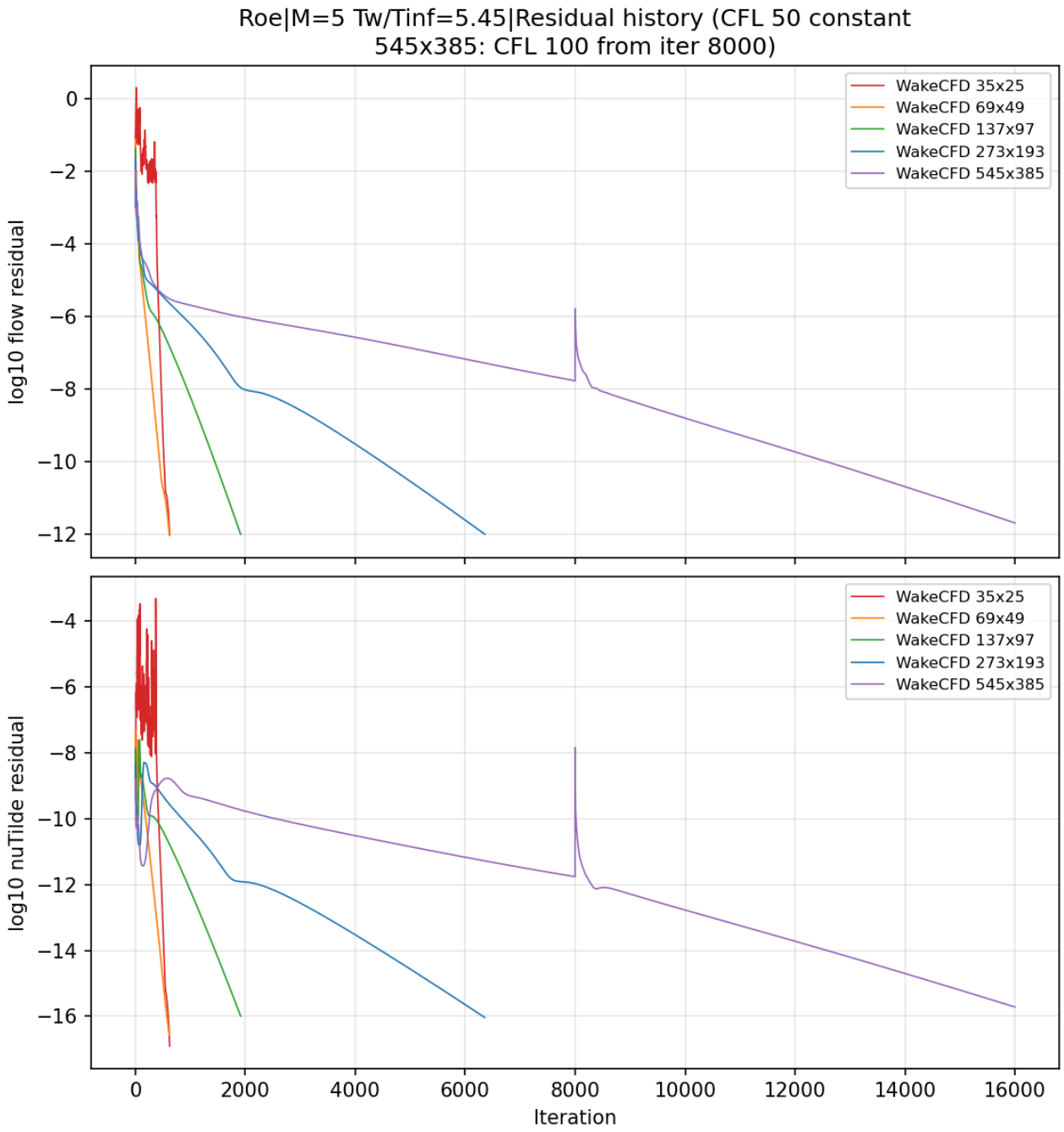


Figure 6.5: Residual history — M=5, Tw/Tinf=5.45

6.8.2 Skin Friction

`Cf` was taken from the wall shear stress, and `Re_` from the momentum thickness computed from the density and velocity profile at each streamwise station, integrated up to the first point where `u/U∞ 0.99`. The figures show `Cf` over `Re_ 1,000`; closer to the leading edge `Cf` rises steeply near the first points and `Re_` is not monotonic in `x`, so that region is not plotted. All errors below are at `Re_ = 10,000`.

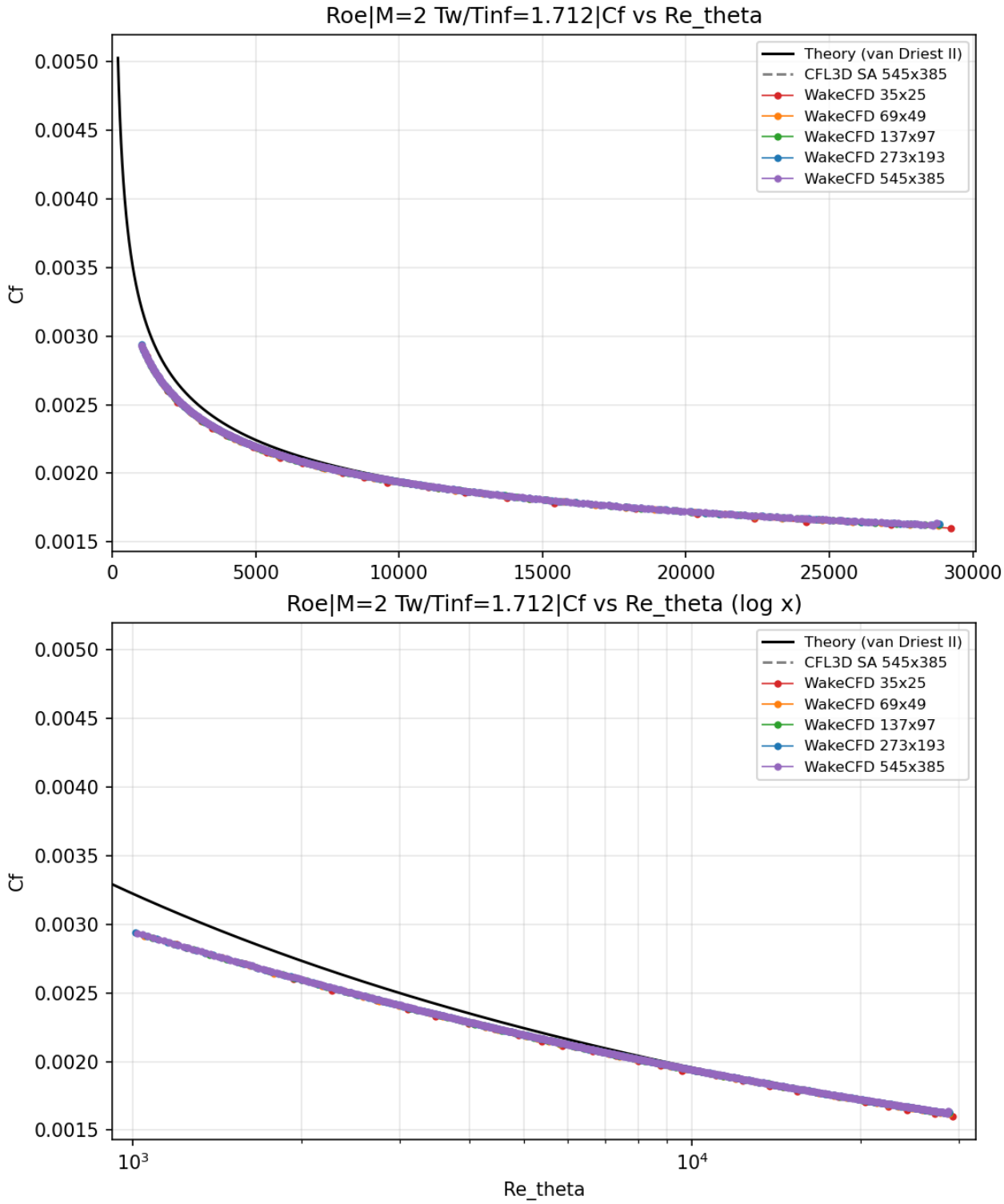


Figure 6.6: `Cf` versus `Re_` — M=2, Tw/Tinf=1.712, five meshes, linear (top) and logarithmic (bottom) `Re_` axis

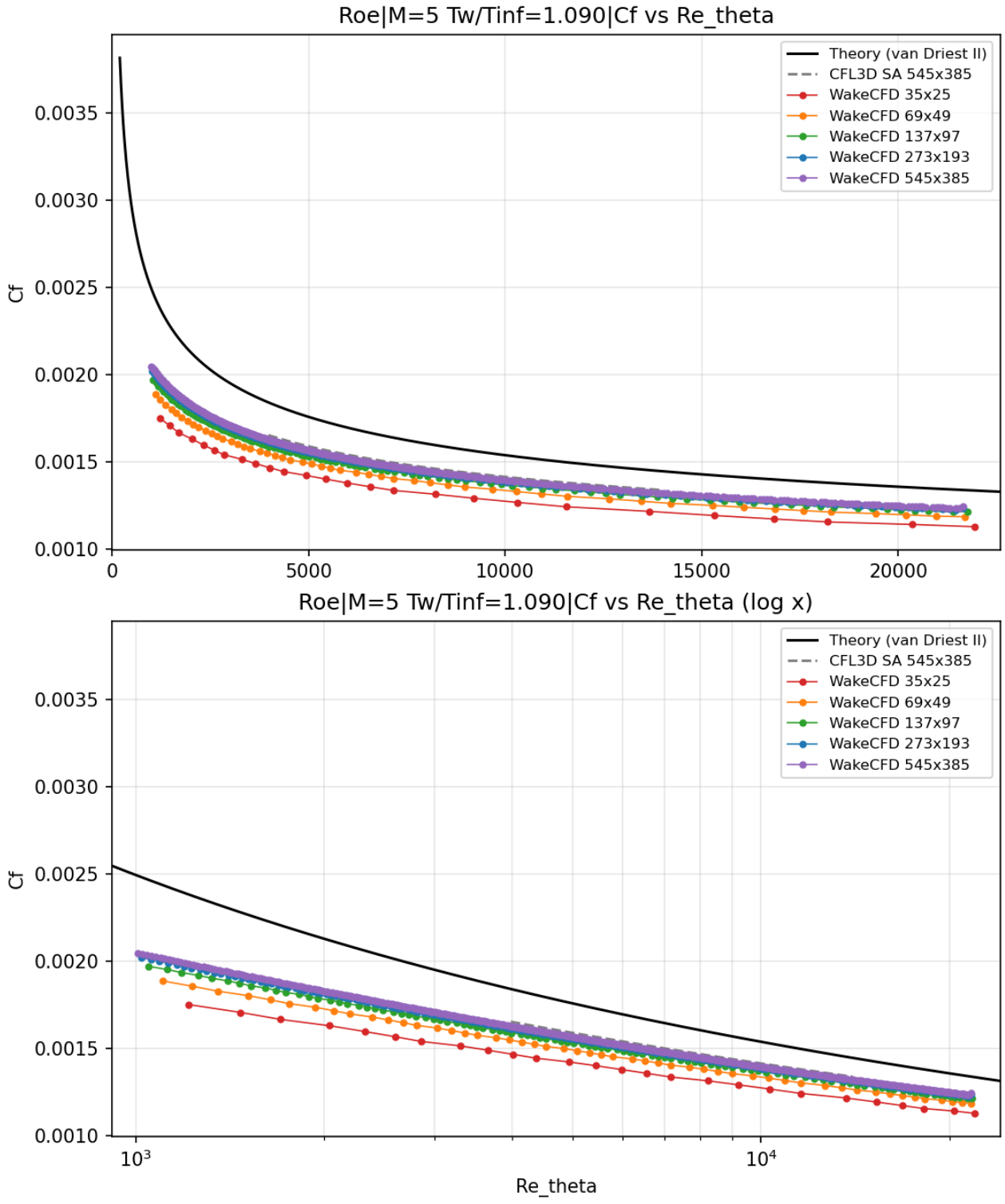


Figure 6.7: `Cf` versus `Re_` — M=5, Tw/Tinf=1.090

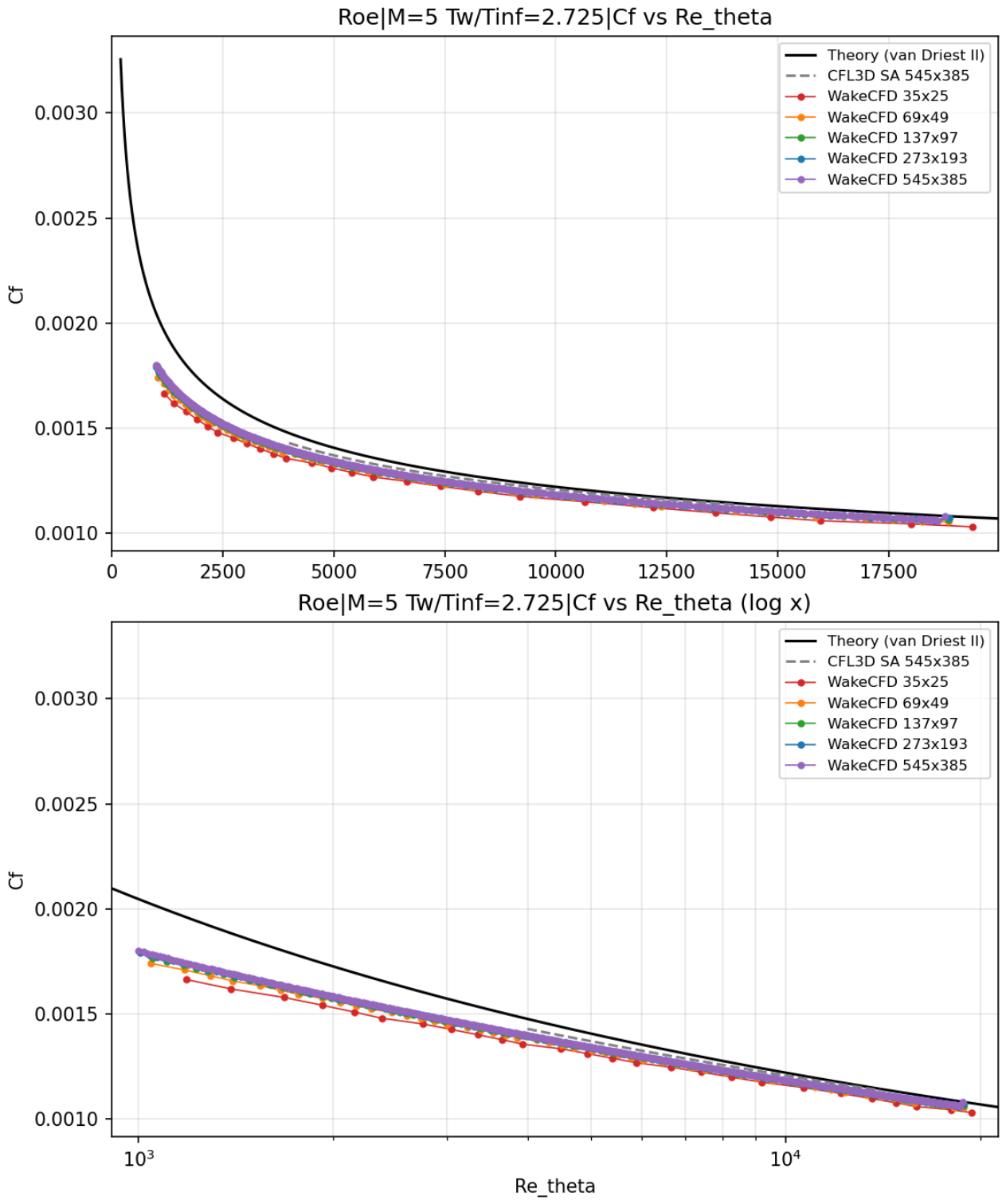


Figure 6.8: `Cf` versus `Re_` — M=5, Tw/Tinf=2.725

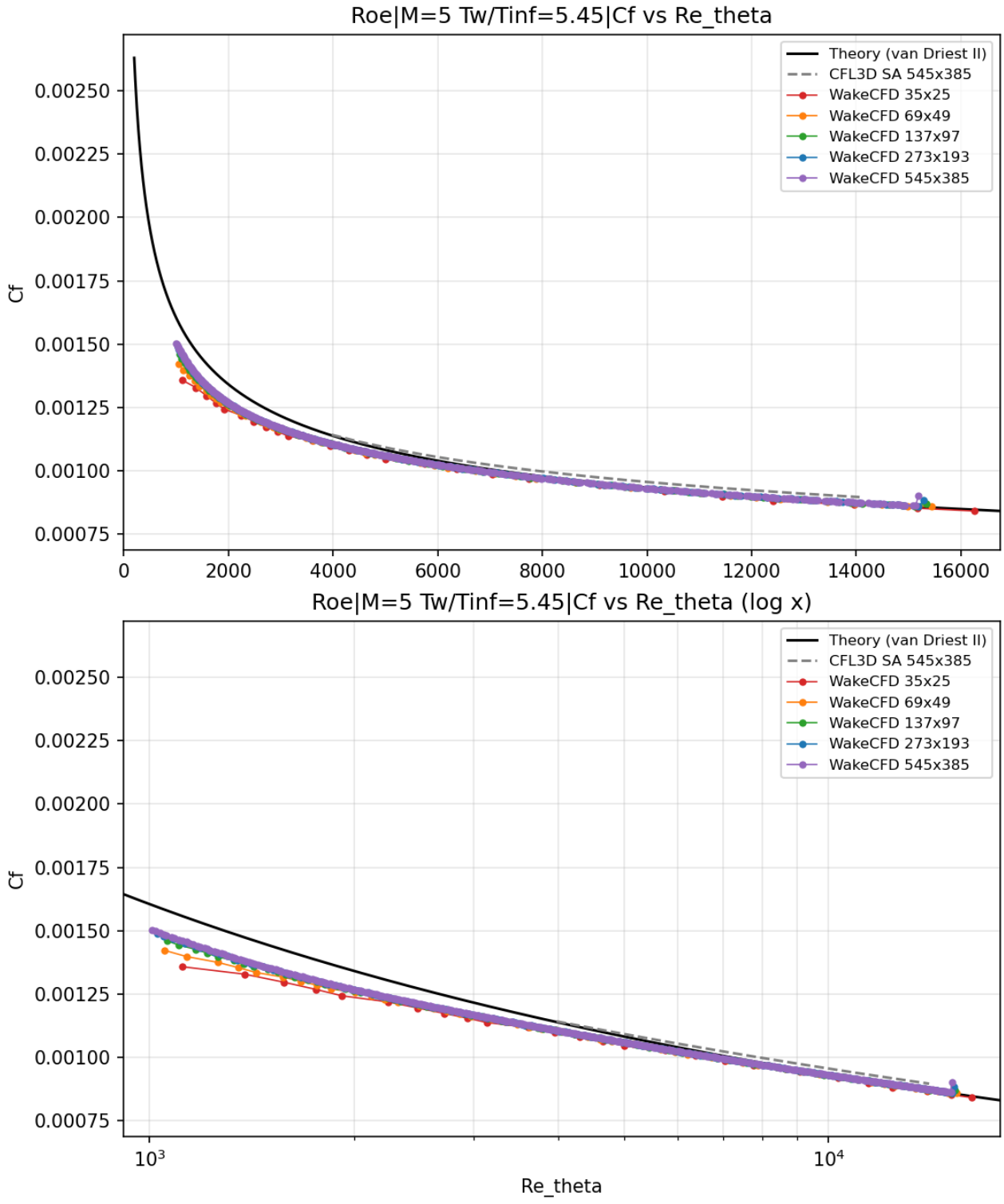


Figure 6.9: `Cf` versus `Re_` — M=5, Tw/Tinf=5.45

Difference of Wake CFD `Cf` relative to van Driest II theory at `Re_ = 10,000`:

Condition	35×25	69×49	137×97	273×193	**545×385**
M=2, Tw/Tinf=1.712	−1.60%	−0.85%	−0.81%	−0.73%	**−0.72%**
M=5, Tw/Tinf=1.090	−17.14%	−13.13%	−11.05%	−9.87%	**−9.28%**
M=5, Tw/Tinf=2.725	−4.88%	−3.71%	−3.14%	−3.01%	**−2.97%**
M=5, Tw/Tinf=5.45	−0.73%	−0.54%	−0.38%	−0.17%	**−0.22%**

Difference of Wake CFD `Cf` relative to the CFL3D SA result at `Re_ = 10,000` (CFL3D is on the `545×385` mesh only):

Condition	CFL3D vs. theory	35×25	69×49	137×97	273×193	**545×385**
M=2, Tw/Tinf=1.712	−0.15%	−1.49%	−0.74%	−0.69%	−0.62%	**−0.61%**
M=5, Tw/Tinf=1.090	−8.08%	−9.86%	−5.50%	−3.23%	−1.94%	**−1.30%**
M=5, Tw/Tinf=2.725	−1.08%	−3.84%	−2.65%	−2.08%	−1.95%	**−1.91%**
M=5, Tw/Tinf=5.45	+2.44%	−3.09%	−2.91%	−2.75%	−2.55%	**−2.60%**

- **`M = 2` and `M = 5, Tw/Tω = 5.45`** (the warmest wall): the error against theory falls with the mesh and ends within 0.8% of theory on the three finest meshes for `M = 2` and within 0.4% for `Tw/Tω = 5.45`. On the finest mesh Wake CFD is 0.22% (`Tw/Tω = 5.45`) and 0.72% (`M = 2`) below theory.
- **`M = 5, Tw/Tω = 2.725`**: the error against theory goes from −4.88% to −2.97%, changing little over the last two refinements (−3.01% to −2.97%).
- **`M = 5, Tw/Tω = 1.090`** (the most strongly cooled wall): the error against theory remains large, −9.28% on the finest mesh, and is still moving with the mesh (−11.05%, −9.87%, −9.28% over the last three meshes). CFL3D SA is also 8.08% below theory at this `Re_` , and Wake CFD on the finest mesh is within 1.30% of CFL3D. For this condition the difference from theory therefore appears to be a property of the SA model rather than a discretization error of this run, but that attribution was not tested (for example with another turbulence model).
- **Offset from CFL3D at the warmer `M = 5` walls.** For `Tw/Tω = 2.725` and `5.45` Wake CFD stays about 1.9% and 2.6% below CFL3D on the two finest meshes, with almost no change from `273×193` to `545×385`, so it does not decrease with refinement. It was not isolated whether this comes from differences in setting (for example the viscosity law or the `Re_` extraction) or from the models. The theory comparison is the primary result for this case, and Wake CFD is close to theory for these two conditions (−2.97% and −0.22%).

6.8.3 Law of the Wall

u+ = u/u_ with u_ = sqrt(_w/ _w) is plotted against y+ at the station nearest Re_ = 10,000 on each mesh, together with the van Driest I curve and the CFL3D SA result from TMR. Compared visually, the curves of the three finest meshes lie on top of each other and on the CFL3D curve; the coarser meshes sit above them in the log region and the outer plateau. The theory curve lies below the computed profiles in the buffer and log regions; the gap is largest for Tw/Tw = 1.09, where the Cf error against theory is also largest. Only the Cf values above were quantified.

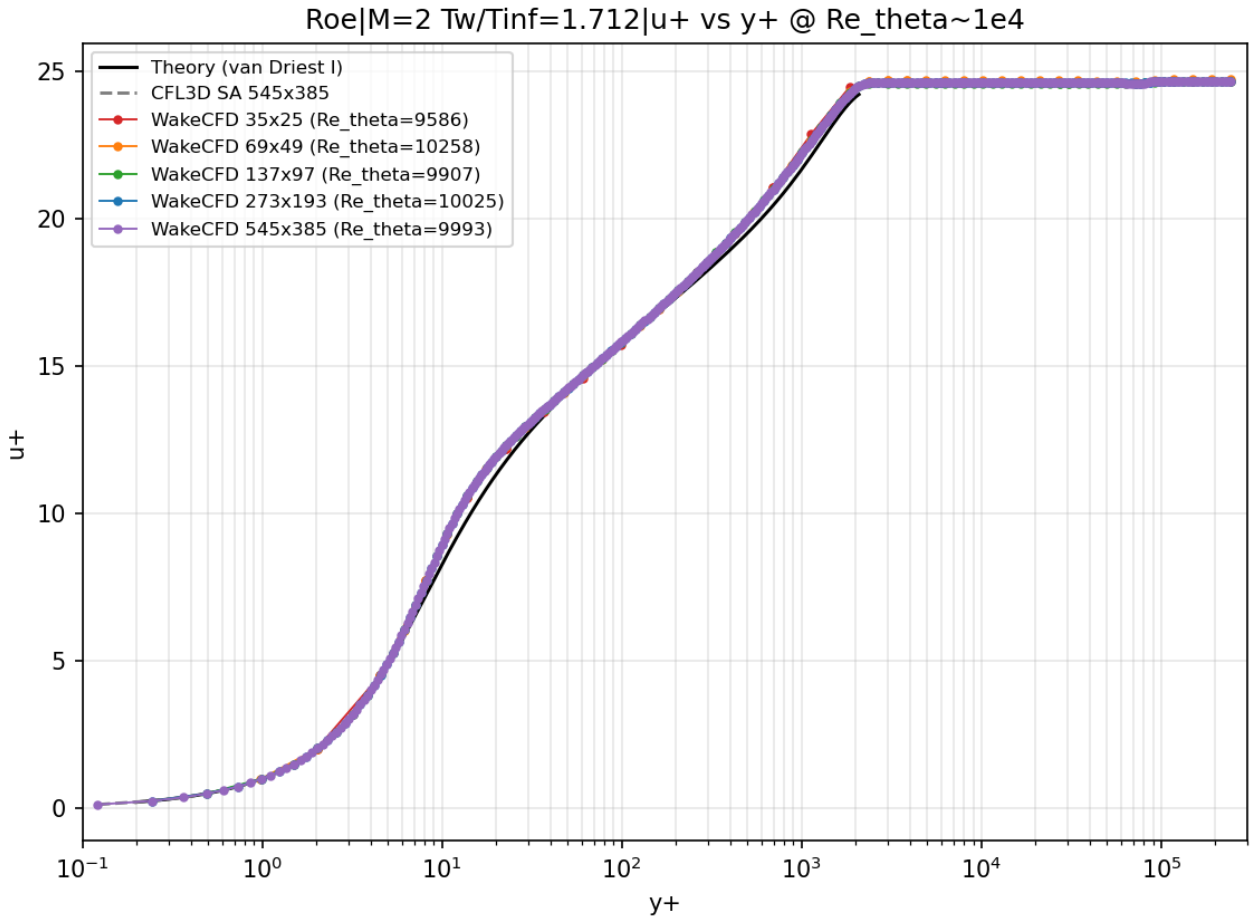


Figure 6.10: u+ versus y+ at Re_ 10,000 — M=2, Tw/Tinf=1.712

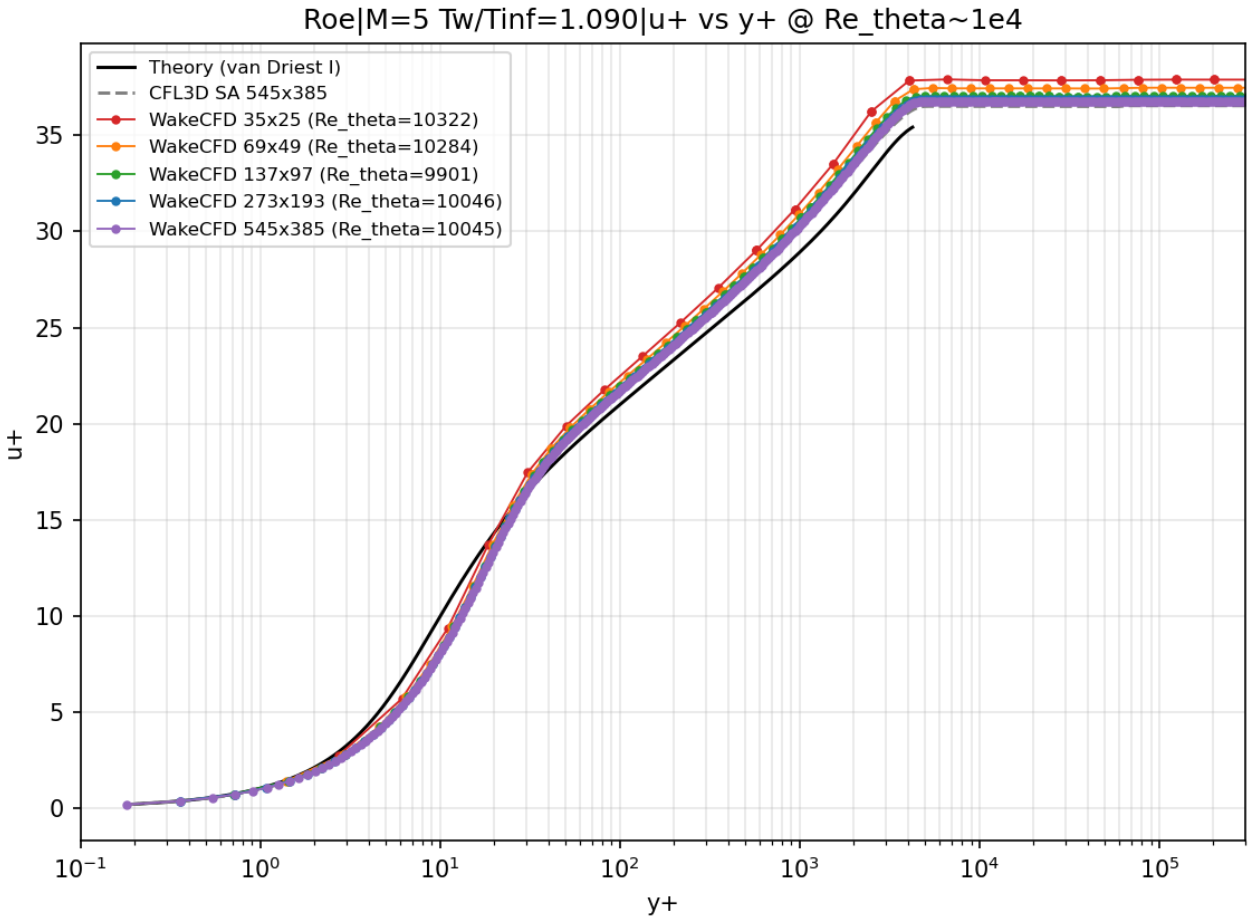


Figure 6.11: u+ versus y+ — M=5, Tw/Tinf=1.090

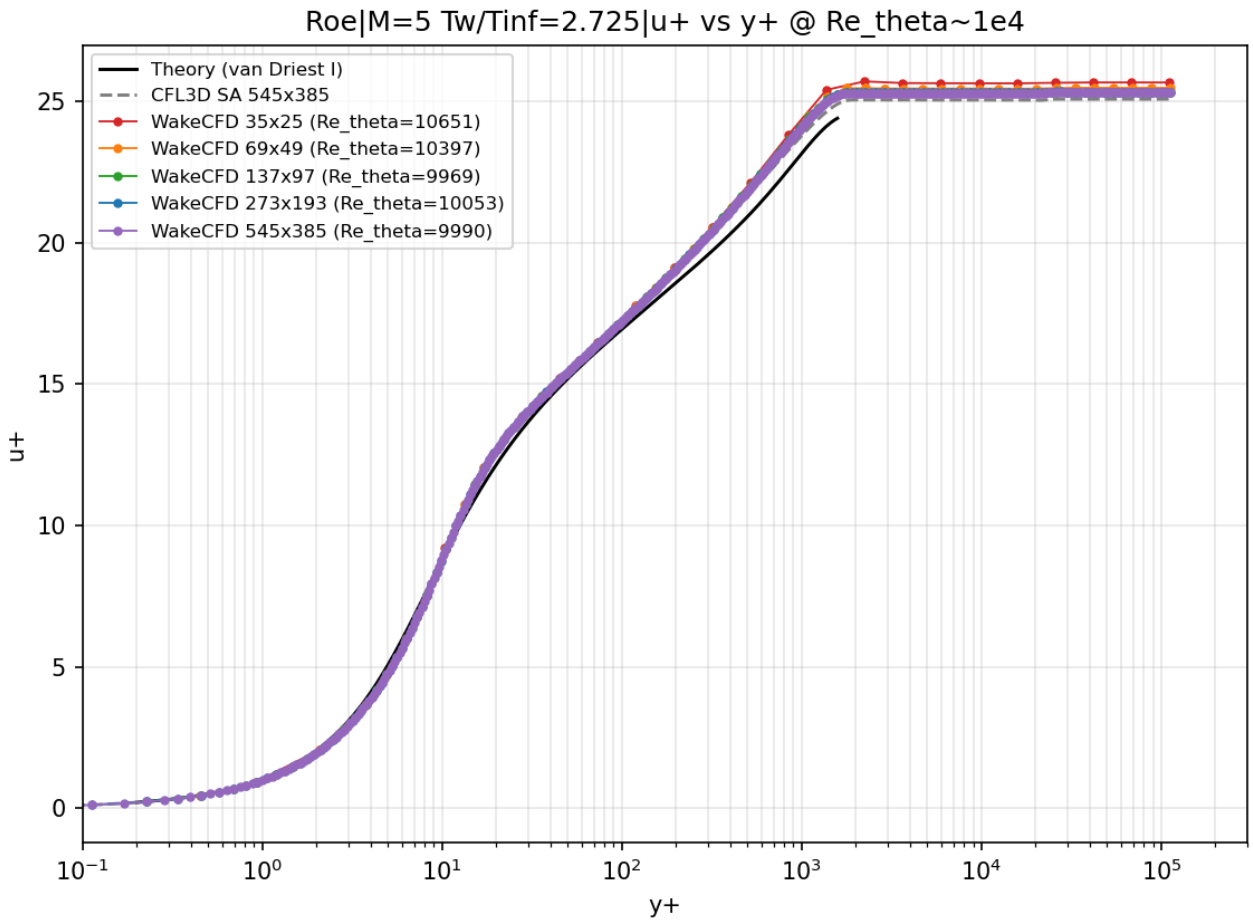


Figure 6.12: u+ versus y+ — M=5, Tw/Tinf=2.725

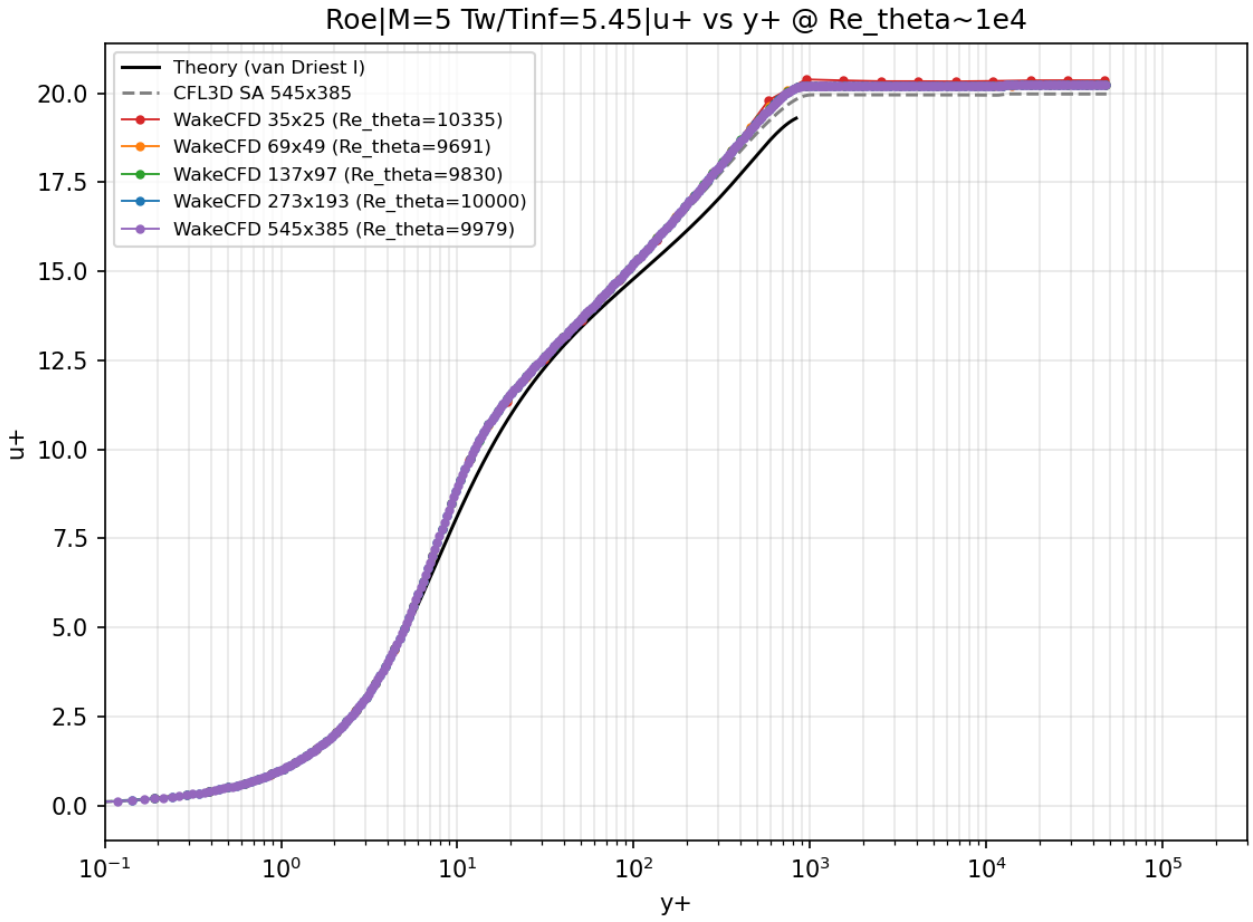


Figure 6.13: `u+` versus `y+` — M=5, Tw/Tinf=5.45

6.9 Conclusions and Applicable Scope

- On the finest mesh, Wake CFD's SA result agrees with van Driest II theory at `Re_ = 10,000` within 0.72% (`M=2, Tw/Tω=1.712`), 0.22% (`M=5, Tw/Tω=5.45`) and 2.97% (`M=5, Tw/Tω=2.725`). For the strongly cooled `M=5, Tw/Tω=1.09` wall it is 9.28% below theory, where the CFL3D SA result published by TMR is also 8.08% below theory and Wake CFD is within 1.30% of CFL3D.
- Refining the mesh moves `Cf` toward its finest-mesh value in all four conditions, with one small exception: for `Tw/Tω = 5.45` the last step goes from −0.17% to −0.22% against theory. For `Tw/Tω = 1.09` the change from `273×193` to `545×385` is still 0.6 percentage points, so grid independence is not established for that condition.
- Fifteen of the twenty runs met the residual criterion. Five (the two `273×193` and three `545×385` `M = 5` runs listed above) ended on the iteration cap at residuals between `-9.7` and `-11.8` and are treated as converged for the comparison; they were not run longer to confirm the `Cf` values no longer change.
- Against CFL3D, Wake CFD shows a difference of about 2% to 3% on the finest mesh at the two warmer `M = 5` walls that does not decrease with refinement; its cause was not identified.

- These results apply to a zero-pressure-gradient, isothermal flat plate at `M = 2` and `M = 5` with the SA model, over the fully turbulent range `Re_  4,000` to `13,000`. They cannot be generalized to pressure gradients, shock–boundary-layer interaction, transition, or other turbulence models. The effect of the wall treatment option and the leading-edge region were not examined.

6.10 References

- NASA Turbulence Modeling Resource: 2D Zero Pressure Gradient Flat Plate, Supersonic/Hypersonic (SS) Verification Case
- NASA Turbulence Modeling Resource: SA results for the 2D supersonic flat plate
- NASA Turbulence Modeling Resource: 2D Flat Plate Validation Case (mesh family)

7 3D Laminar Flat-Plate Boundary Layer — PBNS Blasius Verification

Verification of the constant-density pressure-based solver against the Blasius velocity profile and skin-friction solution

7.1 Run Provenance and Artifacts

Item	Value
Wake CFD baseline version	`0.22.2`
Solver	PBNS
Compute device	GPU (NVIDIA RTX A2000)
Parallel execution	1 MPI rank
Arithmetic precision	FP64
Run date	2026-09-23

> **Note**
>
> Results depend on the solver build that produced them. Read every figure in this report together with the version and date above — re-running the same input on a later build may give different numbers.

7.1.1 Downloadable Files

Not available: standalone input decks and solver result files have not yet been published for download.

7.2 Verification Objective

This case simulates a steady, constant-density laminar boundary layer over a flat plate with Wake CFD's pressure-based Navier–Stokes (PBNS) solver. It compares the computed velocity profiles and local skin-friction coefficient with the Blasius similarity solution to verify:

- the incompressible, constant-density PBNS formulation for a low-speed external flow

- no-slip wall treatment and viscous momentum diffusion
- pressure–velocity coupling on a three-dimensional mesh
- recovery of the Blasius similarity profile and wall shear at `Re_L=1×10^5`

The physical setup follows the DBNS laminar flat-plate case, while the two-dimensional mesh is extruded by one cell in the spanwise direction because PBNS uses the three-dimensional solver path. Only the incompressible result is reported here; no compressible low-Mach or heat-transfer result is included.

7.3 Reference Solution and Data

7.3.1 Analytical Solution

Let `x` denote distance from the plate leading edge, `y` the wall-normal distance, `U_inf` the inlet velocity, and `nu=mu/rho` the kinematic viscosity. The similarity coordinate and local Reynolds number are

$$\eta = y\sqrt{\frac{U_\infty}{\nu x}}, \qquad Re_x = \frac{U_\infty x}{\nu}.$$

The Blasius solution gives `u/U_inf=f'(eta)` and

$$C_f(x) = \frac{0.664}{\sqrt{Re_x}}, \qquad \delta_{99} \approx 4.91\sqrt{\frac{\nu x}{U_\infty}}.$$

Velocity profiles at different streamwise stations should therefore collapse onto one curve when plotted in similarity coordinates.

7.4 Simulation Conditions

Item	Setting
Dimension	3D, one-cell spanwise extrusion
Domain	`x=[0, 0.762] m`, `y=[0, 0.1524] m`, `z=[0, 0.003048] m`
Flat plate	`x=[0.1524, 0.4572] m`, `L=0.3048 m`
Analysis	Steady, laminar PBNS, incompressible constant-density Navier–Stokes
Density	`rho=1.1827 kg/m^3`
Dynamic viscosity	`mu=1.8×10^-5 Pa·s`
Inlet velocity	`U_inf=4.994 m/s`
Reynolds number	`Re_L 1.0×10^5`
Reference pressure	`101325 Pa`

7.5 Mesh

The mesh contains 58,050 nodes and 28,672 hexahedral cells. It is a one-cell spanwise extrusion of the same two-dimensional flat-plate mesh used by the DBNS case. The figures below show that shared two-dimensional plane; the PBNS mesh adds only the spanwise extrusion, with symmetry conditions on both extrusion faces.

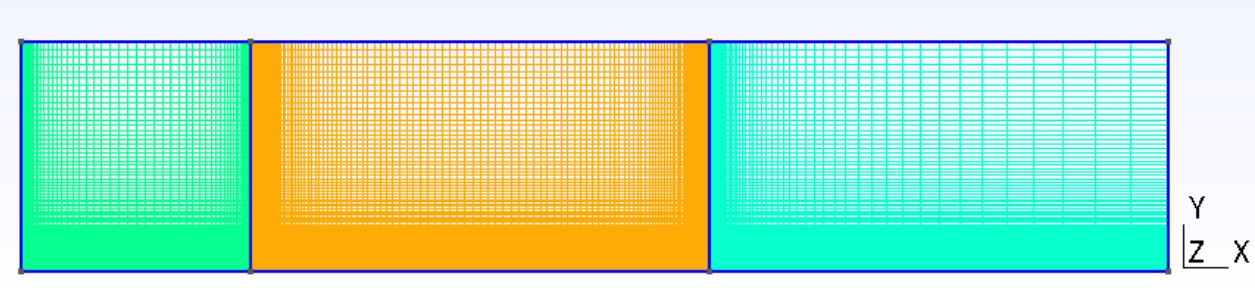


Figure 7.1: Full two-dimensional flat-plate mesh before one-cell spanwise extrusion

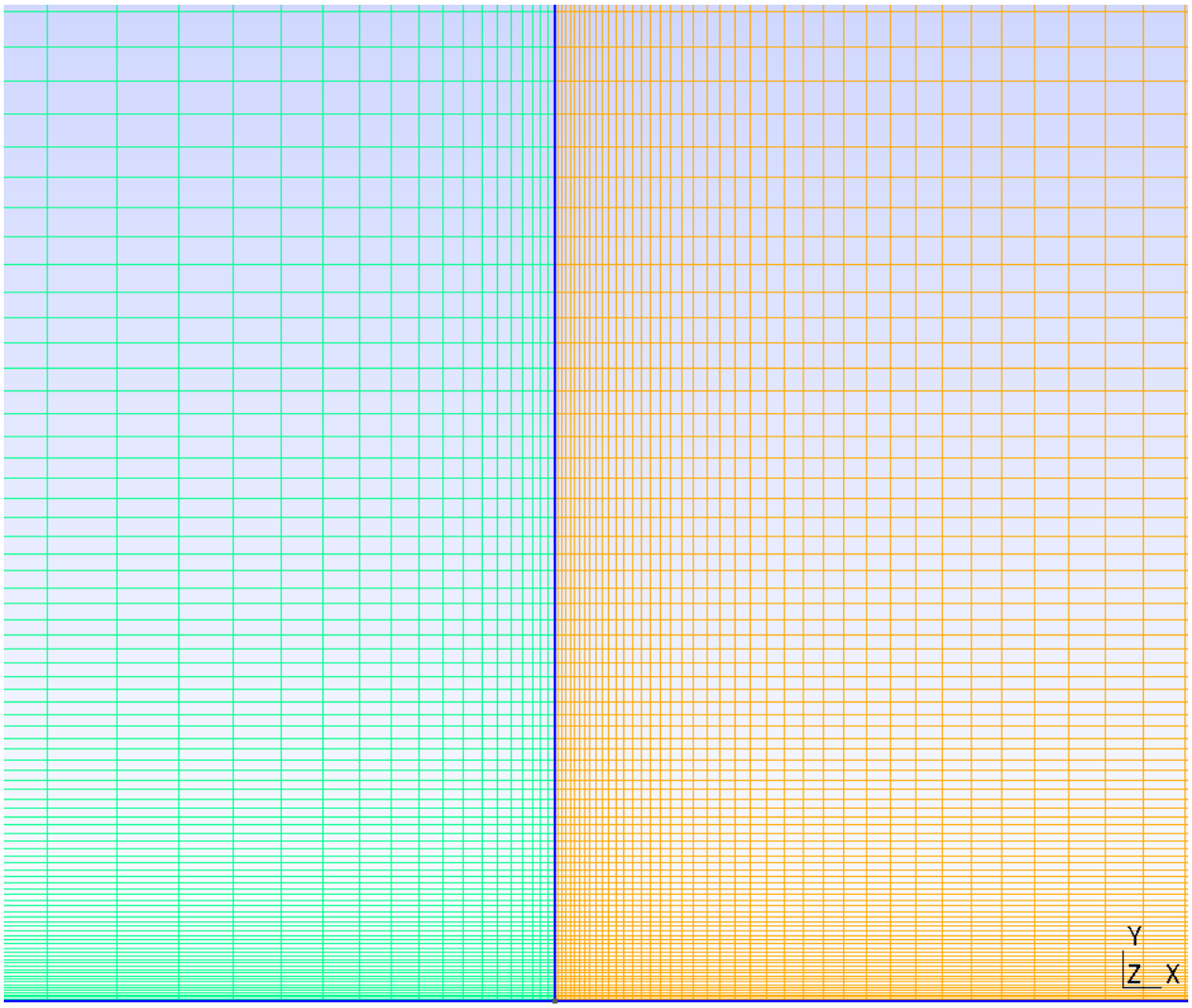


Figure 7.2: Mesh refinement around the flat-plate leading edge

7.6 Boundary and Initial Conditions

Boundary	Type	Setting
Plate	Wall	no-slip
Bottom, upstream and downstream of plate	Symmetry	slip
Inlet	Velocity inlet	`U=4.994 m/s` in the streamwise direction
Outlet	Pressure outlet	`p=101325 Pa`
Top	Symmetry	slip
Front and back extrusion faces	Symmetry	one-cell spanwise slab

Initial field: Not reported.

7.7 Numerical Methods

Item	Setting
Solver	Coupled PBNS, constant density
Spatial discretization	Second order, Green–Gauss gradients
Pressure–velocity coupling	Rhie–Chow interpolation
Pseudo-time control	Constant convective `CFL=1`
Linear solver	FGMRES, maximum 100 iterations, relative tolerance `10^-3`
Preconditioner	DILU, 5 sweeps
Outer-iteration limit	2,000
Configured convergence target	Scaled residual reduction of 10 orders

The run reached the 2,000-iteration limit rather than the configured 10-order residual target. The combined flow scaled residual nevertheless decreased from `10^-3.41` at the first reported iteration to `10^-6.78` at the final iteration. The verification metrics below are evaluated from that final solution and are reported separately from the residual stopping condition.

7.8 Results

The velocity profile was sampled at three stations. RMS error was computed after interpolating each profile onto the Blasius reference points in similarity coordinates.

`x/L`	`Re_x`	RMS error in `u/U_inf`	Computed `delta_99` in similarity coordinates
0.25	25,177	0.72%	4.59
0.50	50,008	0.94%	4.52
0.75	74,839	1.27%	4.44

All three profiles remain within 1.3% RMS of the Blasius solution. The computed boundary-layer thickness is slightly below the Blasius value of approximately `eta_99=4.91`, with the difference increasing toward the trailing edge.

Local skin friction was reconstructed from the final solution using a second-order one-sided wall-normal velocity gradient. Over the assessment window `0.1<x/L<0.7`, the mean relative difference from the Blasius relation is `+2.224%`. The window excludes the leading-edge singularity and the downstream portion where the finite plate and following slip boundary produce an increasing trailing-edge effect. Across the wider `0.1<x/L<0.9` interval, the mean absolute difference is 3.586% and the largest local difference is 10.349% near the end of that interval.

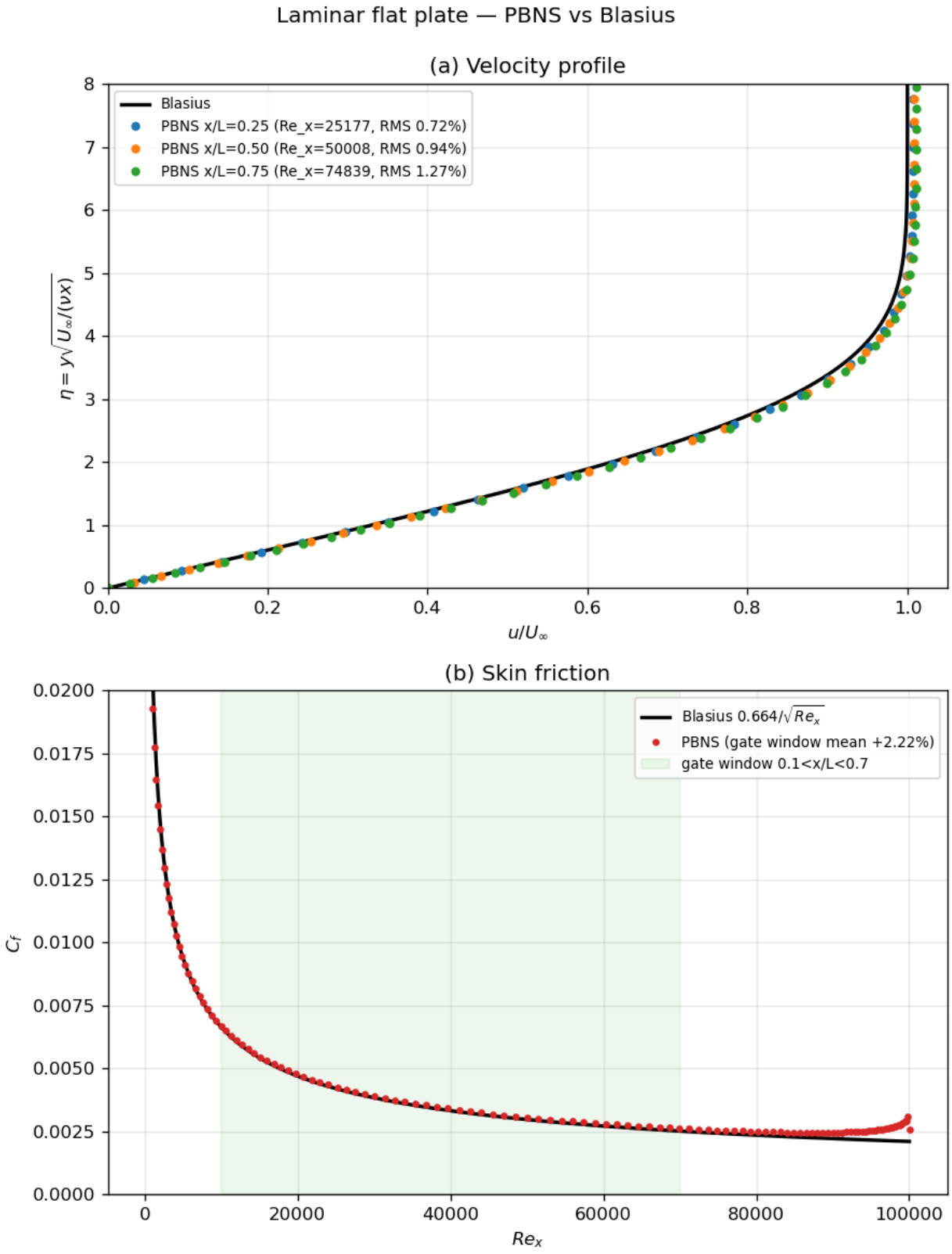


Figure 7.3: PBNS velocity profiles and local skin friction compared with the Blasius solution

The velocity-magnitude field shows the expected boundary layer growing from the plate leading edge. Mesh lines are overlaid to show the wall-normal clustering used to resolve the near-wall gradient.

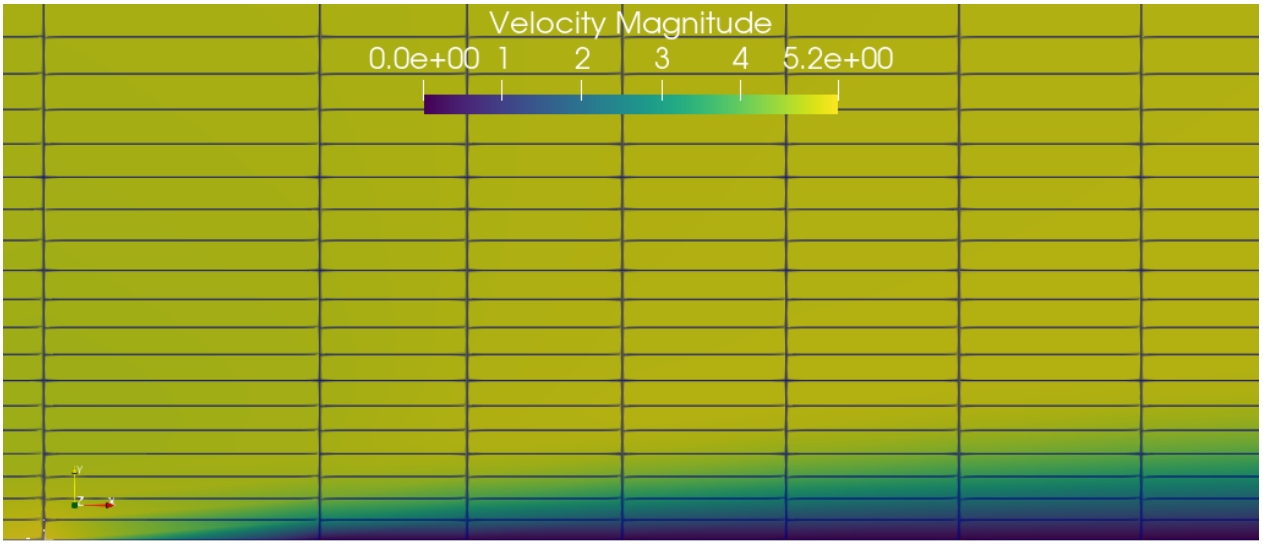


Figure 7.4: Velocity-magnitude contour of the incompressible PBNS solution

7.9 Conclusions and Applicable Scope

- The incompressible PBNS solution reproduces the Blasius velocity profile with `0.72-1.27%` RMS error at the three sampled stations.
- Mean local skin friction is `2.224%` above the Blasius relation over the primary `0.1<x/L<0.7` assessment window.
- The case confirms the constant-density PBNS pressure–velocity coupling, viscous wall treatment, and one-cell three-dimensional path for this steady laminar flow.
- The run stopped at its 2,000-iteration limit, at a final combined scaled residual of approximately `10^-6.78`, rather than satisfying the configured 10-order target.
- These results apply to one mesh and one Reynolds number for a zero-pressure-gradient, incompressible laminar boundary layer. They do not establish PBNS accuracy for turbulent flow, pressure gradients, separation, unsteady flow, or other Reynolds numbers.

This case fills the PBNS track in Wake CFD's flat-plate verification family. The related DBNS and FR reports use the same physical baseline with solver-specific meshes and numerical methods.

7.10 References

- Blasius, H., "Grenzschichten in Flüssigkeiten mit kleiner Reibung," *Zeitschrift für Mathematik und Physik*, 56, 1908, pp. 1–37.
- White, F.M., *Viscous Fluid Flow*, 3rd ed., McGraw-Hill, 2006 (Blasius similarity solution, Chapter 4).

8 2D Laminar Flat-Plate Boundary Layer — FR Blasius Verification

Verification of the p2 Flux Reconstruction solver against the Blasius velocity profile and skin-friction solution

8.1 Run Provenance and Artifacts

Item	Value
Wake CFD baseline version	`0.22.0`
Solver	FR
Compute device	GPU (NVIDIA RTX A2000 12GB)
Parallel execution	1 MPI rank
Arithmetic precision	FP64
Run date	2026-09-23

> **Note**
>
> Results depend on the solver build that produced them. Read every figure in this report together with the version and date above — re-running the same input on a later build may give different numbers.

8.1.1 Downloadable Files

Not available: standalone input decks and solver result files have not yet been published for download.

8.2 Verification Objective

This case simulates the developing laminar boundary layer over a two-dimensional flat plate with the Flux Reconstruction (FR) solver. The final numerical solution is compared with the Blasius similarity solution to verify:

- the no-slip viscous-wall treatment in the FR solver

- third-order `p2` solution accuracy on a stretched quadrilateral mesh
- collapse of velocity profiles at several streamwise stations in similarity coordinates
- local skin-friction evaluation from FR wall flux points
- dual-time integration of a low-Mach viscous flow

The geometry and freestream condition match the DBNS laminar flat-plate case, so the result also adds an independently implemented solver track to the common flat-plate verification family.

8.3 Reference Solution and Data

8.3.1 Analytical Solution

For a zero-pressure-gradient laminar boundary layer, let `x` denote distance from the plate leading edge, `y` the wall-normal distance, `U_inf` the freestream velocity, and `nu` the kinematic viscosity. The similarity coordinate and local Reynolds number are

$$\eta = y\sqrt{\frac{U_\infty}{\nu x}}, \qquad Re_x = \frac{U_\infty x}{\nu}.$$

The Blasius solution gives `u/U_inf = f'(eta)` and

$$\delta_{99}\sqrt{\frac{U_\infty}{\nu x}} \approx 4.91, \qquad C_f(x) = \frac{0.664}{\sqrt{Re_x}}.$$

Velocity profiles taken at different `x/L` stations should therefore collapse onto one curve when plotted against `eta`.

8.4 Simulation Conditions

Item	Setting
Dimension	2D
Domain	`x=[0, 0.762] m`, `y=[0, 0.1524] m`
Flat plate	`x=[0.1524, 0.4572] m`, `L=0.3048 m`
Analysis	Unsteady, compressible laminar Navier–Stokes, evaluated at `t=12 s`
Mach number	`0.1`
Reynolds number	`Re_L=100,270`
Freestream	`P_inf=101325 Pa`, `T_inf=297.62 K`, `rho_inf=1.1827 kg/m^3`, `U_inf=34.63 m/s`
Viscosity	Constant, `mu=1.245×10^-4 Pa·s`

The viscosity is selected to obtain `Re_L 10^5` at `M=0.1`; this is a numerical verification condition rather than a specific ambient-air experiment. Although the wall is isothermal, this report does not

make a heat-transfer claim because the retained run output does not contain the required integrated heat-flux monitor.

8.5 Mesh

The structured mesh has `80×40=3,200` linear quadrilateral cells. It is clustered at the plate leading and trailing edges and stretched in the wall-normal direction, with a first wall-cell height of `1.5×10^-4 m`. With an FR `p2` basis, each cell contains nine solution points, giving 28,800 solution points and 144,000 scalar conservative-variable degrees of freedom.

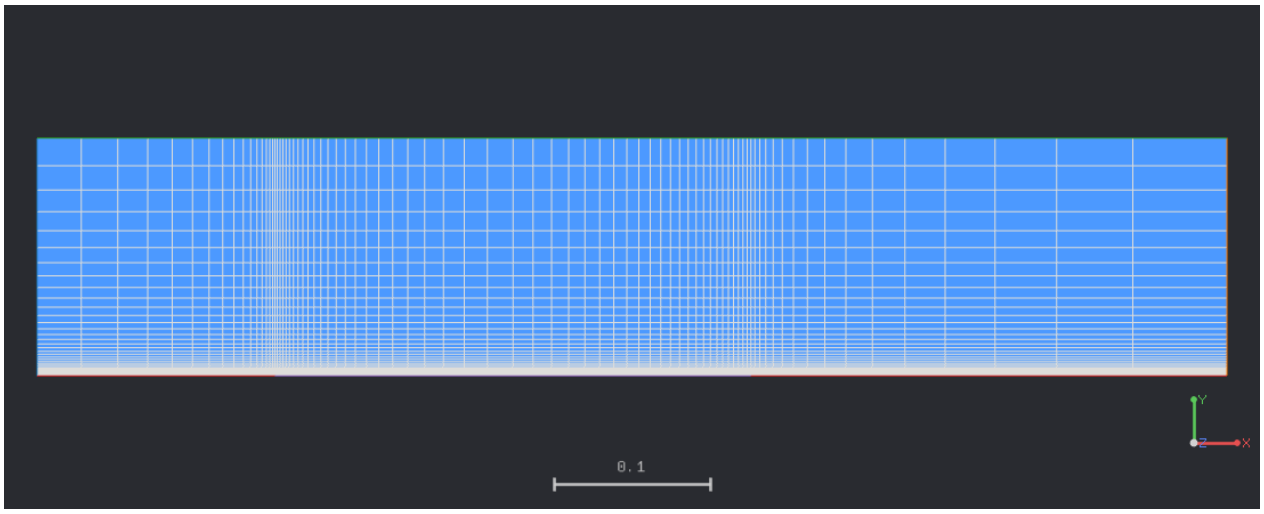


Figure 8.1: Structured quadrilateral mesh with streamwise edge clustering and wall-normal stretching

8.6 Boundary and Initial Conditions

Boundary	Type	Setting
Left	Farfield inlet	`M=0.1`, `P=101325 Pa`, `T=297.62 K`
Right	Pressure outlet	`P=101325 Pa`
Top	Farfield	Freestream condition
Bottom outside plate	Free-slip wall	Zero normal velocity
Plate	No-slip isothermal wall	`T_wall=327.38 K`

Initial field: Not reported.

8.7 Numerical Methods

Item	Setting
Spatial discretization	FR `p2` (third order), quadrilateral elements
Convective interface flux	Rusanov
Viscous interface parameters	LDG `beta=0.5`, `tau=0.3`
Physical-time integration	Dual-time BDF1, `dt=5×10^-3 s`, 2,400 steps
Pseudo-time integration	RK45 with local-PI control, `CFL=0.3`
Inner iterations	10 minimum, 300 maximum per physical step

The run advances from a uniform freestream state to `t=12 s`. Each physical step reached the configured 300-inner-iteration cap, and no inner residual stopping tolerance was enabled. The comparison below therefore assesses the final time-marched solution; it is not evidence of formal pseudo-time or grid convergence.

8.8 Results

The final velocity profiles at `x/L=0.25`, `0.50`, and `0.75` follow the Blasius curve closely. RMS errors in normalized velocity remain below 1% at all three stations. The boundary-layer thickness is slightly underpredicted, with the largest difference at the downstream station.

`x/L`	`Re_x`	RMS error in `u/U_inf`	Computed `delta_99(eta)`	Difference from 4.91
0.25	25,068	0.53%	4.673	-4.8%
0.50	50,135	0.66%	4.621	-5.9%
0.75	75,203	0.97%	4.517	-8.0%

Over `0.2` `x/L` `0.9`, the median absolute deviation of local `Cf` from the Blasius solution is 2.0%; the worst sampled deviation is 10.8%. The median signed ratio is `Cf_FR/Cf_Blasius=1.021`, indicating a small overall overprediction of wall shear in the evaluated interval.

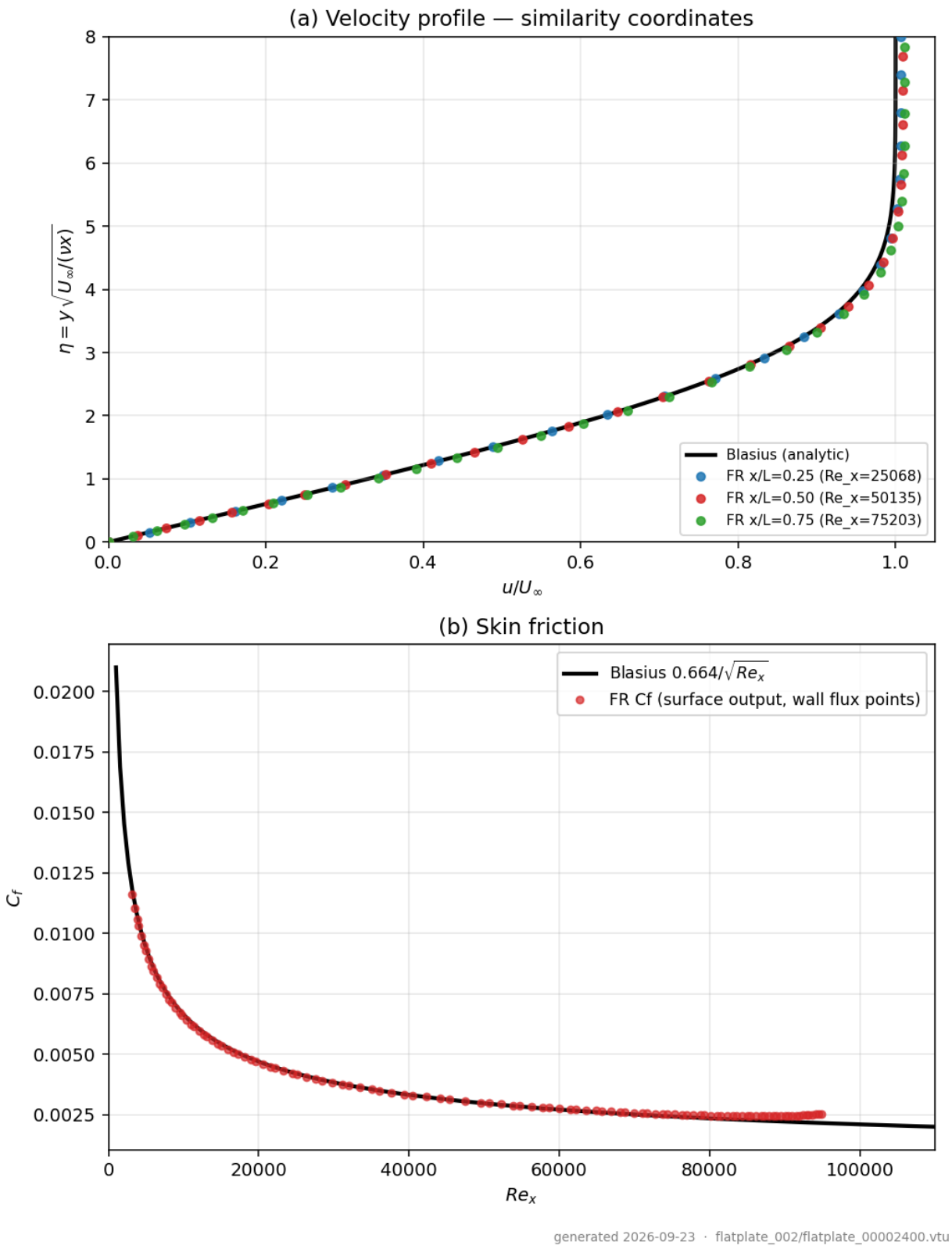


Figure 8.2: FR velocity profiles and local skin friction compared with the Blasius solution

The velocity contour shows the boundary layer growing downstream from the plate leading edge. The plotted region is limited to the near-wall field so that the thin low-speed layer remains visible.

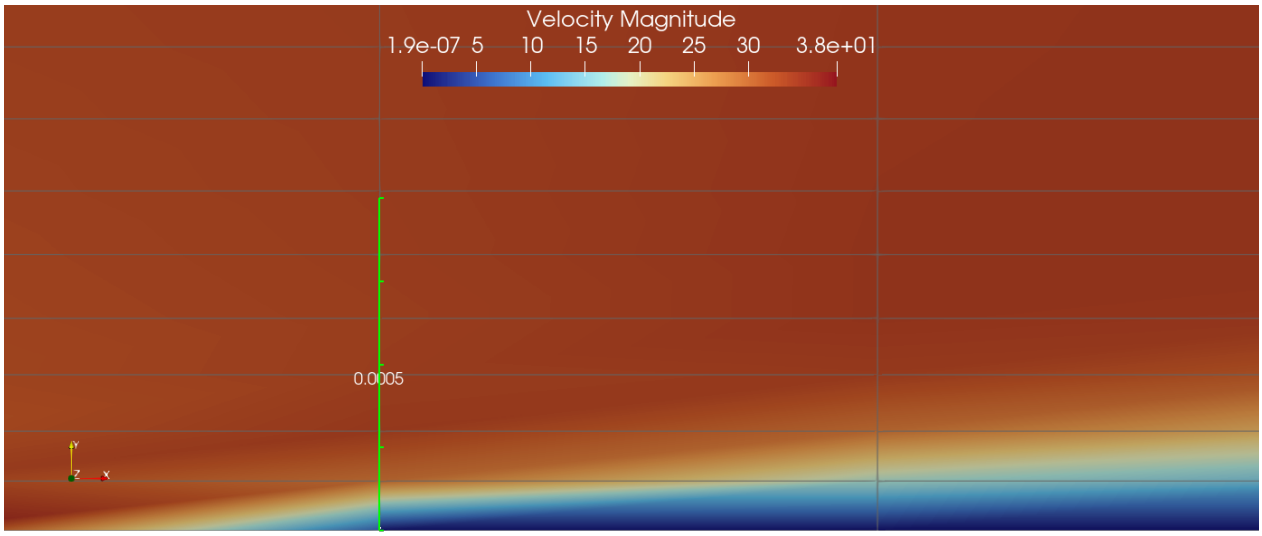


Figure 8.3: Velocity-magnitude contour near the flat-plate leading edge

8.9 Conclusions and Applicable Scope

- The FR `p2` solution reproduces the Blasius normalized velocity profiles with less than 1% RMS error at all three sampled stations.
- Local skin friction agrees with the analytical solution to a 2.0% median absolute deviation over `0.2` `x/L` `0.9`; the largest sampled deviation is 10.8%.
- The boundary-layer thickness is underpredicted by 4.8–8.0%, with the discrepancy increasing downstream.
- This result verifies the combined FR viscous-wall, wall-flux, and dual-time path for one `p2` mesh at `M=0.1` and `Re_L` `10^5`.
- The run does not establish mesh, polynomial-order, time-step, or pseudo-time convergence. Those variables should be varied independently before broader accuracy claims are made.
- No Pohlhausen heat-transfer result is reported because the retained history file lacks the integrated heat-flux quantities required for that comparison.

This case establishes a baseline for laminar flat-plate calculations with the FR solver. It does not cover turbulent flow, pressure gradients, separation, transition, curved walls, or other Reynolds and Mach numbers.

8.10 References

- Blasius, H., "Grenzschichten in Flüssigkeiten mit kleiner Reibung," *Zeitschrift für Mathematik und Physik*, 56, 1908, pp. 1–37.
- White, F. M., *Viscous Fluid Flow*, 3rd ed., McGraw-Hill, 2006, Chapter 4.

Part III

Shock & Expansion Flows

9 Supersonic Wedge — Oblique-Shock Verification

Comparison with the exact theta–beta–Mach and Rankine–Hugoniot relations

9.1 Run Provenance and Artifacts

Item	Value
Wake CFD baseline version	`0.22.0`
Solver	DBNS
Compute device	CPU
Parallel execution	1 MPI rank
Arithmetic precision	FP64
Run date	2026-08-20

> **Note**
>
> Results depend on the solver build that produced them. Read every figure in this report together with the version and date above — re-running the same input on a later build may give different numbers.

9.1.1 Downloadable Files

Not available: standalone input decks and solver result files have not yet been published for download.

9.2 Verification Objective

This is a code-verification case, not an experimental validation case. The two-dimensional Euler solution over a 15° wedge is compared directly with the exact oblique-shock relations. It verifies shock capturing, inviscid wall treatment, and supersonic inflow and outflow boundary conditions.

The geometry and freestream condition reproduce the NASA GRC WIND verification case, Oblique Shock on a 15 Degree Wedge at Mach 2.5.

9.3 Reference Solution and Data

9.3.1 Analytical Solution

For an upstream Mach number `M_1`, wedge deflection `theta`, and specific-heat ratio `gamma`, the weak-shock angle `beta` is obtained from the theta–beta–Mach relation:

$$\tan\theta = 2\cot\beta\,\frac{M_1^2\sin^2\beta - 1}{M_1^2(\gamma + \cos 2\beta) + 2}.$$

The downstream state follows from the normal-shock Rankine–Hugoniot relations using `M_1n=M_1\sin\beta`. For `M_1=2.5`, `theta=15°`, and `gamma=1.4`, the reference values are:

Quantity	Reference value
Weak-shock angle, `beta`	36.94490°
Downstream Mach number, `M_2`	1.873526
Pressure ratio, `p_2/p_1`	2.467500
Density ratio, `rho_2/rho_1`	1.866549
Temperature ratio, `T_2/T_1`	1.321958

9.4 Simulation Conditions

Item	Setting
Geometry	2D wedge; 15° half-angle
Physics	Steady Euler equations, ideal-gas air (`gamma=1.4`)
Freestream	`M=2.5`, `p=101325 Pa`, `T=288.15 K`, zero angle of attack

9.5 Mesh

Item	Setting
Mesh	Unstructured triangular mesh; 8,789 nodes

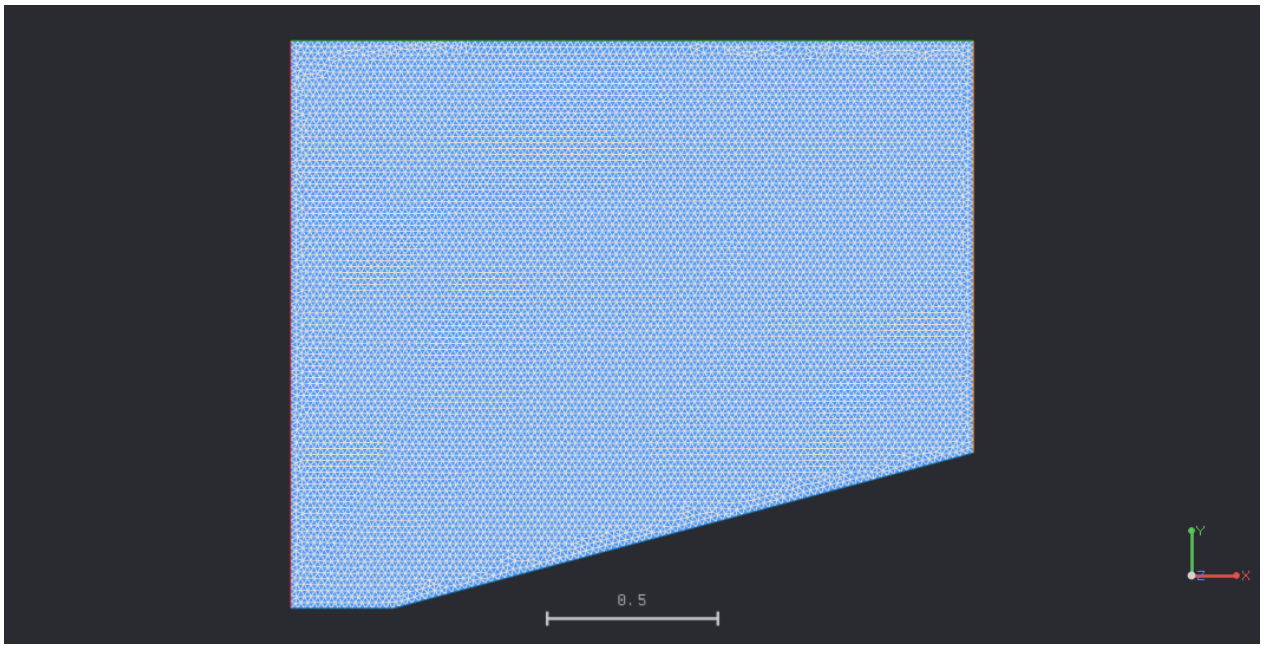


Figure 9.1: Triangular mesh for the supersonic wedge

9.6 Boundary and Initial Conditions

Item	Setting
Wall	Free-slip inviscid wall
Inlet	Supersonic farfield inflow
Outlet and top boundary	Supersonic pressure outlet; interior state extrapolated

Initial field: Not reported.

9.7 Numerical Methods

Item	Setting
Convective schemes	AUSM, AUSM+up2, AUSM+up, HLLC, JST, Roe, SLAU2, and SLAU (compared below)
Spatial method	Green–Gauss gradients with Venkatakrishnan limiter
Time integration	Implicit, adaptive CFL ramp

9.8 Results

The Roe result captures the attached oblique shock and the uniform post-shock region expected for this inviscid flow.

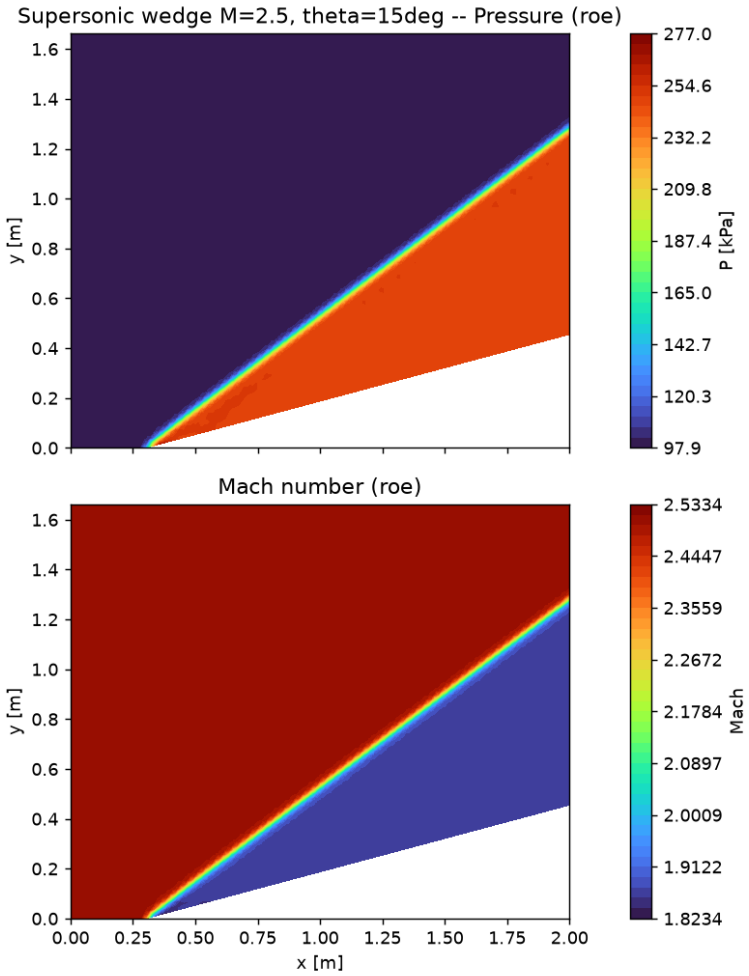


Figure 9.2: Pressure and Mach contours for the Roe result

Eight convective schemes were evaluated on the same mesh and boundary conditions. All reached the specified convergence criterion. Post-shock values were sampled downstream of the shock and compared with the exact solution.

Scheme	`p_2/p_1`	Error in `p_2/p_1`	`M_2`	Error in `M_2`
AUSM	2.46752	+0.0008%	1.86655	−0.372%
AUSM+up2	2.46750	−0.0001%	1.86539	−0.434%
AUSM+up	2.46744	−0.0025%	1.86402	−0.507%
HLLC	2.46746	−0.0017%	1.86528	−0.440%
JST	2.46729	−0.0086%	1.87445	+0.049%
Roe	2.46749	−0.0003%	1.86451	−0.481%

Scheme	p_2/p_1	Error in p_2/p_1	M_2	Error in M_2
SLAU2	2.46747	−0.0012%	1.86295	−0.564%
SLAU	2.46744	−0.0023%	1.86152	−0.641%

The pressure-ratio error is below 0.01% for every scheme, and the downstream-Mach error is below 0.7%. This case is deliberately simple: its purpose is to verify the exact shock jump and boundary-condition treatment, not to differentiate scheme robustness for complex shock interactions.

9.9 Conclusions and Applicable Scope

- Wake CFD reproduces the exact pressure jump for the attached oblique shock to within 0.01% across the tested schemes.
- The downstream Mach number agrees with the exact solution to within 0.7%.
- These results apply to a single attached shock in steady, two-dimensional inviscid flow on one mesh. They do not establish accuracy for viscous effects, separated flow, shock interaction, or mesh convergence.

9.10 References

- NASA GRC WIND Verification and Validation Archive: Oblique Shock on a 15 Degree Wedge at Mach 2.5

10 Forward-Facing Step — Supersonic Shock-System Verification

Qualitative comparison with the Woodward–Colella benchmark and a global mass-balance check

10.1 Run Provenance and Artifacts

Item	Value
Wake CFD baseline version	`0.22.0`
Solver	DBNS
Compute device	CPU
Parallel execution	1 MPI rank
Arithmetic precision	FP64
Run date	2026-08-20

> **Note**
>
> Results depend on the solver build that produced them. Read every figure in this report together with the version and date above — re-running the same input on a later build may give different numbers.

10.1.1 Downloadable Files

Not available: standalone input decks and solver result files have not yet been published for download.

10.2 Verification Objective

This case evaluates Wake CFD on the classical Mach 3 forward-facing-step problem. Unlike the oblique-wedge case, this problem has no closed-form solution. Verification is therefore based on reproduction of the characteristic inviscid shock system reported in the benchmark literature, supplemented by a global mass-conservation check.

The case is based on the forward-facing-step problem of Emery and of Woodward and Colella.

10.3 Reference Solution and Data

10.3.1 Numerical Reference

The qualitative benchmark is the forward-facing-step flow described by Emery and by Woodward and Colella (see References). No pointwise reference dataset is reported here.

10.4 Simulation Conditions

Item	Setting
Geometry	2D channel, `3.0 × 1.0 m`; step at `x=0.6 m` with height `0.2 m`
Physics	Steady Euler equations, ideal-gas air (`gamma=1.4`)
Freestream	`M=3.0`, `p=101325 Pa`, `T=288.15 K`, zero angle of attack

10.5 Mesh

Item	Setting
Mesh	Unstructured triangular mesh; 53,565 nodes; rounded inside step corner

10.6 Boundary and Initial Conditions

Item	Setting
Wall	Free-slip inviscid wall
Inlet	Supersonic farfield inflow
Outlet	Supersonic pressure outlet; interior state extrapolated

Initial field: Not reported.

10.7 Numerical Methods

Item	Setting
Convective scheme	Roe with Harten–Hyman entropy fix
Spatial method	Green–Gauss gradients with Venkatakrishnan limiter

Item	Setting
Time integration	Implicit, adaptive CFL ramp

10.8 Results

The density contours reproduce the benchmark's characteristic features: a bow shock upstream of the step, an expansion fan at the step corner, a reflected shock from the upper wall, and a secondary reflection downstream.

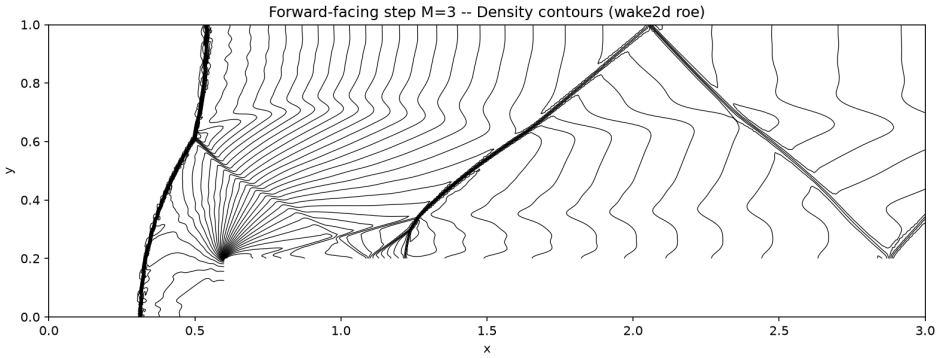


Figure 10.1: Density contours for the forward-facing-step result

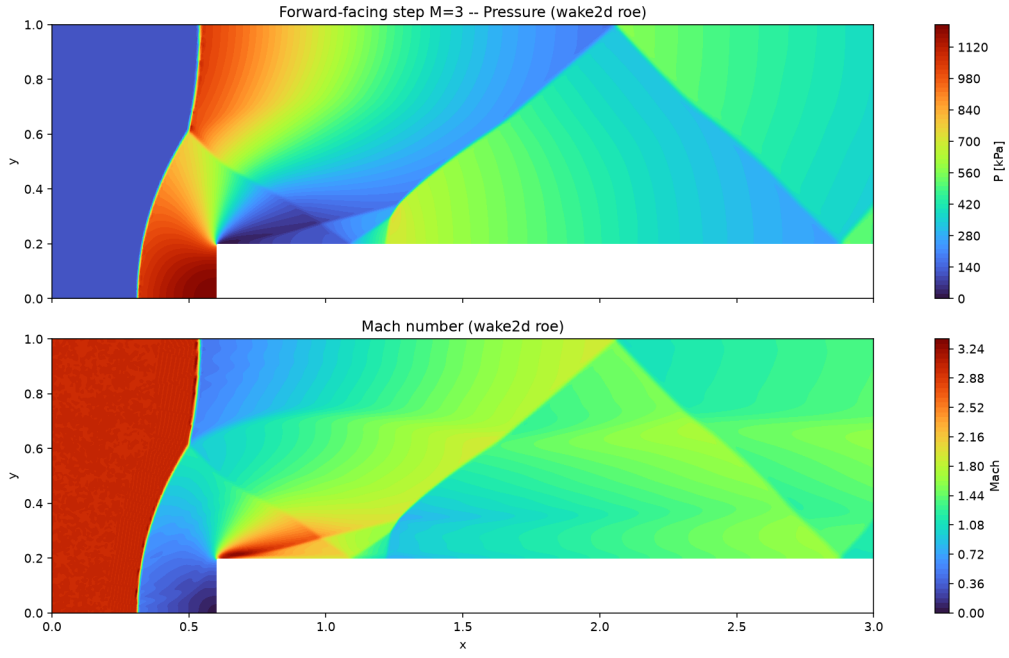


Figure 10.2: Pressure and Mach contours for the forward-facing-step result

As a quantitative consistency check, the integrated inlet mass flow is approximately `1250.59`

`kg/(s·m)` and the outlet mass flow is approximately `1250.94 kg/(s·m)`, excluding the blocked region below the step. The resulting mass-flow difference is 0.03%.

10.9 Conclusions and Applicable Scope

- The computed shock structure is qualitatively consistent with the established Woodward–Colella forward-facing-step benchmark.
- The global inlet/outlet mass-flow mismatch is 0.03% for the reported steady solution.
- This is a qualitative benchmark with a global conservation check, not a pointwise comparison with an analytical or experimental reference solution.
- The result is limited to steady, two-dimensional inviscid flow on the reported mesh. It does not establish mesh convergence, viscous-flow accuracy, or general scheme robustness.

10.10 References

- Emery, A. F., *An Evaluation of Several Differencing Methods for Inviscid Fluid Flow Problems*, Journal of Computational Physics, 2(3), 306–331, 1968.
- Woodward, P., and Colella, P., *The Numerical Simulation of Two-Dimensional Fluid Flow with Strong Shocks*, Journal of Computational Physics, 54(1), 115–173, 1984.

11 Prandtl-Meyer Expansion Fan — Isentropic Verification

Post-expansion Mach number, pressure, and temperature ratios against the exact Prandtl-Meyer / isentropic relations

11.1 Run Provenance and Artifacts

Item	Value
Wake CFD baseline version	`0.22.1`
Solver	DBNS
Compute device	CPU
Parallel execution	1 MPI rank
Arithmetic precision	FP64
Run date	2026-09-21

> **Note**
>
> Results depend on the solver build that produced them. Read every figure in this report together with the version and date above — re-running the same input on a later build may give different numbers.

11.1.1 Downloadable Files

Not available: standalone input decks and solver result files have not yet been published for download.

11.2 Verification Objective

This case simulates a supersonic flow expanding around a 15° convex corner, reproducing the NASA GRC WIND validation archive's Prandtl-Meyer expansion case. The Prandtl-Meyer function combined with the isentropic relations gives an exact closed-form solution for the post-expansion Mach number, pressure ratio, and temperature ratio, against which the Wake CFD Euler solution is compared directly. It verifies Wake CFD's inviscid solver for:

- resolution of a centered expansion (simple) wave originating at a sharp corner
- isentropic accuracy (pressure, Mach number, and temperature all following the exact relations consistently)

11.3 Reference Solution and Data

Item	Setting
Reference	Exact Prandtl-Meyer function + isentropic relations

11.4 Simulation Conditions

Item	Setting
Geometry	Flat wall to `x = 0.3 m`, then a 15° convex corner; domain to `x = 2.0 m`, `y = 1.0 m`
Analysis	Steady, inviscid (Euler), ideal-gas air (`=1.4`)
Freestream	`M = 2.5`, `p = 82,737.09 Pa`, `T = 305.56 K`

Exact solution at `=15°`, `M =2.5`: solving `(M ) = (M ) +` for the Prandtl-Meyer function `(M)` gives `M = 3.2368`, with isentropic ratios `p /p = 0.3274`, `T /T = 0.7269`, `/ = 0.4505`. (These values agree with the temperature and density ratios independently published in the NASA WIND-US reference solution — `T /T = 0.7282`, `/ = 0.4497` — to within the reference CFD solution's own discretization error.)

A uniform background mesh under-resolves the corner, which is a point singularity in the exact solution (a centered fan originating from a single point). This locally generates numerical entropy that does not fully relax downstream, causing the Mach number and temperature (which depend on the full entropy state) to diverge further from the exact isentropic solution than the pressure ratio (which is set mostly by local wave structure). Corner-local mesh refinement resolves this; limiter freezing after the initial transient was needed for the refined-mesh case to reach a stable converged state efficiently (rather than a bounded, non-decaying residual oscillation) without changing the converged solution itself.

11.5 Mesh

Item	Setting
Mesh	Unstructured triangular (gmsh), locally refined near the corner (cell size reduced 4× within a 0.05 m radius of the corner, blending back to the background size) — `8,772` nodes

11.6 Boundary and Initial Conditions

Item	Setting
Wall	Free-slip (inviscid)
Outlet / top	Supersonic pressure outlet

Initial field: Not reported.

11.7 Numerical Methods

Item	Setting
Convective scheme	Roe with Venkatakrishnan limiter, frozen after the initial transient (`limiter.freeze_iter`)
Gradient method	Green–Gauss
Time integration	Implicit, adaptive CFL (`1 → 100`)
Convergence criterion	Absolute residual `-12` OR reduction `8` orders

11.8 Results

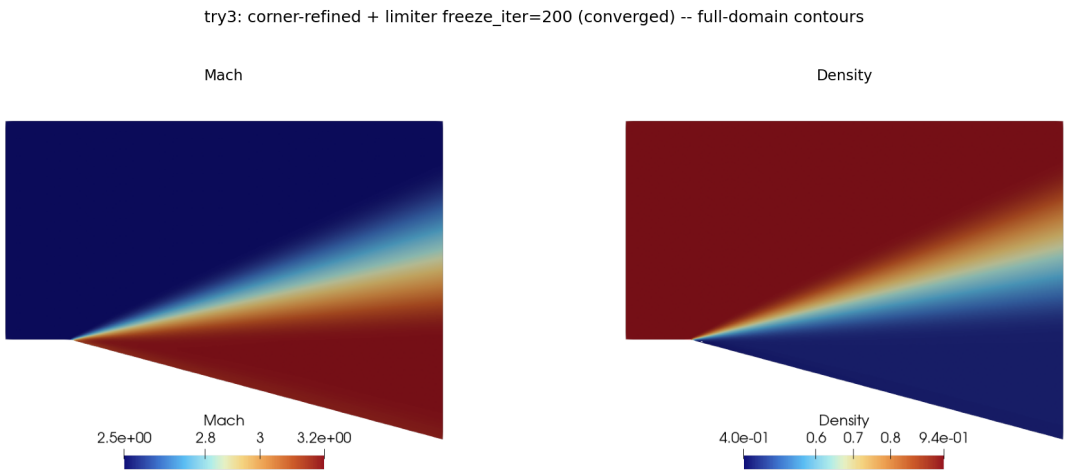


Figure 11.1: Full-domain Mach and density contours, converged solution

The freestream (`M=2.5`, dark blue) transitions smoothly through the fan region into the uniform downstream state (`M 3.2`, dark red), with the fan's leading and trailing characteristics visible as clean, nearly straight boundaries.

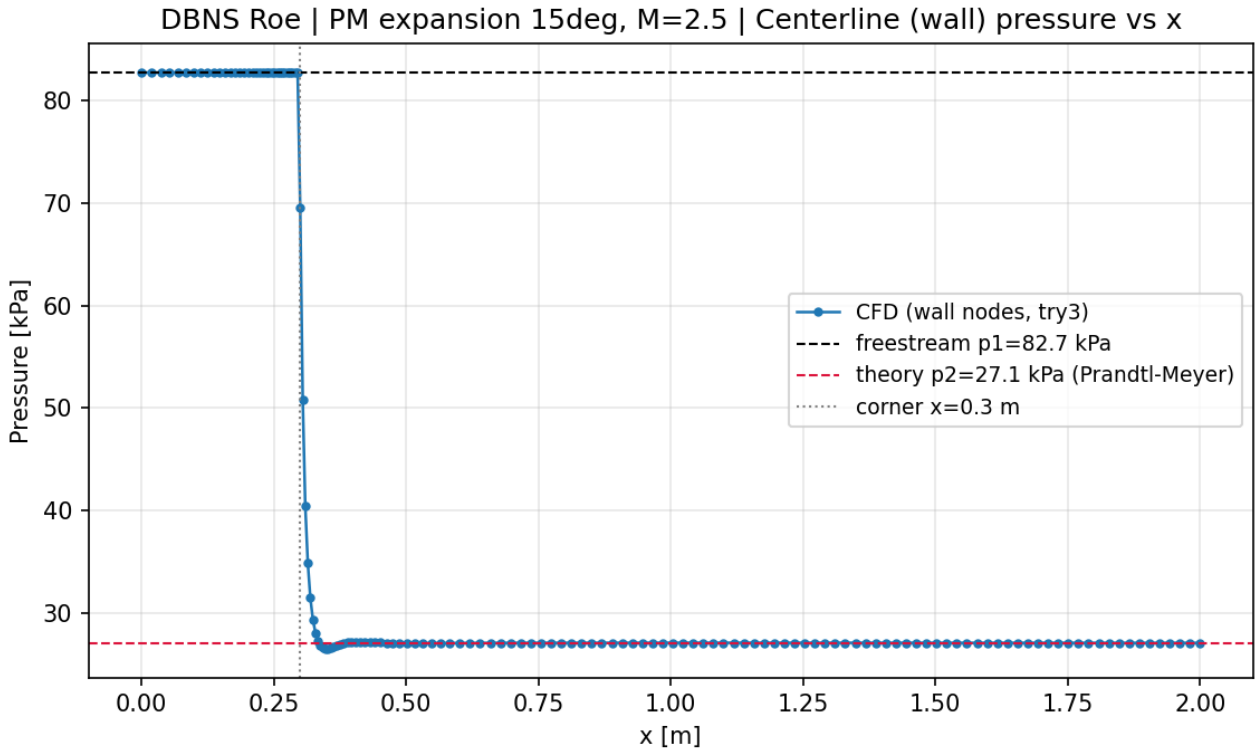


Figure 11.2: Wall (centerline) pressure versus streamwise position

Pressure is uniform at the freestream value upstream of the corner (`x=0.3 m`), then drops sharply through the fan over a few mesh cells' width, settling close to the theoretical post-expansion value downstream, with a small local ripple typical of a finite mesh resolving a rapid (near-discontinuous) expansion.

Quantitative comparison at the converged, corner-refined solution:

Quantity	Exact theory	Wake CFD	Error
`M`	3.2368	3.2147	−0.68%
`p /p`	0.3274	0.3274	+0.005%
`T /T`	0.7269	0.7336	+0.91%

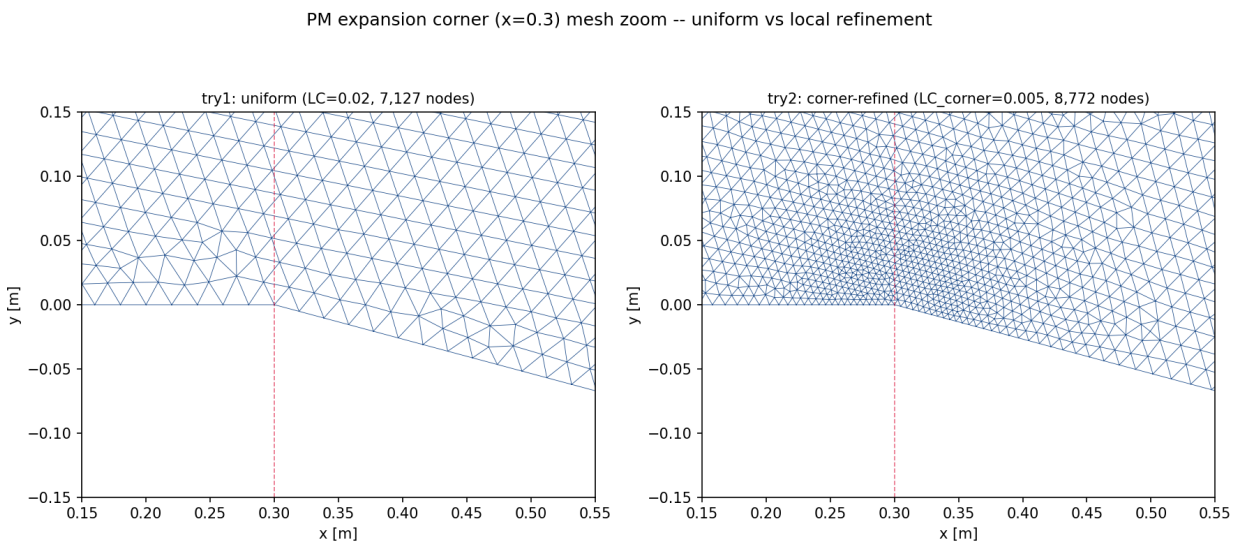


Figure 11.3: Corner mesh refinement: uniform background mesh (left) versus locally refined mesh (right)

11.9 Conclusions and Applicable Scope

- Wake CFD's inviscid solver reproduces the exact Prandtl-Meyer expansion to within 1% on all three compared quantities (Mach number, pressure ratio, temperature ratio) when the corner singularity is locally mesh-resolved.
- Pressure ratio is markedly less sensitive to corner mesh resolution than Mach number and temperature, because those depend on the full entropy state rather than local wave structure alone — a useful general lesson for interpreting partial agreement in expansion/compression-corner flows.
- This result applies to a single 2D inviscid expansion-corner configuration at one Mach number and turn angle. It does not establish accuracy for viscous corner flows, compression corners, or three-dimensional geometries.

11.10 References

- NASA Glenn Research Center WIND validation archive, Prandtl-Meyer 15° Expansion, M∞=2.5.

Part IV

Heat Transfer

12 Conjugate Heat Transfer — Flat Plate Verification

Interface temperature and Nusselt number against the Vynnycky (1998) closed-form conjugate solution, 2D/3D and conformal/non-conformal interfaces

12.1 Run Provenance and Artifacts

Item	Value
Wake CFD baseline version	`0.22.0`
Solver	DBNS
Compute device	GPU (NVIDIA RTX A6000)
Parallel execution	1 MPI rank
Arithmetic precision	FP64
Run date	2026-08-29

> **Note**
>
> Results depend on the solver build that produced them. Read every figure in this report together with the version and date above — re-running the same input on a later build may give different numbers.

12.1.1 Downloadable Files

Not available: standalone input decks and solver result files have not yet been published for download.

12.2 Verification Objective

This case checks Wake CFD's conjugate heat transfer (CHT) capability — coupled fluid-solid heat conduction with continuity of temperature and heat flux at the interface — against the closed-form asymptotic solution of Vynnycky, Kimura, Kanev, and Pop (1998) for forced convection over a conducting flat plate. It verifies Wake CFD for:

- interface-averaged temperature (`T_b`) and Nusselt number (`Nu`) against the analytical correlation
- consistency between four independent discretization paths (2D/3D geometry, conformal/non-conformal fluid-solid interface mesh)

12.3 Reference Solution and Data

Item	Setting
Reference	Vynnycky, Kimura, Kanev, and Pop (1998), closed-form asymptotic solution

12.4 Simulation Conditions

Item	Setting
Geometry	Conducting solid slab (`x [-0.5,0.5]`, `y [-0.5,0]`) beneath a fluid domain (`x [-1.0,2.0]`, `y [0,1.0]`); interface at `y=0`, `|x| 0.5`
Analysis	Steady, laminar, compressible DBNS with conjugate fluid-solid coupling
`Re` (plate-length based)	`500`
`Pr`	`0.72`
Conductivity ratio `k = k_solid/k_fluid`	`5`
Thickness ratio `= a/b`	`0.5`
Freestream	`M = 0.1`, `T_∞ = 300 K`

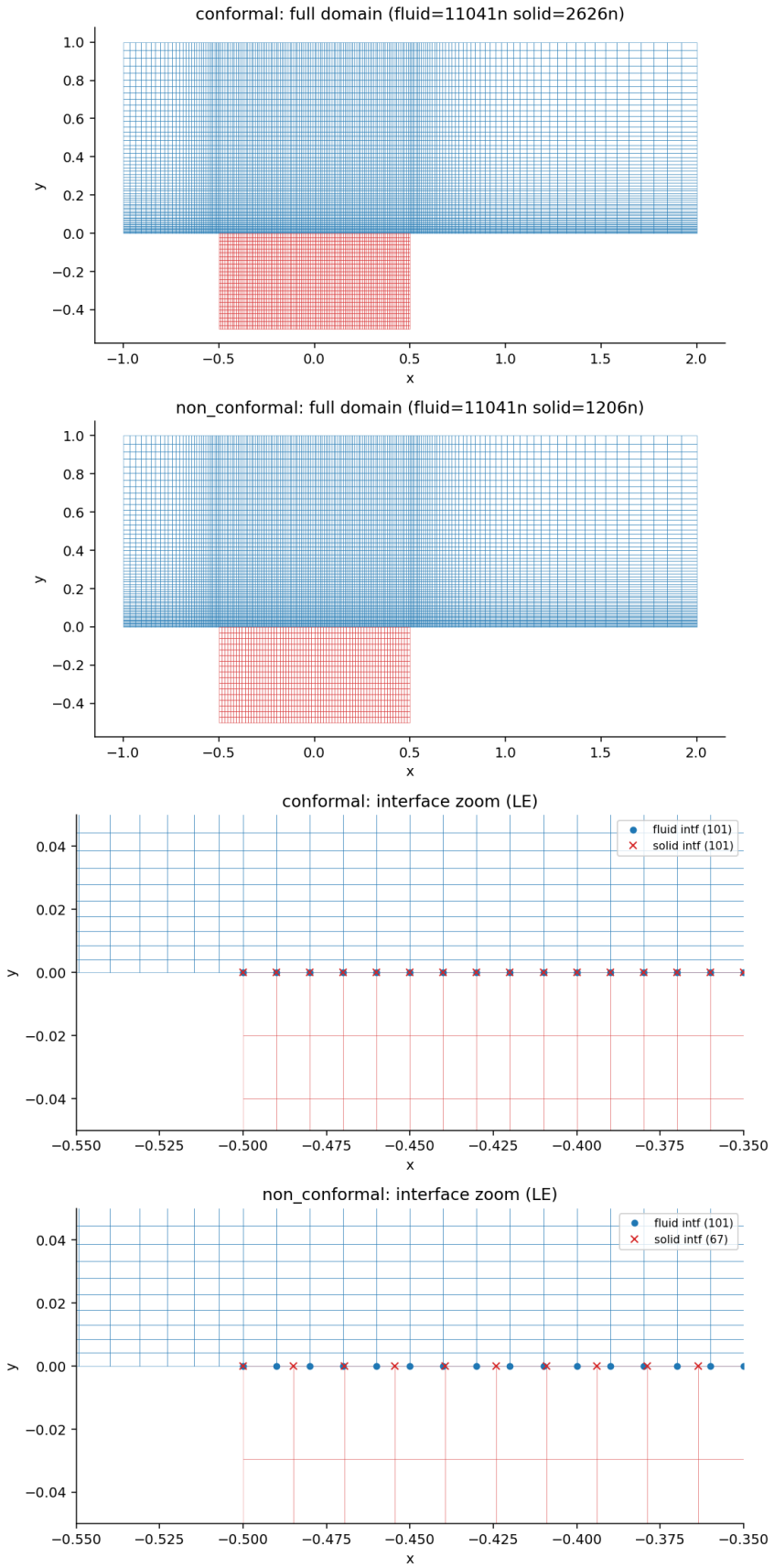


Figure 12.1: Conformal vs. non-conformal 2D mesh: full domain and interface close-up (conformal interface: 101 matching nodes each side; non-conformal: 101 fluid vs. 67 solid nodes, GGI-interpolated)

12.5 Mesh

Item	Setting
Mesh variants	2D and 3D (one-cell spanwise extrusion + symmetry), each with a conformal (matching interface node count) and non-conformal (mismatched, GGI-interpolated) fluid-solid interface

12.6 Boundary and Initial Conditions

Item	Setting
Solid bottom face	Isothermal, `T_c = 330 K`
Solid side faces	Adiabatic
Interface coupling	Temperature continuity (`_solid = _fluid`) and heat-flux continuity (`_fluid/ y = k· _solid/ y`)

Initial field: Not reported.

12.7 Numerical Methods

Item	Setting
Convective scheme	SLAU
Time integration	Implicit, CFL constant `5.0`
Convergence criterion	`residual_reduction = 8` orders (deep convergence; confirmed against a 5,000-iteration snapshot with no meaningful difference)

12.8 Results

At the given conditions (`Re=500`, `Pr=0.72`, `k=5`, `=0.5`), the analytical solution gives `= ·Pr^(1/3)·Re^(1/2) / (1.506·k) 1.331`, `¯_b = 1/(1+ ) 0.429`, and `Nu = (k/ )· /(1+ ) 5.71`.

Case	Converged iteration	$\bar{\theta}_b$ (area-weighted)	vs. analytical (0.429)	Nu	vs. analytical (5.71)
2D conformal	10,637	0.4223	−1.6%	5.7738	+1.1%
2D non-conformal	9,408	0.4251	−0.9%	5.8122	+1.8%
3D conformal	13,023	0.4223	−1.6%	5.7738	+1.1%
3D non-conformal (GGI)	11,873	0.4251	−0.9%	5.8122	+1.8%

All four discretization paths agree with the analytical correlation within 2%, inside the correlation's own stated approximation error. The 2D and 3D results match to four decimal places (expected, since the 3D case is a one-cell spanwise extrusion of the same physical problem), which also confirms that the GGI interpolation used at the non-conformal interface does not degrade accuracy relative to the conformal case (difference between conformal and non-conformal results is about 0.3 percentage points).

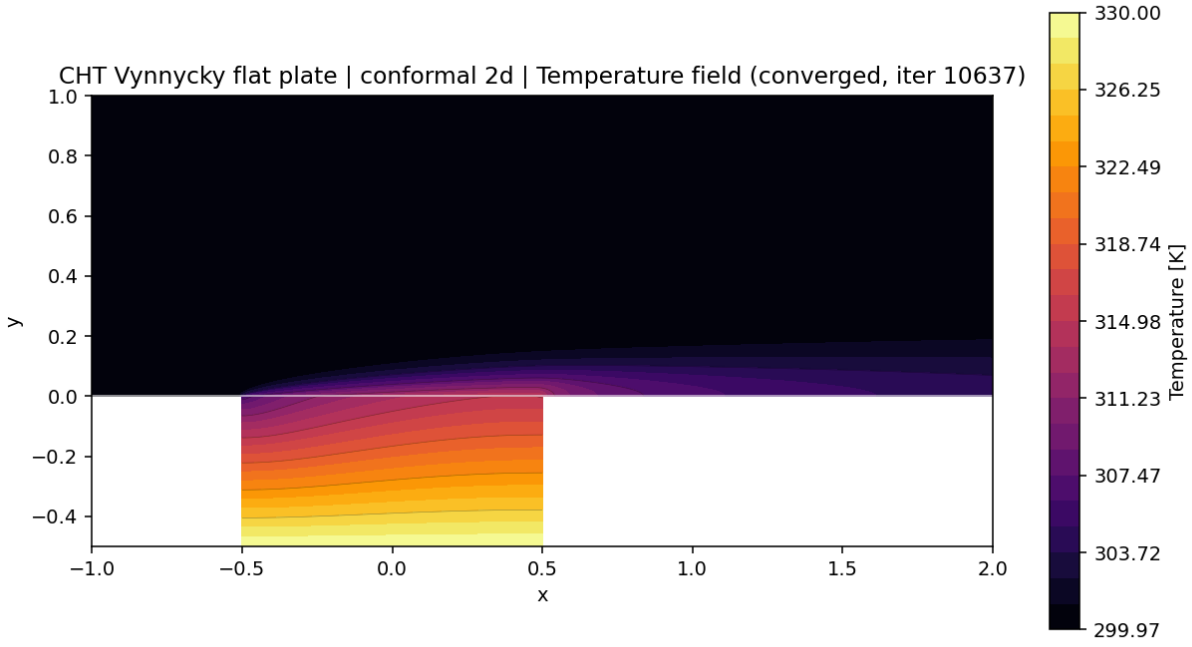


Figure 12.2: Coupled fluid-solid temperature field, conformal 2D case, deep-converged

The local (as opposed to area-averaged) interface temperature distribution $\theta_b(x)$ was also compared against a separate constant-heat-flux asymptotic approximation from the same reference (valid, per the reference's own statement, only for Pr 1):

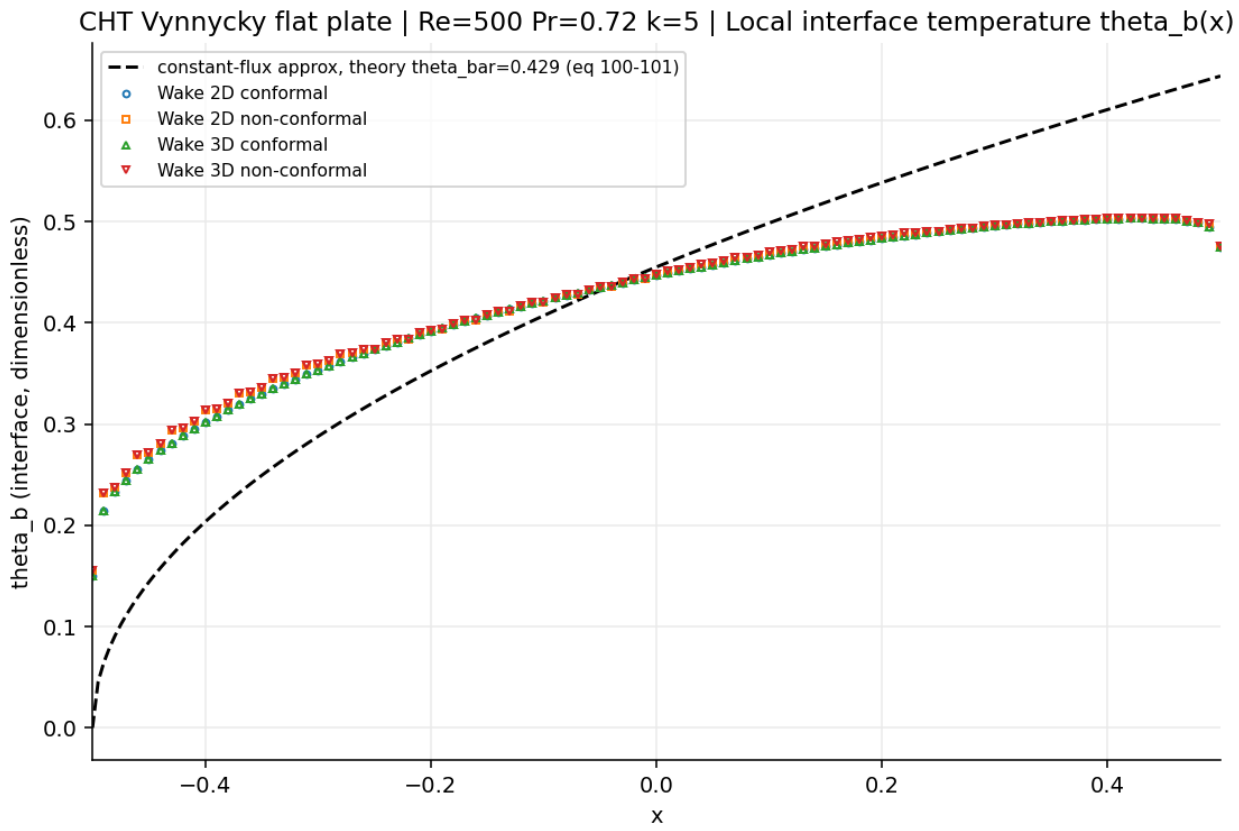


Figure 12.3: Local interface temperature distribution `_b(x)`: Wake CFD (all four discretizations) versus the constant-flux approximation evaluated at `Pr=0.72`

The area-averaged quantities (`_b`, `Nu`) match well, but the local *shape* of `_b(x)` differs clearly from the constant-flux approximation. This is expected: that specific local approximation is derived and validated by its authors only for `Pr 1`, and this case runs at `Pr=0.72` — outside its stated range of applicability. It is not evidence against the CHT implementation; it is a direct measurement of that particular approximation's scope of validity at a `Pr` value the original reference does not cover, as distinct from the general-`Pr` area-averaged correlation used above.

12.9 Conclusions and Applicable Scope

- Wake CFD's conjugate heat transfer implementation reproduces the Vynnycky (1998) area-averaged interface temperature and Nusselt number within 2% across four independent discretization paths (2D/3D, conformal/non-conformal interface).
- The non-conformal (GGI-interpolated) interface path introduces no measurable accuracy penalty relative to the conformal path for this case.
- This result applies to steady, laminar, incompressible-regime forced convection over a flat conducting slab at one Reynolds number, Prandtl number, and conductivity/thickness ratio. It does not establish CHT accuracy for turbulent flow, unsteady conjugate problems, or other property ratios.

- The local interface temperature distribution does not match a `Pr 1`-specific asymptotic approximation at this case's `Pr=0.72` — consistent with that approximation's own stated range of validity, not a discrepancy in the area-averaged result.

12.10 References

- Vynnycky, M., Kimura, S., Kanev, K., and Pop, I., "Forced Convection Heat Transfer from a Flat Plate: The Conjugate Problem," *International Journal of Heat and Mass Transfer*, 41(1), 1998, pp. 45–59.

Part V

Shear Flows & Jets

13 2D Planar Mixing Layer — SA/SST Validation

Comparison of mean velocity and Reynolds shear stress against the Delville (1989) experiment and CFL3D reference solutions

13.1 Run Provenance and Artifacts

Item	Value
Wake CFD baseline version	`0.22.2`
Solver	DBNS
Compute device	GPU (NVIDIA RTX A6000)
Parallel execution	1 MPI rank
Arithmetic precision	FP64
Run date	2026-09-09

> **Note**
>
> Results depend on the solver build that produced them. Read every figure in this report together with the version and date above — re-running the same input on a later build may give different numbers.

13.1.1 Downloadable Files

Not available: standalone input decks and solver result files have not yet been published for download.

13.2 Validation Objective

This case simulates a planar, incompressible free-shear mixing layer formed by two parallel streams (`U1=22.40 m/s`, `U2=41.54 m/s`) developing from separate splitter-plate boundary layers, using the Spalart–Allmaras (SA) and SST turbulence models. It compares Wake CFD against the NASA Turbulence Modeling Resource (TMR) Delville mixing-layer case, which provides both the Delville

et al. (1989) experimental data and CFL3D reference solutions for each turbulence model on the same mesh family. It validates Wake CFD for:

- mean-velocity and Reynolds-shear-stress (`u'v'`) prediction across the mixing layer with SA and SST
- grid convergence toward the reference solution
- code-to-code agreement with CFL3D for the same turbulence model, which isolates model accuracy from implementation accuracy

13.3 Reference Solution and Data

Item	Setting
References	Delville et al. (1989) experiment; CFL3D (SA and SST), published by NASA TMR

13.4 Simulation Conditions

Item	Setting
Geometry	Two parallel ducts (asymmetric length, to match the reported inlet boundary-layer thickness) separated by a splitter plate, merging into a single free-shear domain
Analysis	Steady, compressible DBNS, RANS (SA and SST, `v2003`, production = strain, run independently)
Fast stream	`U1 = 41.54 m/s`
Slow stream	`U2 = 22.40 m/s`

Freestream turbulence input follows each reference code's convention: SA uses the community-standard `nu_factor=3` (matching the CFL3D/FUN3D sample inputs), and SST uses the experimentally measured turbulence intensity (`Tu 0.3%`), which differs from the CFL3D/FUN3D SST reference's convention value (`Tu=0.064%`). This difference in freestream input, not model or code accuracy, is the most likely source of any residual disagreement at the reference near the free-stream edges of the profiles.

13.5 Mesh

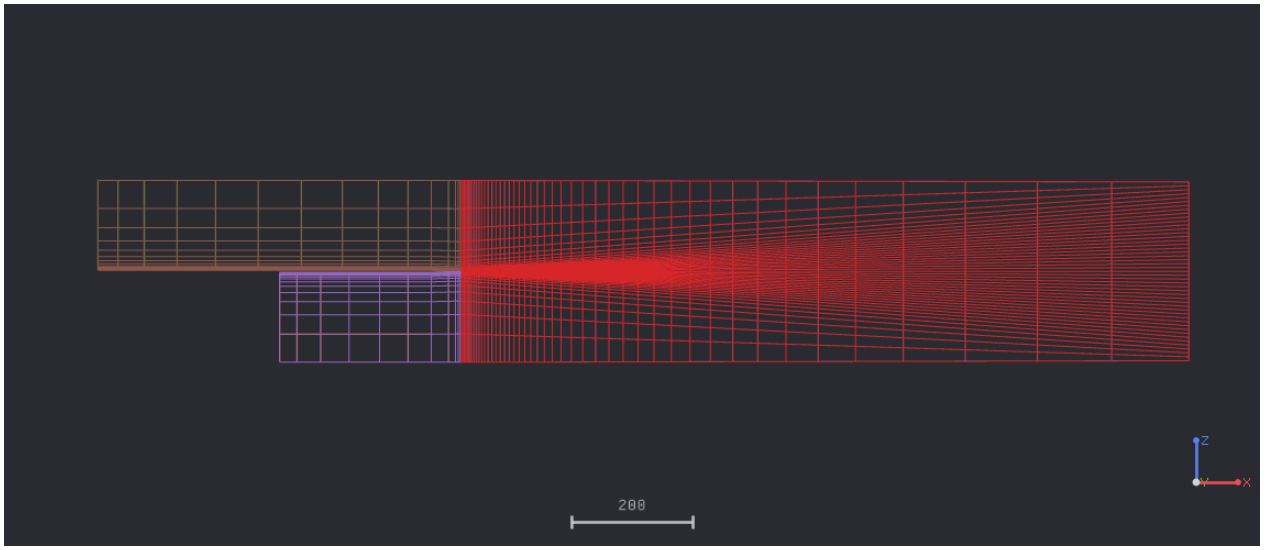


Figure 13.1: Coarsest-level (L1) mesh near the splitter plate: the long upper duct (z>0) and the short lower duct (z<0), with the mesh clustered in the mixing layer behind the plate

The figure shows the coarsest mesh (`L1`, 2,636 cells) enlarged around the splitter plate. The upper duct (z>0) is the long one (plate length 600 mm, fast stream 41.54 m/s) and the lower duct (z<0) is the short one (plate length 300 mm, slow stream 22.40 m/s). Behind the plate (x>0) the cells are clustered in the mixing-layer region.

Item	Setting
Mesh	Unstructured quadrilateral, single-zone (one-cell spanwise extrusion), four-level nested grid-convergence family (SA: `L1`–`L4`, `2,636`–`168,704` cells; SST: `L1`–`L5`, `2,636`–`674,816` cells)

13.6 Boundary and Initial Conditions

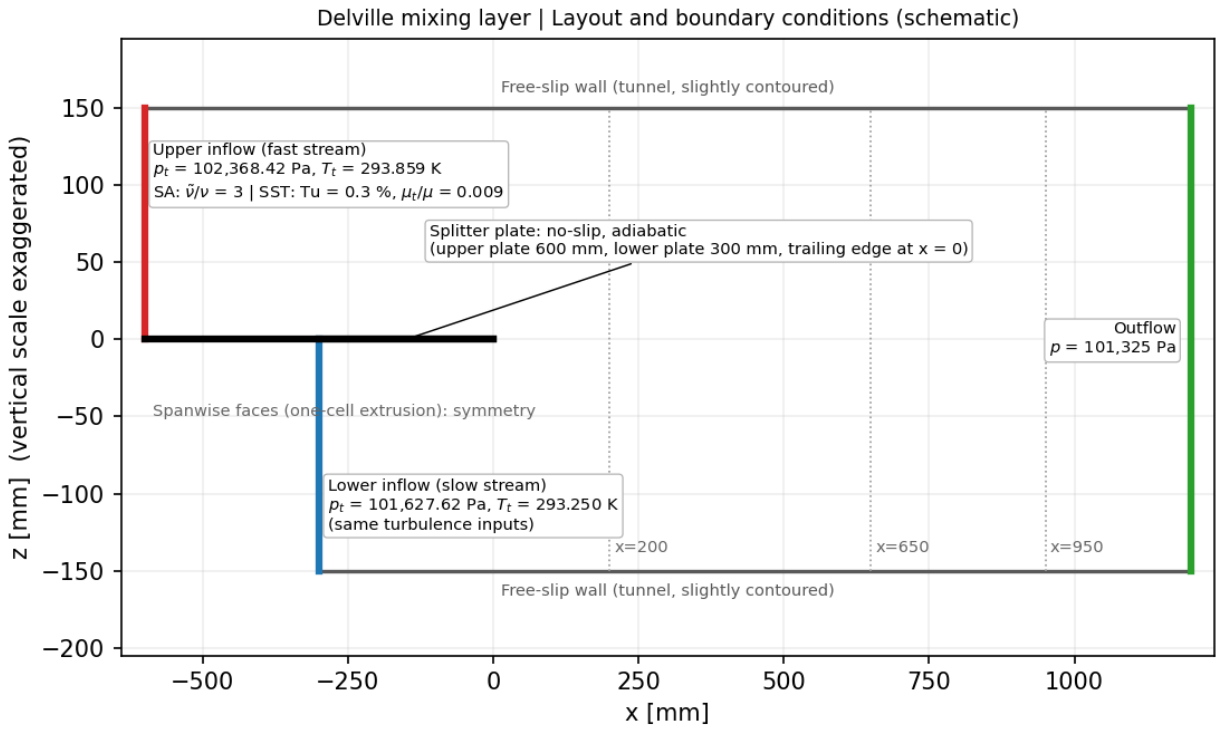


Figure 13.2: Layout and boundary conditions of the mixing-layer case (schematic, vertical scale exaggerated)

The schematic was drawn from the simulation inputs and the geometry published by NASA TMR (grid units in millimetres, splitter-plate trailing edge at `x = 0`, tunnel width 300 mm, outflow at `x = 1200 mm`); the vertical scale is exaggerated.

Boundary	Condition
Upper inflow (fast stream, `z > 0`)	Total-pressure inlet, `p_t = 102,368.42 Pa`, `T_t = 293.859 K`, flow direction `+x`
Lower inflow (slow stream, `z < 0`)	Total-pressure inlet, `p_t = 101,627.62 Pa`, `T_t = 293.250 K`, flow direction `+x`
Outflow	Pressure outlet, back pressure `101,325 Pa`
Tunnel walls (top and bottom)	Free-slip wall, slightly contoured so that the streamwise pressure gradient is close to zero downstream of `x = 0`
Splitter plate (upper, lower, trailing edge)	No-slip, adiabatic wall
Spanwise faces	Symmetry (the mesh is a one-cell extrusion)

The two streams enter through separate total-pressure inflows; the boundary layers on the two sides of the plate develop naturally along plates of different length (upper plate 600 mm, lower

plate 300 mm), which sets the different boundary-layer thicknesses at the trailing edge. The total pressures correspond to the pressure ratios in the reference FUN3D input (1.00299 and 1.01031 of the reference pressure).

Freestream turbulence at both inflows: for SA, `nu_factor = 3`; for SST, a turbulence intensity of `0.3%` with an eddy-viscosity ratio of `0.009`. The initial field is uniform, with `M = 0.12107`, `p = 101,325 Pa`, `T = 293 K`, and flow direction `+x`.

13.7 Numerical Methods

Item	Setting
Convective scheme	Roe
Gradient method	Green–Gauss
Time integration	Euler implicit
CFL	Constant, `5.0`
Convergence criterion	Absolute residual `-15` (log10 RMS of the flow-equation residual; deep convergence)

13.8 Results

Both turbulence models were run through a grid-convergence sequence and confirmed to reach an asymptotic mesh-independent solution (SA: `L3`/`L4`; SST: `L4`/`L5`). The finest converged results for each model (SA `L4`, `168,704` cells; SST `L4`, `168,704` cells) are compared directly against the Delville (1989) experiment and the CFL3D reference solution for each model, at three streamwise stations (`x = 200, 650, 950 mm`).

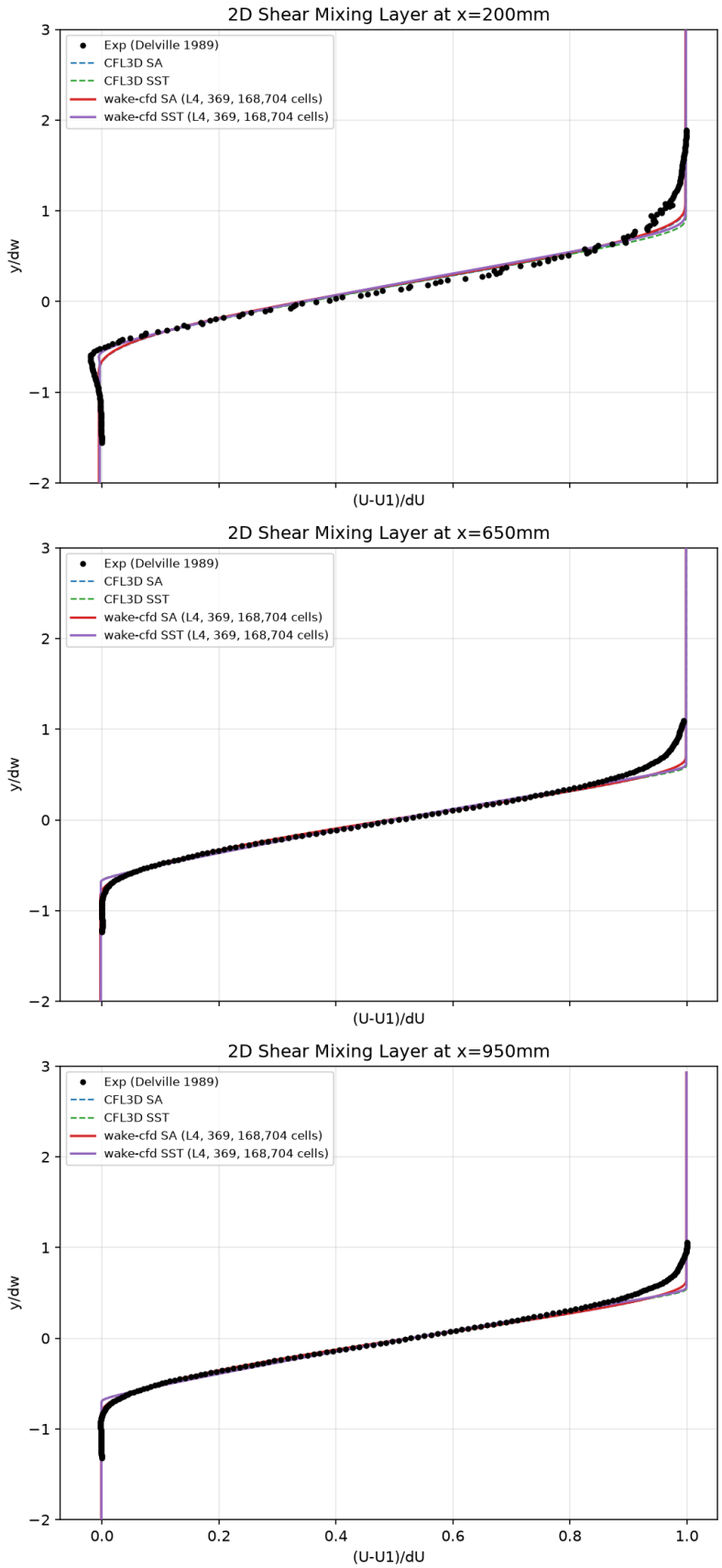


Figure 13.3: Mean-velocity profiles at x=200/650/950mm: Wake CFD SA and SST versus CFL3D (SA/SST) and the Delville (1989) experiment

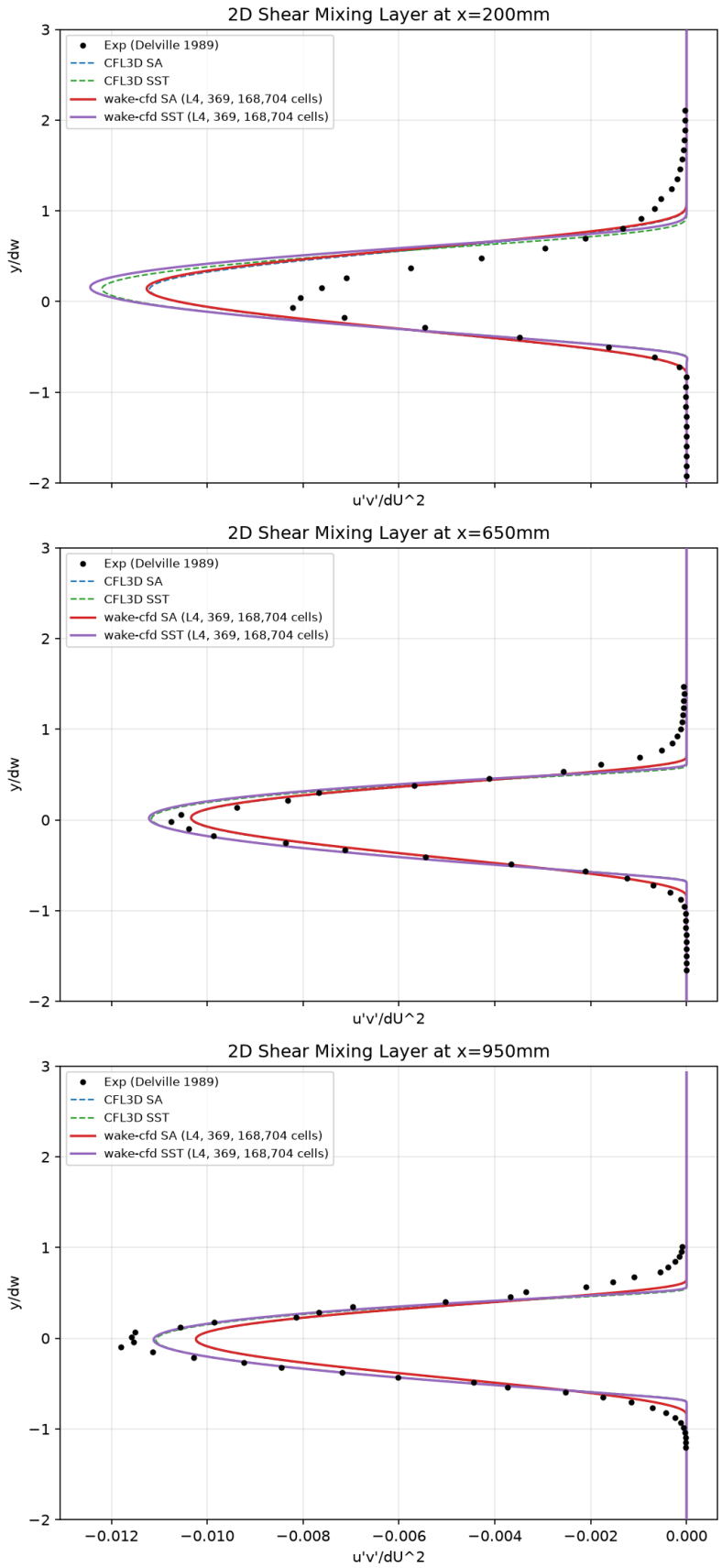


Figure 13.4: Reynolds shear-stress profiles at x=200/650/950mm: Wake CFD SA and SST versus CFL3D (SA/SST) and the Delville (1989) experiment

Peak Reynolds shear stress (`u'v'/ΔU²`) at each station, converged grid:

Model	x=200mm	x=650mm	x=950mm	CFL3D (same model)
Wake CFD SA	−0.0102	−0.0113	−0.0102	matches within the plotted resolution
Wake CFD SST	−0.0124	−0.0112	−0.0111	−0.0122 / −0.0112 / −0.0111 (within 0.0002)

Within the core mixing-layer region (`|y/ | < 3`), both models agree closely with the CFL3D reference computed with the same turbulence model, confirming that Wake CFD's SA and SST implementations reproduce the reference codes' numerical solution. Both models also agree well with the experiment in the core region. SST reproduces the shear-stress peak magnitude and the profile asymmetry (the peak location shifted toward `y/  > 0`) slightly better than SA; SA and SST agree with each other near the wall-normal center but differ measurably in peak shear-stress magnitude and shape, which is consistent with the two models' known differences.

13.9 Conclusions and Applicable Scope

- Wake CFD's SA and SST implementations, at grid-converged and deeply iteration-converged conditions, reproduce the CFL3D reference solution for the same turbulence model within the resolution of the plotted profiles for this case.
- Both models agree with the Delville (1989) experiment in the core mixing-layer region for this planar, incompressible, two-stream configuration.
- The comparison establishes code-to-code (SA CFL3D-SA, SST CFL3D-SST) and model-versus-experiment agreement for one specific mixing-layer geometry and one pair of stream velocities. It does not establish accuracy for compressible mixing layers, three-dimensional effects, or other velocity ratios.
- The SST run's freestream turbulence intensity differs from the CFL3D/FUN3D SST reference's convention value; this setup difference, rather than model or code error, is the most likely explanation for any residual disagreement near the free-stream edges of the profiles.

13.10 References

- Delville, J. et al., "Generation of Turbulent Mixing Layer with a Chevron Splitter Plate," *Advances in Turbulence 2*, Springer, 1989.
- NASA Turbulence Modeling Resource, 2D Mixing Layer Validation Case.

14 2D Coflowing Jet — NASA TMR SA Verification

Code-to-code verification of thin-plate drag and free-shear-layer development against CFL3D and FUN3D, five-level grid convergence

14.1 Run Provenance and Artifacts

Item	Value
Wake CFD baseline version	`0.22.2`
Solver	DBNS
Compute device	GPU (NVIDIA RTX A6000)
Parallel execution	1 MPI rank
Arithmetic precision	FP64
Run date	2026-09-15

> **Note**
>
> Results depend on the solver build that produced them. Read every figure in this report together with the version and date above — re-running the same input on a later build may give different numbers.

14.1.1 Downloadable Files

Not available: standalone input decks and solver result files have not yet been published for download.

14.2 Verification Objective

This case simulates a compressible free jet (`M 0.5`) discharging alongside a coflow stream (`M 0.25`) from a zero-thickness splitter plate, using the Spalart–Allmaras (SA) model. It compares Wake CFD against the NASA Turbulence Modeling Resource (TMR) 2D Coflowing Jet verification case, which is explicitly designed by TMR as a code-to-code verification case (not an experiment-matching case)

and provides CFL3D and FUN3D reference solutions on the same five-level grid family. It verifies Wake CFD for:

- thin-plate drag coefficient (`Cd`) prediction and its grid-convergence trajectory
- downstream centerline-velocity development in the merged free-shear layer
- eddy-viscosity distribution in the shear layer
- behavior of pressure-inflow boundary conditions for two adjacent streams at different total pressure and temperature

14.3 Reference Solution and Data

The TMR coflowing-jet case places a zero-thickness splitter plate (adiabatic, no-slip on both sides) between an inner jet stream and an outer coflow stream. Downstream of the plate trailing edge, the two streams merge into a free-shear layer. The reference solutions (CFL3D, cell-centered; FUN3D, node-centered) are computed on the same mesh family, both using the Roe scheme, which makes the comparison a genuine code-to-code discretization check rather than a physical-model comparison. Reference values are taken directly from TMR's published `convergence.dat` and profile data files.

Item	Setting
References	CFL3D and FUN3D, both SA + Roe FDS on the same mesh, published by NASA TMR

14.4 Simulation Conditions

Item	Setting
Geometry	Splitter plate at `-10 < x < 0`, `y = 0.5` (zero thickness); domain `-10 < x < 200`, `0 < y < 100`
Analysis	Steady, compressible DBNS, RANS (Spalart–Allmaras)
Inner jet stream	`Pt/pω = 1.1862`, `Tt/Tω = 1.050` (`M  0.5`)
Outer coflow stream	`Pt/pω = 1.046`, `Tt/Tω = 1.000` (`M  0.25`)

14.5 Mesh

Item	Setting
Mesh	Unstructured quadrilateral, single-cell spanwise extrusion; five-level nested grid family, `1,280`–`327,680` cells

14.6 Boundary and Initial Conditions

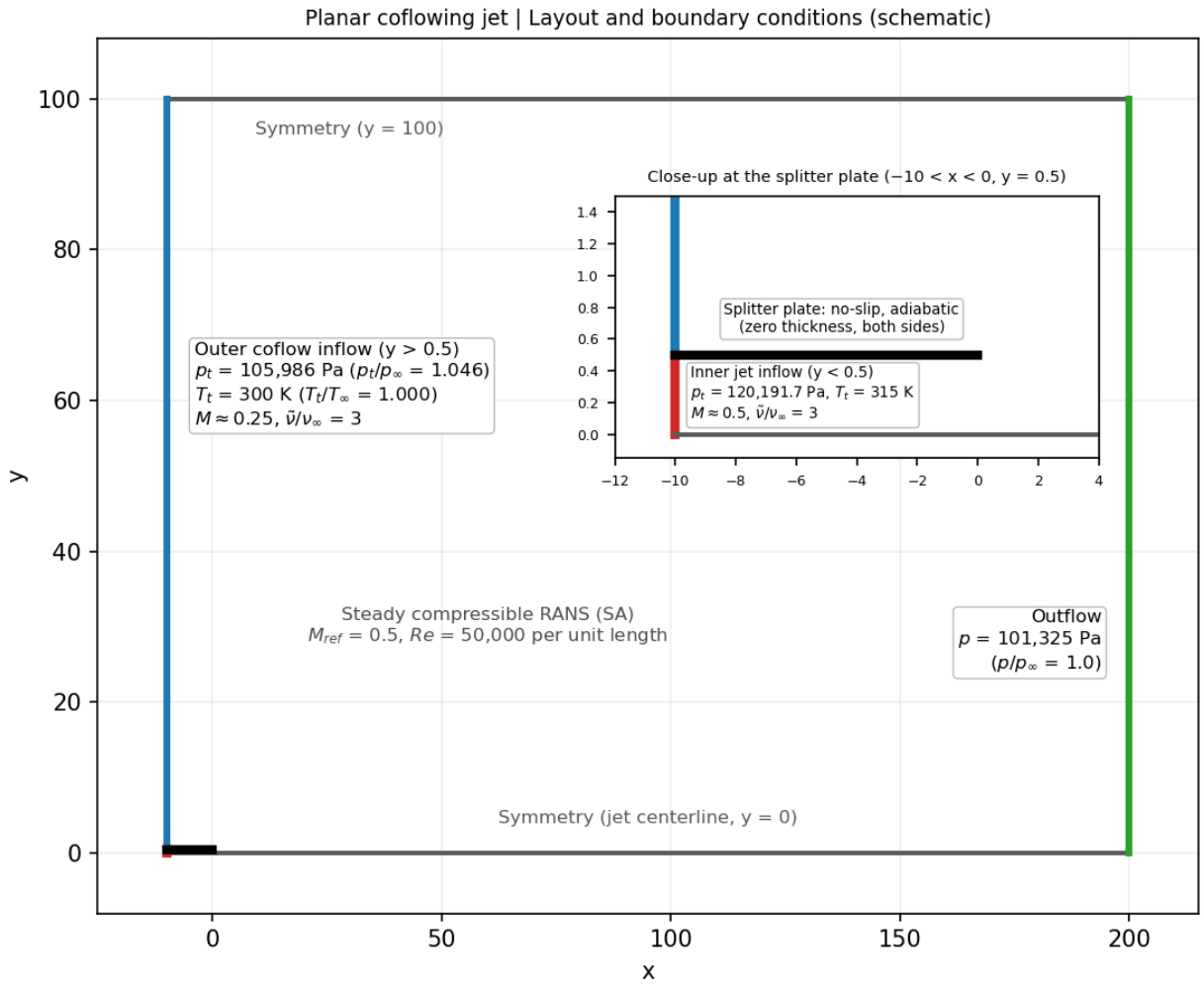


Figure 14.1: Layout and boundary conditions of the coflowing-jet case (schematic), with a close-up of the splitter plate

The schematic was drawn from the simulation inputs and the geometry published by NASA TMR (inflow at `x = -10`, outflow at `x = 200`, splitter plate at `y = 0.5`).

Boundary	Condition
Inner jet inflow (`y < 0.5`)	Total-pressure inlet, `p_t = 120,191.7 Pa` (`p_t/p∞ = 1.1862`), `T_t = 315 K` (`T_t/T∞ = 1.050`), flow direction `+x`
Outer coflow inflow (`y > 0.5`)	Total-pressure inlet, `p_t = 105,986 Pa` (`p_t/p∞ = 1.046`), `T_t = 300 K` (`T_t/T∞ = 1.000`), flow direction `+x`
Outflow (`x = 200`)	Pressure outlet, back pressure `101,325 Pa` (`p/p∞ = 1.0`)

Boundary	Condition
Jet centerline (`y = 0`)	Symmetry
Upper boundary (`y = 100`)	Symmetry (not a farfield condition)
Splitter plate, both sides	No-slip, adiabatic wall
Spanwise faces	Symmetry (the mesh is a one-cell extrusion)

The reference state is `p∞ = 101,325 Pa` and `T∞ = 300 K` (540 °R in the TMR specification), `M_ref = 0.5`, and `Re = 50,000` per unit grid length. The turbulence working variable at both inflows is `~/ ∞ = 3`. The initial field is uniform, with `M = 0.5`, `p = 101,325 Pa`, `T = 300 K`, and flow direction `+x`.

14.7 Numerical Methods

Item	Setting
Convective scheme	Roe, UMUSCL (`=0.5`), no limiter
Gradient method	Green–Gauss
Time integration	Euler implicit
CFL	Constant, `50`
Convergence criterion	Absolute residual `-12` (log10 RMS of the flow-equation residual)

14.8 Results

14.8.1 Grid Convergence

Reference profile and contour data are published only for the finest grid level; grid-convergence trajectories are compared across all five levels using TMR's published convergence table.

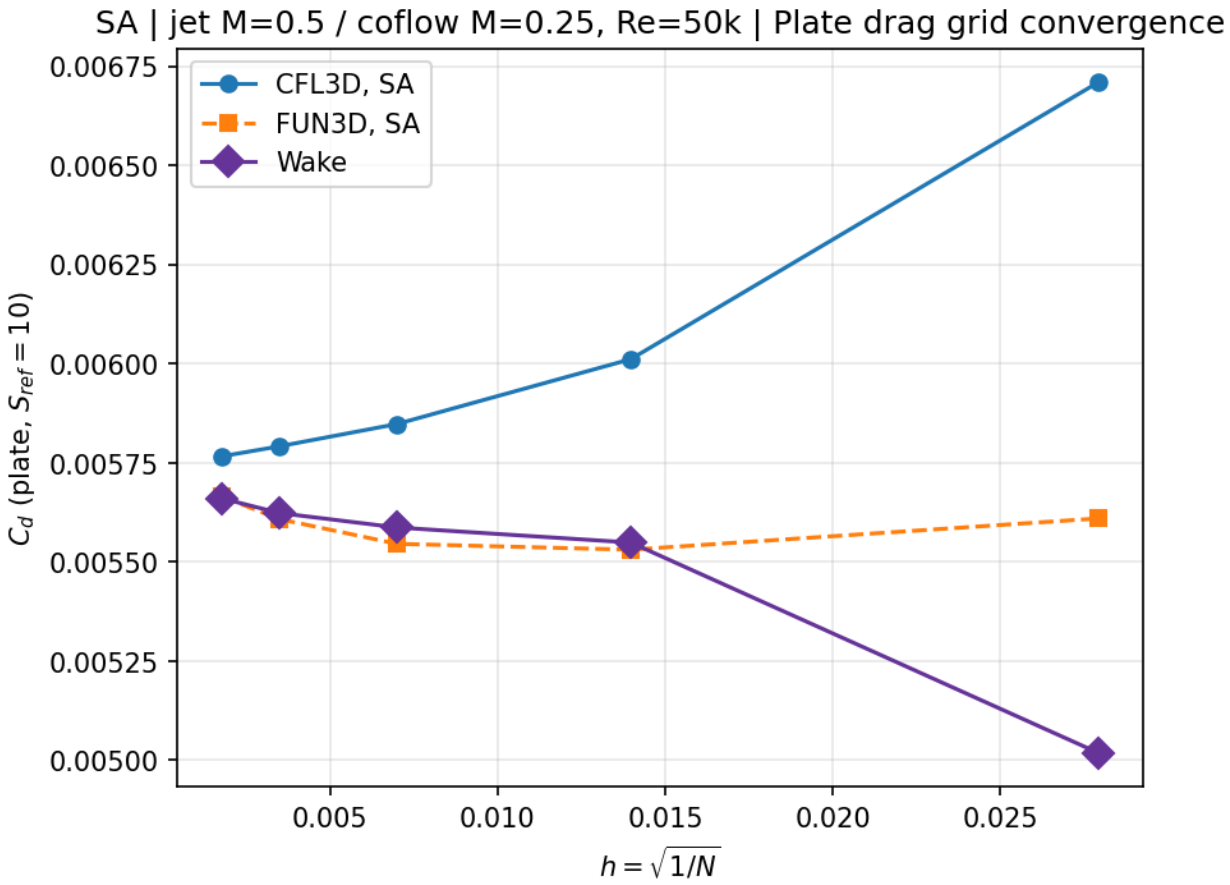


Figure 14.2: Plate-drag-coefficient grid convergence, Wake CFD versus CFL3D and FUN3D, five grid levels

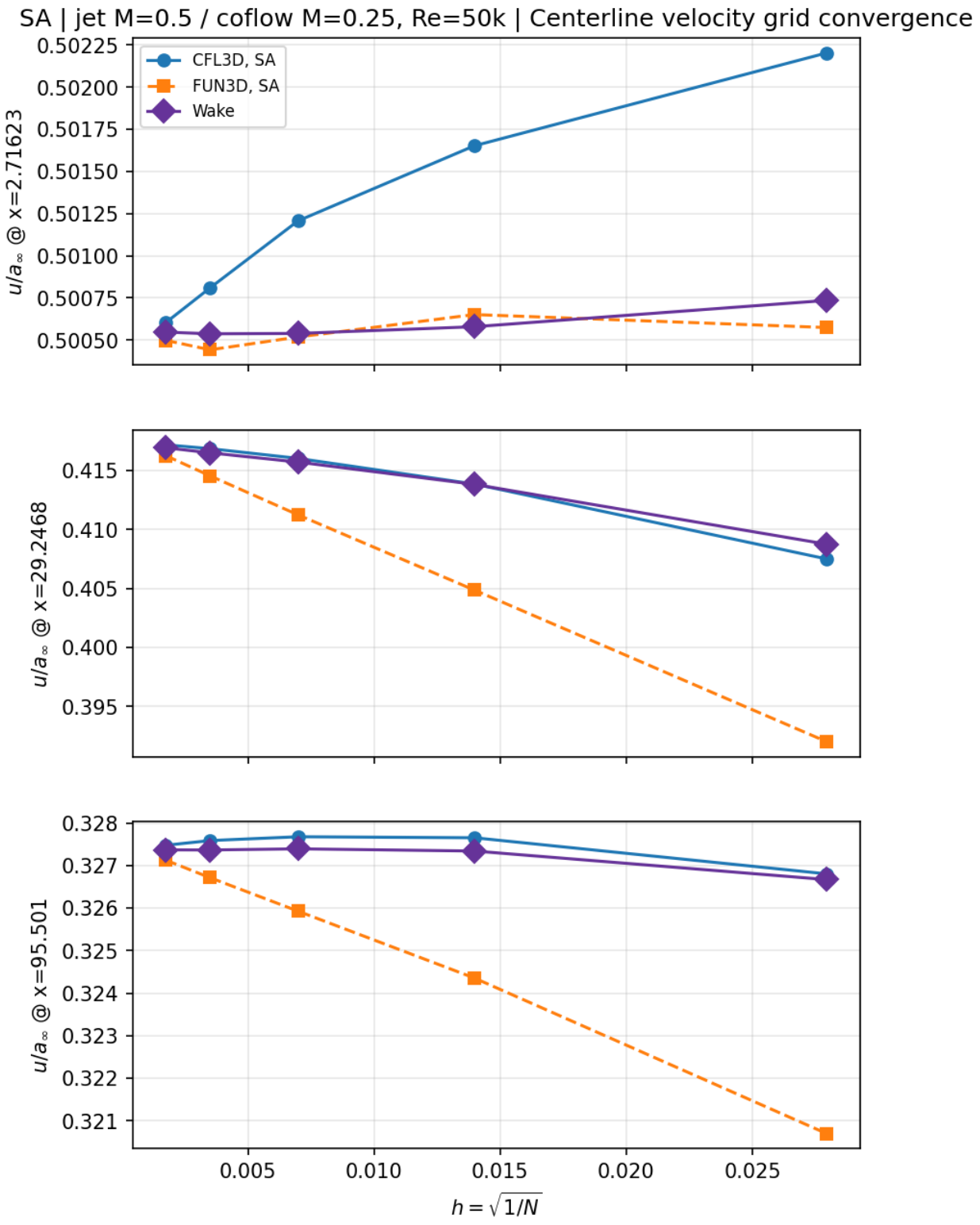


Figure 14.3: Centerline-velocity grid convergence at three downstream stations, Wake CFD versus CFL3D and FUN3D

Grid level	Cells	`Cd` (Wake CFD)	`Cd` (CFL3D)	`Cd` (FUN3D)	Wake CFD vs. FUN3D
4 (coarsest)	1,280	5.0172e-3	6.7104e-3	5.6094e-3	−10.6%
3	5,120	5.5485e-3	6.0111e-3	5.5304e-3	+0.33%
2	20,480	5.5865e-3	5.8473e-3	5.5453e-3	+0.74%
1	81,920	5.6228e-3	5.7914e-3	5.6075e-3	+0.27%
0 (finest)	327,680	**5.6603e-3**	5.7658e-3	**5.6648e-3**	**−0.08%**

The finest-grid drag coefficient is within 0.08% of FUN3D and 1.8% of CFL3D. The two reference codes themselves differ from each other by up to 16% at the coarsest level and converge toward each other only on the two or three finest grids — the coarsest-level Wake CFD result (−10.6% vs. FUN3D) reflects the same discretization sensitivity, not a Wake CFD-specific error, since both reference codes also show large deviations from their own fine-grid values at that resolution. The plate-drag coefficient is a known difficult convergence metric for this case: TMR's published observed order of convergence is `p=1.13` for CFL3D and `p=0.12` for FUN3D (the finest three levels remain outside the asymptotic range for FUN3D). Wake CFD's convergence trajectory shows the same non-monotonic behavior as the FUN3D curve.

Centerline velocity at the three downstream stations (finest grid):

Station	Wake CFD	CFL3D	FUN3D
`x = 2.71623`	0.50055	0.50060	0.50049
`x = 29.2468`	0.41692	0.41717	0.41625
`x = 95.501`	0.32737	0.32748	0.32712

All three stations agree with both reference codes within the CFL3D–FUN3D band at every grid level.

14.8.2 Detailed Comparison on the Finest Grid

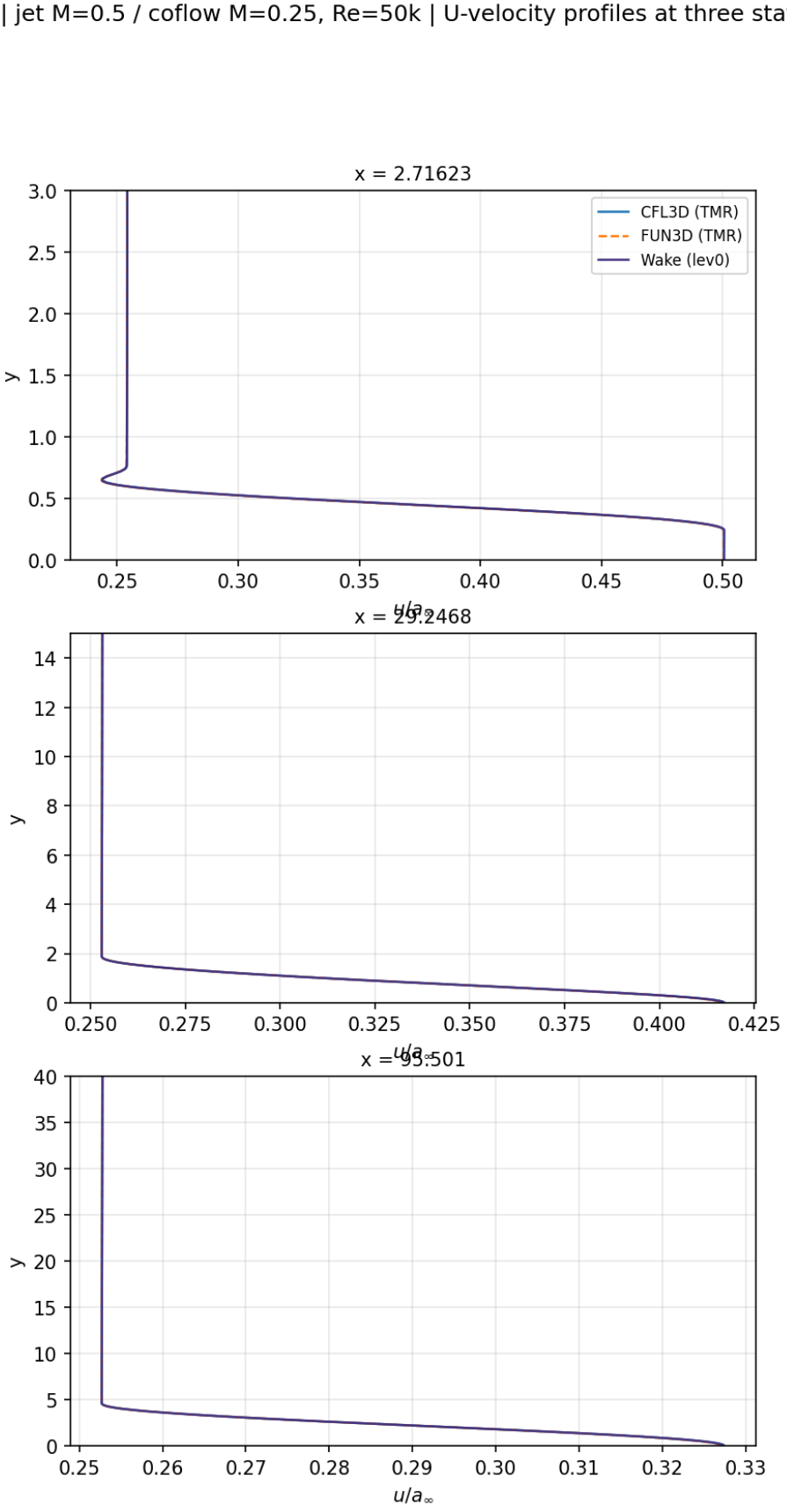


Figure 14.4: Downstream centerline- and station-velocity profiles on the finest grid, Wake CFD versus CFL3D and FUN3D

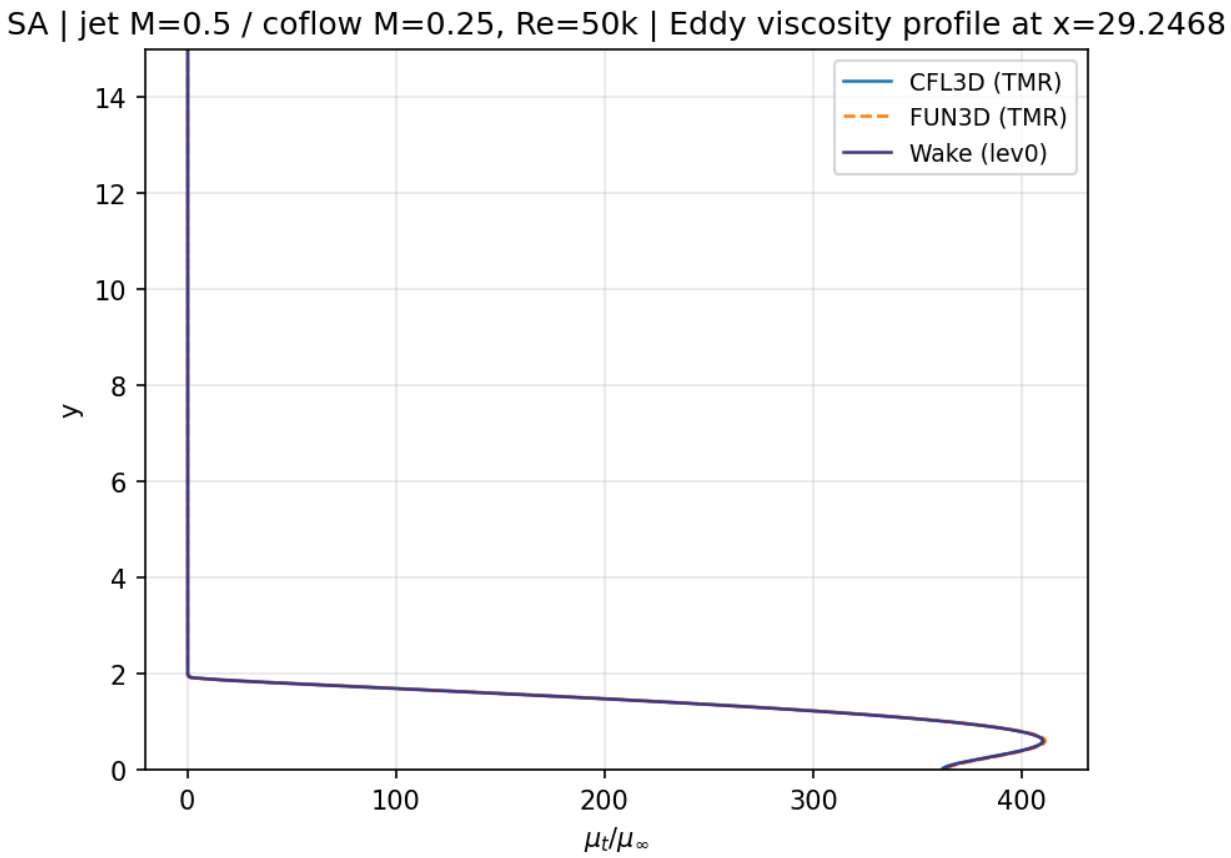


Figure 14.5: Eddy-viscosity profile at x=29.2468 on the finest grid, Wake CFD versus CFL3D and FUN3D

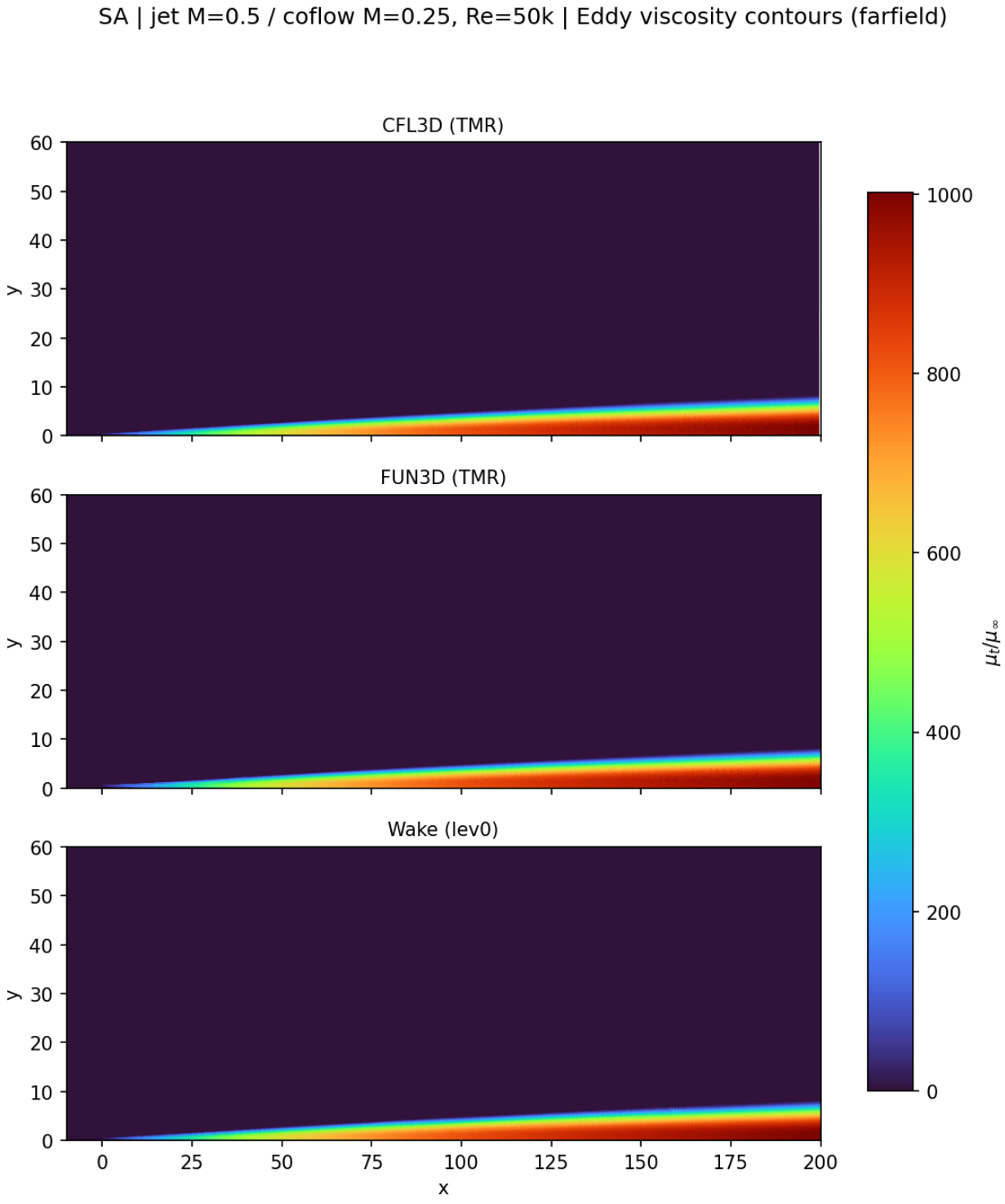


Figure 14.6: Eddy-viscosity contours in the far field on the finest grid, Wake CFD versus CFL3D and FUN3D

On the finest grid, Wake CFD's velocity profiles, eddy-viscosity profile, and eddy-viscosity contours are visually indistinguishable from both reference codes.

14.9 Conclusions and Applicable Scope

- Wake CFD's SA implementation agrees with the CFL3D and FUN3D reference solutions within the same code-to-code spread the two reference codes show against each other, for the full five-level grid family.
- On the finest grid, the plate-drag coefficient is within 0.08% of FUN3D and within 1.8% of CFL3D; all velocity and eddy-viscosity comparisons fall within the CFL3D–FUN3D band.
- This is a verification result: the reference is computed solutions from independent codes on the same mesh, not an experimental measurement. It establishes that Wake CFD solves the same discretized equations correctly for this compressible free-shear-layer and thin-plate-drag configuration.
- The result applies to a two-dimensional, compressible (`M 0.5`/`M 0.25`), zero-thickness-plate free-shear-layer configuration at one Reynolds number. It does not establish accuracy against experimental turbulent free-shear-layer data (see the companion validation case for the planar mixing layer), three-dimensional effects, or other Mach-number combinations.

14.10 References

- NASA Turbulence Modeling Resource, 2D Coflowing Jet Verification Case and SA Expected Results.
- Bradbury, L. J. S., and Riley, J., "The Spread of a Turbulent Plane Jet Issuing into a Parallel Moving Airstream," *Journal of Fluid Mechanics*, 27(2), 1967, pp. 381–394.

Part VI

Vortex Shedding

15 Laminar Cylinder Vortex Shedding — Strouhal/CD/CL Validation

Validation of unsteady flow, curved meshes, and force integration in the Flux Reconstruction solver (against literature and DBNS)

15.1 Run Provenance and Artifacts

Item	Value
Wake CFD baseline version	`0.22.2`
Solver	FR
Compute device	GPU (NVIDIA A2000)
Parallel execution	1 MPI rank
Arithmetic precision	FP64
Run date	2026-07-19

> **Note**
>
> Results depend on the solver build that produced them. Read every figure in this report together with the version and date above — re-running the same input on a later build may give different numbers.

15.1.1 Downloadable Files

Not available: standalone input decks and solver result files have not yet been published for download.

15.2 Validation Objective

This case simulates laminar vortex shedding around a circular cylinder with the FR (Flux Reconstruction) solver and compares the results with published values and those from Wake CFD's FVM-based DBNS solver. Unlike the steady-flow Cases 01 and 02, this is an **unsteady** flow case that verifies the FR solver implementation in terms of:

- vortex-shedding frequency (Strouhal number)
- mean drag coefficient and lift-coefficient amplitude
- viscous-force integration on curved high-order elements (a Q2 O-grid)
- cross-solver validation between the independently implemented FVM (DBNS) and FR solvers

15.3 Reference Solution and Data

Flow around a circular cylinder at `Re_D=100` is a representative unsteady validation case that produces a regular Kármán vortex street and has well-established literature values for Strouhal number, drag, and lift amplitude. A low-Mach (`M=0.05`) compressible formulation is used to model an essentially incompressible flow.

The same physical condition is also simulated with Wake CFD's production FVM solver (DBNS), providing cross-validation through two independent numerical paths.

Item	Setting
References	Williamson 1988 (`St`), Henderson 1995 (`C_D`), and the Wake CFD DBNS solver for cross-validation

15.4 Simulation Conditions

Item	Setting
Geometry	Circular cylinder, `D=1 m`, outer boundary `R_out=20D`
Analysis	Unsteady, compressible laminar Navier–Stokes
`Re_D`	`100`
Mach	`0.05` (`mu=0.2081` is used to match `Re_D`)
Reference state	ISA sea level — `P=101325 Pa`, `T=288.15 K` → `rho=1.2218`, `U=17.03 m/s`
Total simulation time	`t=24 s` (24,000 steps)
FFT window	`t=12→24 s` (about 34 cycles; initial transient excluded)

15.5 Mesh

Item	Setting
Mesh	Curved `Q2` O-grid, `96( ) × 64(r)`, first wall-cell height `Δr` `0.030`

15.6 Boundary and Initial Conditions

Item	Setting
Wall	no-slip, adiabatic
Outer boundary	farfield

Initial field: Not reported.

15.7 Numerical Methods

Item	Setting
Physical time step	`dt=1×10^-3 s`
Spatial accuracy	FR `p2` (third order)
Time integration	Dual time — physical: `BDF1`; pseudo-time: `RK45` + local-PI CFL control + p-multigrid

15.8 Results

Time averaging and FFT analysis over `t=12→24 s` (about 34 cycles) are compared with literature values and DBNS results at the same condition.

Metric	FR `p2` (BDF1, `dt=1e-3`)	DBNS BDF1 (same scheme and `dt`)	DBNS BDF2	Literature
`St`	0.1615	0.1651	0.1670	0.164 (Williamson 1988)
Mean `C_D`	1.3203 ± 0.0041	1.3430 ± 0.0058	1.3592	1.35 (Henderson 1995)
`C_L` amplitude	0.2678	0.3088	0.3347	0.33
`St` (drag component, `2·St`)	0.3229	0.3303	0.3340	0.328

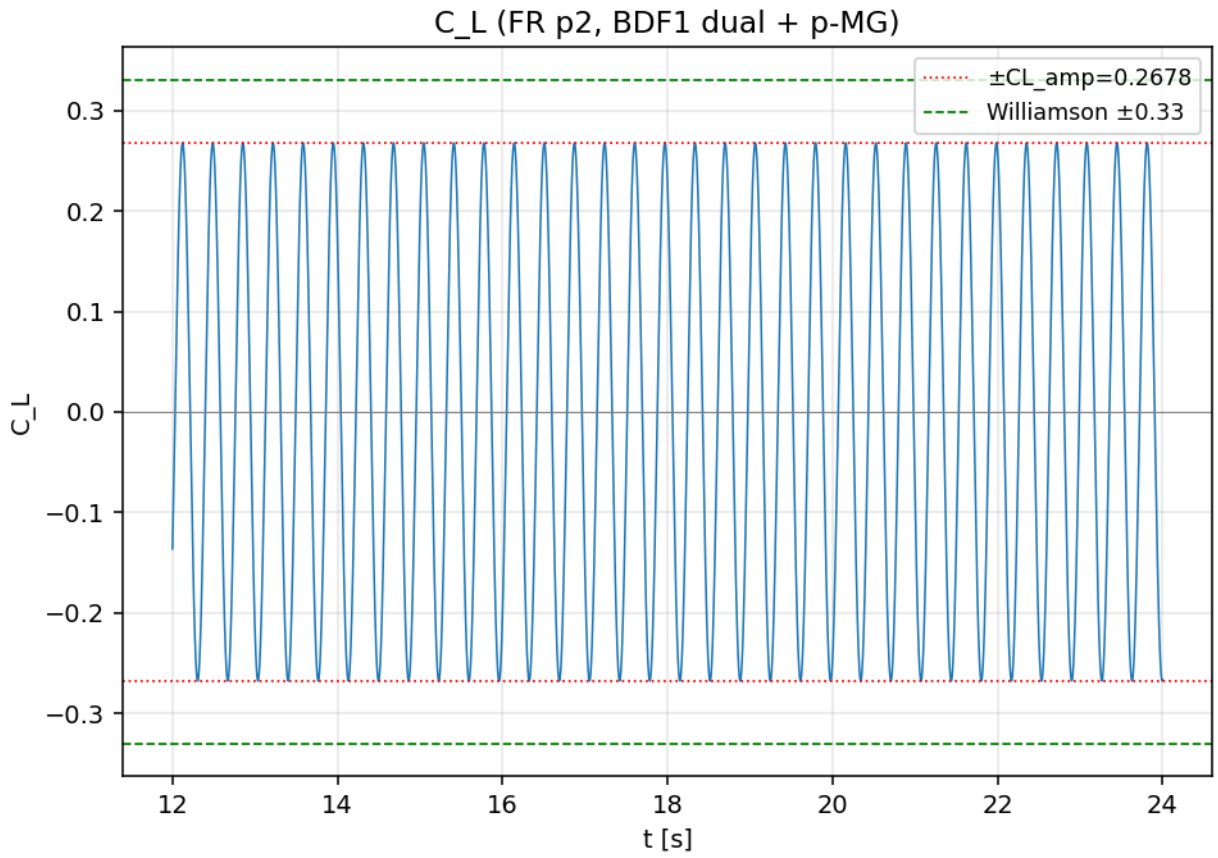


Figure 15.1: `C_L(t)` time history — reaches a regular vortex-shedding amplitude after the initial transient

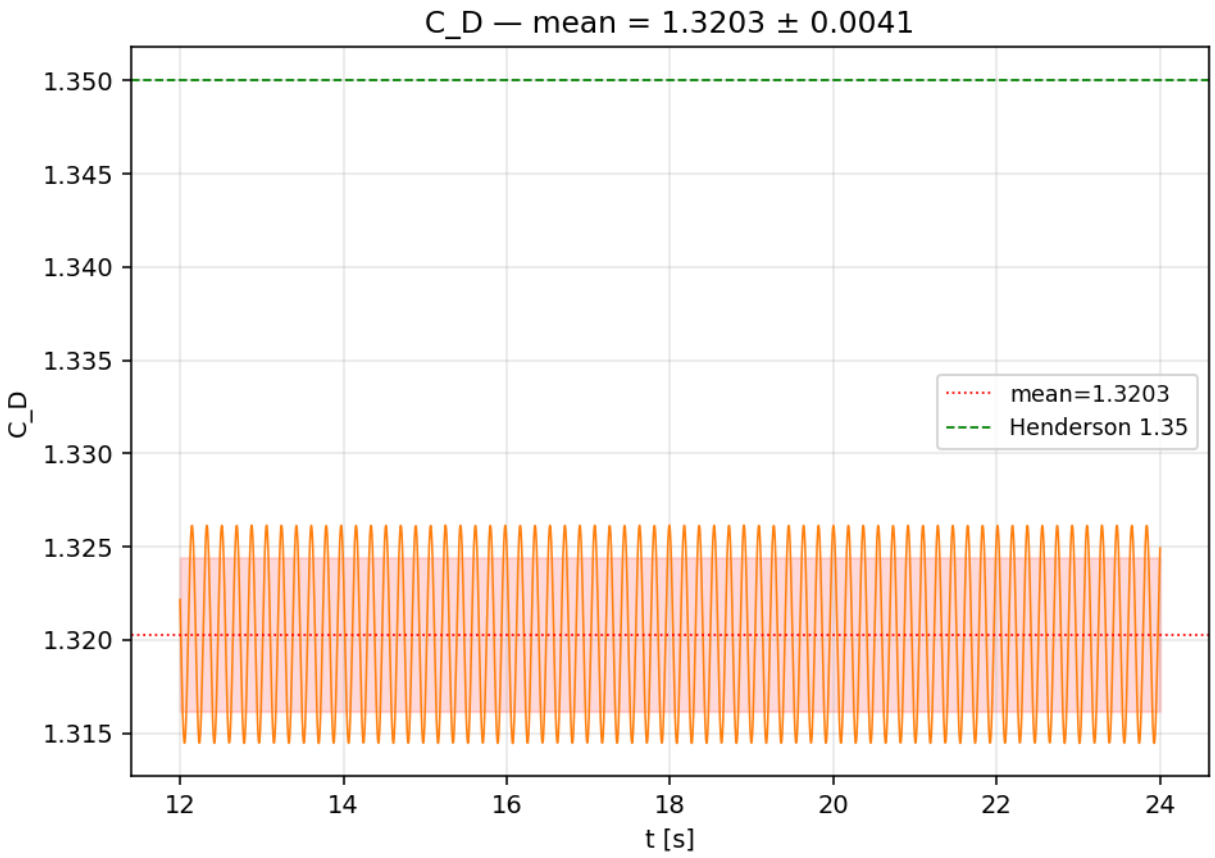


Figure 15.2: `C_D(t)` time history — comparison of the time mean with the Henderson reference

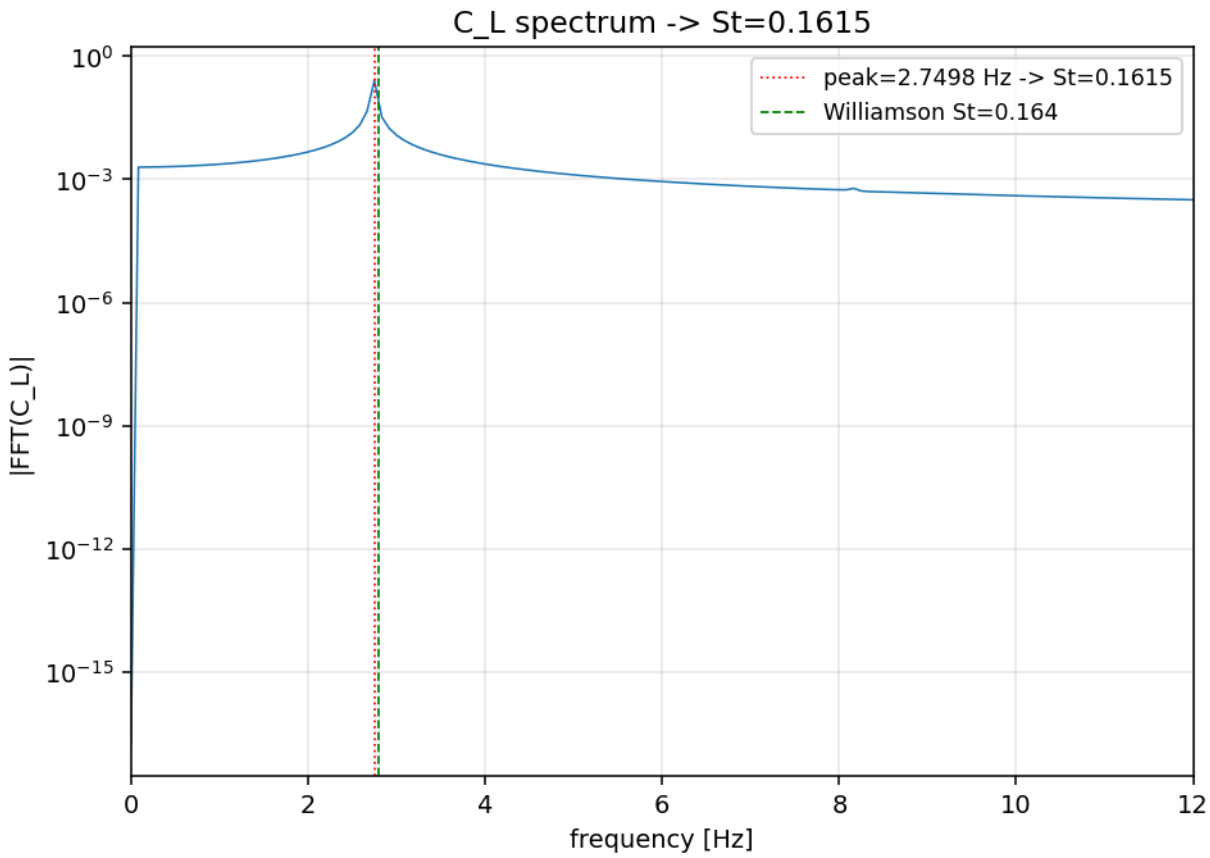


Figure 15.3: `C_L` spectrum — Strouhal number extracted from the dominant frequency

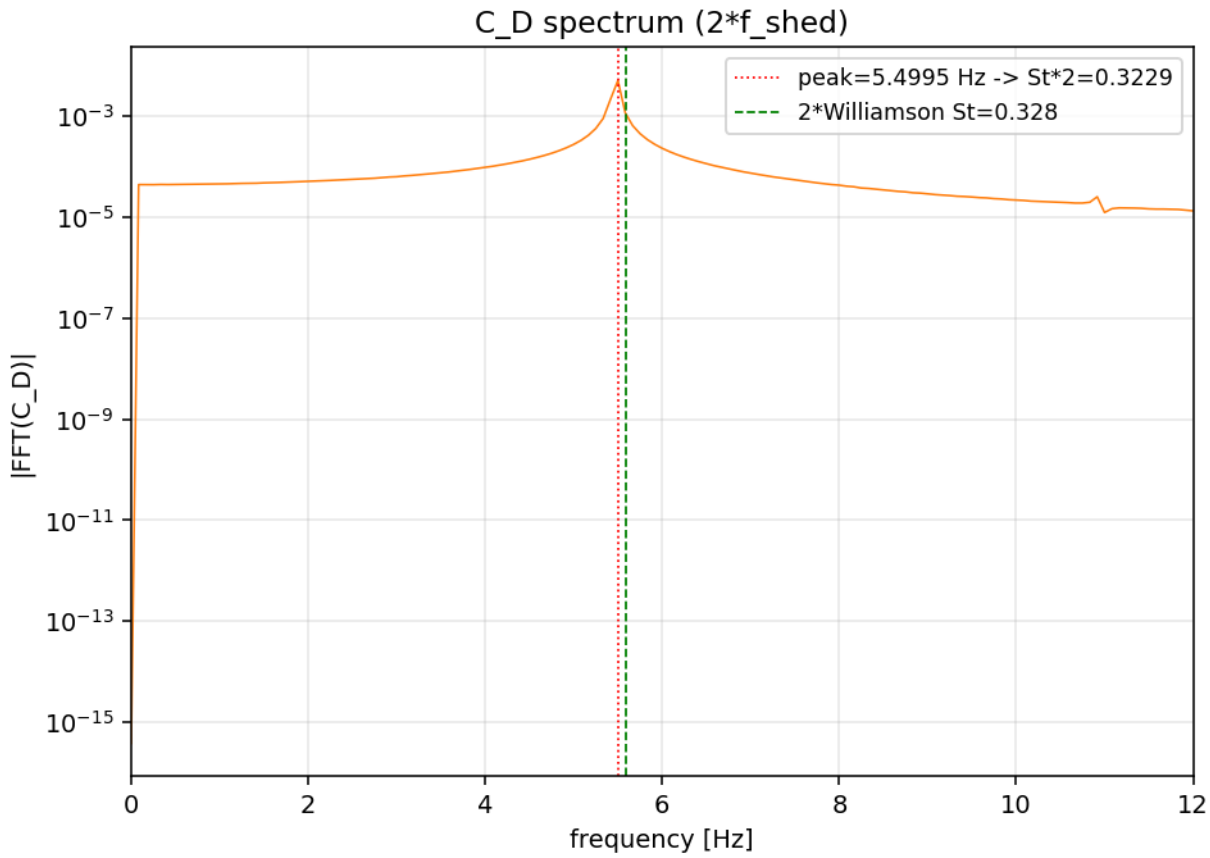


Figure 15.4: `C_D` spectrum — peak at twice the vortex-shedding frequency

`St` agrees with the literature value within 2%. The drag-spectrum peak occurs at exactly twice the lift-spectrum frequency, reproducing the expected physics: vortices shed alternately from the two sides of the cylinder, so drag oscillates at twice the lift frequency. The `C_L` amplitude is somewhat lower than the literature and DBNS values. This is consistent with numerical damping from first-order `BDF1` time integration; DBNS likewise gives a lower value with `BDF1` than with `BDF2`.

FR and DBNS are two independent numerical paths that do not share a code base. With the same time-integration scheme (`BDF1`) and `dt`, they agree broadly, with differences of -2.2% in `St`, -1.7% in `C_D`, and -13.3% in `C_L` amplitude.

15.9 Conclusions and Applicable Scope

- For vortex shedding from a cylinder at `Re_D=100`, the FR solver agrees with literature within 5% for `St` and `C_D`, and within 25% for `C_L` amplitude, which is the case acceptance criterion.
- Wake CFD's two solvers (FR and DBNS), which do not share a code base, agree in `St` and `C_D` at the same condition, confirming that both implementations reproduce the same physics independently. The comparatively larger discrepancy in `C_L` amplitude among the solvers and literature requires further study.

- These results were obtained for one Reynolds number (`Re_D=100`), one mesh, and one time-integration scheme (`BDF1`). They cannot be generalized to mesh or time-step convergence, higher Reynolds numbers, or three-dimensional effects.
- Follow-on validation should compare polynomial-order (`p`) convergence, `dt` convergence, and higher-order time integration (`sdirk33`) as independent variables.
- The effects of time-integration order (`BDF1` versus `BDF2`) and arithmetic precision (`FP32` versus `FP64`) on this flow are covered separately for the DBNS solver in the time-integration and precision comparison case.

This case shows, through literature comparison and cross-solver validation, that the FR solver's integrated unsteady viscous-flow, curved high-order-element, and force-integration path functions correctly. It establishes a minimum validation baseline for this range of conditions rather than an absolute accuracy guarantee.

15.10 References

- Williamson, C. H. K., "Defining a Universal and Continuous Strouhal–Reynolds Number Relationship for the Laminar Vortex Shedding of a Circular Cylinder," *Physics of Fluids*, 31(10), 1988, pp. 2742–2744.
- Henderson, R. D., "Details of the Drag Curve near the Onset of Vortex Shedding," *Physics of Fluids*, 7(9), 1995, pp. 2102–2104.

16 Laminar Cylinder Vortex Shedding — Time Integration and Precision Comparison

Temporal order of accuracy of implicit dual-time BDF1/BDF2 against explicit RK4, and FP32/FP64 arithmetic precision

16.1 Run Provenance and Artifacts

This case combines two independent campaigns that answer different questions and should not be cross-compared as if they were one controlled sweep.

Item	`BDF1/BDF2` Δt sweep	`SLAU2` FP64 / FP32
Wake CFD baseline version	`0.22.2`	`0.22.2`
Solver	DBNS	DBNS
Compute device	CPU	GPU (NVIDIA RTX A6000)
Parallel execution	4 MPI ranks	1 MPI rank
Arithmetic precision	FP64	FP64 / FP32
Run date	2026-08-29 – 2026-08-31	2026-06-04

> **Note**
>
> **Updated 2026-09-01.** The time-integration comparison below replaces a single-point `BDF1/BDF2` result from an earlier build (`0.13.1`, 2026-06-25) with a five-point Δt sweep on a current build. A single point cannot distinguish "close to the reference" from "converging at the right rate," so the earlier numbers are superseded rather than compared directly. The FP32/FP64 precision comparison is a separate, unrelated campaign and is unchanged.

16.1.1 Downloadable Files

Not available: standalone input decks and solver result files have not yet been published for download.

16.2 Verification Objective

This case asks two questions about Wake CFD's implicit dual-time integration (`BDF1`, first order; `BDF2`, second order), holding mesh, physics, and build fixed:

- **Does it converge to the same answer as an independent time-integration path?** The explicit-RK4 case solves the same flow with explicit classical RK4 — no pseudo-time loop, so it carries no dual-time convergence question of its own — and serves as the time-axis reference here.
- **Does it converge at the theoretically expected rate?** Refining the physical step Δt over a five-point sweep (`T/32` through `T/512`, `T` = the shedding period) and fitting `|q(Δt) - q_ref|` against Δt on a log-log plot gives the **observed order of accuracy** directly. Theory predicts a slope of 1 for `BDF1` and 2 for `BDF2`.

Comparing against the explicit-RK4 case rather than the literature values directly is intentional: literature comparison mixes spatial discretization error and physical-model error into the same number as temporal error, so it cannot isolate the effect being tested here. That case uses the same mesh and build with a time step (`4.29×10^-6 s`) fine enough that its own temporal error is negligible, making it a clean reference for the time axis alone.

A second, independent question — FP32 versus FP64 arithmetic precision — is examined in the same case document because it was run on the same physical setup, but the two should be read separately (see Run Provenance).

16.3 Reference Solution and Data

16.3.1 Numerical Reference

The explicit-RK4 case provides the independent time-integration reference for this `Re_D=100` Kármán vortex street: `St=0.1661`, mean `C_D=1.3473`, and `C_L` amplitude `0.3327`. The same mesh and physical conditions are used here for the BDF1/BDF2 time-step sweep.

16.4 Simulation Conditions

Item	Setting
`Re_D`	`100`
Mach	`0.05`
Reference state	ISA sea level, `U=17.0387 m/s` (as in the explicit-RK4 case)
Total simulated time	`12 s` per run
Readout window	`t=6→12 s` (16 cycles), after discarding the transient

16.5 Mesh

Item	Setting
Geometry / mesh	Same as the explicit-RK4 case — `52,428` cells, `1.67%` blockage

16.6 Boundary and Initial Conditions

The cylinder boundary conditions follow the explicit-RK4 case.

Item	Setting
Initial condition	Uniform free stream, cold start

> **Note**
>
> **Why cold start rather than a restart from the explicit-RK4 case.** Inheriting that case's saturated solution would make agreement between the two partly a statement about shared initial conditions rather than independent convergence to the same limit cycle. Each `BDF1`/`BDF2` run develops its own vortex street from a uniform free stream instead.

16.7 Numerical Methods

Item	Setting
Convective scheme	`SLAU2`, second order, weighted least-squares gradient, no limiter
Time integration	Implicit dual-time `BDF1` / `BDF2`; pseudo-time `CFL=30` (constant, does not affect the physical step)
Δt sweep	`T/32, T/64, T/128, T/256, T/512` (`T=0.353341 s`, from the explicit-RK4 case's measured `St`)

16.8 Results

16.8.1 Convergence to the reference solution

At the finest step (`Δt=T/512`), `BDF2` reproduces the explicit-RK4 result to four significant figures:

Metric	BDF2 (Δt=T/512)	Explicit-RK4 reference	Deviation
St	0.1661	0.1661	0.00%
Mean C_D	1.3473	1.3473	0.00%
C_L amplitude	0.3326	0.3327	−0.03%

BDF1, being only first order, has not converged at the same step size — even at Δt=T/512 it still differs from the reference:

Metric	BDF1 (Δt=T/512)	Deviation from reference
St	0.1645	−0.96%
Mean C_D	1.3359	−0.85%
C_L amplitude	0.3152	−5.26%

16.8.2 Order of accuracy

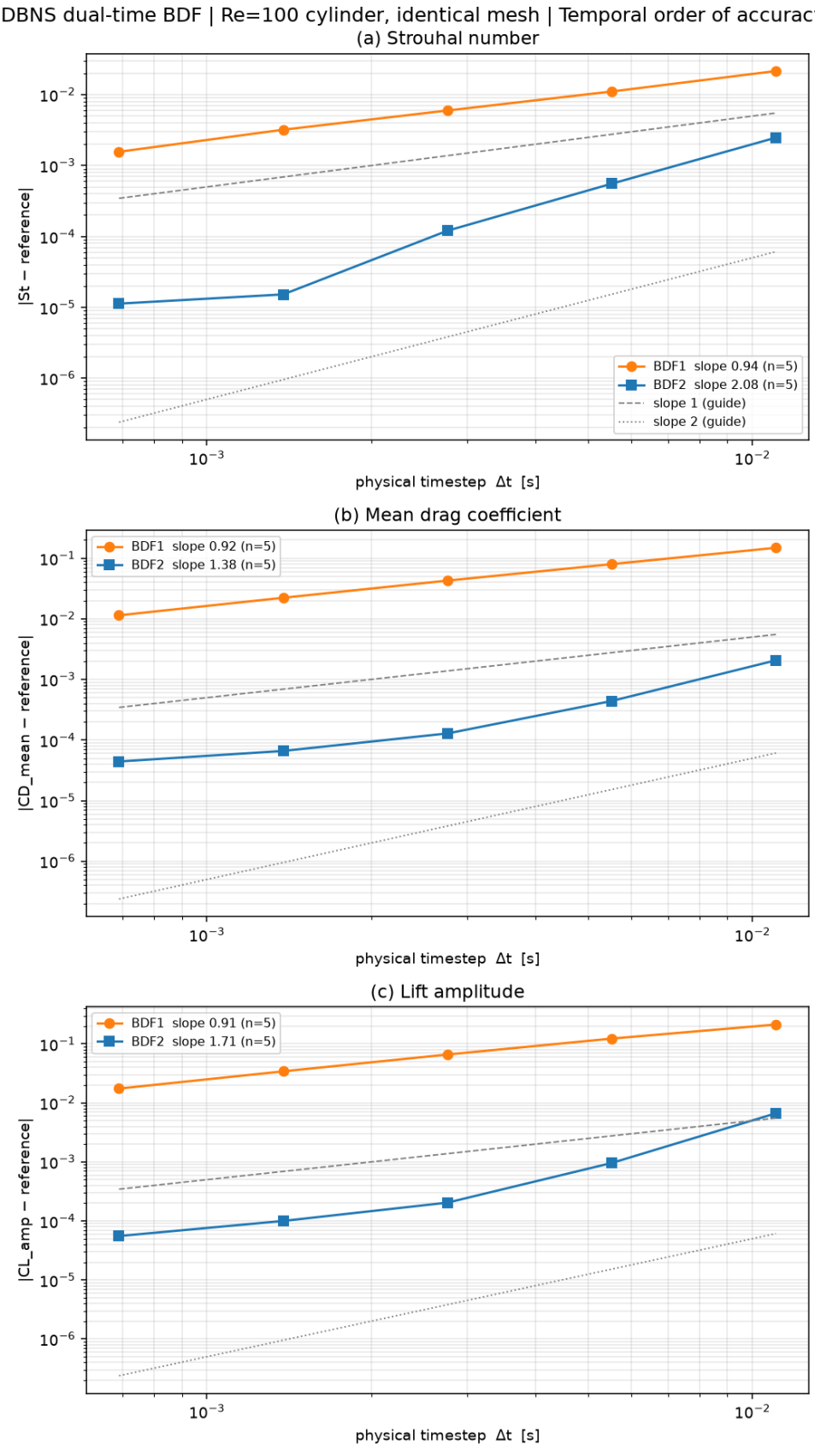


Figure 16.1: Temporal order of accuracy — |error| vs Δt on a log-log plot, fitted slope is the observed order

Metric	BDF1 observed order	BDF2 observed order	Theoretical
St	0.94	**2.08**	1 / 2
Mean C_D	0.92	1.38	1 / 2
C_L amplitude	0.91	1.71	1 / 2

BDF1 matches its theoretical first order on every metric. BDF2 matches its theoretical second order on St (2.08) but comes out lower for mean C_D and C_L amplitude (1.38, 1.71).

> **Note**
>
> **The lower BDF2 orders on C_D/C_L are not a sign of reduced accuracy.** By Δt=T/128, BDF2's error on these two metrics has already fallen to the level of the explicit-RK4 case's own cycle-to-cycle variability (±0.0067 on mean C_D), so the two finer points in the sweep are fitting the reference's statistical noise floor rather than remaining truncation error — the log-log slope flattens once the signal being fit is noise. St does not show this problem because its cycle-to-cycle variability is two orders of magnitude smaller.

> **Warning**
>
> **One data point does not fit the pattern.** BDF1 at the coarsest step (Δt=T/32, 32 steps per shedding period) fails a physical self-consistency check: the drag signal should oscillate at exactly twice the lift-signal frequency, and every other configuration in this sweep reproduces that to within 0.3% — but this one point gives a ratio of 0.026, and its cycle-to-cycle variability is an order of magnitude higher than any other point in the sweep. Excluding it changes the fitted BDF1 order by less than 0.01 on every metric, so it does not affect the order-of-accuracy conclusion. It is, however, a practical warning: on this mesh, 32 steps per period is too coarse for BDF1 to produce a trustworthy force signal, while BDF2 at the same step count is unaffected.

16.8.3 FP64 versus FP32

In the integrated force coefficients the two are indistinguishable: mean C_D is 1.3604 (FP64) versus 1.3603 (FP32), a difference below 0.01%, and both give a C_L amplitude of 0.3354 and the same St.

> **Important**
>
> **"Indistinguishable in C_D" is not "indistinguishable".** The same pair of runs differs clearly in two other places:

Metric	FP64	FP32
Final flow residual (log)	**−8.98**	**−7.09**
Drag spectrum noise floor	decays cleanly	flat floor near 1e-5
Wall-clock time	5.16 h	2.75 h

FP32 stalls about 1.9 orders higher in residual — it reaches its precision floor and cannot converge further. The reported 1.9× speed-up therefore includes doing fewer useful iterations, not only faster arithmetic.
Practical reading: FP32 is adequate when the quantity of interest is an **integrated force averaged over a saturated limit cycle**. It is not adequate when you need deep residual convergence, or when you need weak spectral content such as higher harmonics, which the FP32 noise floor buries.

The `SLAU2` FP64 result agrees with the explicit-RK4 case's reference within 1% for every metric (`St` +0.66%, mean `C_D` +0.97%, `C_L` amplitude +0.81%). Note that this pair also differs in solver version and CPU/GPU execution (see Run Provenance), so this is a useful consistency check rather than a controlled comparison.

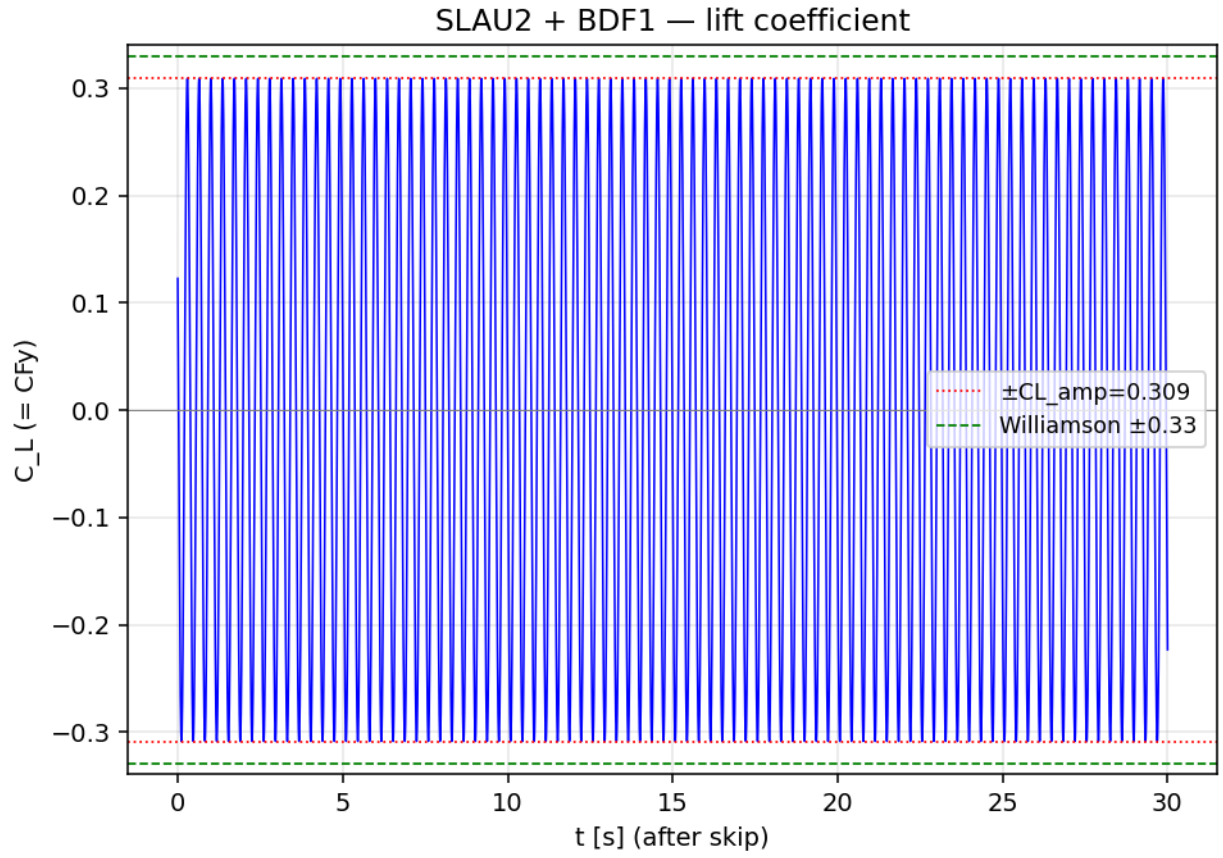


Figure 16.2: BDF1 lift-coefficient time history — amplitude saturates below the literature value

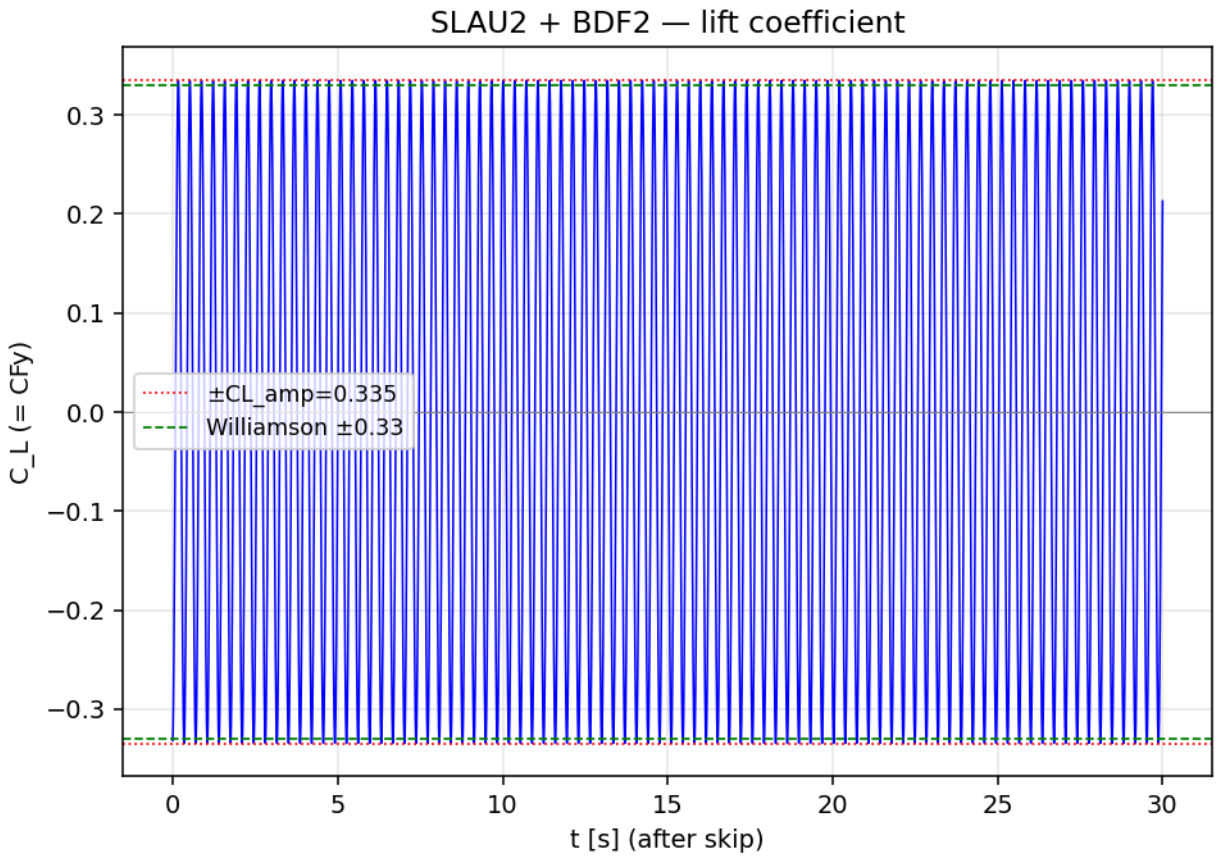


Figure 16.3: BDF2 lift-coefficient time history — amplitude agrees closely with the literature value

16.9 Conclusions and Applicable Scope

- Both `BDF1` and `BDF2` implicit dual-time integration converge to the explicit-RK4 reference as Δt is refined, at close to their theoretical order of accuracy — first order for `BDF1`, second order for `BDF2` (cleanly confirmed via `St`; the `C_D`/`C_L`-amplitude orders are limited by the reference's own statistical noise floor rather than by the scheme).
- `BDF2` at `Δt=T/512` already matches the RK4 reference to four significant figures. `BDF1` needs a substantially finer step for comparable accuracy — even at `Δt=T/512` it is still 5.3% off in `C_L` amplitude.
- For `BDF1`, keep at least on the order of 64 steps per period of the unsteady phenomenon of interest; 32 steps per period was shown empirically to corrupt the force signal on this mesh. `BDF2` remained clean at 32 steps per period. These step counts are specific to this Reynolds number and mesh and should be re-verified under other conditions.
- FP32 matches FP64 in integrated force coefficients (below 0.01%) but converges about 1.9 orders less deeply and raises the spectral noise floor. Choose FP32 for integrated loads on a saturated limit cycle, not for deep convergence or weak spectral content.
- These results were obtained for one Reynolds number (`Re_D=100`), one mesh, and one convective scheme (`SLAU2`). They cannot be generalized to other Reynolds numbers, mesh resolutions, or flux schemes.

16.10 References

- Williamson, C. H. K., "Defining a Universal and Continuous Strouhal–Reynolds Number Relationship for the Laminar Vortex Shedding of a Circular Cylinder," *Physics of Fluids*, 31(10), 1988, pp. 2742–2744.
- Henderson, R. D., "Details of the Drag Curve near the Onset of Vortex Shedding," *Physics of Fluids*, 7(9), 1995, pp. 2102–2104.

17 Laminar Cylinder Vortex Shedding — Explicit Classical RK4

Physical-time explicit integration on a blockage-controlled mesh, validated against Williamson and Henderson

17.1 Run Provenance and Artifacts

Item	Value
Wake CFD baseline version	`0.22.0`
Solver	DBNS
Compute device	CPU
Parallel execution	4 MPI ranks
Arithmetic precision	FP64
Run date	2026-08-24

> **!** Important
>
> **This build contains a correction to the strong wall boundary condition on the classical-RK4 path.** Classical RK4 keeps a weighted accumulator in addition to the base state, and the no-slip Dirichlet condition was previously applied to the base state only. On earlier builds the wall value drifted, which inflated the friction component of drag while leaving the pressure field — and therefore contour plots — visually unaffected.
> Any explicit-RK4 result from a build earlier than 2026-08-23 is not comparable with the numbers below. Implicit dual-time integration is unaffected, because the weighted accumulator exists only on the RK4 path.

17.1.1 Downloadable Files

Not available: standalone input decks and solver result files have not yet been published for download.

17.2 Validation Objective

This case establishes the reference result for laminar cylinder vortex shedding in Wake CFD, using **explicit physical-time integration**: there is no pseudo-time loop, and the CFL number sets the physical time step directly.

Explicit integration was chosen for the reference because it removes a degree of freedom that implicit dual-time methods carry. A dual-time result depends on how far the inner pseudo-time loop is converged at each physical step, and that convergence is a setting rather than a property of the discretization. Explicit marching has no such setting: each step is the scheme, and the only numerical parameter is the step size itself.

Classical RK4 is fourth-order in time and introduces no amplitude damping at the step sizes used here, so the reported lift amplitude and shedding frequency are not shaped by time-integration error at the level being compared.

17.3 Reference Solution and Data

The Kármán vortex street at `Re_D=100` is a standard unsteady validation case with well-established experimental values for Strouhal number, mean drag, and lift amplitude. At this Reynolds number the wake is laminar and two-dimensional — three- dimensional instability sets in near `Re_D 190` — so a 2D simulation is physically appropriate rather than a simplification.

17.4 Simulation Conditions

Item	Setting
Geometry	Circular cylinder, `D=1 m`
Analysis	Unsteady, compressible laminar Navier–Stokes
`Re_D`	`100`
Mach	`0.05` (`mu=0.2081` is used to match `Re_D`)
Reference state	ISA sea level — `P=101325 Pa`, `T=288.15 K` → `rho=1.2218`, `U=17.0387 m/s`
Total simulated time	`12 s` — about 34 shedding cycles
Readout window	`t = 6→12 s` (16 cycles), see Section 18.8.2

With explicit physical-time marching the time step is not prescribed; the CFL number determines it every step from the local mesh and flow state. The step therefore drifts slightly as the flow develops — here from `4.3663×10^-6` to `4.2857×10^-6 s`, a 1.9% change over the run — which matters when frame times are assigned for animation (Section 18.8.2).

17.5 Mesh

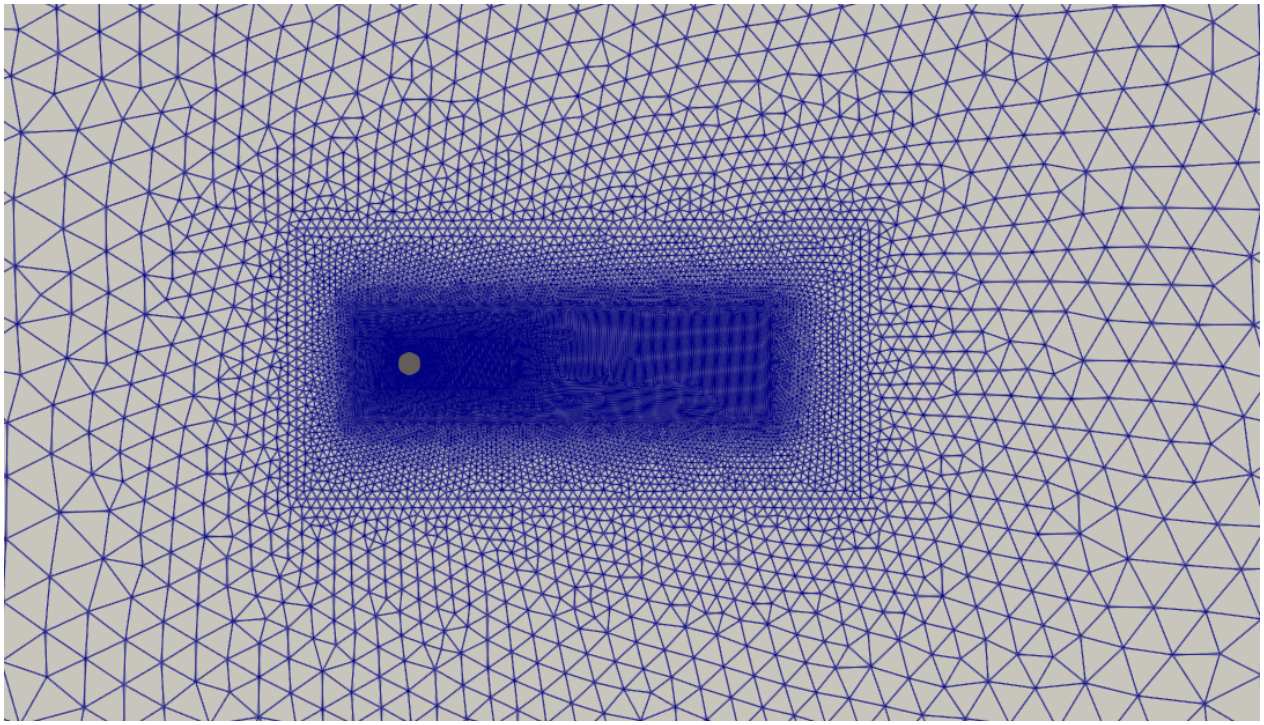


Figure 17.1: Unstructured mesh with graded refinement zones around the cylinder and along the wake

Item	Value
Cells	52,428 (unstructured triangles with a structured near-wall layer)
Domain	`20D` upstream, `40D` downstream, `±30D` lateral
Blockage	**1.67%** (`D` / lateral extent)
Near-wall first cell	`y_1 = 0.002D`, growth ratio `1.2`, about 13 cells inside the boundary layer
Wake resolution	`D/35` (near wake), `D/23` (`2<x<5`), `D/14` (`10<x<20`)
Maximum cell-size jump in the wake	`5×`

Note

Why blockage is reported. A finite lateral domain accelerates the flow past the cylinder and raises the shedding frequency relative to an unbounded experiment, so blockage is a direct contributor to any Strouhal offset. The commonly used guideline is to keep it below about 2%. Reference values from Williamson and Henderson correspond to an unbounded flow, so a validation report that omits its blockage cannot be checked against them meaningfully.
Abrupt cell-size jumps in the wake are reported for the same reason — they act as partially

> reflecting interfaces for the shed vortices and damp the wake artificially.

The mesh is generated from a parametric definition with a level parameter, so a `sqrt(2)`-ratio family for grid convergence can be produced from the same source. Grid convergence itself was **not** performed in this case and remains outstanding (Section 17.9).

17.6 Boundary and Initial Conditions

Item	Setting
Wall	no-slip, adiabatic
Outer boundary	farfield

Initial field: Not reported.

17.7 Numerical Methods

Item	Setting
Convective scheme	`SLAU2`, second order, weighted least-squares gradient, no limiter
Time integration	explicit classical RK4 (four fixed stages), physical-time marching
`CFL`	`4.0` (constant) → `dt = 4.2857×10^-6 s`

17.8 Results

Metric	This case	Literature	Deviation
`St`	**0.1661**	0.164 (Williamson)	**+1.3%**
Mean `C_D`	**1.3473 ± 0.0067**	1.35 (Henderson)	**−0.2%**
`C_L` amplitude	**0.3327**	0.33	**+0.8%**
Drag/lift frequency ratio	1.9993	2 (physical requirement)	−0.04%

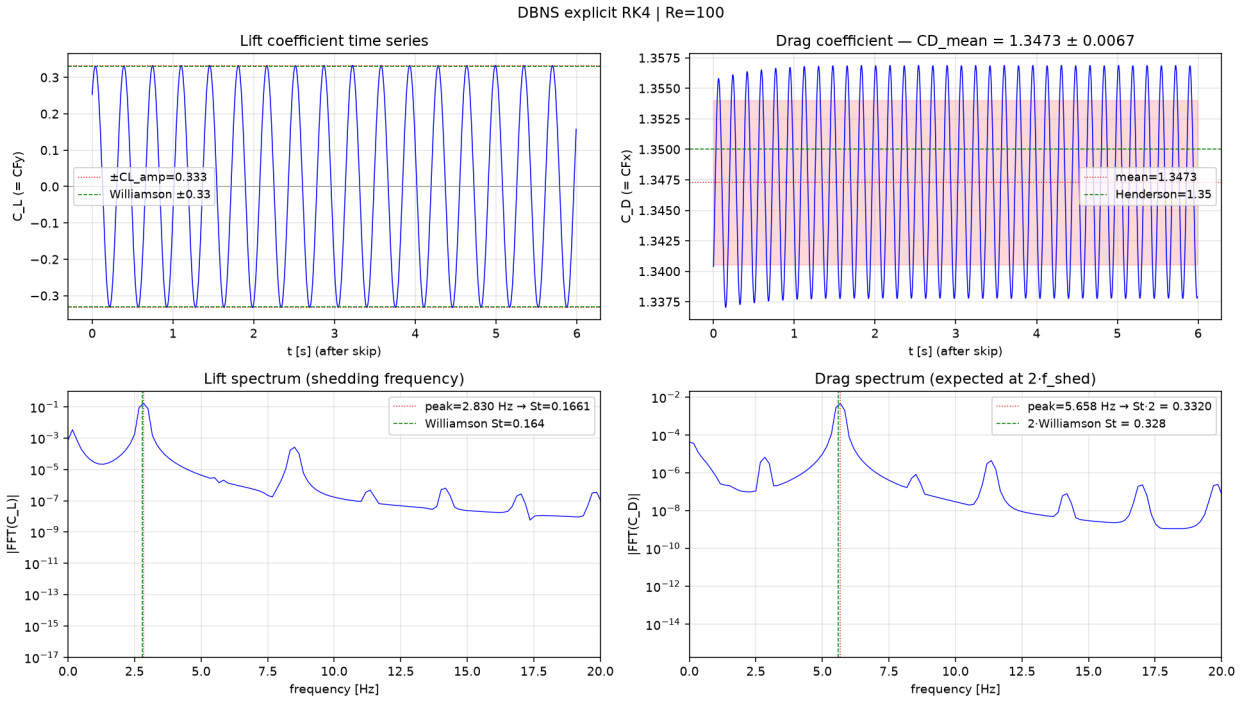


Figure 17.2: Lift and drag time histories with their spectra

The two spectra at full size, since the peak identification is the basis of the reported Strouhal number:

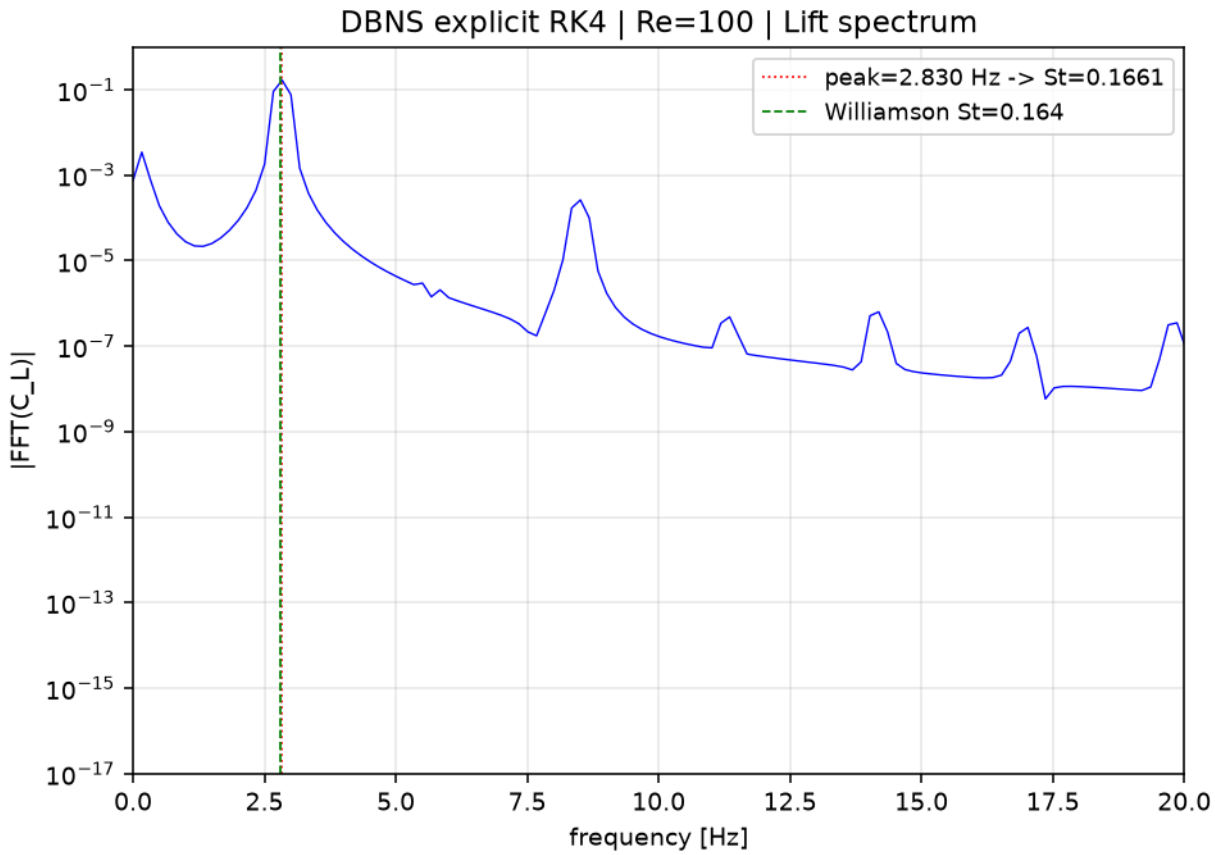


Figure 17.3: Lift spectrum — single peak at the shedding frequency with a clean harmonic series

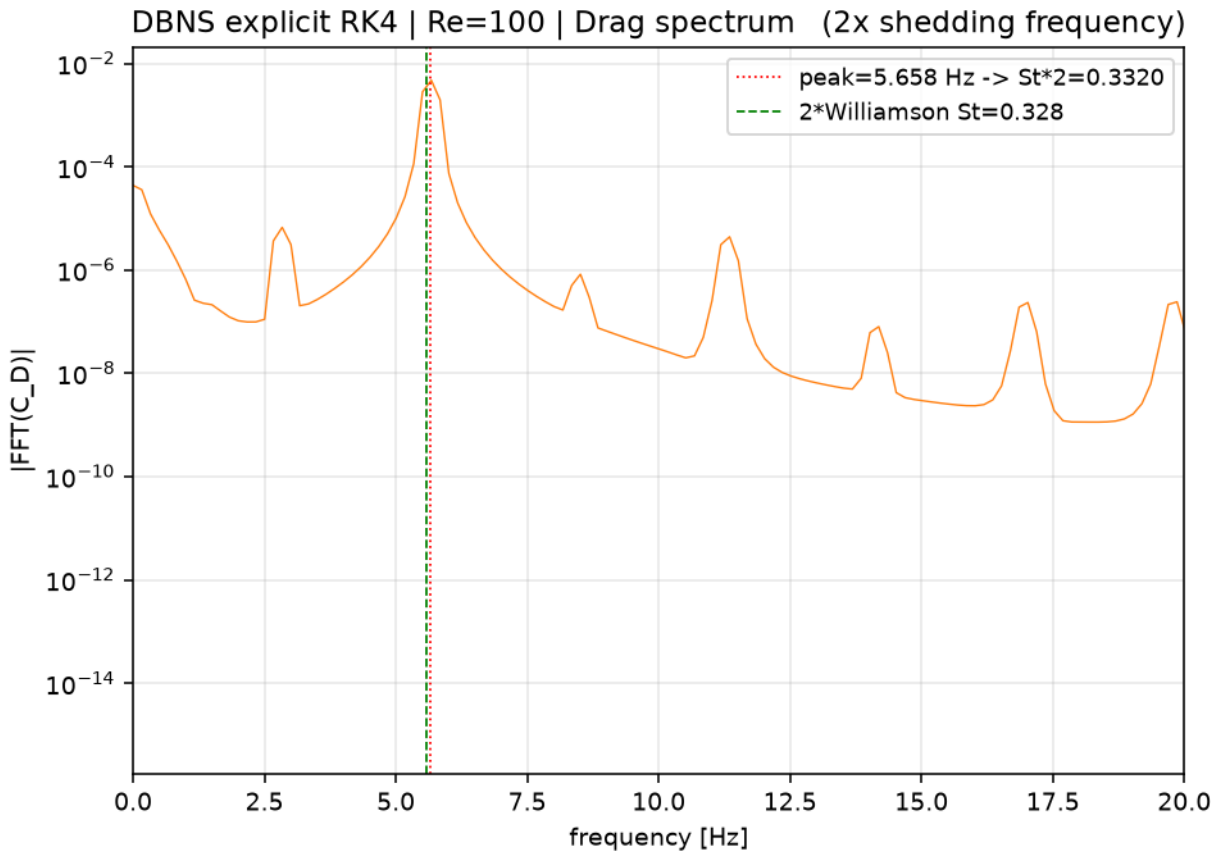


Figure 17.4: Drag spectrum — peak at twice the shedding frequency, as required

17.8.1 Drag Decomposition

Component	This case	Literature
Pressure	1.0039	1.02
Friction	0.3391	0.33
Friction share	25.2%	24%

> **!** Important
>
> **The decomposition is the stronger statement, not the total.** A mean `C_D` within 0.2% of the reference can arise from compensating errors in the pressure and friction components. Here both components agree independently, which additionally confirms that the no-slip wall condition is enforced correctly — the wall shear stress is the quantity most sensitive to it.

17.8.2 Development History

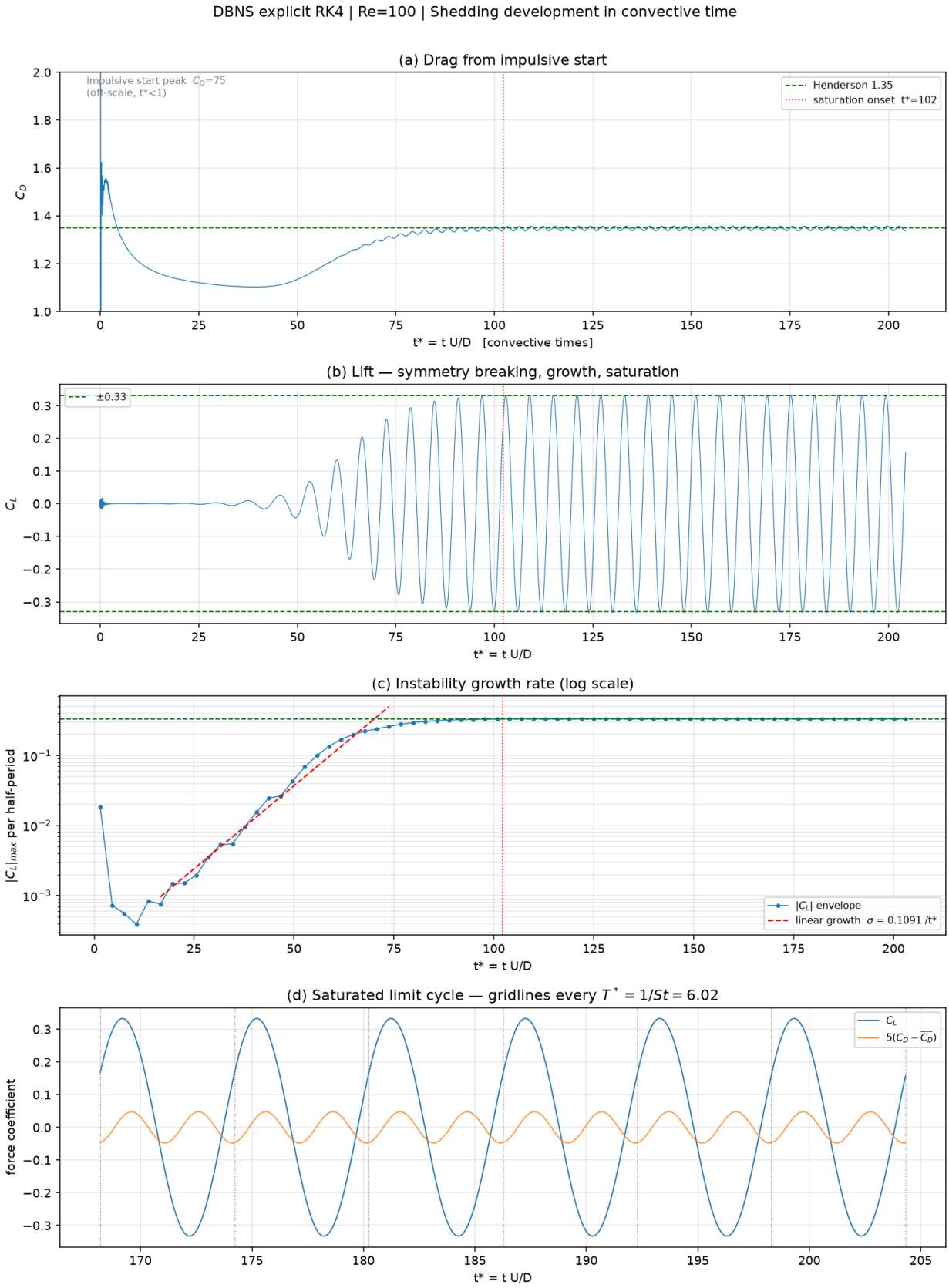


Figure 17.5: Shedding development in convective time

Plotting against convective time `t* = tU/D` rather than seconds makes the record comparable across geometries and flow speeds, and the shedding period is read directly as `T* = 1/St = 6.02`. The run covers `t* = 0→204`, about 34 cycles.

Stage	`t*`	Behaviour
Impulsive start	`<1`	`C_D` spike of 75 (added mass and starting vortex)
Recirculation growth	`1→40`	`C_D` falls to **1.10** — symmetric steady wake, no shedding yet
Instability growth	`15→70`	`C_L` grows exponentially, `sigma = 0.1091` per `t*`
Nonlinear saturation	`70→85`	`C_D` recovers to 1.35
Limit cycle	`>85`	Fully saturated

The drag minimum at `t* 40` is lower than the saturated value of 1.347. This is the well-known result that vortex shedding *increases* mean drag relative to the symmetric steady wake, and it appears here without being sought.

The exponential growth rate `sigma` corresponds to the linear term of the Landau amplitude equation and can be compared with global linear stability analysis. That comparison was **not** made here; the value is recorded so that a future Reynolds-number sweep can construct `sigma(Re)` and extrapolate to the critical Reynolds number.

17.8.3 Flow Field

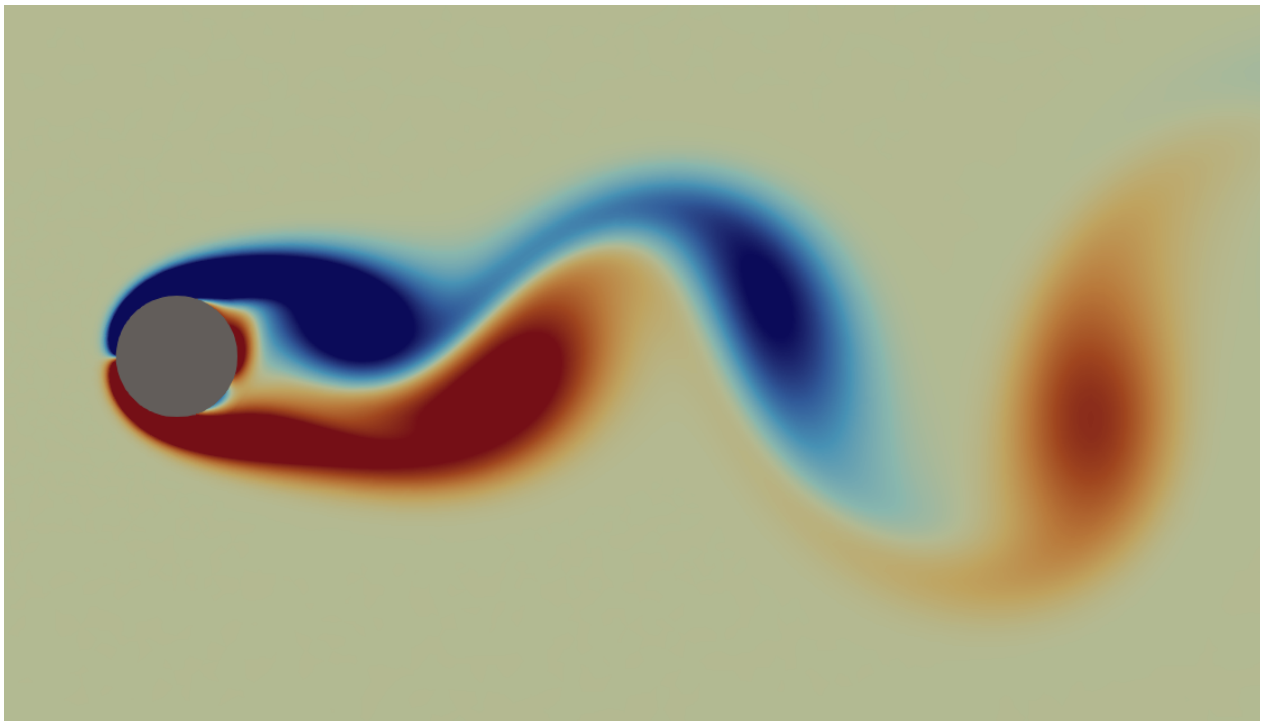


Figure 17.6: Vorticity

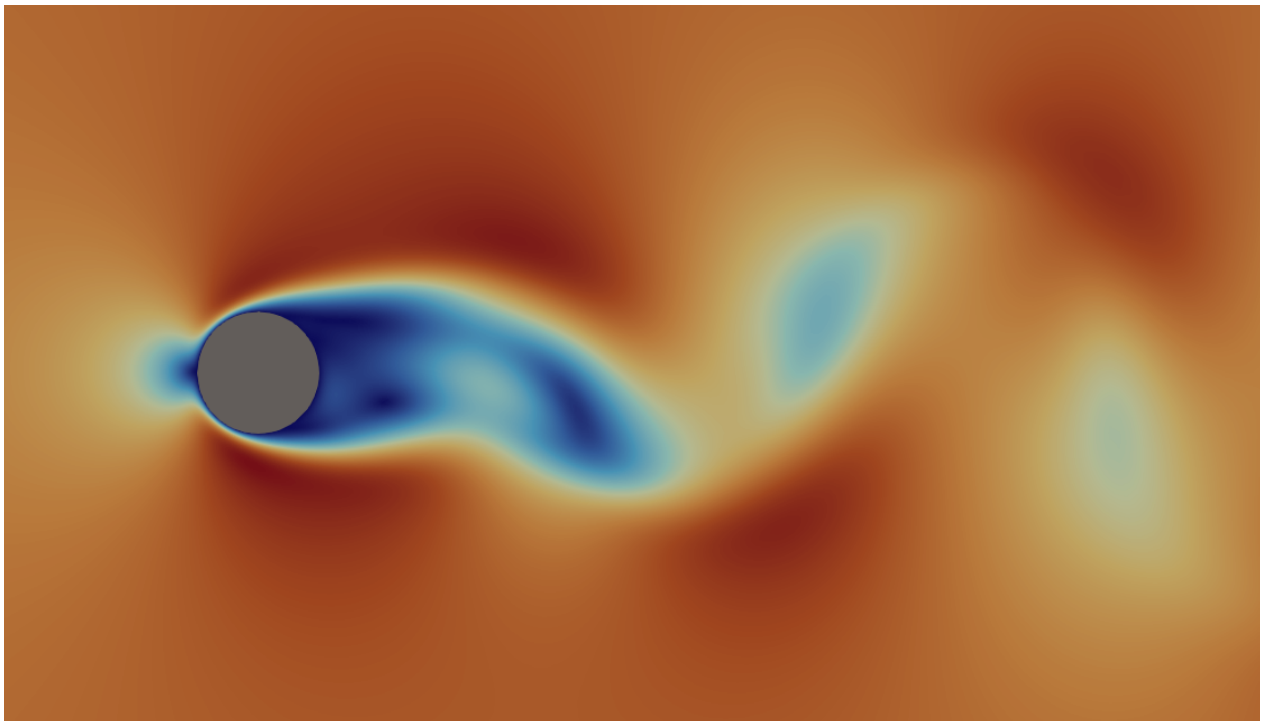


Figure 17.7: Velocity magnitude

17.8.4 Readout Methodology

Two choices affect the reported numbers enough to be stated explicitly.

17.8.5 Readout window

The transient was initially assumed to end at `t = 4 s`. It does not. The window was selected by requiring the statistics to stop changing:

Skip [s]	Window [s]	Cycles	Mean `C_D`	Std. dev.	`C_L` amp.	`St`
4.0	7.99	22	1.3430	**0.0132**	0.3325	0.1657
5.0	6.99	19	1.3467	0.0069	0.3326	0.1660
6.0	5.99	16	**1.3473**	**0.0067**	0.3326	0.1661
7.0	4.99	14	1.3473	0.0068	0.3326	0.1662
8.0	3.99	11	1.3473	0.0068	0.3326	0.1662

The standard deviation halves at `6 s` and the mean is then stable to four decimal places. The reported window is `t = 6→12 s`. Period-to-period variation of the limit cycle over that window is 0.00%.

17.8.6 Frequency estimation

⚠ Warning

A raw FFT peak was not accurate enough for this run. With a 6-second window the frequency resolution is `df/f = 5.9%`, so the discrete bin spacing alone bounds the Strouhal error at `±2.9%` — the same size as the deviation being reported.

Method	`St`
FFT maximum bin	0.1665
Parabolic interpolation of the log-magnitude peak	0.1659
Upward zero-crossing (adopted)	**0.1661**

Zero-crossing is not limited by bin spacing. It agrees with the independent parabolic estimate to within 0.1%, and it is the estimate for which the drag/lift frequency ratio comes out as `1.9993` against the physical requirement of exactly 2 — a self-check on the method itself. The bound scales as `1/(2·T_window)`, so the distinction matters less for longer runs — a 32-second window would bound the same error at 0.6%. It is stated here because this run traded window length for wall-clock time, and the resulting bound is not negligible against the deviation being reported.

17.9 Conclusions and Applicable Scope

- Explicit classical RK4 reproduces all three reference quantities within 1.3% on a blockage-controlled mesh, with the readout window and frequency estimator both shown to be converged. This is the reference result for this flow in Wake CFD.
- The pressure and friction components of drag agree with the reference *separately*, which is a stronger statement than agreement of the total and confirms correct enforcement of the no-slip wall.
- The residual `+1.3%` Strouhal offset is **not resolved into its causes**. Three candidates remain open: compressibility at `M=0.05` (the reference values are incompressible), the remaining 1.67% blockage, and discretization error. Separating them requires a Mach sweep, a domain sweep, and a grid-convergence study respectively.

⚠ Warning

What this case does not establish.

- **Grid convergence was not performed.** A `sqrt(2)`-ratio mesh family exists in the parametric source but was not run, so discretization error is not bounded. Agreement with experiment at a single grid level can include error cancellation.
- **The `+1.3%` offset is not attributed.** No Mach or domain sweep was run.
- **The linear growth rate is reported, not validated.** It is not compared with global stability analysis.
- Results apply to one Reynolds number (`Re_D=100`), one mesh, one convective scheme

(`SLAU2`), and one time-integration scheme. They do not transfer to other conditions without repeating the exercise.

17.10 References

- Williamson, C. H. K., "Defining a Universal and Continuous Strouhal–Reynolds Number Relationship for the Laminar Vortex Shedding of a Circular Cylinder," *Physics of Fluids*, 31(10), 1988, pp. 2742–2744.
- Henderson, R. D., "Details of the Drag Curve near the Onset of Vortex Shedding," *Physics of Fluids*, 7(9), 1995, pp. 2102–2104.

18 Laminar Cylinder Vortex Shedding — PBNS Strouhal/CD/CL Validation

Validation of the compressible pressure-based coupled solver against literature values at Re=100

18.1 Run Provenance and Artifacts

Item	Value
Wake CFD baseline version	`0.23.0`
Solver	PBNS
Compute device	GPU (NVIDIA RTX A2000)
Parallel execution	1 MPI rank
Arithmetic precision	Mixed
Run date	2026-10-20

> **Note**
>
> Results depend on the solver build that produced them. Read every figure in this report together with the version and date above — re-running the same input on a later build may give different numbers.
> A first attempt with an older build (2026-08-21) did not reach a usable result and is not reported here; the results below come from the single run of 2026-10-20.

18.1.1 Downloadable Files

Not available: standalone input decks and solver result files have not yet been published for download.

18.2 Validation Objective

This case checks whether the compressible pressure-based coupled solver (PBNS) reproduces the laminar von Kármán vortex street behind a circular cylinder at `Re_D=100`. The comparison is with literature values for three quantities: the Strouhal number `St`, the mean drag coefficient `CD`, and the

lift-coefficient amplitude `CL_amp`. It also checks the frequency relation between drag and lift (drag oscillates at twice the lift frequency) and the split of drag into pressure and friction parts. The case is a validation of one solver at one condition, not a comparison with the density-based solver.

18.3 Reference Solution and Data

The Kármán vortex street at `Re_D=100` is a standard unsteady validation case with established values for `St`, mean drag, and lift amplitude. At this Reynolds number the wake is laminar and two-dimensional — three-dimensional instability sets in near `Re_D 190` — so a two-dimensional simulation is physically appropriate.

18.3.1 Experimental Data

Quantity	Literature value	Source
`St`	0.164	Williamson (1988)
`CD` (mean)	1.35	Henderson (1995)
`CL` amplitude	0.33	Williamson (1996)

The literature values correspond to unbounded, incompressible flow. The simulation uses a compressible solver at `M=0.05` in a finite domain, so a small offset from these values is expected.

18.4 Simulation Conditions

Item	Setting
Geometry	Circular cylinder, `D=1 m`
Analysis	Unsteady, laminar, compressible Navier–Stokes (ideal gas)
`Re_D`	`100` (`mu=0.2081` is used to match `Re_D`)
Mach	`0.05`
Reference state	ISA sea level — `P=101325 Pa`, `T=288.15 K` → `rho=1.2215`, `U=17.0389 m/s`
Reference area	`D·dz = 0.1` (one-cell-thick extrusion, `dz=0.1`)
Total simulated time	`40 s` (convective time `t* = tU/D  682`, about 113 shedding cycles)
Readout window	`t = 20→40 s` (55 periods), see *Readout Window*

18.5 Mesh

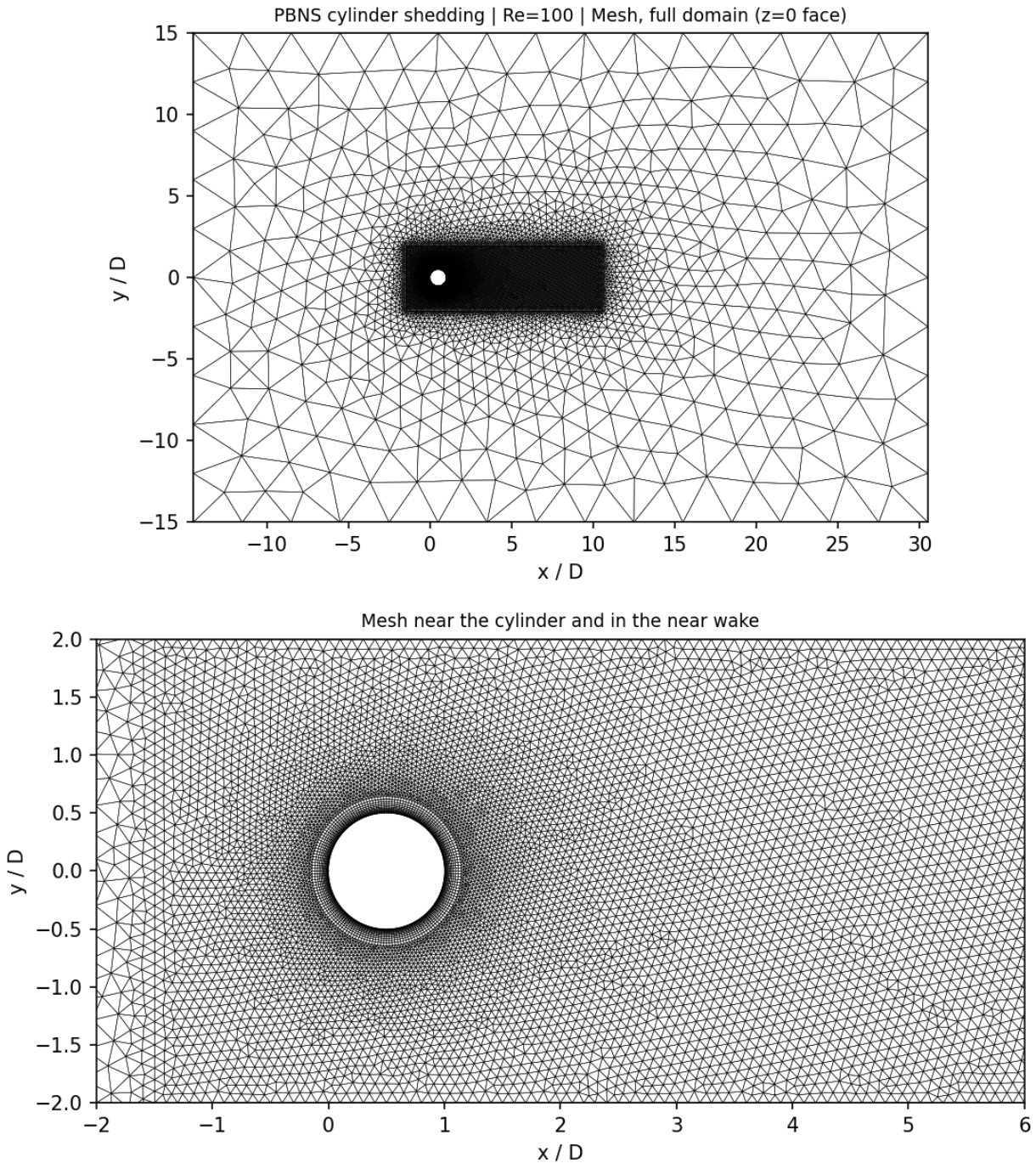


Figure 18.1: Mesh of the z=0 face: full domain and the region near the cylinder

Item	Value
Points	26,606
Elements	21,596 prisms (triangular base) + 2,400 hexahedra
Extrusion	One cell in the spanwise direction, `dz = 0.1`
Domain	`15D` upstream, `30D` downstream, `±15D` lateral
Blockage	**3.33%** (`D` / lateral extent)
Wake resolution	about `D/15` in the near wake, about `D/7` for `x > 10D`

The solver is three-dimensional, so the two-dimensional planar mesh is extruded by one cell and both spanwise faces are symmetry planes. Every point then lies on a symmetry plane and the spanwise velocity is zero, which makes the problem mathematically two-dimensional. The spanwise force and the in-plane moments confirm this: over `t  20 s` the maximum of `|CFz|` is `3.2×10^-20`, of `|CMx| 5.9×10^-8`, and of `|CMy| 4.7×10^-8`.

The blockage of 3.33% is higher than the usual guideline of about 2%. A finite lateral domain accelerates the flow past the cylinder and raises the shedding frequency and drag relative to the unbounded reference values, so the offsets reported below include this effect. No grid-convergence study was run.

18.6 Boundary and Initial Conditions

Item	Setting
Cylinder	No-slip, adiabatic wall
Outer boundary	Farfield at `M=0.05`
Spanwise faces	Symmetry

The run starts impulsively from the uniform freestream. The initial field is not described further here.

18.7 Numerical Methods

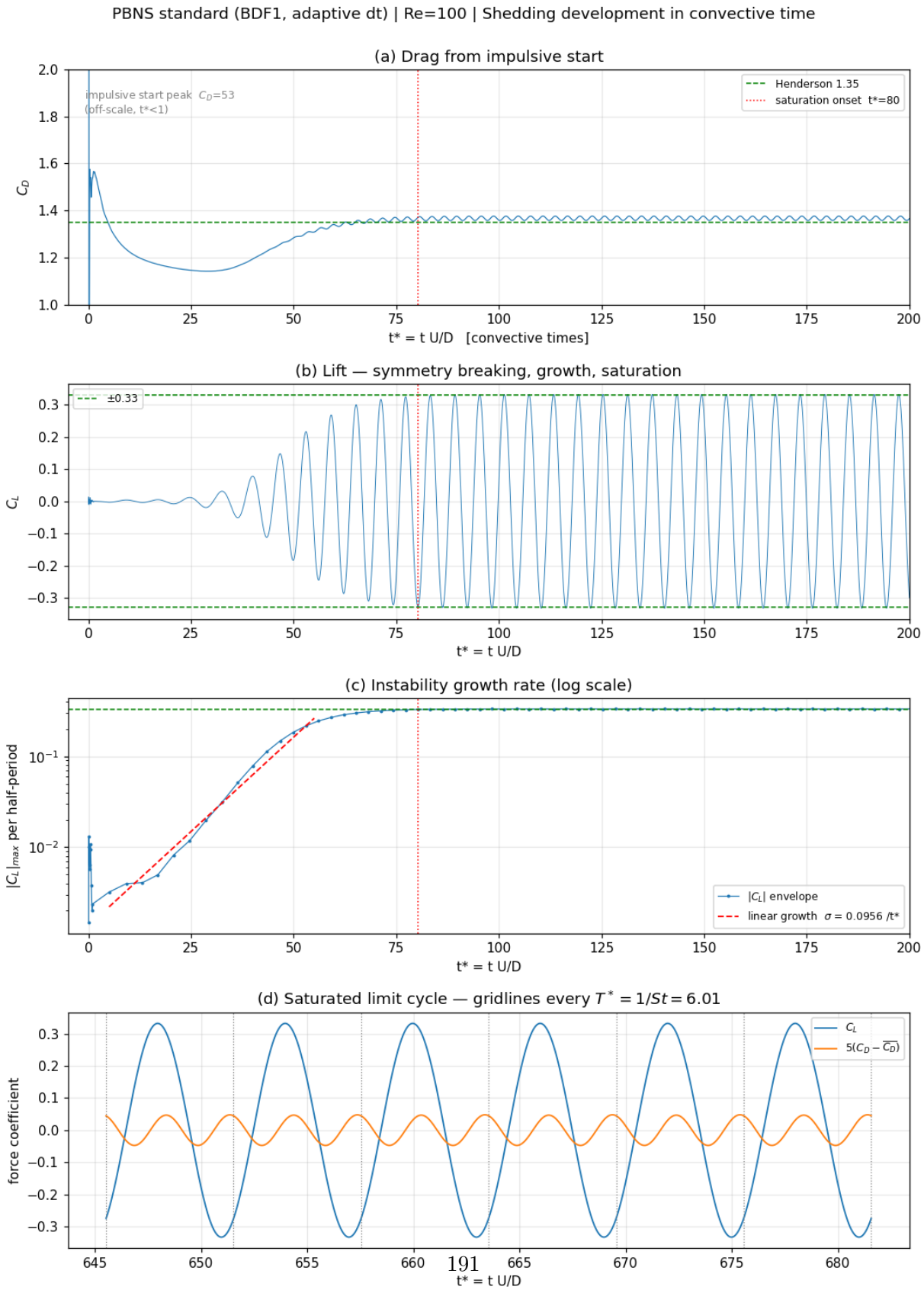
Item	Setting
Solver	PBNS: coupled velocity–pressure (`u, v, w, p`) solve with a finite-difference Newton linearization and the energy equation
Time integration	First-order implicit (backward Euler, BDF1) with adaptive time step, initial `dt = 10^-3 s`

Item	Setting
Time step actually used	`dt = 2.893×10^-4 s`, constant for the whole run (minimum `2.750×10^-4`, maximum `2.901×10^-4`), `T/1219` for a shedding period `T = 0.3526 s`
Linear solver	FGMRES with algebraic-multigrid preconditioner, `max_iter` 50, tolerance `10^-3`; 2.02 iterations on average, 9 at most

The time step is set automatically each step from CFL-type limits and stays at its limiting value; which limit was active was not separated.

18.8 Results

18.8.1 Development of the Shedding



Stage	t*	What happens
Impulsive start	< 1	CD spike of 53 (off the axis of the figure)
Recirculation growth	1–30	CD falls to 1.14 — symmetric steady wake
Instability growth	5–50	CL grows exponentially, = 0.0956 per t*
Saturation	80	the |CL| envelope reaches 98% of its final value
Limit cycle	> 80	the readout window starts at t = 20 s (t* 341), 260 convective times after saturation

The growth rate is a fit to the |CL| envelope between 3×10^-3 and 0.3 times the saturated value for t* > 5 (10 half-periods). It is reported, not compared with a stability analysis.

18.8.2 Readout Window

Window start [s]	Length [s]	Periods	CD mean	± std	CL amplitude	St (zero crossing)	CFx/CFy frequency ratio
5	35.00	98	1.3666	0.0067	0.3323	0.1665	2.0002
10	30.00	84	1.3666	0.0067	0.3323	0.1665	2.0000
15	25.00	70	1.3666	0.0067	0.3323	0.1665	2.0000
20	**20.00**	**55**	**1.3666**	**0.0067**	**0.3323**	**0.1665**	**2.0001**
25	15.00	41	1.3666	0.0067	0.3323	0.1665	2.0000
30	10.00	27	1.3666	0.0067	0.3323	0.1665	2.0000

The four reported digits are fixed from a window start of 5 s on, because saturation ends at about 4.7 s (t* 80). The window used for the reported values starts at 20 s. St is evaluated from the zero crossings of CL (the coefficient of variation of the period is 0.000%).

18.8.3 Comparison with Literature

Quantity	Wake CFD (PBNS)	Literature	Difference
St (zero crossing)	**0.1665**	0.164 (Williamson 1988)	**+1.5%**
CD (mean)	**1.3666 ± 0.0067**	1.35 (Henderson 1995)	**+1.2%**
CL amplitude	**0.3323**	0.33 (Williamson 1996)	**+0.7%**

Quantity	Wake CFD (PBNS)	Literature	Difference
`CFx`/`CFy` frequency ratio	2.0001	2 (physical requirement)	+0.005%

All three quantities are within 1.5% of the literature values, with `St` and `CD` slightly high. This is the direction expected from the finite blockage (3.33%) and the compressibility at `M=0.05`; neither effect was separated by a domain or Mach-number sweep.

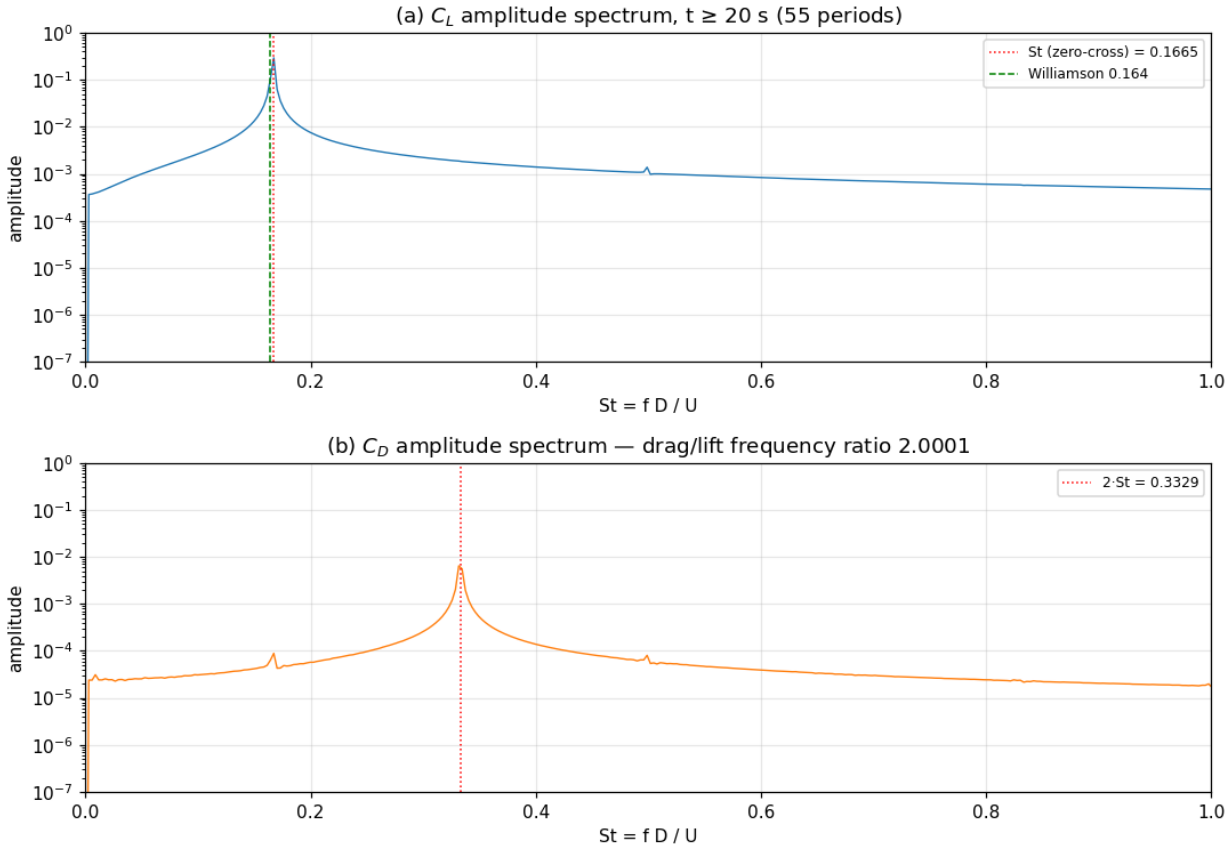


Figure 18.3: Amplitude spectra of lift and drag over the readout window

The lift peaks at 2.8365 Hz and the drag (zero crossing) at 5.6732 Hz, a ratio of 2.0001. The largest FFT bin gives `St = 0.1673`; the bin width of the 20 s window is `df/f = 1.76%`, so this agrees with the zero-crossing value within the bin uncertainty of ±0.9%. The zero-crossing value is the one reported.

18.8.4 Pressure and Friction Drag

	`CD`	= pressure	+ friction	Friction share
Wake CFD (PBNS)	1.3666	1.0224	0.3442	25.2%

	CD	= pressure	+ friction	Friction share
Literature	1.35	1.02	0.33	24%

Both components agree with the literature separately, which is a stronger statement than agreement of the total drag.

18.8.5 Flow Field

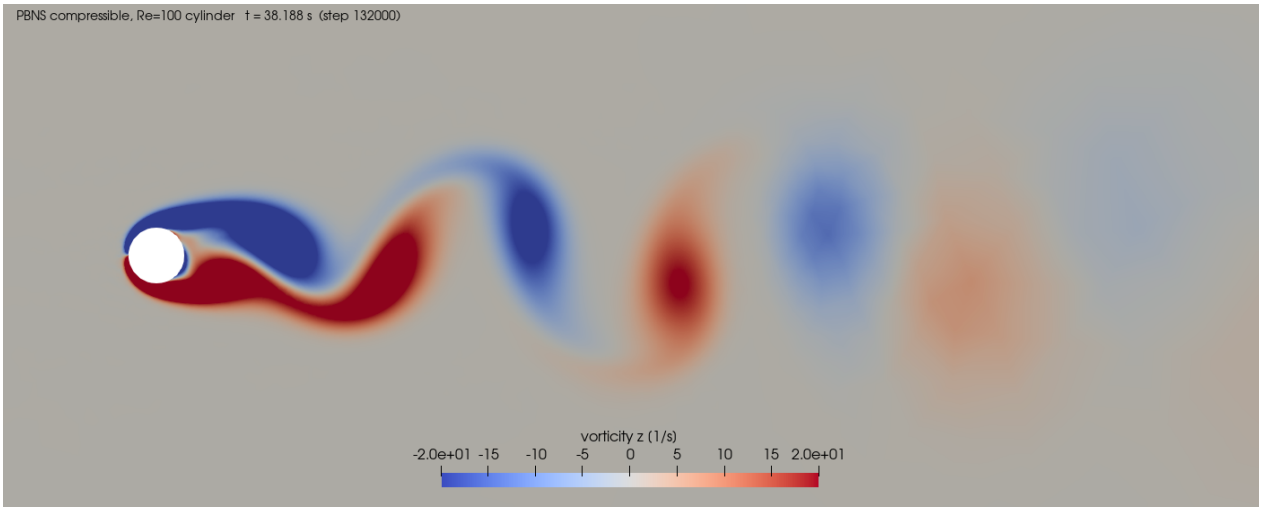


Figure 18.4: Spanwise vorticity of the saturated limit cycle at t = 38.19 s

The Kármán vortex street is visible to about 14D downstream. The cores spread quickly downstream because the mid-wake resolution of this mesh (D/15, D/7 for x > 10D) is coarse.

> **Note**
>
> The vorticity is not a solver output field. The PBNS volume output does not write gradient-derived fields, so the vorticity shown was computed in post-processing from the solver's velocity field with a gradient filter.

18.9 Conclusions and Applicable Scope

- The compressible PBNS solver reproduces the laminar vortex street at Re_D=100: St 0.1665 (+1.5%), mean CD 1.3666 (+1.2%), and CL amplitude 0.3323 (+0.7%) against literature, with a drag-to-lift frequency ratio of 2.0001.
- The pressure and friction parts of the drag agree with the literature separately (friction share 25.2%).
- The run reached the saturated limit cycle by t* 80; the reported values are stable against the choice of readout window start from 5 s to 30 s.

- A one-cell-thick extrusion with symmetry planes behaves as a two-dimensional problem (spanwise force `10^-20`).

> **Warning**
>
> **What this case does not establish.**
>
> - **No cross-check against the density-based solver.** The density-based reference runs (case-08, case-04) use different meshes (case-08 has 1.67% blockage), so differences of the order of 1% in `CD` and `St` cannot be attributed to the solver rather than the mesh.
> - **Grid convergence and time-step convergence were not performed.** The time integration is first order (BDF1) at a single time step; the effect of the time step on the result was not measured in this case.
> - **The offsets from the literature are not attributed.** The finite blockage (3.33%) and the compressibility at `M=0.05` are the candidates; no domain or Mach-number sweep was run.
> - **The constant-density (incompressible) formulation is not covered.** The constant-density input for this case diverges in the current build, so only the compressible formulation produced a result.
> - Results apply to one Reynolds number (`Re_D=100`), one mesh, and one time-integration scheme.

This case shows that the compressible PBNS solver captures the frequency, mean drag, and lift amplitude of laminar vortex shedding at `Re_D=100` to within 1.5% of the literature values on one mesh. It establishes a baseline for this condition, not an absolute accuracy guarantee.

18.10 References

- Williamson, C. H. K., "Defining a Universal and Continuous Strouhal–Reynolds Number Relationship for the Laminar Vortex Shedding of a Circular Cylinder," *Physics of Fluids*, 31(10), 1988, pp. 2742–2744.
- Henderson, R. D., "Details of the Drag Curve near the Onset of Vortex Shedding," *Physics of Fluids*, 7(9), 1995, pp. 2102–2104.
- Williamson, C. H. K., "Vortex Dynamics in the Cylinder Wake," *Annual Review of Fluid Mechanics*, 28, 1996, pp. 477–539.

Part VII

Airfoils & Wings

19 2D Transonic Airfoil — RAE2822 RANS Validation

Comparison of shock location and surface pressure distribution against the AGARD Case 6 experiment

19.1 Run Provenance and Artifacts

Item	Value
Wake CFD baseline version	`0.22.2`
Solver	DBNS
Compute device	CPU
Parallel execution	1 MPI rank
Arithmetic precision	FP64
Run date	2026-08-18

> **Note**
>
> Results depend on the solver build that produced them. Read every figure in this report together with the version and date above — re-running the same input on a later build may give different numbers.

19.1.1 Downloadable Files

Not available: standalone input decks and solver result files have not yet been published for download.

19.2 Validation Objective

For a transonic airfoil, small changes in conditions can substantially alter the shock location and lift. This case compares the surface pressure distribution of the widely used RAE2822 airfoil with experiment to establish the range over which Wake CFD reproduces two-dimensional transonic turbulent flow with a shock.

For users, this result supports review of airfoil pressure distributions, shock locations, and lift levels during early design. In particular, the default Roe scheme reproduces both the suction-side shock and lift level observed in experiment.

19.3 Reference Solution and Data

Item	Setting
Reference	AGARD AR-138 RAE2822 Case 6 pressure distribution and lift (`C_L=0.743`)

19.4 Simulation Conditions

Item	Setting
Geometry	RAE2822 2D airfoil
Analysis	Steady, compressible RANS
Freestream Mach	`0.729`
Angle of attack	`2.31°`
Reynolds number	`Re_c=6.5×10^6`
Reference temperature	`288.15 K`

This setup uses the free-air-corrected condition for AGARD Case 6. The Case 9 pressure data in the same data set use a different angle of attack and lift level, and therefore are not compared directly with the Case 6 result. Checking the case number for both conditions and experimental data is essential when reproducing this case.

19.5 Mesh

Item	Setting
Mesh	2D C-mesh, 192 points on the airfoil surface

The baseline mesh is a 2D C-mesh with 192 points on the airfoil surface, comprising 13,937 nodes and 22,842 elements. The airfoil surface and near field where the shock forms are refined, with progressively coarser spacing toward the farfield.

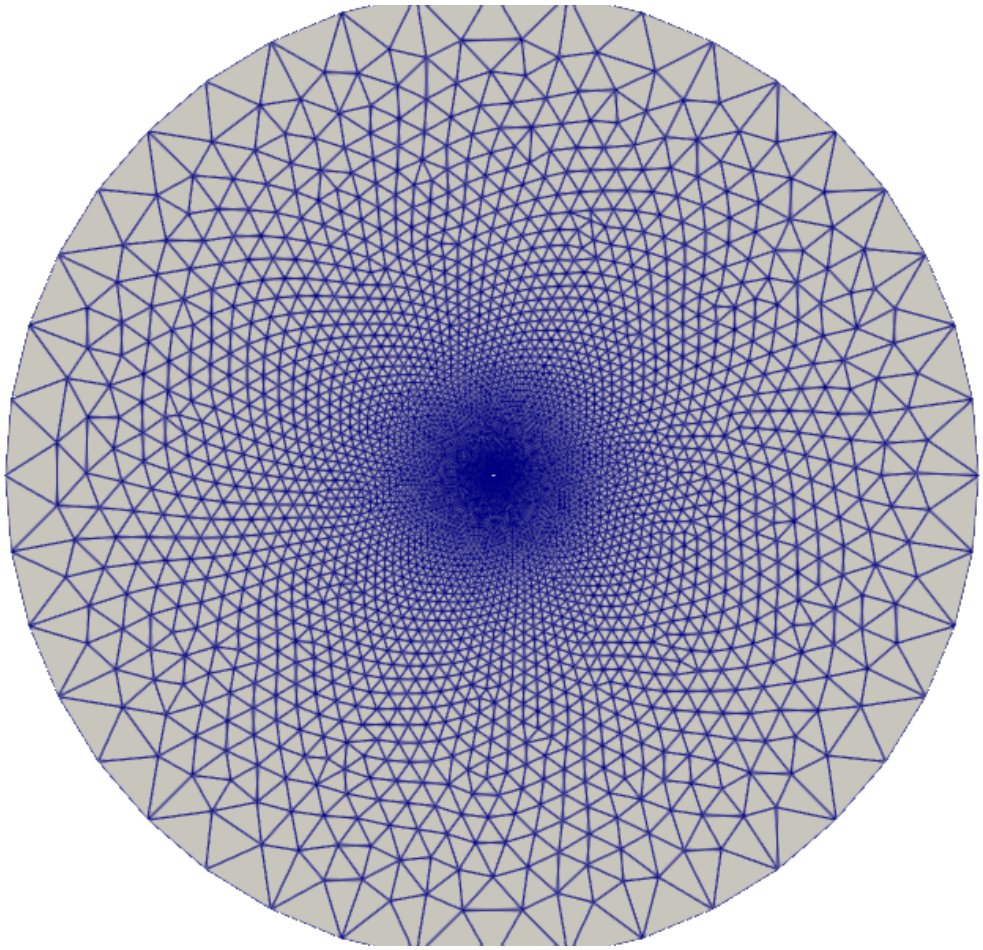


Figure 19.1: Full domain of the RAE2822 Case 6 baseline C-mesh

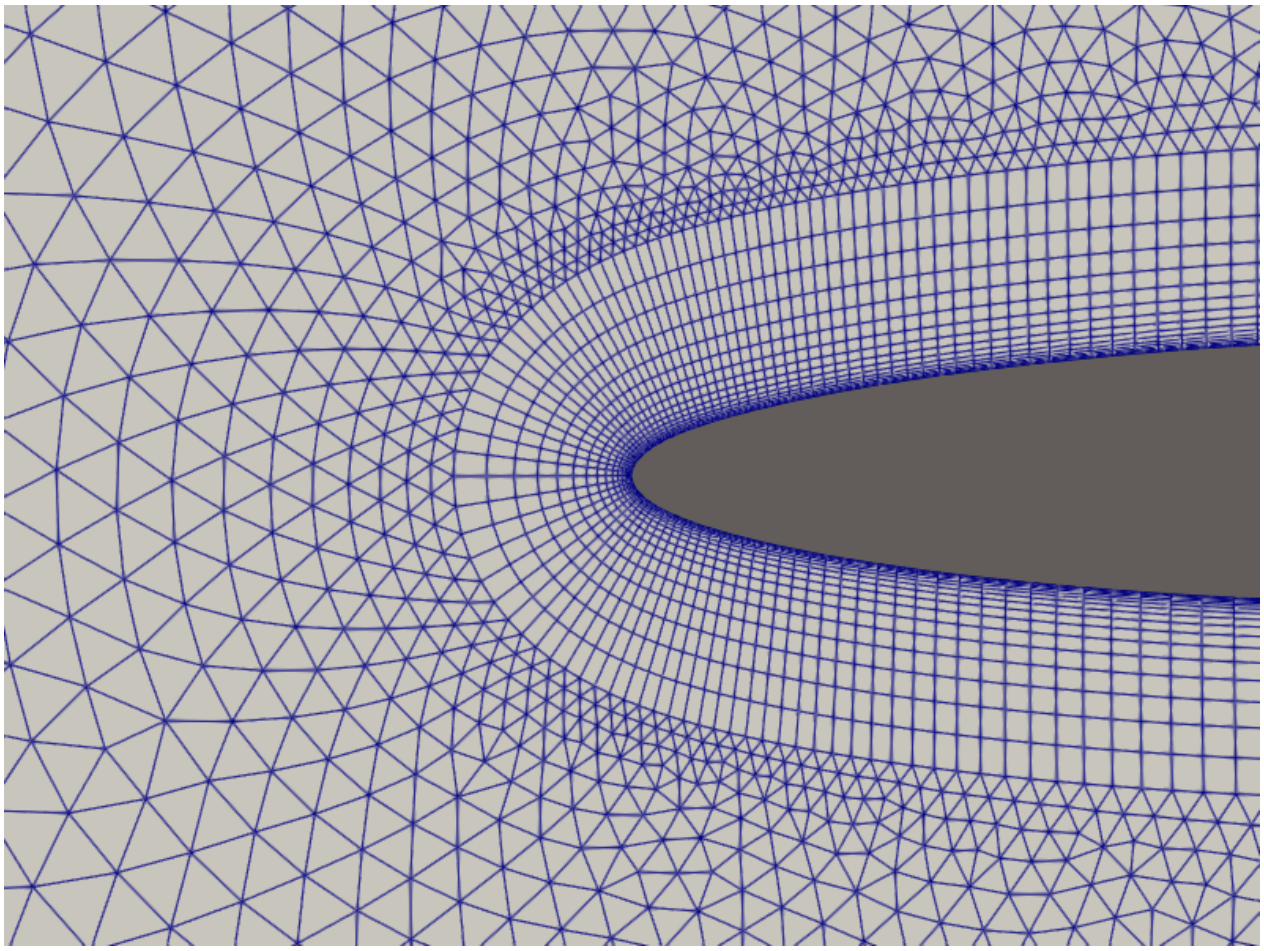


Figure 19.2: Leading-edge region of the RAE2822 Case 6 baseline C-mesh

19.6 Boundary and Initial Conditions

N/A: Detailed boundary and initial conditions are not documented for this case.

19.7 Numerical Methods

Item	Setting
Turbulence model	Spalart–Allmaras (SA)
Convective schemes	Roe, HLLC, JST, AUSM+up, AUSM+up2, SLAU, SLAU2, and AUSM (compared below)

Time integration and convergence settings: Not reported.

19.8 Results

19.8.1 Key Results

The baseline Roe configuration converged in 4,697 iterations and predicted `C_L=0.7455`, a 0.3% difference from the Case 6 experimental value of `0.743`. The suction-side shock was also captured near the experimental location, `x/c` `0.55`.

The Mach contour shows the flow accelerating over the suction side to form a local supersonic region, followed by sharp compression near `x/c` `0.55`. The pressure-coefficient contour likewise shows a distinct pressure recovery at the same location, consistent with the shock location identified in the surface pressure comparison.

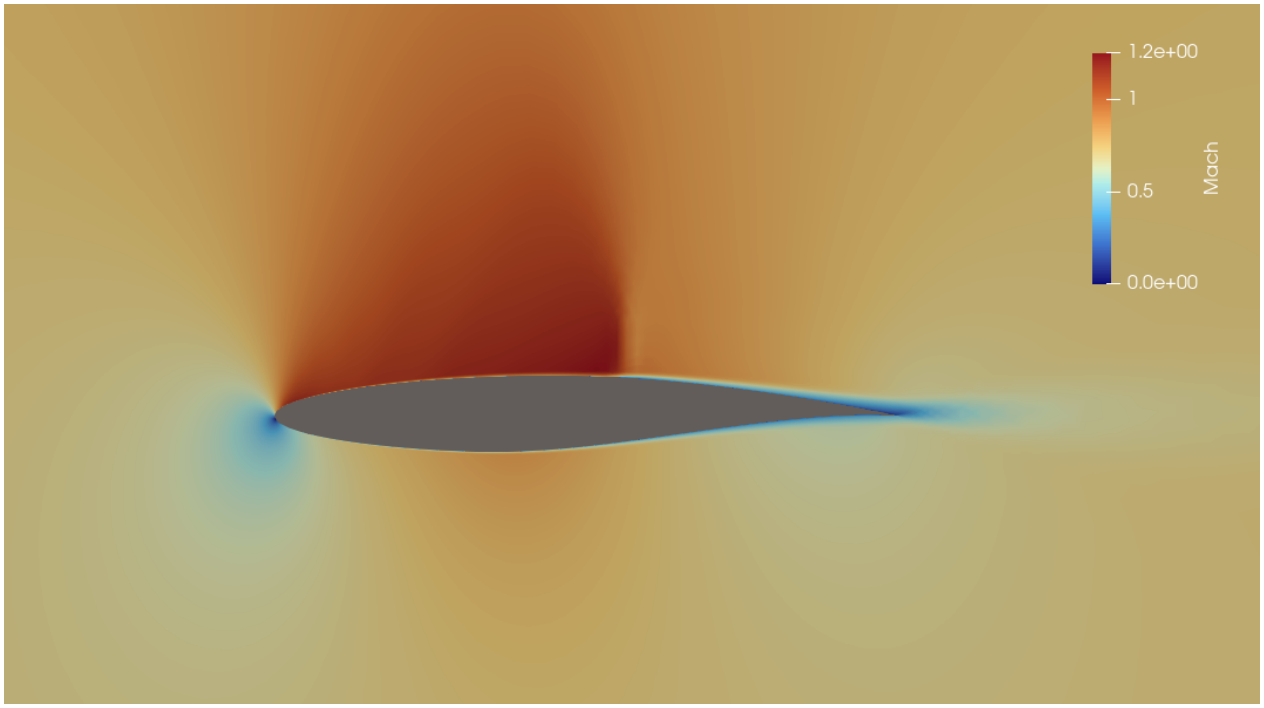


Figure 19.3: RAE2822 Case 6 — Roe-scheme Mach contour

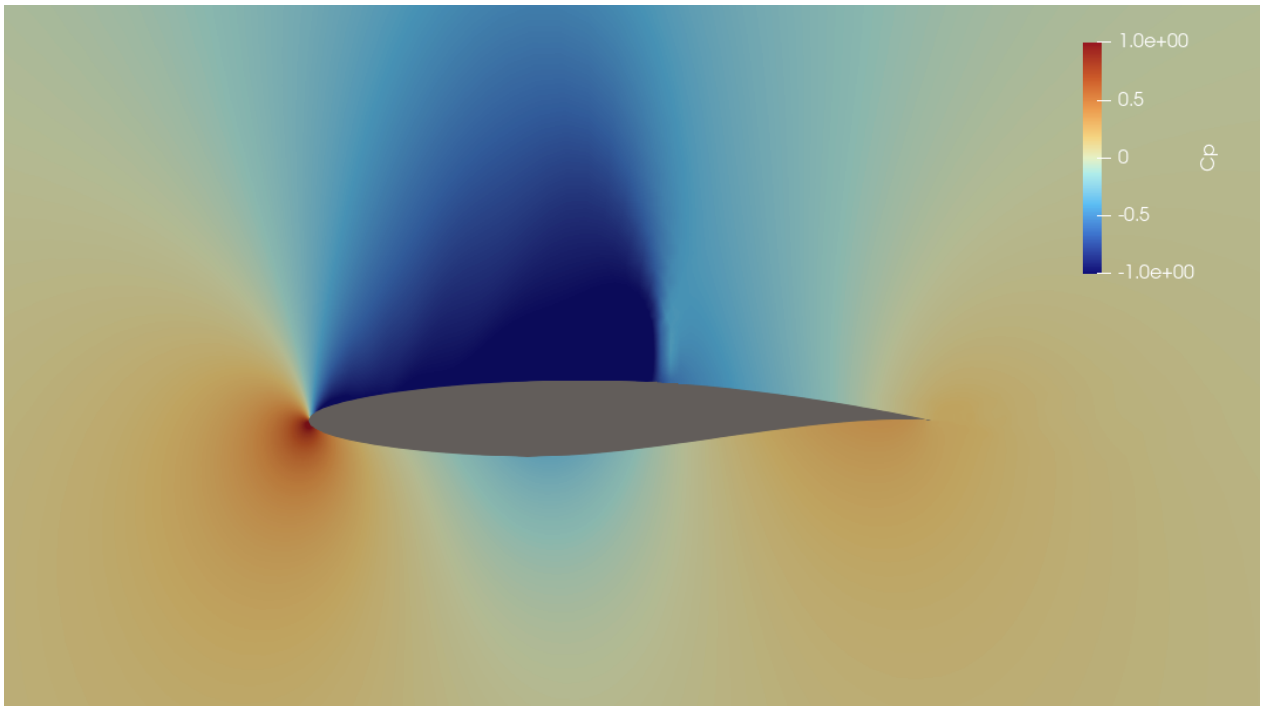


Figure 19.4: RAE2822 Case 6 — Roe-scheme pressure-coefficient contour

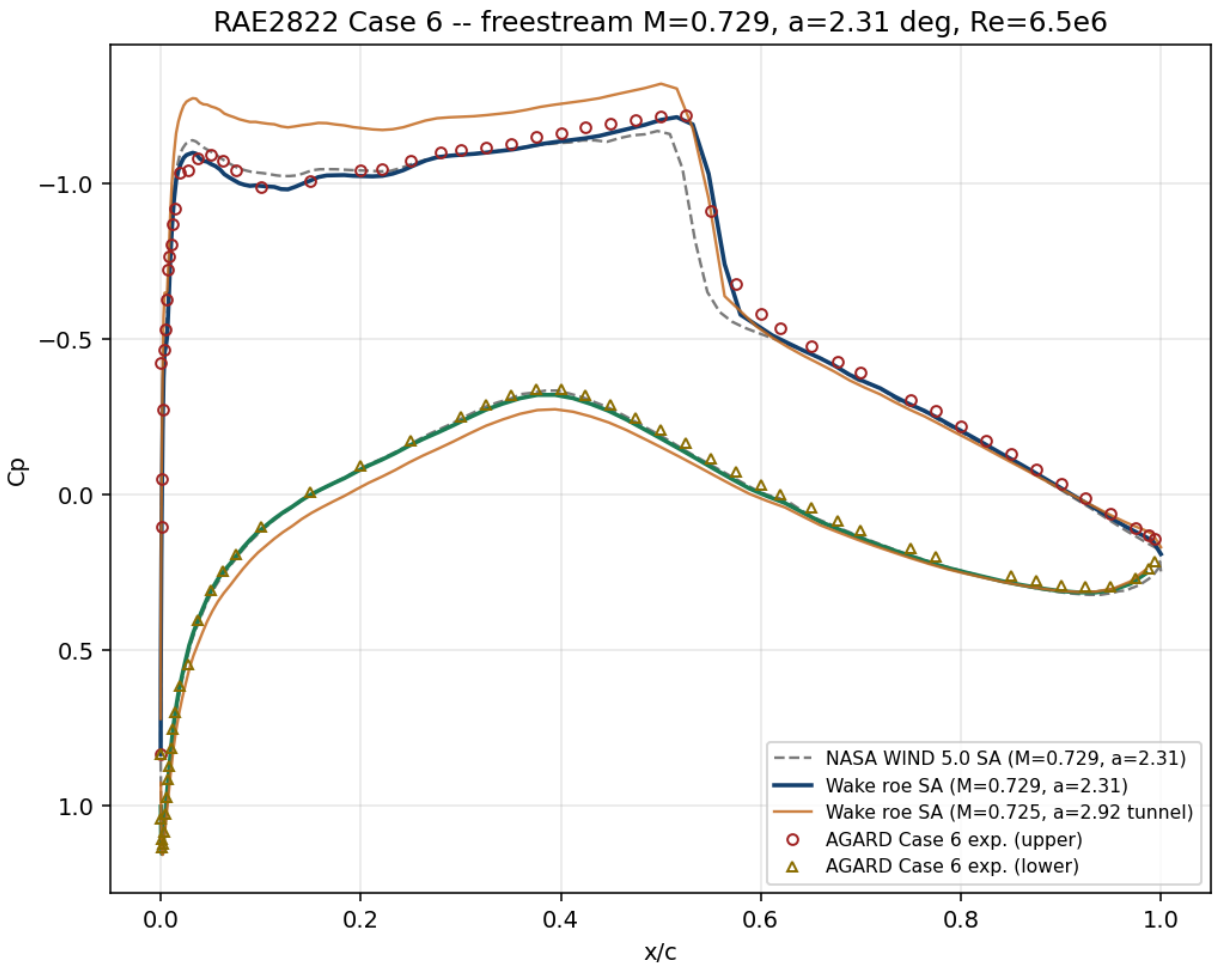


Figure 19.5: RAE2822 Case 6 — comparison of Wake CFD Roe results with AGARD experiment and NASA WIND 5.0 SA results

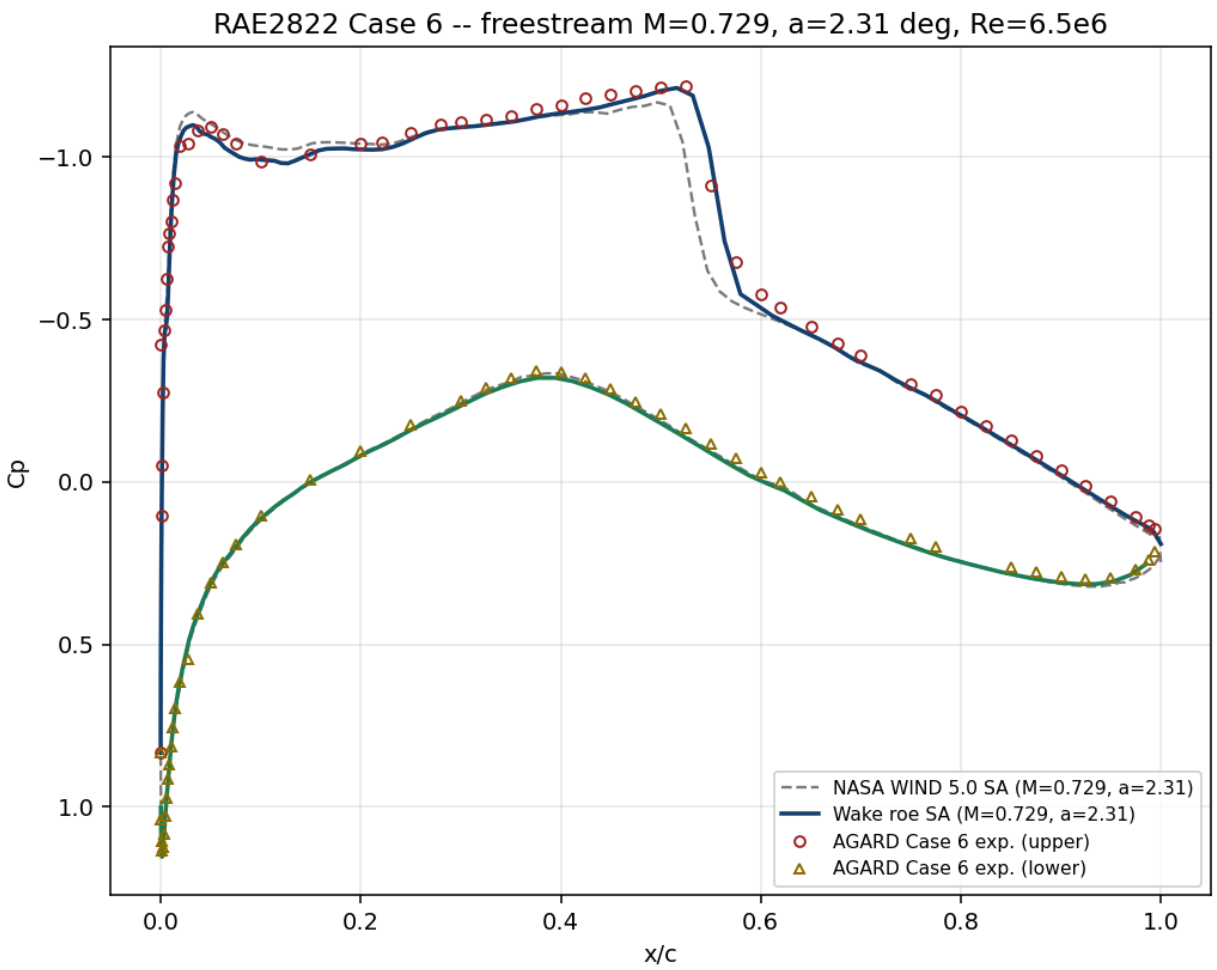


Figure 19.6: RAE2822 Case 6 — surface pressure-coefficient distribution from the Roe scheme, compared with experiment and NASA WIND

The pressure-distribution shape on both sides of the shock and the pressure recovery agree well overall with the experimental points. Because interpolation near the sharp leading-edge pressure variation can make RMS error appear large, this case considers shock location, pressure-distribution shape, and lift coefficient together.

19.8.2 Comparisons for Scheme Selection

Only the convective scheme was varied while keeping the mesh and turbulence model fixed. The pressure distribution is reproduced similarly by several schemes, but reaching the target convergence is as important as accuracy in practice.

Scheme	Lift coefficient	Iterations	Convergence status	Assessment
Roe	0.7455	4,697	Converged	Default choice
HLLC	0.7471	4,693	Converged	Roe alternative

Scheme	Lift coefficient	Iterations	Convergence status	Assessment
JST	0.7266	5,205	Converged	Usable
AUSM+up	0.7564	4,663	Converged	Usable
AUSM+up2	0.7383	4,712	Converged	Usable
SLAU / SLAU2	0.7404 / 0.7385	20,000	Residual stagnation*	Further tuning required
AUSM	0.7589	20,000	Leading-edge oscillation	Not recommended

* The pressure distribution and force coefficients stabilized, but the specified residual-reduction criterion was not reached.

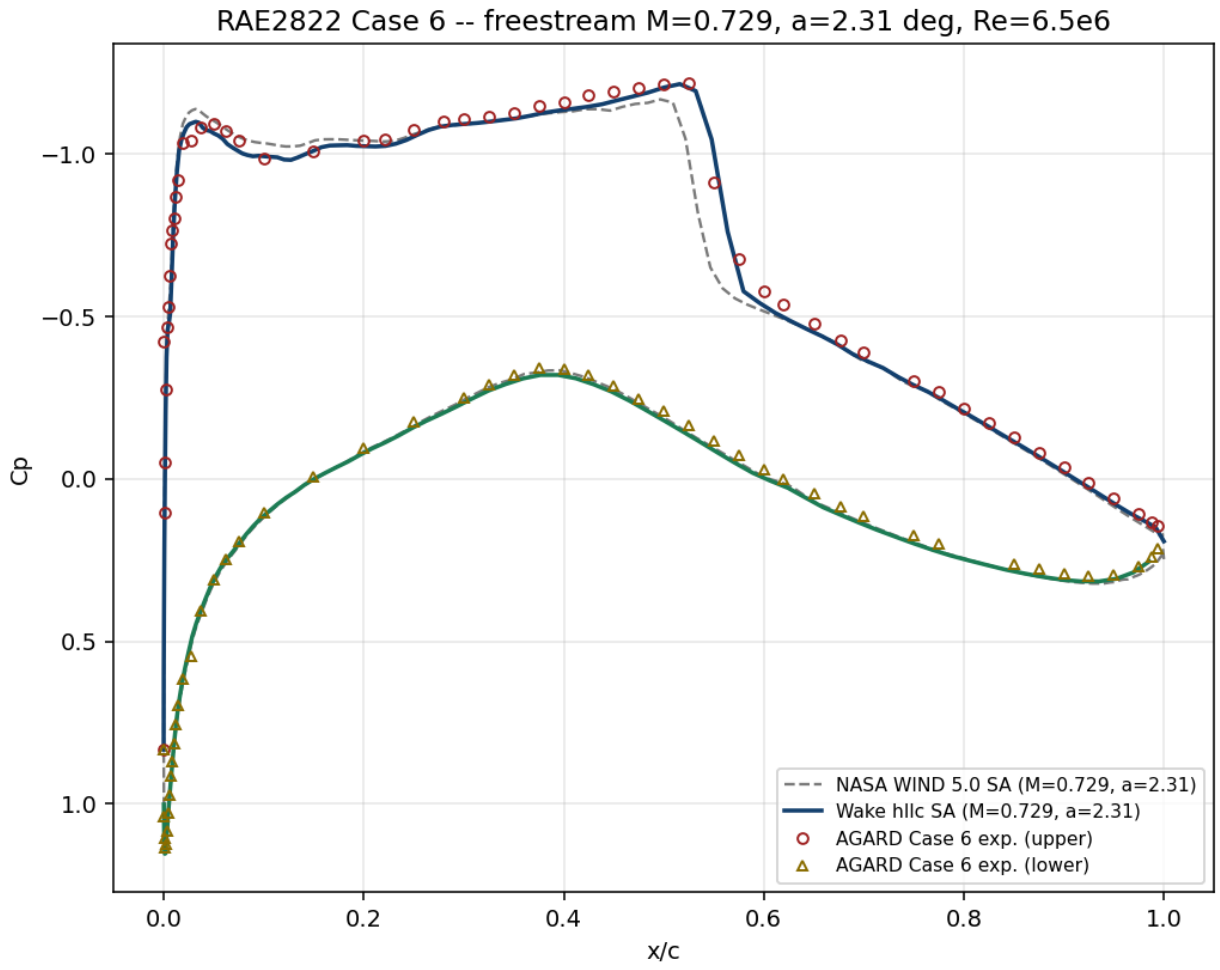


Figure 19.7: RAE2822 Case 6 — surface pressure-coefficient distribution with HLLC

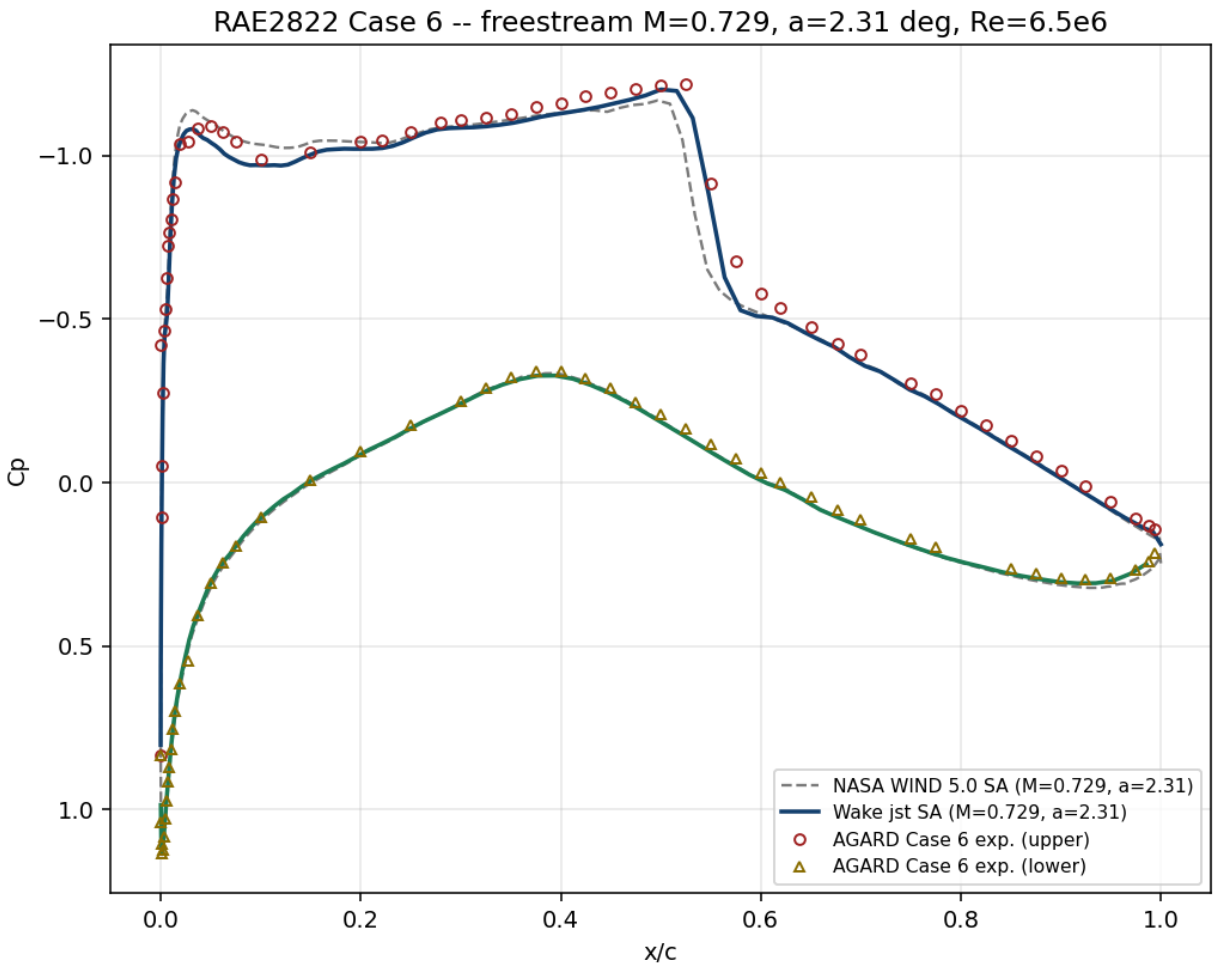


Figure 19.8: RAE2822 Case 6 — surface pressure-coefficient distribution with JST

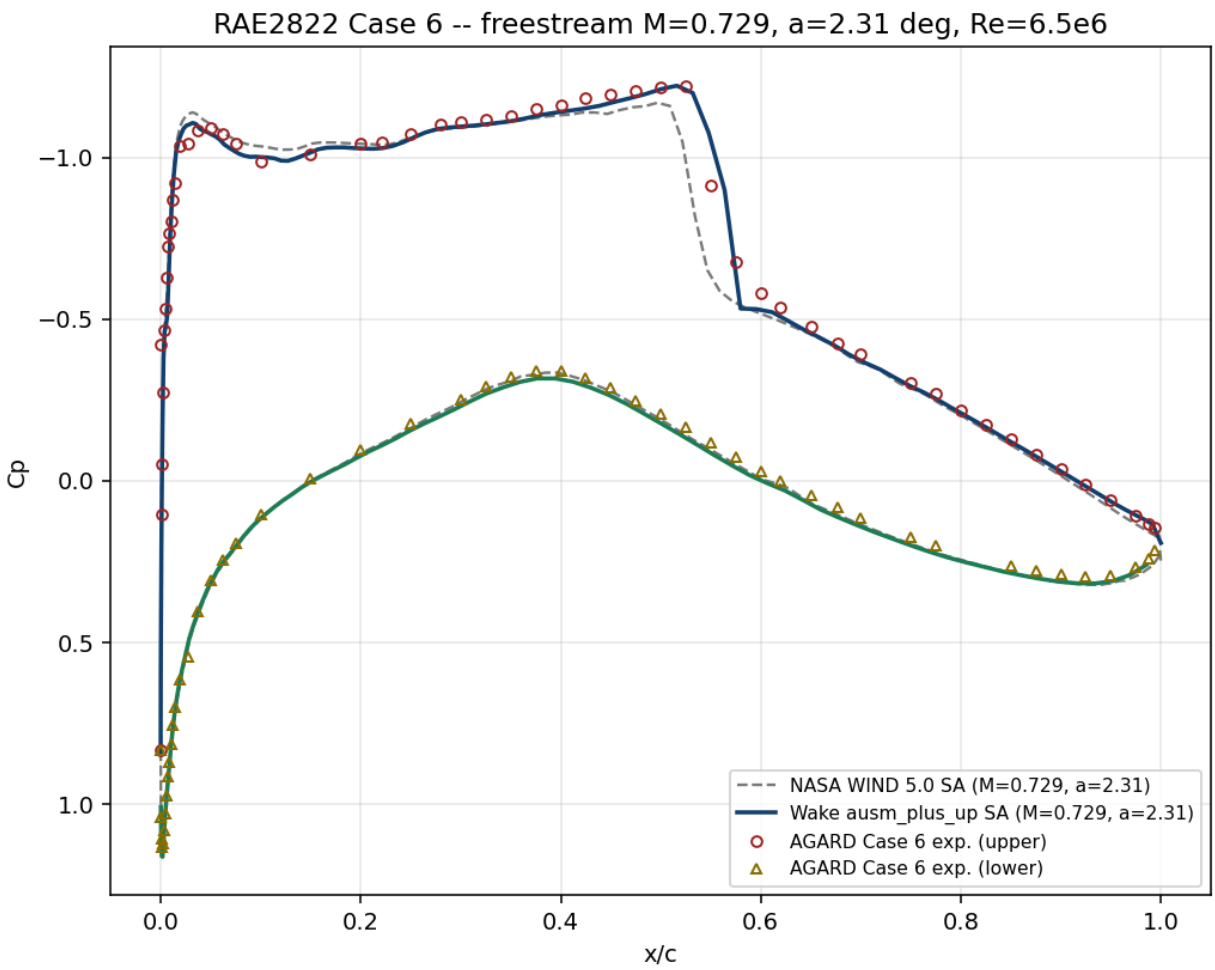


Figure 19.9: RAE2822 Case 6 — surface pressure-coefficient distribution with AUSM+up

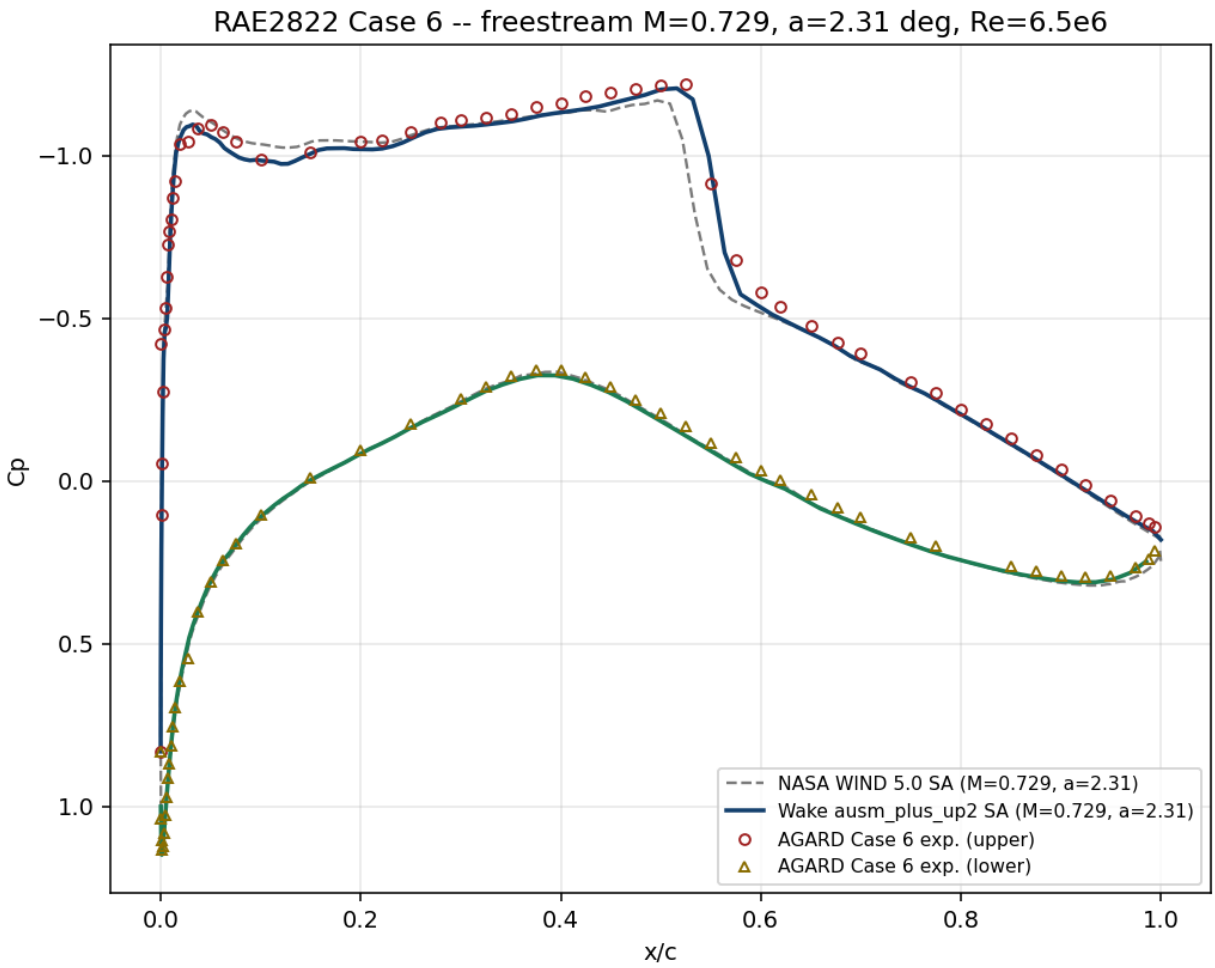


Figure 19.10: RAE2822 Case 6 — surface pressure-coefficient distribution with AUSM+up2

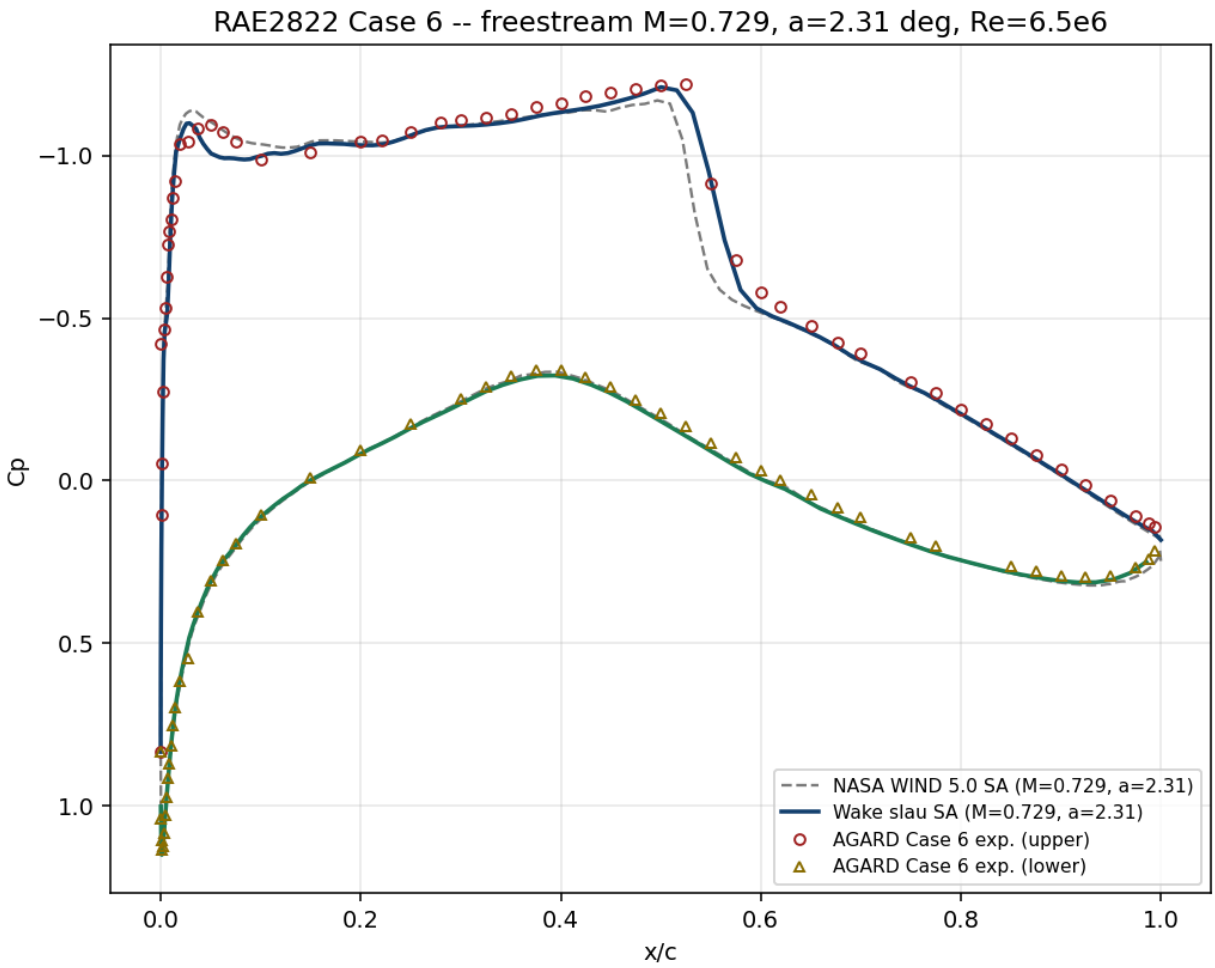


Figure 19.11: RAE2822 Case 6 — surface pressure-coefficient distribution with SLAU

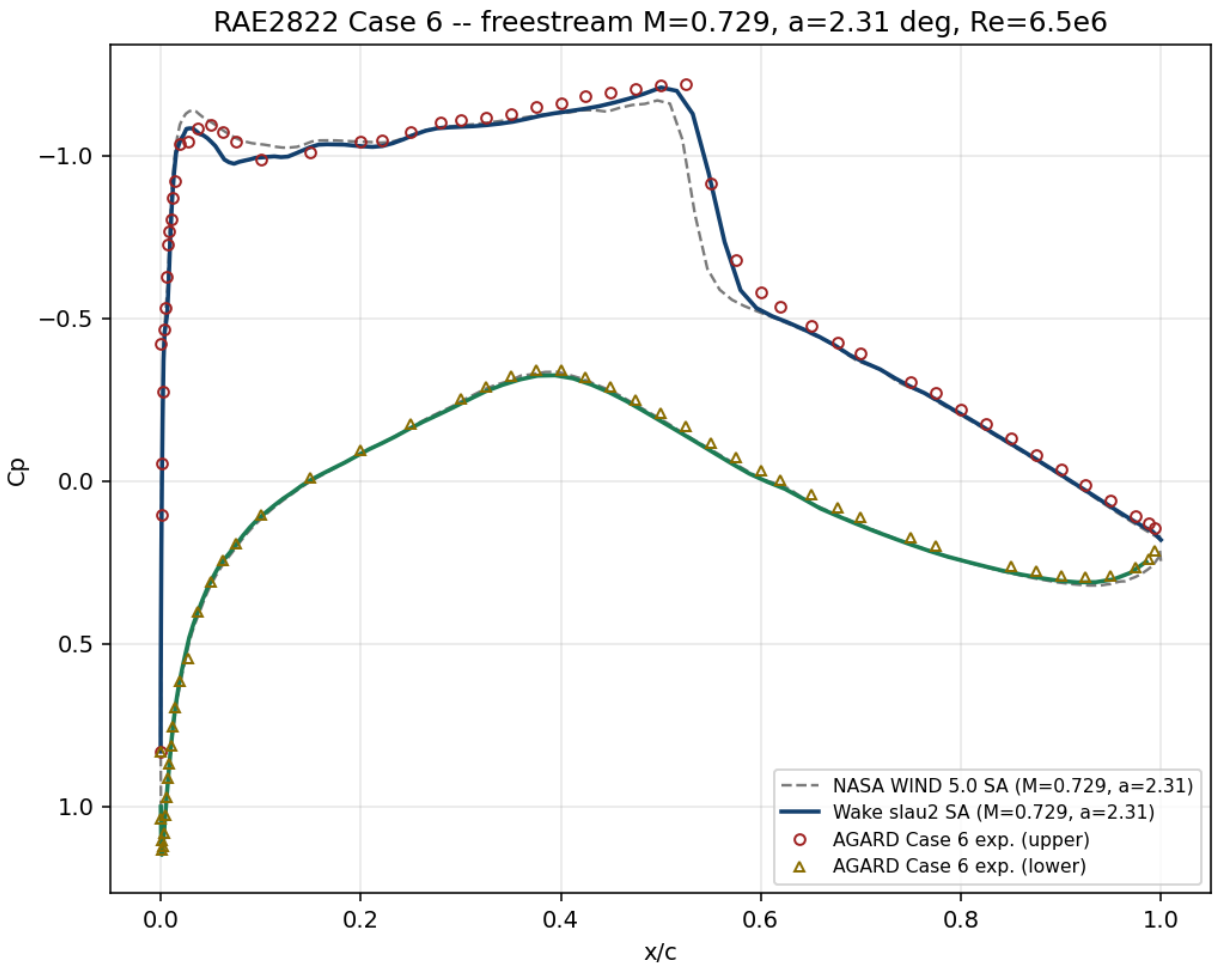


Figure 19.12: RAE2822 Case 6 — surface pressure-coefficient distribution with SLAU2

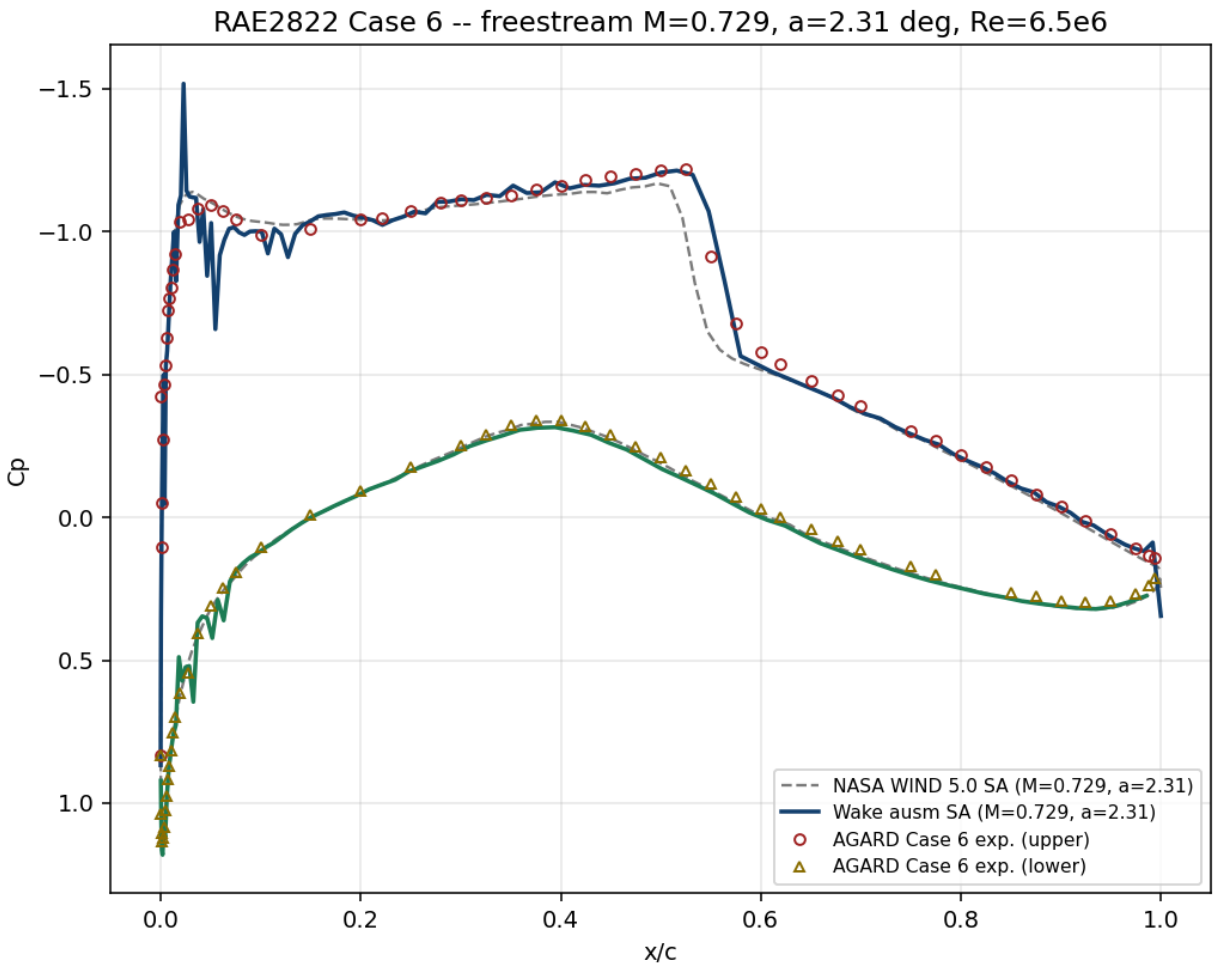


Figure 19.13: RAE2822 Case 6 — surface pressure-coefficient distribution with AUSM

19.9 Conclusions and Applicable Scope

- **Roe** is recommended as the default scheme for this condition. It gives the closest lift to experiment and reaches the specified convergence criterion robustly.
- If an alternative is required, consider **HLLC**, **JST**, **AUSM+up**, or **AUSM+up2**. All reproduced the shock and pressure distribution stably in this case.
- Plain **AUSM** produced leading-edge pressure oscillations. **SLAU/SLAU2** did not reach the target residual without additional CFL or linear-solver tuning.
- This result validates one airfoil, one Reynolds number, and a two-dimensional steady RANS condition. It does not guarantee the same accuracy for a real three-dimensional wing, transition or separation, unsteady buffet, other turbulence models, or other mesh quality.

19.10 References

- Cook, P. H., McDonald, M. A., Firmin, M. C. P., *Aerofoil RAE 2822 — Pressure Distributions, and Boundary Layer and Wake CFD Measurements*, AGARD AR-138, 1979.
- NASA NPARC Alliance RAE2822 Verification & Validation Archive

20 2D NACA0012 Airfoil — SA RANS Polar Validation

Lift, drag, and stall behavior against wind-tunnel data (Ladson/Abbott), with code-to-code agreement against NASA TMR CFL3D-SA in the attached-flow range

20.1 Run Provenance and Artifacts

Item	Value
Wake CFD baseline version	`0.22.2`
Solver	DBNS
Compute device	GPU (NVIDIA RTX A6000)
Parallel execution	1 MPI rank
Arithmetic precision	FP64
Run date	2026-09-09

> **Note**
>
> Results depend on the solver build that produced them. Read every figure in this report together with the version and date above — re-running the same input on a later build may give different numbers.

20.1.1 Downloadable Files

Not available: standalone input decks and solver result files have not yet been published for download.

20.2 Validation Objective

The NACA0012 airfoil is one of the most widely used cases for validating RANS turbulence models, in part because the NASA Turbulence Modeling Resource (TMR) publishes both curated wind-tunnel data (Ladson; Abbott & von Doenhoff) and matched-condition Spalart–Allmaras (SA) computations from the established CFL3D code. This case reproduces the NACA0012 lift/drag polar

with Wake CFD's SA implementation on a TMR-family mesh, and checks two different things at once:

- **Code-to-code agreement with CFL3D-SA** in the linear, attached-flow range, where two independent RANS codes solving the same equations on comparable meshes should agree closely if both are implemented correctly.
- **Agreement with experiment** (Ladson, Abbott & von Doenhoff) across the full angle-of-attack range, including lift-curve slope, maximum lift, and stall.

For users, this result supports confidence in Wake CFD's SA implementation for conventional 2D lift/drag prediction in attached flow, and documents the size and direction of the expected error near and beyond stall.

20.3 Reference Solution and Data

Item	Setting
Reference (linear range)	CFL3D-SA, NASA TMR (code-to-code)
Reference (full range)	Ladson (NASA TM-4074, 80/120/180-grit trip) and Abbott & von Doenhoff (untripped), wind-tunnel experiment

20.4 Simulation Conditions

Item	Setting
Geometry	NACA0012 2D airfoil, chord `c=1`
Analysis	Steady, compressible DBNS, RANS
Freestream Mach	`0.15`
Reynolds number	`Re_c=6.0×10^6`
Angle of attack	`-10°` to `19°`, 20 points

Constant viscosity is used in place of Sutherland's law so that `Re_c` matches the target value exactly, following the same practice as other Wake CFD TMR verification cases.

20.5 Mesh

Item	Setting
Mesh	2D structured mesh, NASA TMR NACA0012 family (single-cell-thick 2D extraction of the 3D family used in TMR's grid-convergence study); primary grid `897×257`, spot-checked against `449×129` at `AoA=0°, 10°, 15°`

20.6 Boundary and Initial Conditions

N/A: Detailed boundary and initial conditions are not documented for this case.

20.7 Numerical Methods

Item	Setting
Turbulence model	Spalart–Allmaras, `standard/ft2=true` ("classic" SA, matching the CFL3D convention used by TMR)
Convective scheme	Roe (default entropy fix)
Spatial accuracy	Second order, no limiter
Gradient reconstruction	Green–Gauss
Nonlinear control / preconditioner	HANIM (adaptive nonlinear control) with a Jacobi linear-solver preconditioner
Convergence criterion	Cauchy-window monitor on `CD` (`eps=1e-6` over a `1000`-iteration window), `max_iter=40000`

20.8 Results

20.8.1 Linear Range (`-10°` to `10°`)

Wake CFD's lift-curve slope lies on top of both the CFL3D-SA point and the Ladson/Abbott experimental scatter over the full linear range.

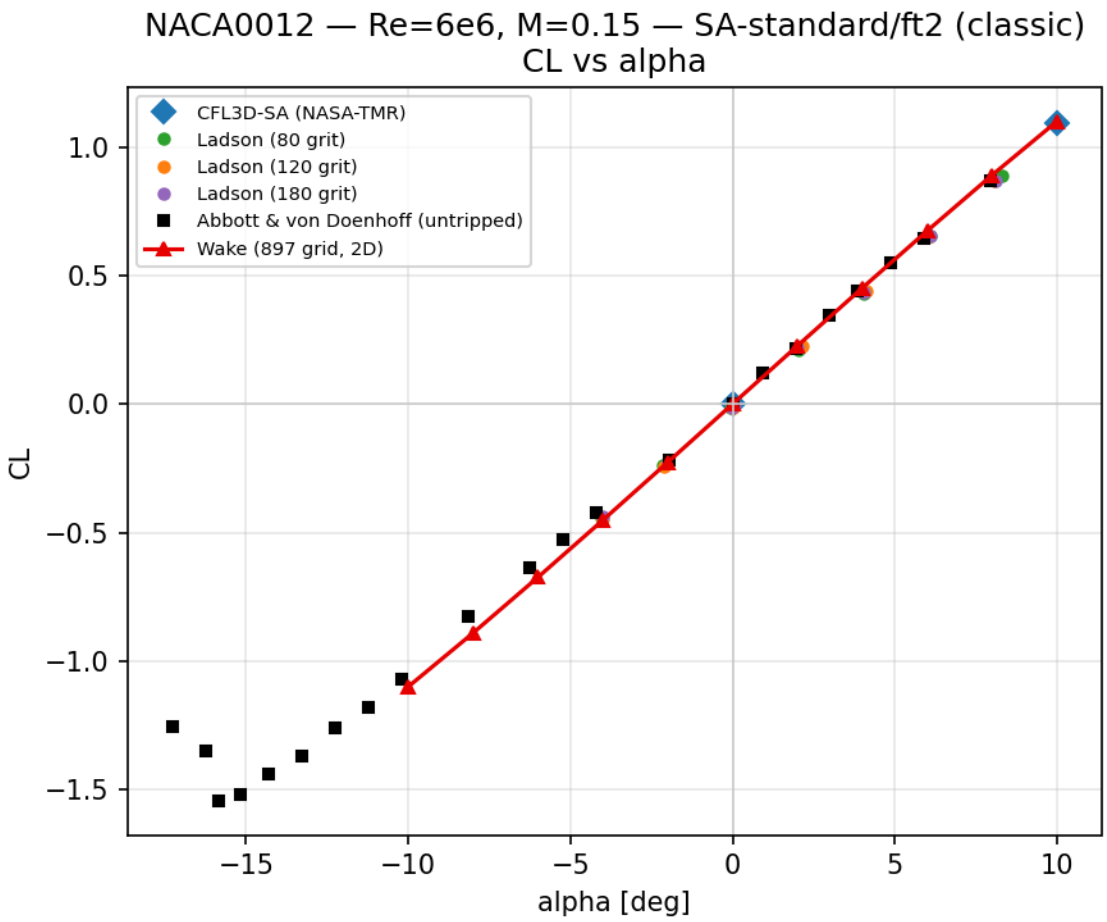


Figure 20.1: NACA0012, `Re_c=6×10^6`, `M=0.15`: `CL` vs `alpha`, linear range

Drag is compared on an expanded axis (`5`-count ticks) to make small differences visible:

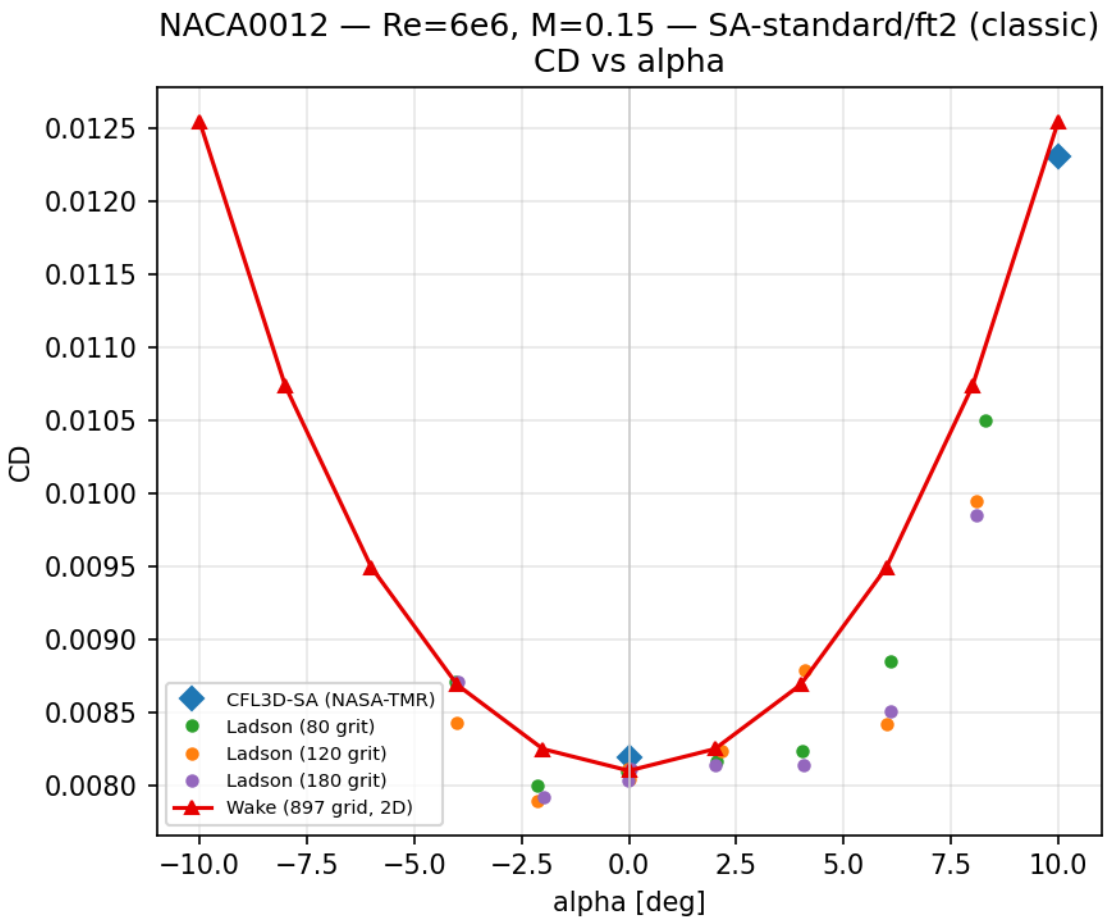


Figure 20.2: NACA0012, `Re_c=6×10^6`, `M=0.15`: `CD` vs `alpha`, linear range

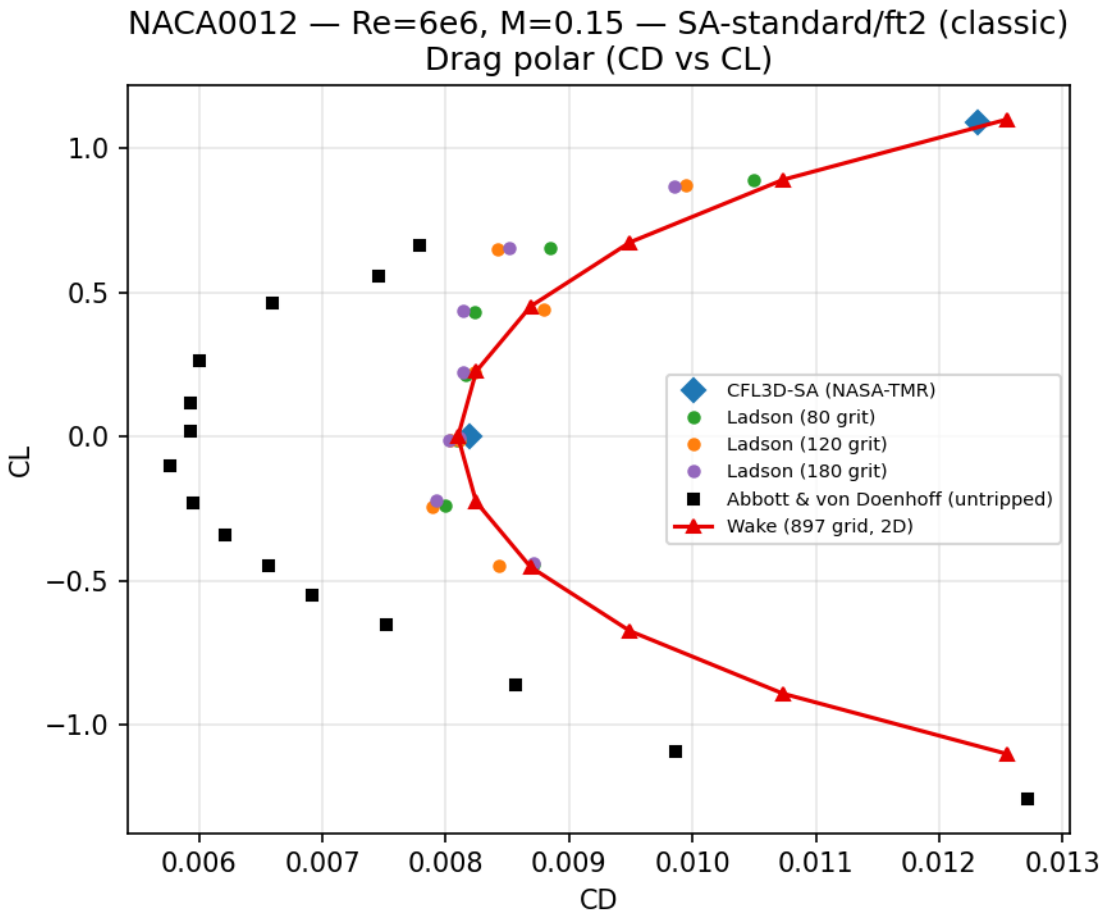


Figure 20.3: NACA0012, `Re_c=6×10^6`, `M=0.15`: drag polar, linear range

A direct CFL3D-SA comparison for these angles is given together with `15°` in the next section (**Near and Beyond Stall**), since the trend across all three points is easier to read as one table.

Left–right symmetry was also checked directly: `CD` at `±2°, ±4°, ±6°, ±8°, ±10°` on the `897×257` mesh agrees to within `0.01` count between positive and negative angle of attack, confirming correct handling of the rotation and force-projection convention.

20.8.2 Near and Beyond Stall (11° to 19°)

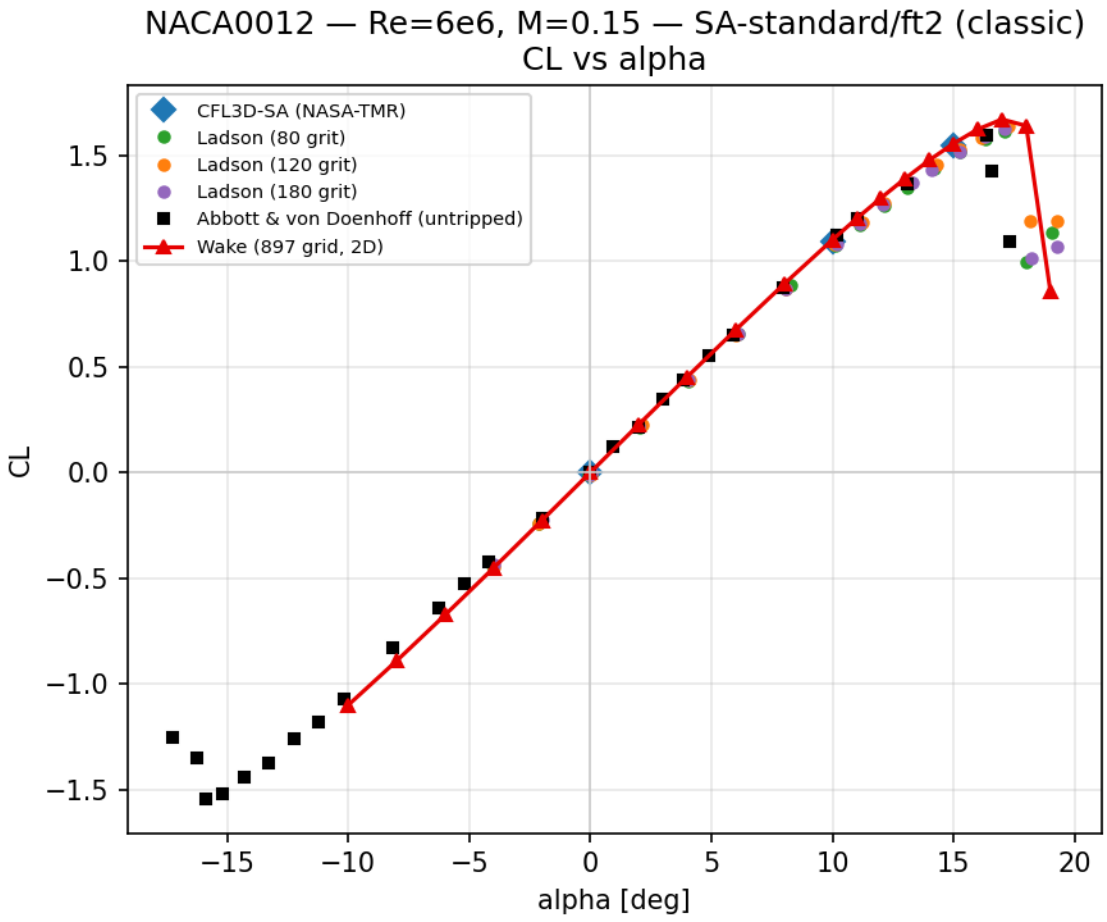


Figure 20.4: NACA0012, `Re_c=6×10^6`, `M=0.15`: `CL` vs `alpha`, full range including stall

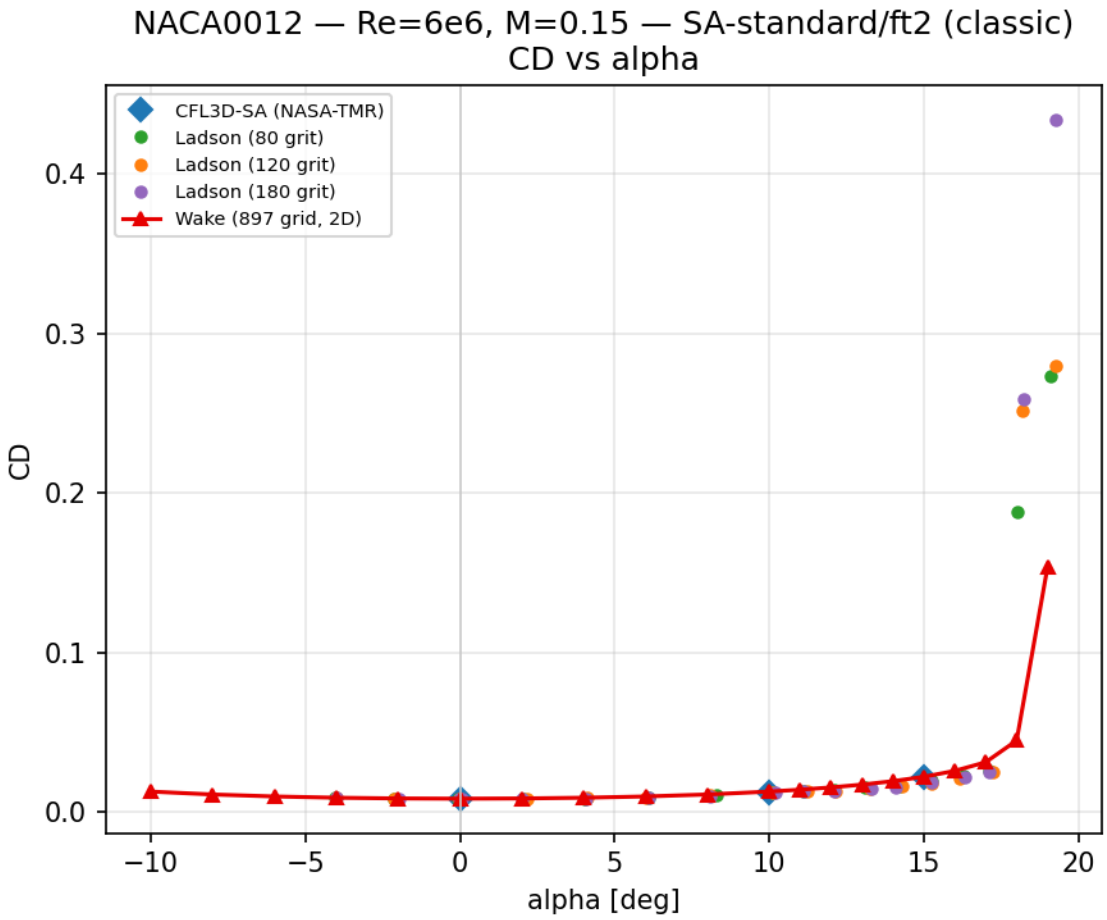


Figure 20.5: NACA0012, `Re_c=6×10^6`, `M=0.15`: `CD` vs `alpha`, full range including stall

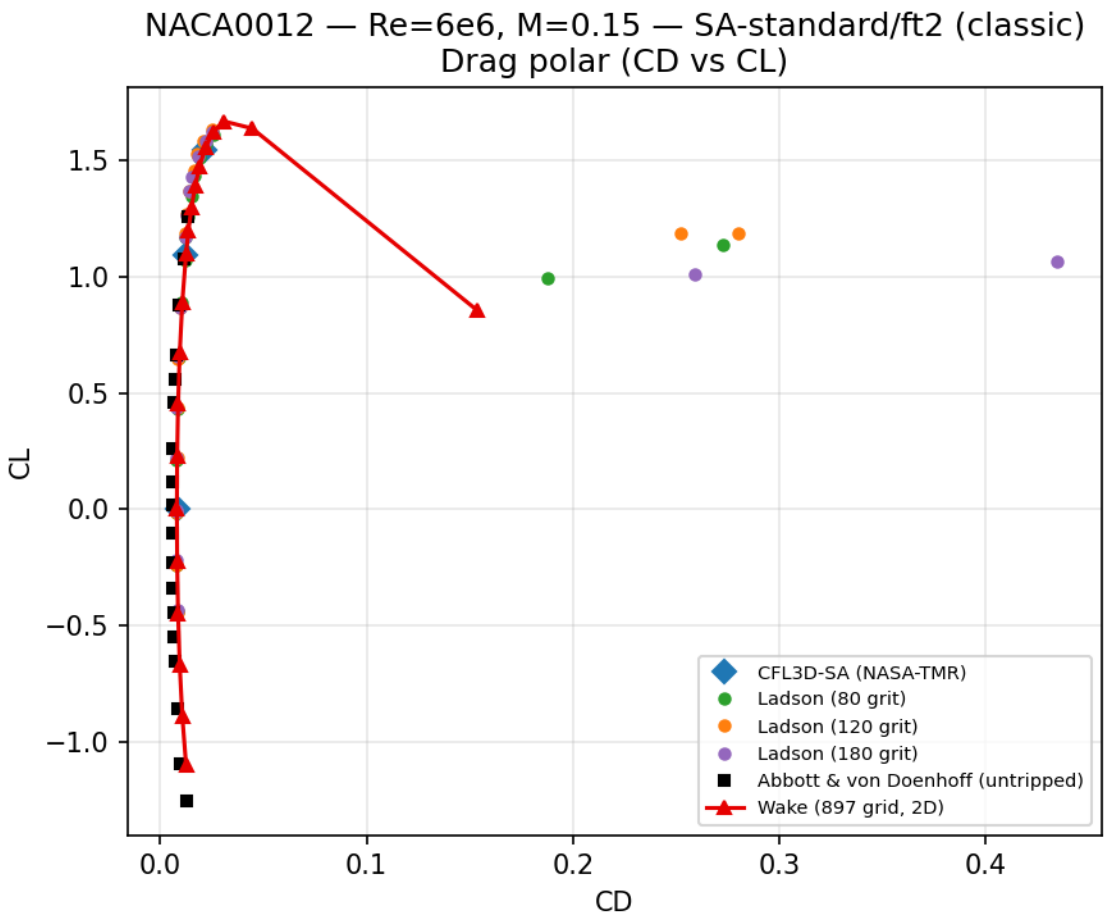


Figure 20.6: NACA0012, `Re_c=6×10^6`, `M=0.15`: drag polar, full range including stall

Wake CFD reaches `CL_max=1.669` at `AoA=17°`. The experimental references (Ladson 80-grit, Abbott & von Doenhoff untripped) peak about `1°–2°` earlier, near `15°–16°`, at `CL_max` `1.5–1.6`. Drag shows the same pattern: Wake CFD's drag rise beyond stall is real but softer and later than the experimental rise. This is the well-documented tendency of steady RANS with a one-equation turbulence model (SA) to delay separation and over-predict `CL_max` — it is not specific to this solver.

The CFL3D-SA code-to-code comparison covers `AoA=0°, 10°` (linear range) and extends one point further, to `AoA=15°` — still attached, just before the stall break at `17°`:

`AoA`	CFL3D-SA `CD` (counts)	Wake CFD `897×257` difference (counts)	Wake CFD `449×129` difference (counts)
`0°`	81.92	`-0.94`	`-1.40`
`10°`	123.11	`+2.40`	`+11.98`
`15°`	212.37	`+6.13`	`+32.47`

(1 count `= 0.0001` in `CD`.) On the primary `897×257` mesh, Wake CFD matches CFL3D-SA to within about `2.5` counts in the linear range, and the gap keeps growing smoothly with angle of attack out to

15° (−0.94 → +2.40 → +6.13 counts) rather than jumping suddenly — consistent with gradually approaching, but not yet inside, separated flow. The coarser 449×129 mesh shows a larger and faster-growing gap (−1.40 → +11.98 → +32.47 counts), consistent with that mesh being under-resolved relative to the primary grid rather than with a modeling error — grid convergence itself has not been established for this configuration (see **Applicable Scope**).

Two angle-of-attack/mesh combinations did not reach the specified convergence tolerance within 40000 iterations:

- 449×129 at AoA=0° — isolated to this single coarse-mesh/angle combination; the finer 897×257 mesh at the same angle converges normally, and the root cause has not yet been identified.
- 897×257 at AoA=18°, 19° — the two most deeply stalled points. Over the final 1000 iterations, CD oscillates within a bounded range (about 3 and 30 counts respectively) rather than diverging, consistent with genuinely unsteady separated flow that a steady solver cannot bring to a single fixed point.

20.8.3 Convergence History

CFL is controlled by HANIM (adaptive nonlinear control), so its history is reported alongside the residual for four representative cases spanning the sweep: an attached case (AoA=−10°), the baseline (AoA=0°), a pre-stall case (AoA=15°), and the deepest unconverged stall case (AoA=19°).

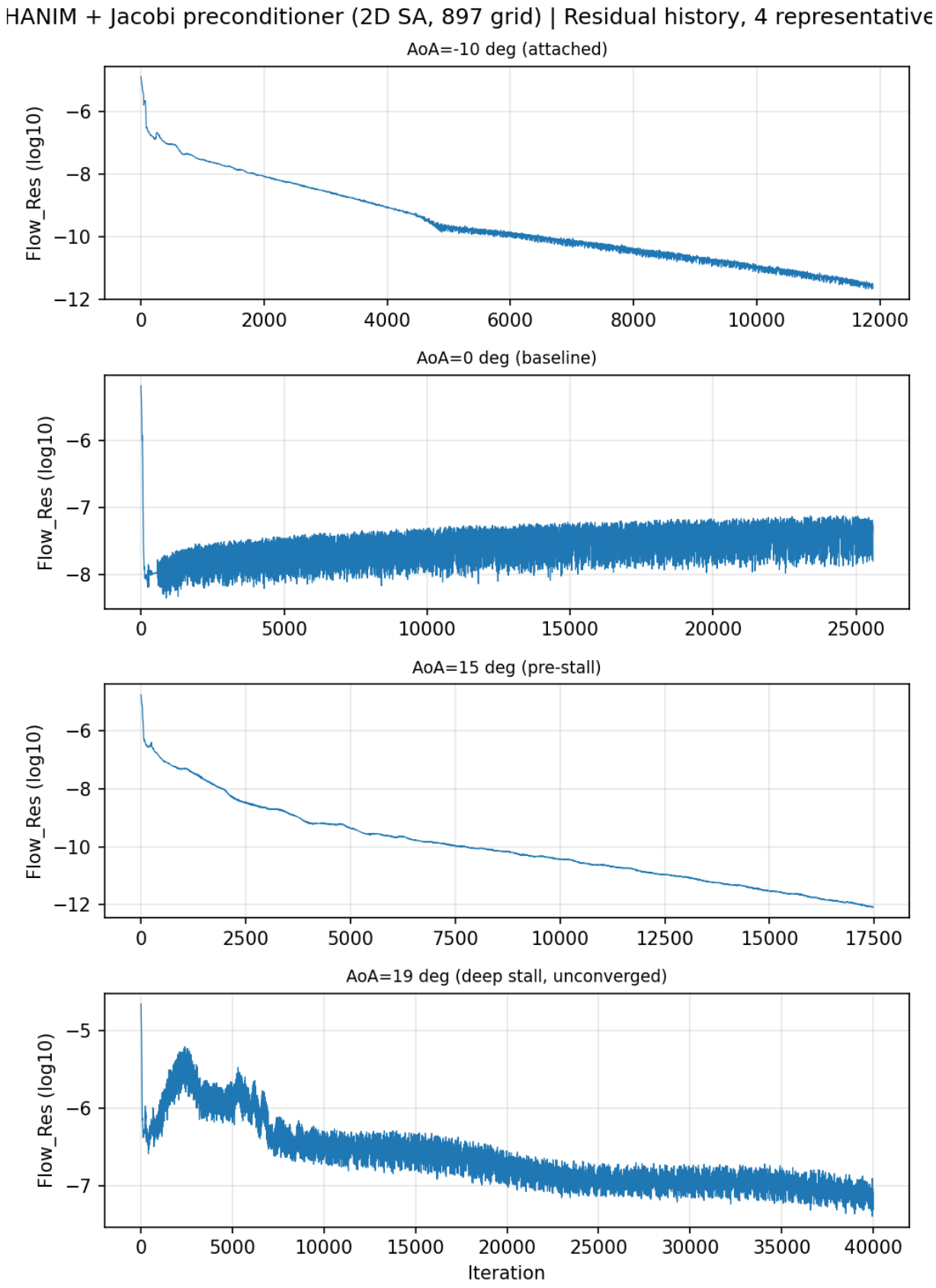


Figure 20.7: NACA0012, 897×257 grid: residual history for four representative angles of attack

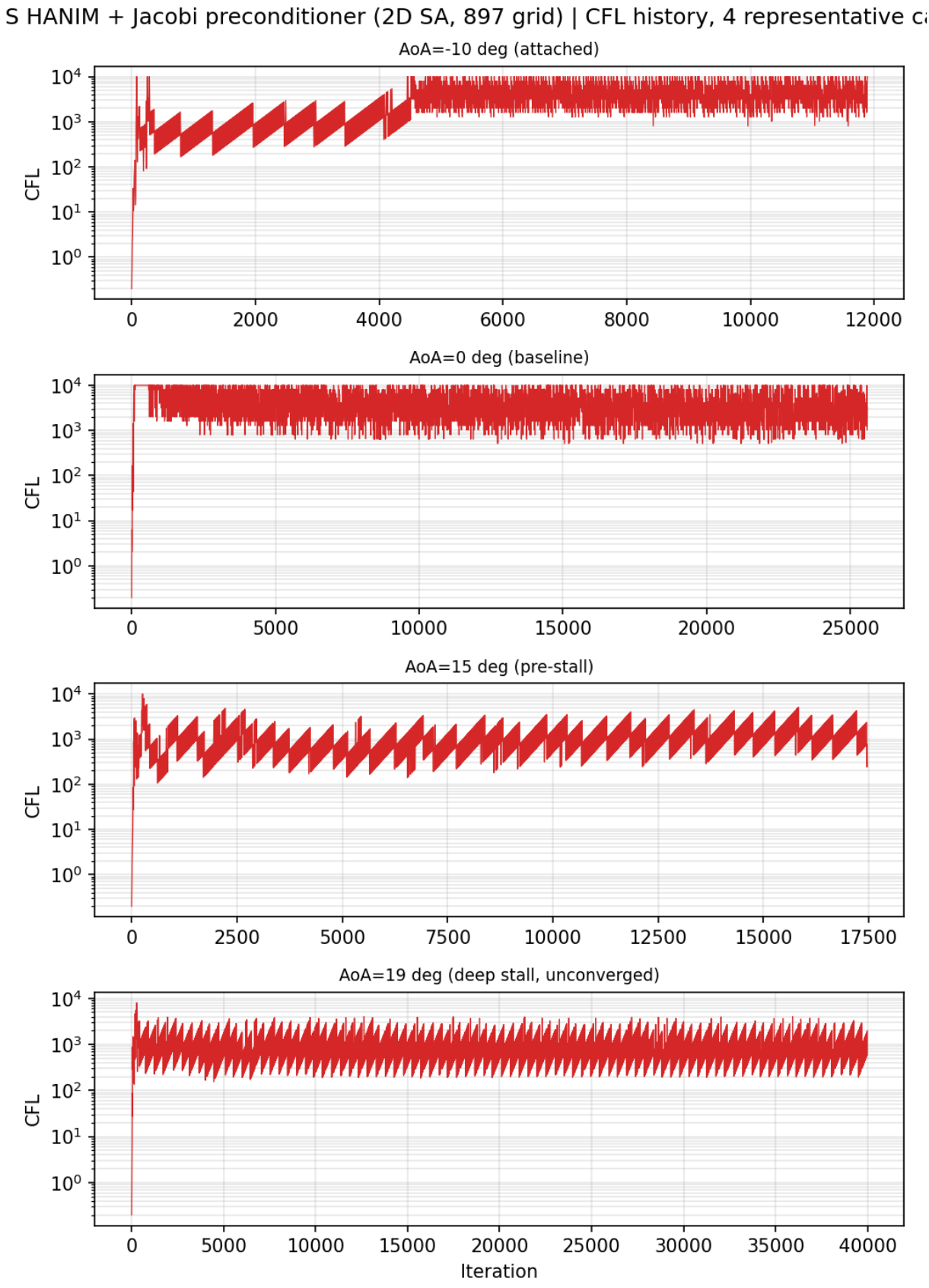


Figure 20.8: NACA0012, 897×257 grid: CFL history for four representative angles of attack

20.9 Conclusions and Applicable Scope

- Wake CFD with SA, the Roe scheme, no limiter, Green–Gauss gradients, and HANIM nonlinear control with a Jacobi preconditioner reproduces CFL3D-SA to within about `2.5` drag counts in attached flow (`-10°` to `10°`) on the primary `897×257` mesh, and matches the Ladson/Abbott lift-curve slope closely.
- Near and beyond stall, expect Wake CFD/SA to predict a `CL_max` roughly `5-10%` higher than experiment, `1°-2°` later in angle of attack, with a correspondingly delayed and softened drag rise — consistent with the known behavior of steady RANS with one-equation turbulence models, not a Wake CFD-specific defect.
- This case establishes 2D, steady RANS/SA performance at one Mach number and one Reynolds number on one mesh family. It does **not** by itself establish grid-converged accuracy — only two mesh densities were compared, and only at three angles of attack — and it does not cover 3D/finite-span effects, transition, or other turbulence models (SST is not covered by this case).
- The two non-converged points (`449×129/0°` and `897×257/18°-19°`) should be treated as open items rather than resolved behavior; see the run notes for follow-up.

20.10 References

- Rumsey, C.L., "2D NACA 0012 Airfoil Validation Case (Numerics)," NASA Turbulence Modeling Resource.
- Ladson, C.L., "Effects of Independent Variation of Mach and Reynolds Numbers on the Low-Speed Aerodynamic Characteristics of the NACA 0012 Airfoil Section," NASA TM-4074, 1988.
- Abbott, I.H., and von Doenhoff, A.E., *Theory of Wing Sections*, Dover Publications, 1959.

21 2D Airfoil Near-Wake — NASA TMR SA and SST Verification

Code-to-code grid-convergence verification of forces and near-wake profiles against CFL3D and FUN3D (Nakayama airfoil, 500-chord farfield)

21.1 Run Provenance and Artifacts

Item	Value
Wake CFD baseline version	`0.23.0`
Solver	DBNS
Compute device	GPU (NVIDIA RTX 4090)
Parallel execution	1 MPI rank
Arithmetic precision	Mixed
Run dates	2026-10-20

> **Note**
>
> Results depend on the solver build that produced them. Read every figure in this report together with the version and date above. The solver build used here included uncommitted changes to the `0.21.5` commit, so it cannot be reproduced exactly from the commit alone. Wall-friction results obtained with the `automatic` wall treatment on version `0.21.4` and earlier are not comparable with this report: they under-predicted skin friction on this mesh family and are excluded.

21.1.1 Downloadable Files

File	Description	Format
Force coefficients	`CL`, `CD`, `CDp`, `CDv` (drag in counts) for all 20 runs, with iteration counts, convergence flag, and the CFL3D and FUN3D values and differences	CSV

File	Description	Format
Near-wake minima	Minimum `u/U_inf` and minimum `u'v'/U_inf^2` at the seven wake stations for every run, with the CFL3D, FUN3D, and experimental values and differences	CSV

Standalone input decks and solver field files are not published for download.

21.2 Verification Objective

This case verifies Wake CFD against the NASA Turbulence Modeling Resource (TMR) 2D Airfoil Near-Wake verification case. The case is a code-to-code comparison on a family of five nested meshes, so the question is whether Wake CFD solves the SA and SST RANS equations the same way as the reference codes, not whether the models match the experiment. The quantities assessed are:

- lift, total drag, pressure drag, and viscous (friction) drag, `CL`, `CD`, `CDp`, `CDv`, and their convergence with mesh refinement
- minimum velocity and minimum turbulent shear stress in the near wake, at seven stations behind the trailing edge
- the effect of the second-order reconstruction parameter (U-MUSCL) on the coarse-mesh results

21.3 Reference Solution and Data

21.3.1 Numerical Reference

The references are the CFL3D (version 6.7, structured) and FUN3D solutions published by NASA TMR on the same five meshes, for the Spalart–Allmaras model (SA) and for the SST model. TMR provides forces versus mesh size, wake velocity and Reynolds-shear-stress profiles at `x/c = 1.01, 1.05, 1.20, 1.40, 1.80, 2.19, 3.00`, and surface `Cp` and `Cf` (not compared here). For SST, TMR uses its SST-Vm variant (`SSTm`).

21.3.2 Experimental Data

The airfoil is the Nakayama (1985) DSMA661 Model A with its originally blunt trailing edge made sharp. The measured wake profiles (NASA TMR) are drawn in the near-wake figures for context. TMR describes this case as a verification of implementation, and SA and SST do not reproduce the measured near wake exactly in any code.

21.4 Simulation Conditions

Item	Setting
Geometry	DSMA661 (Nakayama Model A), sharp trailing edge, chord `c = 1`
Flow	Steady, fully turbulent, compressible RANS
Mach number	`0.088`
Reynolds number	`1.2 × 10` based on chord
Angle of attack	`0°`
Freestream state	`T = 300 K`, `p = 62,428.94 Pa`, `= 0.72495 kg/m³`, `U = 30.555 m/s` (Sutherland viscosity `= 1.8459 × 10 Pa·s`)
Air	Ideal gas, `R = 287.05 J/(kg·K)`, Sutherland viscosity, `Pr = 0.72`
Drag unit	1 count = `0.0001` in the coefficient

21.5 Mesh

The meshes are the TMR 500-chord C-grid family: five nested levels (`L5` coarsest to `L1` finest), each level obtained from the next finer one by removing every other grid line. The TMR files are one-cell-thick extrusions of the two-dimensional grids; they were used as supplied. The minimum wall spacing on `L1` is `2.5 × 10` (`y+` of about 0.1 to 0.2).

Level	Points, zone 1 / zone 2	Cells `N`	`h = √(1/N)`
L1	673×897 / 1025×449	1,060,864	9.709e-4
L2	337×449 / 513×225	265,216	1.942e-3
L3	169×225 / 257×113	66,304	3.884e-3
L4	85×113 / 129×57	16,576	7.767e-3
L5	43×57 / 65×29	4,144	1.553e-2

21.6 Boundary and Initial Conditions

Boundary	Condition
Airfoil	No-slip, adiabatic wall; the solver's default `automatic` wall treatment
Farfield (500 chords)	Riemann farfield at `M = 0.088`, `= 0°`, `p = 62,428.94 Pa`, `T = 300 K`
Spanwise faces	Symmetry (the extruded cell is one layer thick)
Freestream turbulence, SA	`˜ = 3 ϖ`
Freestream turbulence, SST	TMR SST-Vm values: `kϖ = 9×10 aϖ²` and `t/ = 0.009` (turbulence intensity `8.80×10 `)

The flow was initialized automatically from the freestream state.

21.7 Numerical Methods

Item	Setting
Equations	Compressible RANS, steady, finite volume (DBNS)
Turbulence models	SA standard (`ft2` on, blended $\tilde{S}$ form, `Prt = 0.9`); SST (V2003)
Convective flux	Roe, second-order
Reconstruction	Least-squares reconstruction gradient, no limiter; U-MUSCL `= 0.5` (the FUN3D value) and `= 0` (the Wake CFD default)
Physical gradient	Green–Gauss
Time marching	Implicit pseudo-time, adaptive CFL between 1 and 100
Linear solver	Stationary Block-Jacobi, 30 sweeps (flow) and 20 sweeps (turbulence) per iteration, fixed sweep count
Stop rule	`CL` and `CD` monitor (window of 1,000 iterations, tolerance `10`) or 40,000 iterations

`= 0.5` matches the FUN3D input; `= 0` is the Wake CFD default and is run as a separate family to separate its effect on the coarse-mesh drag.

21.8 Results

21.8.1 Iteration Counts and Termination

Sixteen of the 20 runs (all runs on `L5` to `L2`) stopped on the monitor criterion: about 10,000 iterations on `L5` and 20,000 to 22,000 on `L2`, each taking 20 seconds to 18 minutes. The SA runs on `L1` stopped on the monitor after 28,666 (`=0.5`) and 29,528 (`=0`) iterations (about 90 minutes). **The two SST runs on `L1` reached the 40,000-iteration limit without satisfying the monitor.**

The forces of the two SST runs on `L1` were stationary: for SST `=0.5` from 28,000 iterations on, `CD` stays within `101.64` to `101.66` counts and `CL` is `0.1563`. For SST `=0`, `CD` fell by only `0.09` counts (from `101.76` to `101.67`) over the last 15,000 iterations. The `L1` SST values are therefore reported as converged in the forces, but they did not meet the monitor criterion and are marked † below. The residual histories are not reported here.

21.8.2 Force Coefficients

Differences are relative to FUN3D on the same mesh. † marks a run that reached the iteration limit without meeting the monitor criterion. `CDp` and `CDv` are the pressure and viscous parts of `CD`; the complete table, with CFL3D values, is in the downloadable CSV file.

Model	Level	Iterations	`CL`	`CD` [counts]	`CDp` [counts]	`CDv` [counts]	`ΔCL`	`ΔCD`	`ΔCDv`
SA `=0.5`	L5	9,893	0.1527	176.95	91.32	85.63	−0.53%	−0.35%	−0.60%
SA `=0.5`	L4	15,155	0.1572	112.55	27.51	85.04	−0.43%	−0.21%	−0.27%
SA `=0.5`	L3	17,664	0.1587	102.33	17.00	85.32	−0.22%	−0.12%	−0.14%
SA `=0.5`	L2	19,729	0.1592	100.87	15.51	85.36	−0.07%	−0.07%	−0.08%
SA `=0.5`	L1	28,666	0.1595	100.68	15.33	85.35	+0.00%	−0.01%	−0.03%
SA `=0`	L5	9,413	0.1518	242.86	155.09	87.77	−1.13%	+36.77%	+1.88%
SA `=0`	L4	14,855	0.1570	123.92	39.06	84.86	−0.52%	+9.87%	−0.48%
SA `=0`	L3	18,518	0.1588	103.96	18.70	85.26	−0.15%	+1.47%	−0.22%
SA `=0`	L2	20,483	0.1593	101.09	15.73	85.36	−0.01%	+0.15%	−0.08%
SA `=0`	L1	29,528	0.1595	100.71	15.36	85.35	+0.02%	+0.02%	−0.03%
SST `=0.5`	L5	10,126	0.1480	182.19	93.03	89.17	−2.70%	−12.00%	−3.91%
SST `=0.5`	L4	16,611	0.1536	114.36	28.62	85.74	−0.91%	+3.27%	+3.52%
SST `=0.5`	L3	19,013	0.1554	103.81	17.91	85.90	−0.37%	+2.02%	+2.08%
SST `=0.5`	L2	21,421	0.1560	102.16	16.31	85.85	−0.11%	+1.32%	+1.44%
SST `=0.5`	L1	40,000 †	0.1563	101.64	16.06	85.59	−0.02%	+0.88%	+1.04%
SST `=0`	L5	9,754	0.1466	248.51	156.93	91.58	−3.63%	+20.03%	−1.31%
SST `=0`	L4	16,234	0.1530	125.73	40.21	85.52	−1.30%	+13.53%	+3.26%
SST `=0`	L3	20,071	0.1554	105.37	19.62	85.76	−0.39%	+3.55%	+1.91%
SST `=0`	L2	22,315	0.1561	102.38	16.54	85.84	−0.08%	+1.53%	+1.42%

SST =0	L1	40,000 †	0.1563	101.67	16.09	85.59	+0.00%	+0.91%	+1.04%

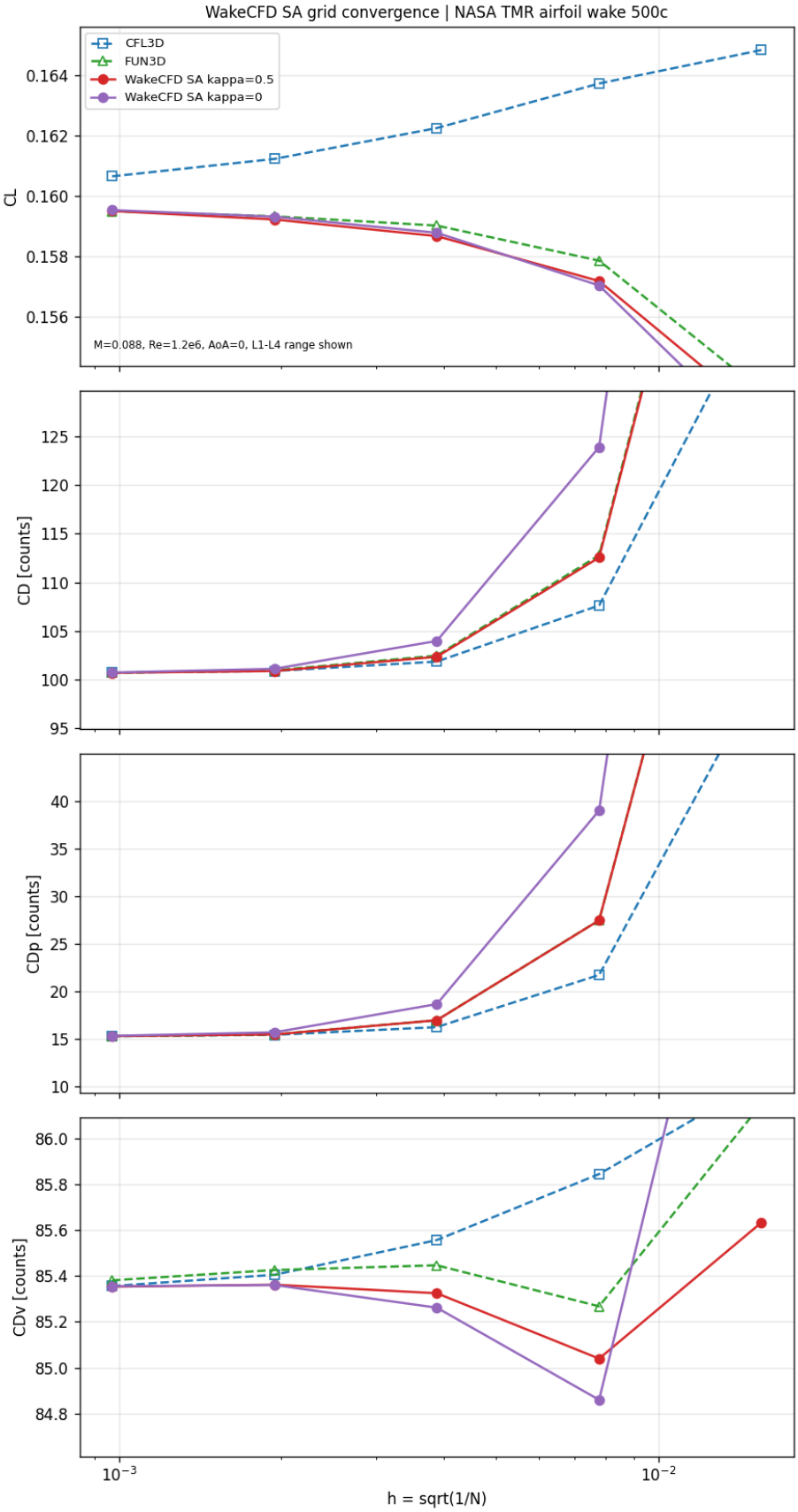


Figure 21.1: Grid convergence of CL, CD, CDp, and CDv for the SA model with =0.5 and =0 against CFL3D and FUN3D

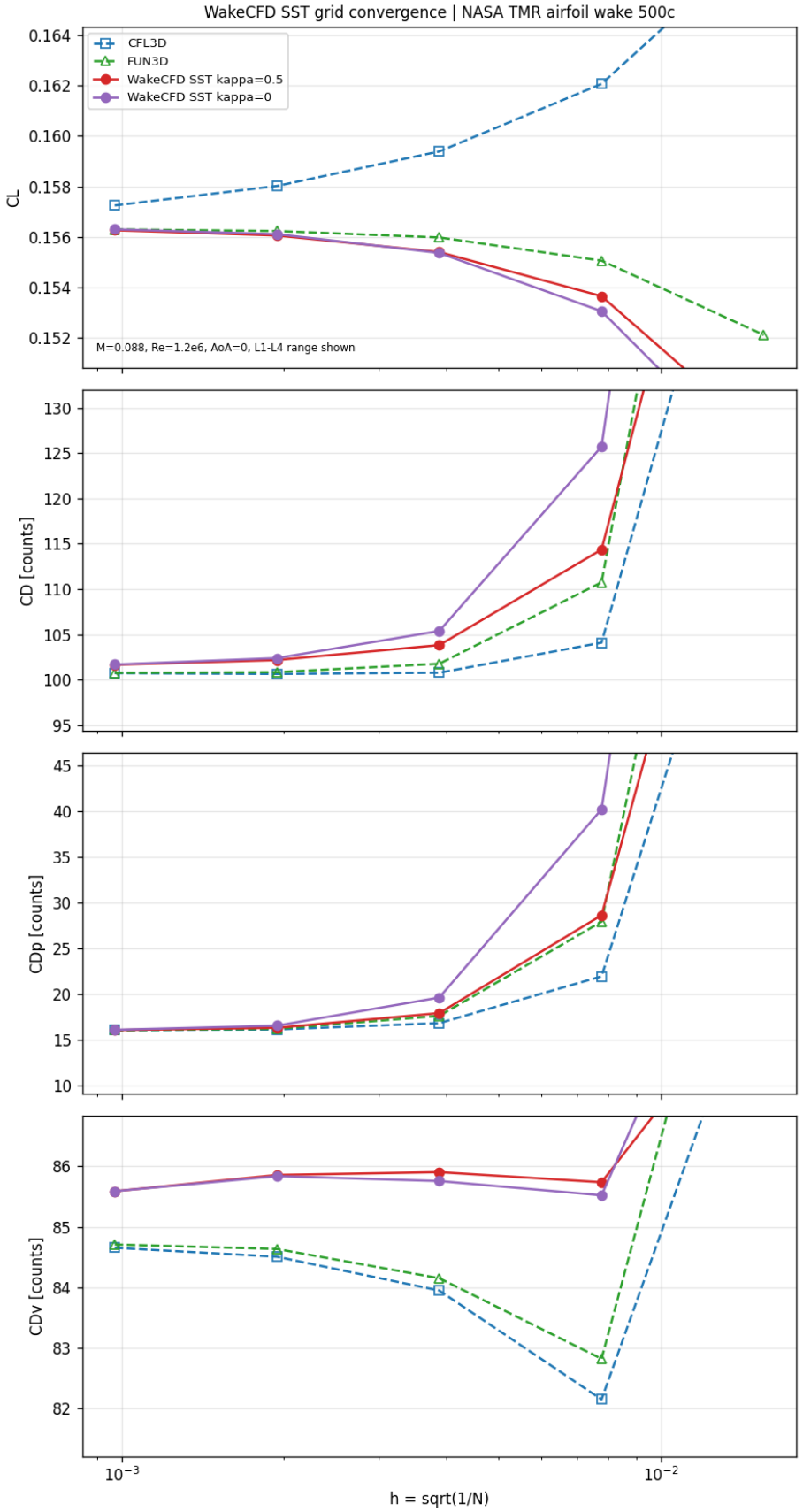


Figure 21.2: Grid convergence of CL, CD, CDp, and CDv for the SST model with =0.5 and =0 against CFL3D and FUN3D

SA. With =0.5, Wake CFD follows the FUN3D curve on every level. On L2 the differences are CL −0.07%, CD −0.07%, and CDv −0.08%; on L1, CL +0.00%, CD −0.01%, CDp 15.33 against 15.31 counts, and CDv −0.03%. The viscous drag is nearly flat from L5 to L1 (85.0 to 85.6 counts), as in FUN3D (85.4 to 86.1).

With =0, the coarse-mesh drag is far higher (L4: CD +9.87%, CDp 39.06 against 27.51 counts for =0.5), and the difference to =0.5 shrinks with refinement (L3 +1.47%, L2 +0.15%, L1 +0.02% against FUN3D). CDv hardly depends on (L4 −0.48%, L2 −0.08%). The setting therefore changes the pressure drag on coarse meshes but not the fine-mesh limit.

SST. Wake CFD's SST drag is above FUN3D by 1.0% to 3.5% in CDv and, on L2, by 1.3% to 1.5% in CD; on L1 the margin is +0.88% and +0.91% in CD and +1.04% in CDv for =0.5 and =0. CFL3D shows CDv +1.6% on L2. The viscous-drag curve of Wake CFD's SST model (85.5 to 89.2 counts) is also flatter than those of the references (FUN3D 82.8 to 84.6 counts, with a minimum at L4). As for SA, =0 has a much larger pressure drag on coarse meshes (L4: CD +13.5% against +3.3% for =0.5) and the two agree within 1.5% on L2 and to 0.03 counts on L1.

21.8.3 Near-Wake Profiles

The near-wake profiles of velocity and turbulent shear stress were compared at the seven TMR stations. The Wake CFD shear stress u'v' is computed from the eddy viscosity by the Boussinesq relation, $-\tau\,(\partial u/\partial z + \partial w/\partial x)/U_\infty^2$, using nodal gradients. For SST the turbulent-kinetic-energy contribution is not included in this conversion; whether this explains part of the SST differences below was not checked.

SA, velocity and shear stress profiles on the finest mesh (L1)

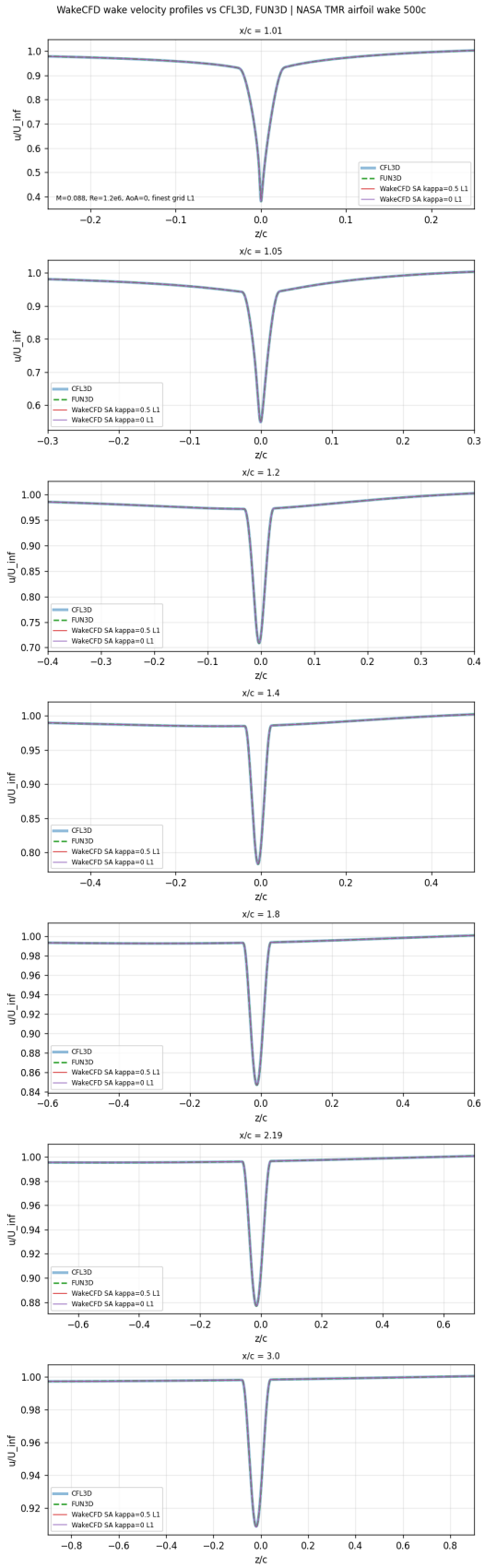


Figure 21.3: Wake velocity profiles of the SA model at seven stations on the finest mesh against CFL3D and FUN3D

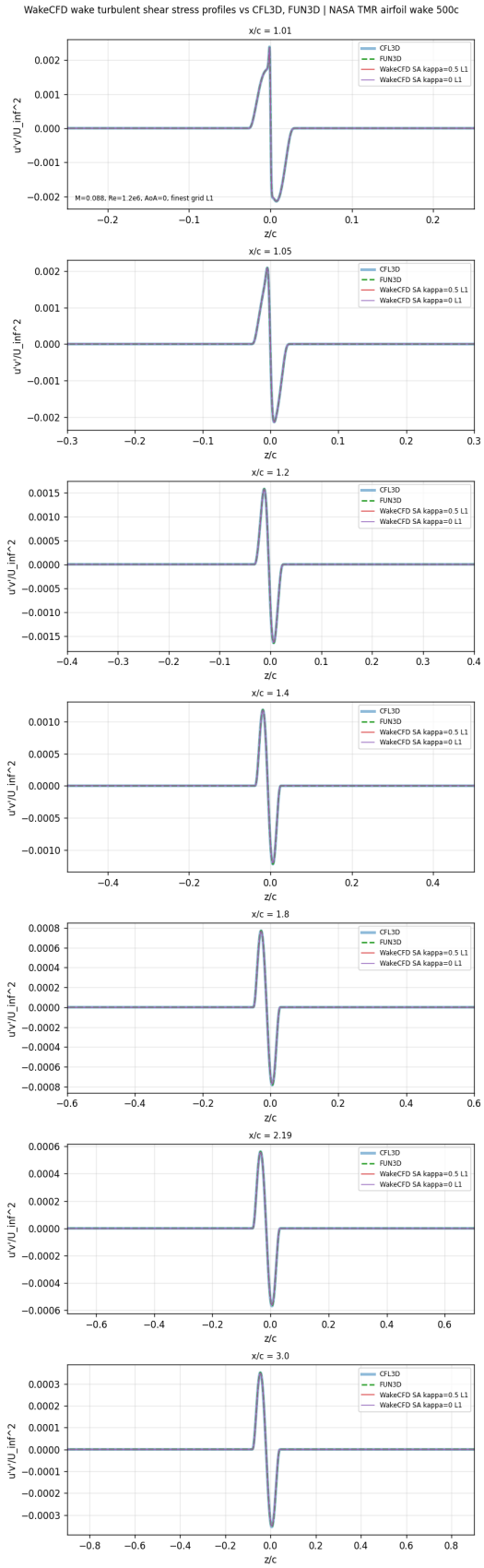


Figure 21.4: Wake turbulent shear stress profiles of the SA model at seven stations on the finest mesh against CFL3D and FUN3D

SST, velocity and shear stress profiles on the finest mesh (`L1`)

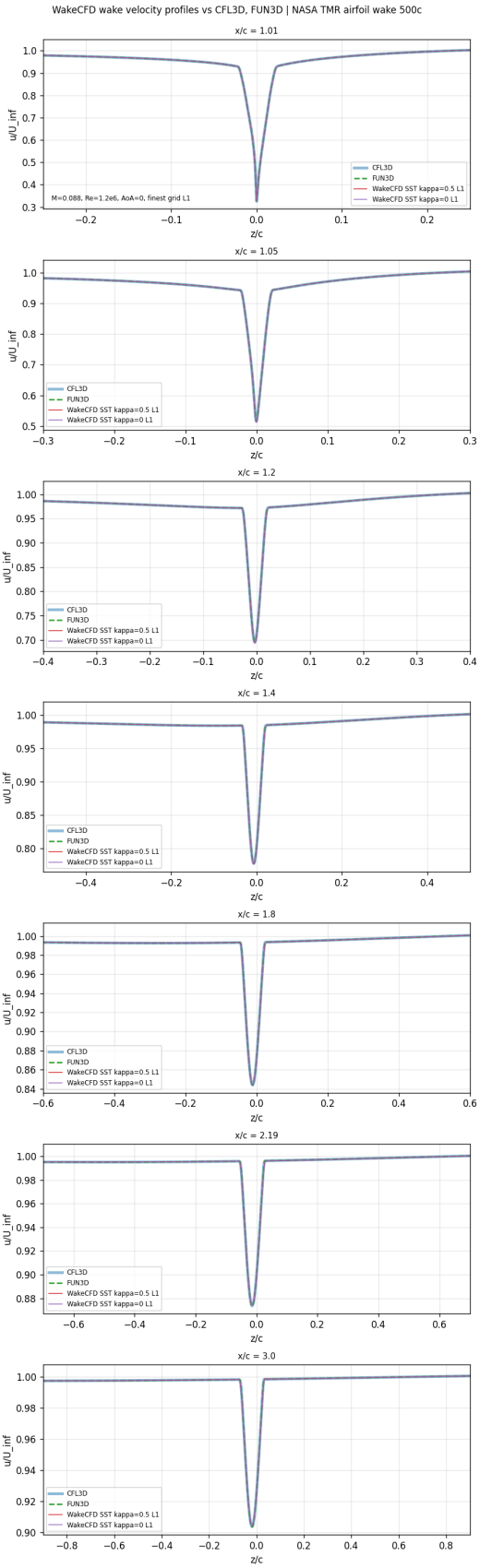


Figure 21.5: Wake velocity profiles of the SST model at seven stations on the finest mesh against CFL3D and FUN3D

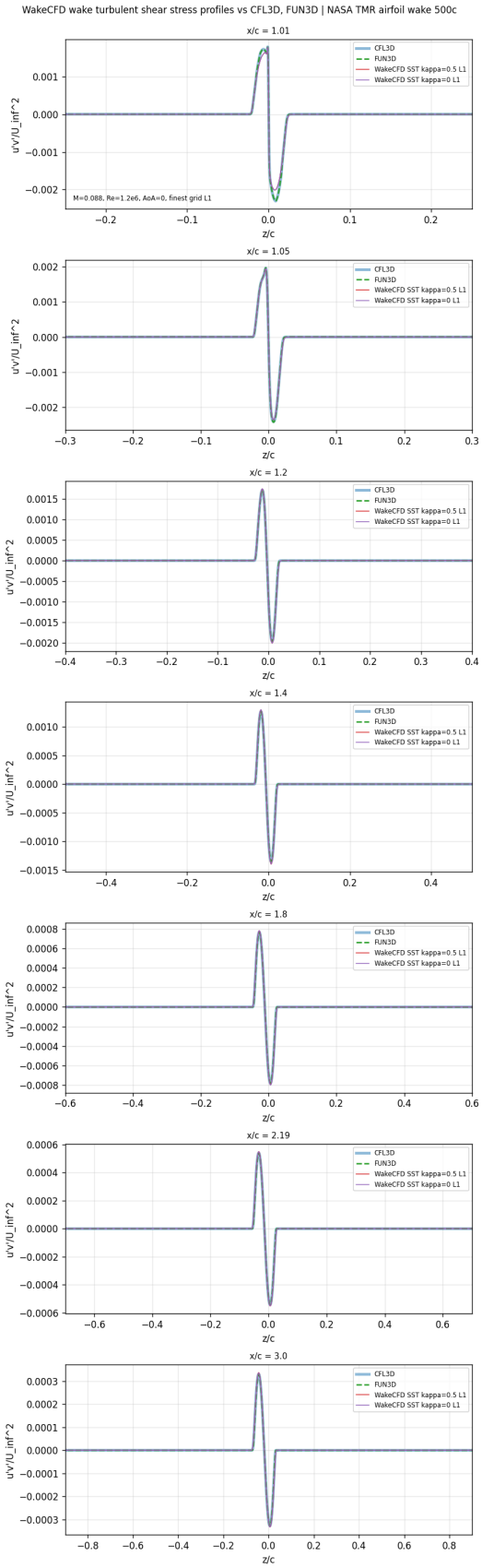


Figure 21.6: Wake turbulent shear stress profiles of the SST model at seven stations on the finest mesh against CFL3D and FUN3D

Differences of the finest-mesh (L1) wake minima relative to FUN3D (CFL3D values and all levels are in the downloadable CSV file):

Minimum velocity u/U_inf

Model	x/c 1.01	x/c 1.05	x/c 1.2	x/c 1.4	x/c 1.8	x/c 2.19	x/c 3.0
SA =0.5	+0.07%	+0.10%	+0.08%	+0.04%	+0.01%	+0.01%	+0.00%
SA =0	+0.06%	+0.10%	+0.08%	+0.04%	+0.02%	+0.01%	+0.00%
SST =0.5	+0.11%	−0.52%	−0.36%	−0.13%	+0.05%	+0.09%	+0.09%
SST =0	+0.11%	−0.52%	−0.35%	−0.13%	+0.04%	+0.09%	+0.11%

Minimum shear stress u'v'/U_inf^2

Model	x/c 1.01	x/c 1.05	x/c 1.2	x/c 1.4	x/c 1.8	x/c 2.19	x/c 3.0
SA =0.5	−0.0%	−0.1%	−1.1%	−1.6%	−1.5%	−1.3%	−1.1%
SA =0	+0.0%	−0.1%	−1.0%	−1.6%	−1.6%	−1.3%	−1.2%
SST =0.5	−12.9%	−3.0%	+1.9%	+3.1%	+1.8%	+1.7%	+1.5%
SST =0	−12.9%	−2.8%	+1.8%	+2.8%	+2.3%	+1.5%	+1.6%

The SA minimum velocity is within 0.1% of FUN3D at every station, and the minimum shear stress is within 0.1% up to x/c = 1.05 and 1.1% to 1.6% lower farther downstream; =0 and =0.5 cannot be told apart on L1. The SST minimum velocity is within 0.6% of FUN3D, but the minimum shear stress directly behind the trailing edge is 12.9% lower at x/c = 1.01 (3.0% at x/c = 1.05) and then 1.5% to 3.1% higher at x/c 1.2. The velocity profile agrees while only the near-trailing-edge shear stress differs; together with the +1% CDv, this points to a model-implementation difference, which was not identified.

Comparison with the experiment (Nakayama)

The same profiles are shown against the measured wake. The Wake CFD curves are the finest-mesh (L1) results for =0.5 and =0.

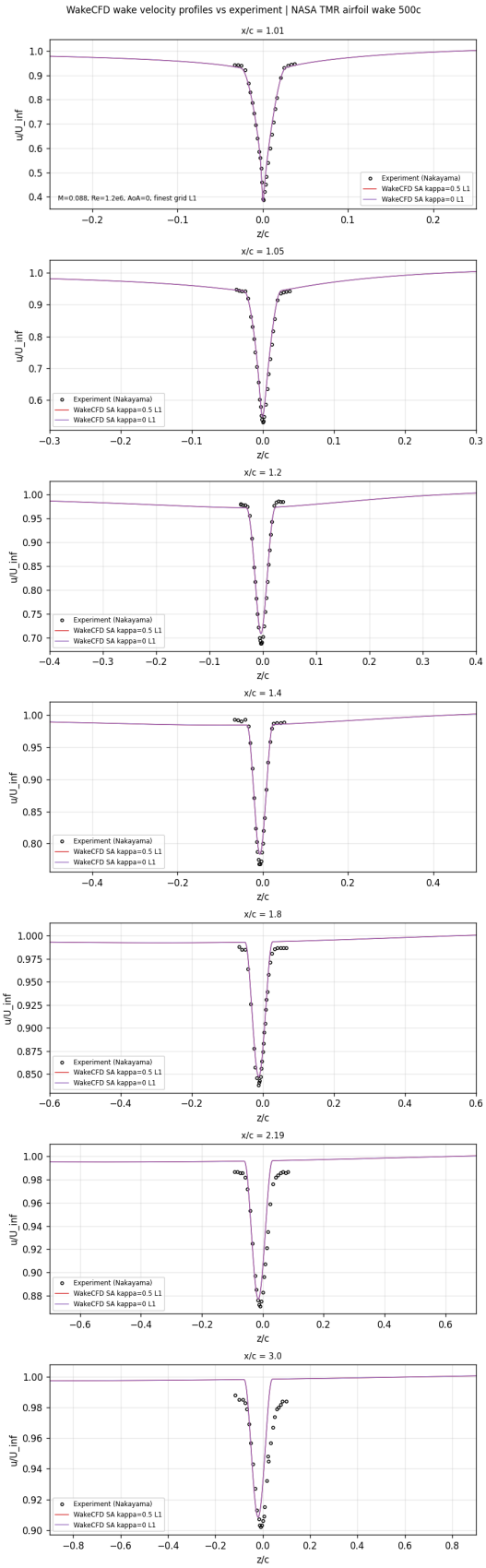


Figure 21.7: SA model velocity profiles at seven stations on the finest mesh against the Nakayama measurements

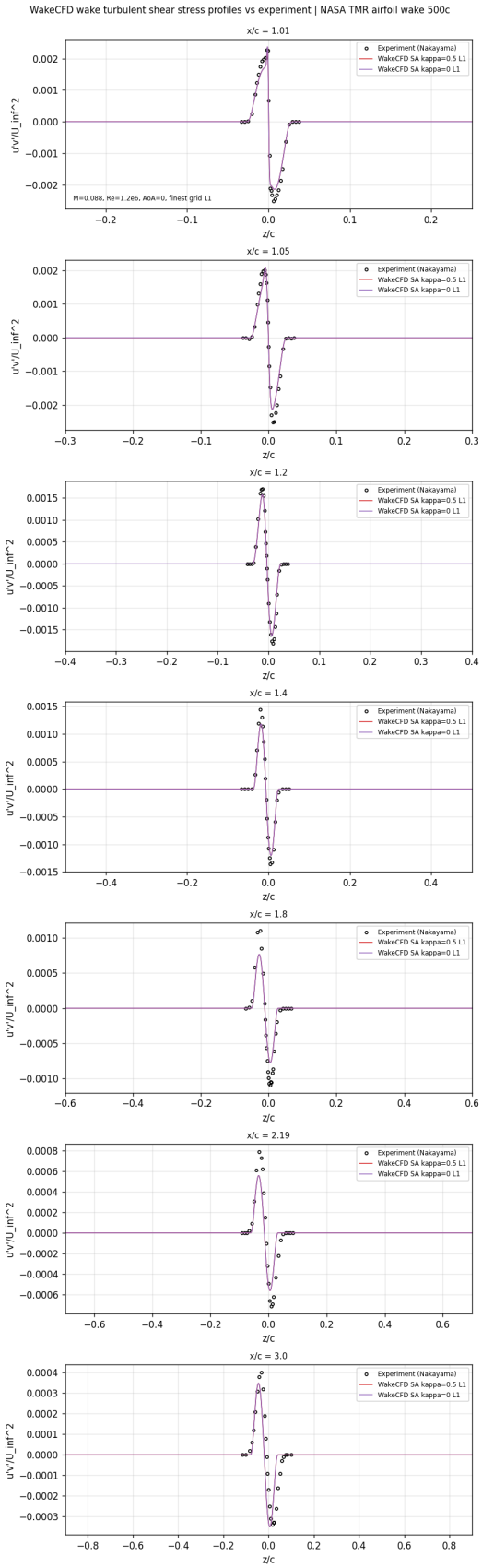


Figure 21.8: SA model turbulent shear-stress profiles at seven stations on the finest mesh against the Nakayama measurements

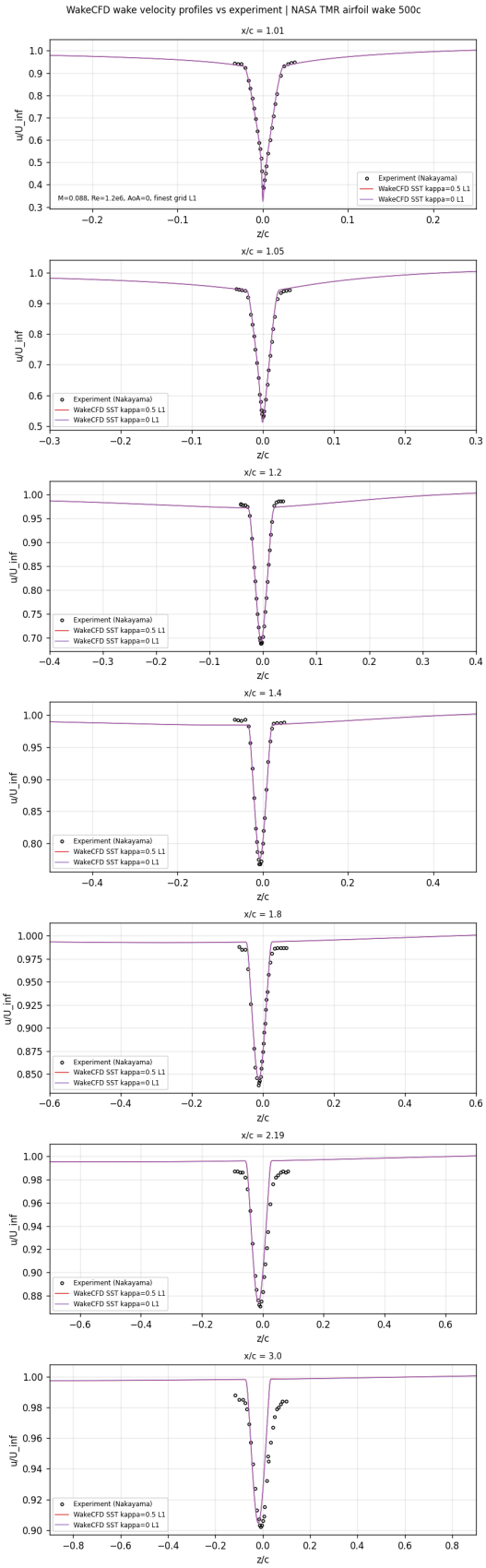


Figure 21.9: SST model velocity profiles at seven stations on the finest mesh against the Nakayama measurements

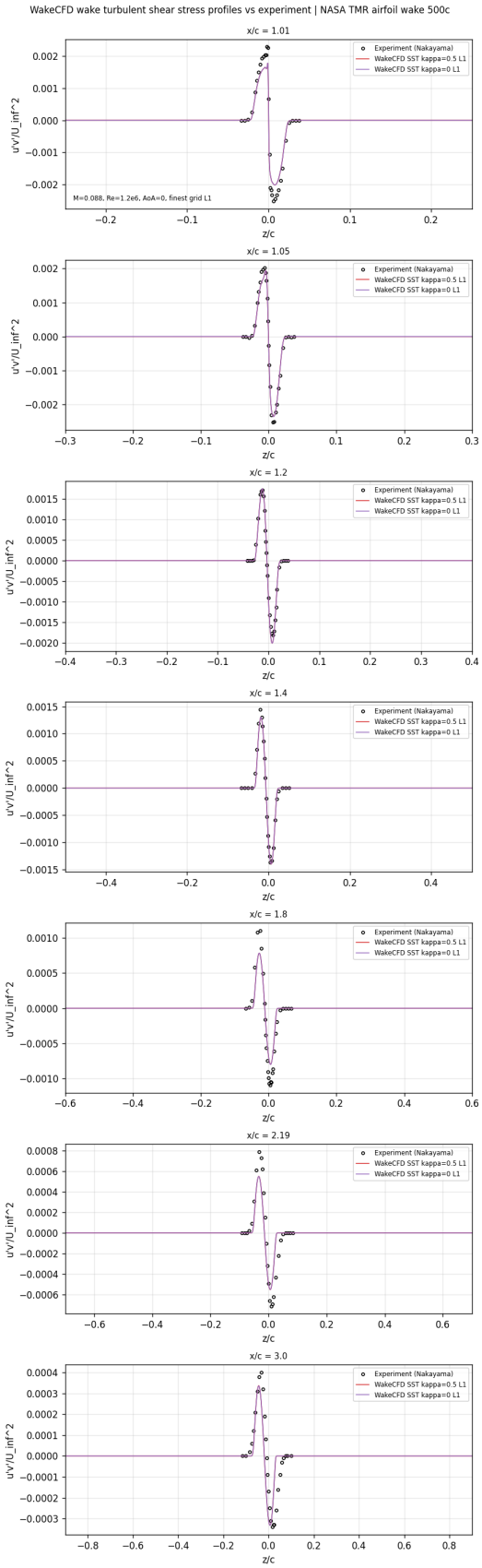


Figure 21.10: SST model turbulent shear-stress profiles at seven stations on the finest mesh against the Nakayama measurements

Against the experiment, the finest-mesh minimum velocity of SA differs from the measurement by −1.2% at `x/c = 1.01`, +1.1% to +3.3% at 1.05 to 1.8, and +0.7% at 2.19 and beyond; SST has a much deeper deficit right behind the trailing edge (−15.7% at `x/c = 1.01`, measured 0.386 against 0.326) and is within +0.3% to +1.1% from `x/c = 1.2` on. The minimum shear stress of both models is 20% to 29% below the measurement at `x/c = 1.8` to 2.19. The reference codes give the same behavior, so this is a feature of the models and not a discrepancy of Wake CFD.

21.9 Conclusions and Applicable Scope

- With the SA model and `= 0.5`, Wake CFD agrees with FUN3D on forces and the near-wake minima at every mesh level: `CL`, `CD`, and `CDv` within 0.08% on `L2` and within 0.03% on `L1`; the minimum wake velocity within 0.1% and the minimum shear stress within 1.6% at all stations on `L1`.
- The `= 0` reconstruction gives much higher pressure drag on the coarse meshes (+9.9% in `CD` on `L4`) but converges to the `= 0.5` result by `L2` (within 0.15%), and to 0.03 counts in `CD` on `L1`.
- The SST model agrees with the references in `CL` (within 0.11% on `L2`) and in the minimum wake velocity (within 0.6%). Its viscous drag is higher than FUN3D by 1.0% on `L1` (1.4% on `L2`), and its minimum shear stress directly behind the trailing edge is 12.9% lower. These differences did not shrink from `L2` to `L1`, so they are not discretization error; their cause was not identified, and SST is therefore not verified to the level of SA in this case.
- The two SST runs on the finest mesh did not satisfy the monitor criterion within 40,000 iterations; their forces were stationary to within the changes quoted under *Convergence History*.
- The `automatic` wall treatment was used on a mesh with `y+` below 1 (finest level about 0.1 to 0.2). The results apply to the `0.21.5` build that includes uncommitted changes (see *Run Provenance and Artifacts*) and to the mesh family used.
- The case is two-dimensional, subsonic (`M = 0.088`), attached, and fully turbulent. The results do not support conclusions for separated flow, transition, stronger compressibility, or turbulence models other than SA and SST.

This case shows that Wake CFD's SA implementation reproduces the forces and the near-wake structure of the mature reference codes on this airfoil to within 0.1% to 1.6% on the finest mesh, and that its SST implementation reproduces them to within about 1% in the forces with an unexplained offset in the wall friction and the shear stress near the trailing edge. It establishes a baseline for this range of conditions and not an absolute accuracy guarantee.

21.10 References

- NASA Turbulence Modeling Resource: 2D Airfoil Near-Wake Verification Case (500c)
- NASA Turbulence Modeling Resource: SA results for the 2D airfoil near wake (500c)
- NASA Turbulence Modeling Resource: 2D Airfoil Near-Wake grids (500c)
- NASA Turbulence Modeling Resource: Airfoil Near-Wake Validation Case
- Nakayama (1985), DSMA661 Model A airfoil near-wake measurements, as documented in the NASA TMR pages above.

22 3D Transonic Wing — ONERA M6 RANS Validation

Wall-function spanwise pressure-coefficient validation against NASA WIND-US and the ONERA S2MA experiment

22.1 Run Provenance and Artifacts

Item	Value
Wake CFD baseline version	`0.22.2`
Solver	DBNS
Compute device	GPU (NVIDIA RTX A6000)
Parallel execution	1 MPI rank
Arithmetic precision	FP64
Run date	2026-09-22

> **Note**
>
> Results depend on the solver build that produced them. Read every figure in this report together with the version and date above — re-running the same input on a later build may give different numbers.

22.1.1 Downloadable Files

Not available: standalone input decks and solver result files have not yet been published for download.

22.2 Validation Objective

The ONERA M6 half-wing is a classic transonic shock/boundary-layer-interaction case: a swept, tapered wing at moderate lift produces the characteristic "lambda" shock pattern on its upper surface, where two shock legs merge as they move outboard. This case compares Wake CFD's spanwise surface-pressure distribution with both the original ONERA S2MA wind-tunnel experiment

and NASA's own WIND-US CFD solution for the same geometry and conditions, across a sweep of four convective schemes.

This case also validates Wake CFD's **wall-function** near-wall treatment on a 3D swept wing. The mesh does not resolve the viscous sublayer (`y+ 1`); instead, the wall function reconstructs the near-wall velocity profile from a coarser first cell sized for `y+ 30`. This is the same near-wall treatment NASA specifies in its own reference WIND-US input ("wall function on"), so the comparison is apples-to-apples on wall treatment as well as on geometry and conditions — not an added source of discrepancy.

For users, this result supports review of 3D transonic wing pressure distributions and shock location during early design using a wall-function mesh, without needing to resolve the boundary layer with a `y+ 1` mesh.

22.3 Reference Solution and Data

Item	Setting
Reference	NASA GRC WIND-US ONERA M6 Wing validation archive (Study #1, `m6wing01`); original experiment: Schmitt & Charpin, AGARD AR-138

22.4 Simulation Conditions

Item	Setting
Geometry	NASA GRC ONERA M6 half wing
Analysis	Steady, compressible RANS
Freestream Mach	`0.8395`
Angle of attack	`3.06°`
Reynolds number	`Re_MAC=11.72×10^6` (mean aerodynamic chord, `MAC=0.540057 ft`)

22.5 Mesh

Item	Setting
Mesh	Unstructured hexahedral, 294,912 cells / 306,577 points; first-cell spacing sized for the wall-function target, not boundary-layer-resolved

22.6 Boundary and Initial Conditions

Item	Setting
Wall treatment	**Wall function** (`wall_function: standard`) on the wing surface, target `y+ 30` — matches the near-wall treatment in NASA's own WIND-US reference input

> **Note**
>
> **Why a wall function here.** A `y+ 1` wall-resolved mesh needs many more near-wall layers than a wall-function mesh at the same accuracy target, which increases cell count and run time substantially on a 3D wing. Using the wall function keeps this mesh at 294,912 cells while still reproducing the shock location and spanwise pressure distribution shown below.

Initial field: Not reported.

22.7 Numerical Methods

Item	Setting
Turbulence model	Spalart–Allmaras (SA)
Convective schemes	Roe, HLLC, AUSM+up2, and SLAU2 (compared below)
Gradients / limiter	Green-Gauss physical gradient, unweighted least-squares reconstruction gradient, Venkatakrishnan limiter (`coeff=0.01`)
Time integration	Implicit, adaptive CFL (start `5`, min `1`, max `100`)

22.8 Results

22.8.1 Key Results

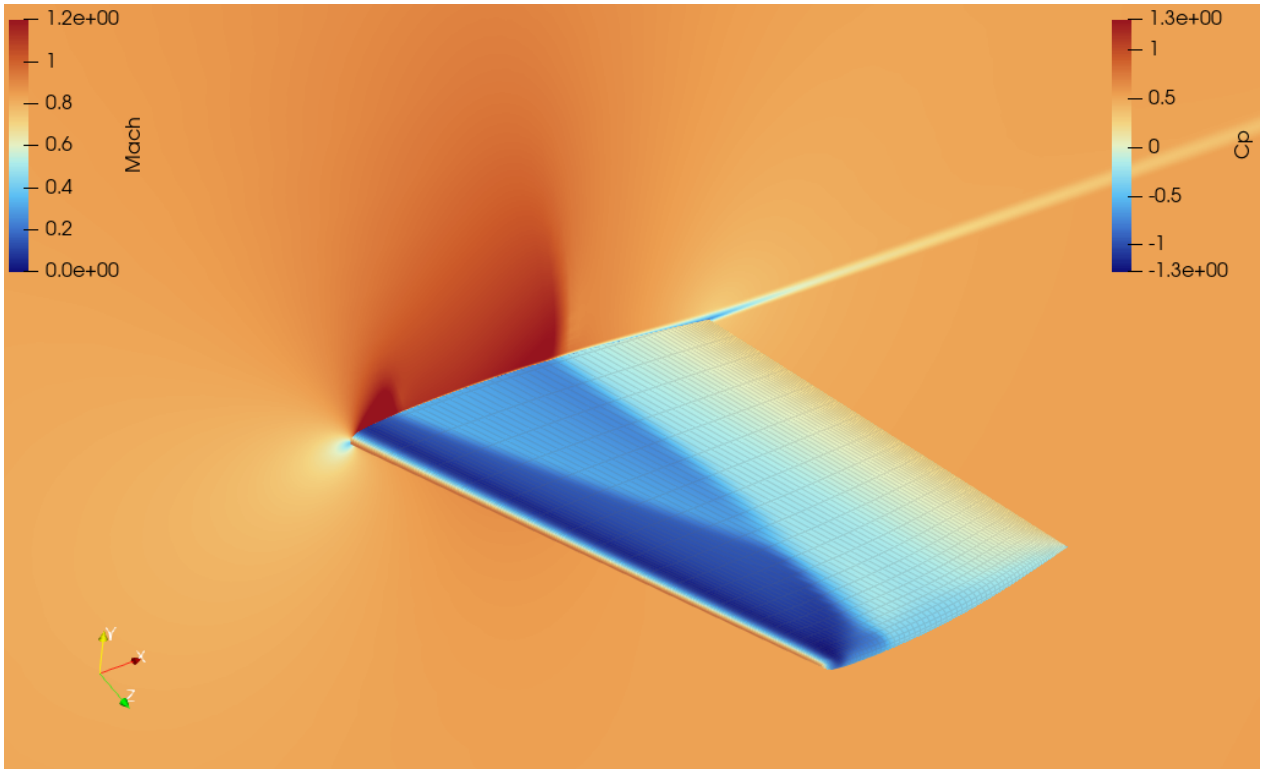
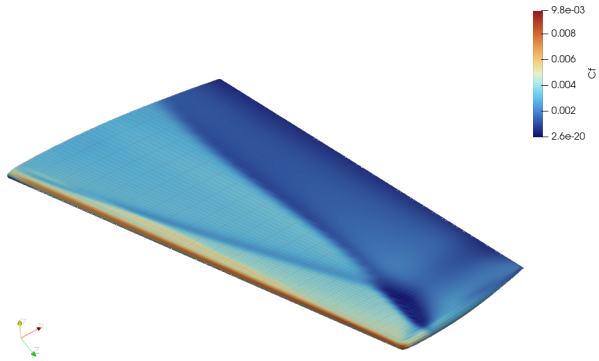
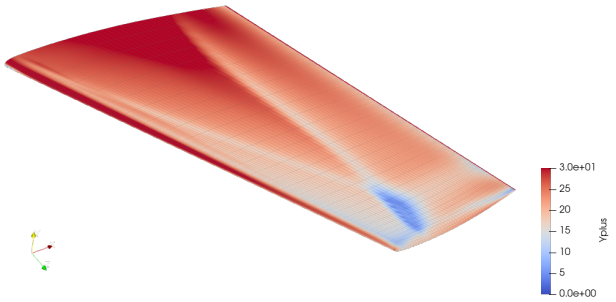


Figure 22.1: Surface `Cp` and farfield Mach contour, showing the ONERA M6's characteristic lambda-shock pattern where the shock's two legs merge outboard



(a) Skin-friction coefficient. The band where `Cf` drops locally follows the shock-foot line visible in the Cp/Mach contour above.



(a) Wall `y+`. Mostly 25-30 as targeted by the wall function, with a local dip at the shock foot.

The `y+` contour confirms the wall function is operating at its intended target across nearly the entire wing, dipping only locally where the shock impinges on the boundary layer.

22.8.2 Comparison with Experiment and NASA WIND-US

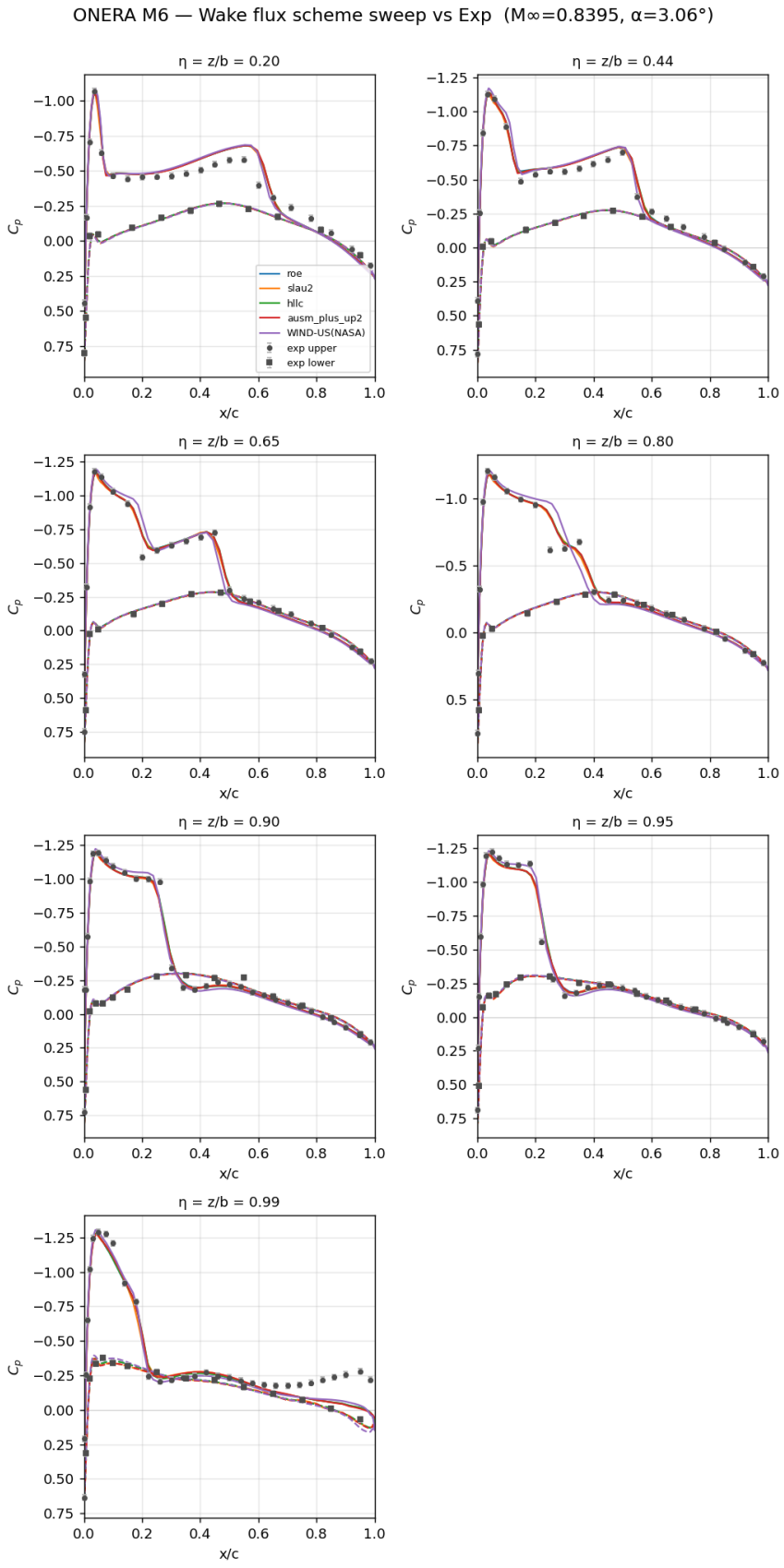


Figure 22.4: Sectional Cp at seven spanwise stations: Roe, AUSM+up2, HLLC, and SLAU2 versus the NASA WIND-US published CFD solution and the ONERA S2MA experiment

Across all seven spanwise stations (=0.20 to 0.99), the four recommended schemes are essentially indistinguishable from each other and track both the WIND-US CFD solution and the experimental points closely, including the suction-side shock location and the leading-edge suction peak. The only visible departure is at =0.80, where WIND-US places the shock slightly further upstream than either Wake CFD or the experiment.

22.8.3 Comparisons for Scheme Selection

All four schemes below converge normally with consistent lift and pressure distribution on this mesh and settings — the same four shown in the Cp comparison above.

Scheme	CL	CD	Residual	Assessment
Roe	0.2664	0.0190	7.21	Default choice
HLLC	0.2675	0.0192	8.14	Recommended
AUSM+up2	0.2669	0.0195	7.61	Recommended
SLAU2	0.2662	0.0195	7.85	Recommended

Residual: orders of magnitude (log) the flow-residual RMS dropped from its initial value.

22.9 Conclusions and Applicable Scope

- **Roe** is recommended as the default scheme for this condition. **HLLC**, **AUSM+up2**, and **SLAU2** all reproduce the same shock location and spanwise pressure distribution and are equally suitable alternatives.
- Lift (CL) agrees within 0.5% across these four schemes. Drag (CD) spreads somewhat more — 2.6% (Roe lowest at 0.0190, AUSM+up2/SLAU2 highest at 0.0195). This does not correlate with residual depth (Roe has the shallowest residual of the four but the lowest CD). Drag comparisons on this or similar transonic cases should account for this scheme-dependent spread until the cause is confirmed.
- This result validates one wing geometry, one Mach number/angle-of-attack condition, and a wall-function near-wall treatment. It does not establish accuracy for a y+ 1 wall-resolved mesh, other Mach numbers or sweep angles, or unsteady/buffet conditions.

22.10 References

- Schmitt, V., and Charpin, F., "Pressure Distributions on the ONERA-M6-Wing at Transonic Mach Numbers," in *Experimental Data Base for Computer Program Assessment*, AGARD AR-138, 1979.
- NASA GRC WIND-US ONERA M6 Wing Validation Archive, Study #1 (m6wing01)

23 CRM DPW-5 Wing–Body — SA Grid-Convergence Verification

WakeCFD SA Hex, Prism, and Hybrid on the common L1–L4 meshes

23.1 Run Provenance and Artifacts

Item	Value
Wake CFD baseline version	`0.23.0`
Solver	DBNS
Compute device	CPU cluster
Parallel execution	120 MPI ranks across 4 nodes
Arithmetic precision	Not recorded in the source report
Run dates	2026-10-12

The published CSV is the SA-only subset of the research run's `cl05_results.csv`. It records the interpolated values used in the table and chart below. Results from the earlier run001–003 campaign are excluded because those runs preceded a wall-distance correction.

23.1.1 Downloadable Files

File	Description	Format
SA grid-convergence results	All 12 mesh-family/level points plotted below; `CD` is in drag counts	CSV
DPW-5 participant band	Digitized reference envelope and median plotted behind the Wake CFD results	CSV
Chart script	Regenerates the SA-only comparison figure from both CSV files	Python

The complete input decks and solver field files are not published here. Some original `0.17.2` run files were lost; the affected values survive in the research results CSV and cannot be rechecked against their run histories.

23.2 Verification Objective

Assess whether the computed lift-matched drag, angle of attack, and pitching moment approach consistent values as the common DPW-5 CRM wing–body meshes are refined from L1 to L4. The comparison uses the workshop's code-to-code results. The wind-tunnel model includes deformation and support effects absent from this rigid, free-air CFD geometry, so this case does not claim direct experimental validation.

23.3 Reference Solution and Data

The reference is the AIAA Fifth Drag Prediction Workshop (DPW-5) Common Grid Study for the NASA Common Research Model wing–body configuration. The grey envelope and dotted median in the figure were digitized from the participant curves in the workshop summary figure; extreme outliers were excluded with a `3 × IQR` rule in the research dataset. The envelope includes multiple codes and modeling choices, so it is context for the Wake CFD refinement trend rather than a unique exact solution or an SA-only target value. The grey band's irregular edges reflect the digitized participant curves and should not be interpreted as a continuous physical uncertainty bound.

23.4 Simulation Conditions

Item	Setting
Geometry	CRM wing–body half model, without horizontal tail
Flow	Steady, fully turbulent, compressible RANS
Freestream	Mach `0.85`, Reynolds number `5 × 10` based on reference chord, static temperature `310.928 K`
Target lift	`CL = 0.500`; interpolated from separate `=` `2.25°` and `2.70°` runs at each mesh level
Drag unit	1 count = `0.0001` in `CD`

23.5 Mesh

DPW-5 common prism, hex, and hybrid mesh families were used with the same node counts at each level. The half-model mesh coordinates were converted from inches to metres.

Level	Nodes
L1	660,177
L2	2,204,089
L3	5,196,193
L4	17,441,905

23.6 Boundary and Initial Conditions

The half model uses a symmetry plane, no-slip adiabatic walls, and a farfield boundary. The SA freestream working variable is initialized at `~/ = 3`. The hybrid L4 `= 2.70°` run required a warm start from its `2.25°` solution; the other initial fields are not documented individually in this report.

23.7 Numerical Methods

Item	Setting
Turbulence	SA-neg, with `ft2`, QCR, and rotation correction off
Convective flux / reconstruction	Roe / second-order U-MUSCL, `= 0.5`, no limiter
Time marching	Backward-Euler implicit, adaptive CFL
Gradient settings	Prism: WLS physical / least-squares reconstruction; hybrid: Green–Gauss / Green–Gauss; hex: Green–Gauss / least-squares at L1–L3, Green–Gauss / Green–Gauss at L4
Hex L4 SA adjustment	Turbulence `cfl_reduction = 0.25` instead of `0.7`, after the original setting diverged
Stop rule	Lift/drag monitor window or the 5,000-iteration limit; several runs reached the limit with forces nearly stationary

and `CMy` at `CL = 0.5` are linearly interpolated between the two angle-of-attack runs. `CD` is evaluated from a two-point fit of `CD = a + b CL²`. These are postprocessed values, not separate fixed-lift solver runs.

23.8 Results

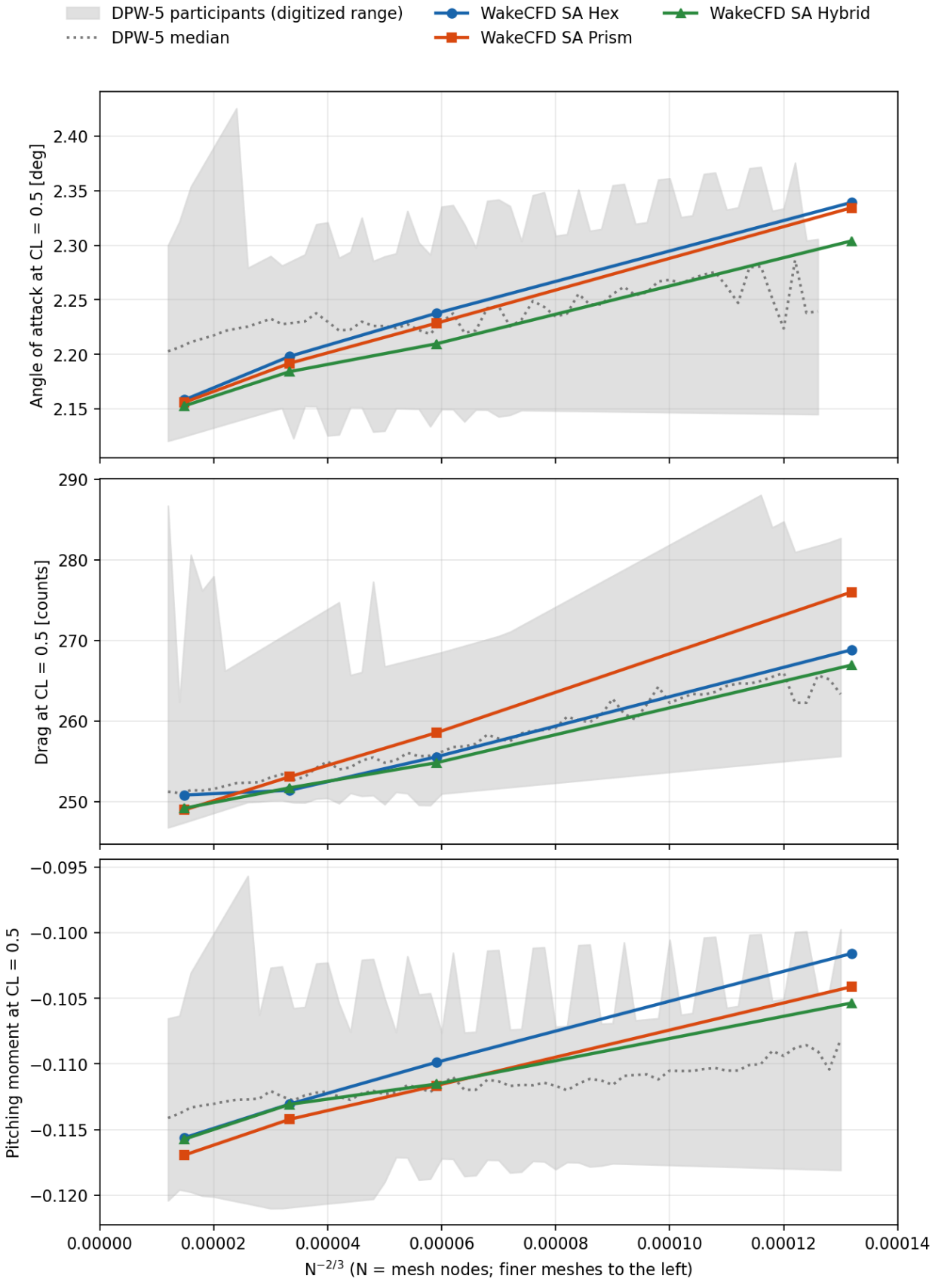


Figure 23.1: SA-only CRM refinement curves for angle of attack, drag, and pitching moment. The three WakeCFD SA mesh-family series overlay a grey DPW-5 participant envelope and

Mesh	Level	at CL=0.5 [°]	CD [counts]	CMy
WakeCFD SA Hex	L1	2.3393	268.8	−0.1016
WakeCFD SA Hex	L2	2.2376	255.6	−0.1099
WakeCFD SA Hex	L3	2.1981	251.4	−0.1131
WakeCFD SA Hex	L4	2.1582	250.8	−0.1156
WakeCFD SA Prism	L1	2.3344	276.0	−0.1041
WakeCFD SA Prism	L2	2.2285	258.6	−0.1117
WakeCFD SA Prism	L3	2.1918	253.1	−0.1142
WakeCFD SA Prism	L4	2.1559	249.0	−0.1169
WakeCFD SA Hybrid	L1	2.3040	267.0	−0.1054
WakeCFD SA Hybrid	L2	2.2096	254.8	−0.1115
WakeCFD SA Hybrid	L3	2.1841	251.7	−0.1131
WakeCFD SA Hybrid	L4	2.1527	249.2	−0.1157

At L4 the three families give = 2.1527–2.1582° and CD = 249.0–250.8 counts. Their drag spread decreases from 9.1 counts at L1 to 1.9 counts at L4. These L4 values fall within the DPW-5 participant range summarized in the research campaign, but that range combines different methods and turbulence models.

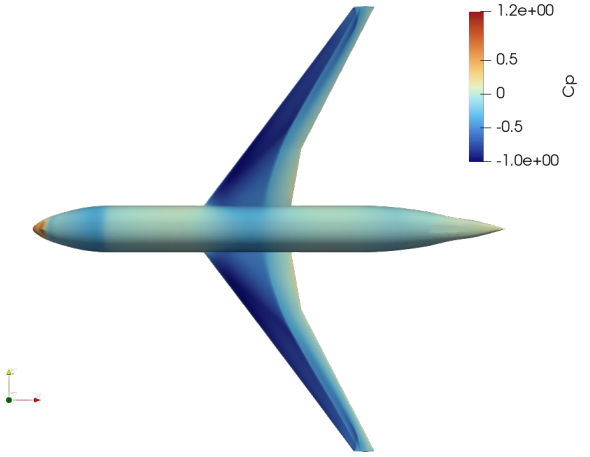
23.8.1 Surface contours: hex L3 SA

The following four images show upper and lower surface pressure coefficient (Cp) and skin-friction magnitude (Cf) from the research campaign's hex L3 SA result. The original images identify the mesh and turbulence model, but **do not identify the exact angle of attack or solver binary**; their association with a specific run could not be verified from the retained field files. They illustrate the surface patterns and are not a quantitative comparison with a CL = 0.5 result or with experiment. The displayed scales are Cp = −1.0…1.2 and Cf = 0…0.01.

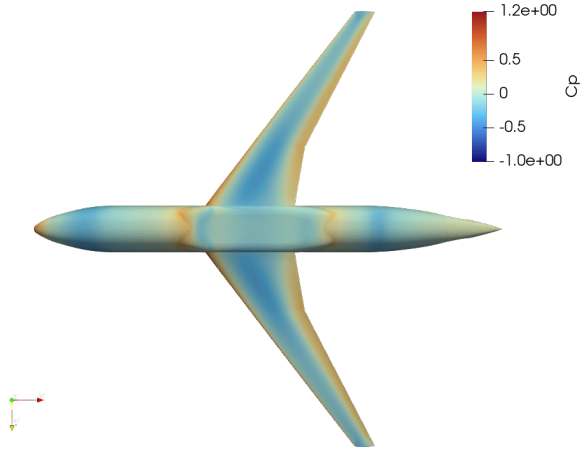
23.9 Conclusions and Applicable Scope

The SA results show a consistent reduction in drag and angle of attack with refinement across three mesh families, with close agreement between families at L4. This is evidence for this specific CRM wing–body setup and numerical configuration; no formal Richardson extrapolation or discretization-error bound is claimed here.

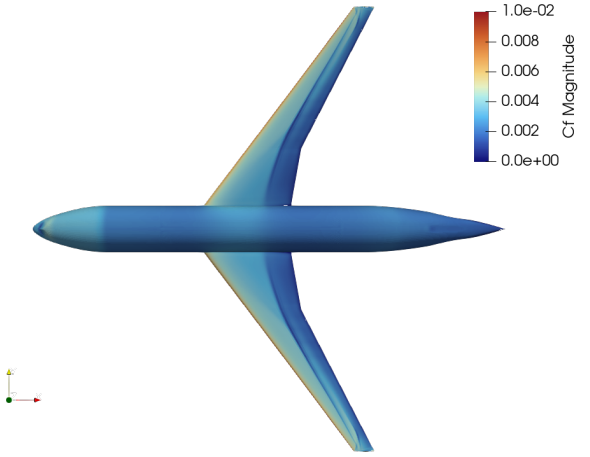
Interpret the hex curve with care: its L4 reconstruction differs from L1–L3. The runs also mix 0.17.2 and 0.19.0 binaries, and a separate repeat of hybrid L1 on those builds differed by 6.4 drag counts for a reason not yet established. The available data therefore do not isolate mesh refinement from every other numerical change. This case does not establish accuracy for SST, buffet onset, other Mach or Reynolds numbers, or different near-wall treatments.



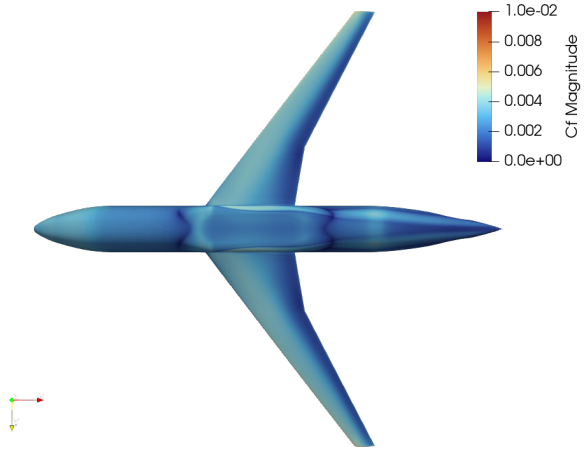
(a) CRM upper-surface pressure coefficient, hex L3 SA



(a) CRM lower-surface pressure coefficient, hex L3 SA



(a) CRM upper-surface skin-friction magnitude, hex L3 SA



(a) CRM lower-surface skin-friction magnitude, hex L3 SA

23.10 References

- Levy et al., Fifth AIAA CFD Drag Prediction Workshop summary, AIAA 2013-0046.
- Park et al., Fifth AIAA CFD Drag Prediction Workshop CFD results, AIAA 2013-0050.

24 3D High-Lift Trap Wing — HiLiftPW-1 Configuration 1 Validation

Lift, drag, moment, and surface pressure from =6° to 34°, and whether the stall is found (SA-neg, against the NASA LaRC 14×22 ft experiment)

24.1 Run Provenance and Artifacts

Item	Value
Wake CFD baseline version	`0.23.0`
Solver	DBNS
Compute device	GPU (NVIDIA RTX A6000)
Parallel execution	4 MPI ranks
Arithmetic precision	Not recorded
Run date	2026-10-15

> **Note**
>
> Results depend on the solver build that produced them. Read every figure in this report together with the version and date above — re-running the same input on a later build may give different numbers.

24.1.1 Downloadable Files

Not available: standalone input decks and solver result files have not yet been published for download.

24.2 Validation Objective

The NASA Trap Wing is the geometry of the 1st AIAA High Lift Prediction Workshop (HiLiftPW-1): a swept, tapered wing with slat, main element and flap, tested in the NASA Langley 14×22 ft wind tunnel. Configuration 1 (slat 30°, flap 25°) is a landing-type setting. Near maximum lift

the flow combines slat and flap wakes merging with the main-element boundary layer, a wing-tip vortex, and the onset of massive separation, which makes it a demanding steady RANS case.

This report compares Wake CFD with the experiment from =6° to =37°, with two questions:

- Does Wake CFD reproduce the lift, drag, pitching moment, and surface pressure up to maximum lift (32–34°)?
- Does it **find the stall** — the abrupt loss of lift after maximum lift (in the experiment, near 36°)? Values after the stall are not treated as reliable; the question is only whether the stall is found or not.

Only Configuration 1 is reported here.

24.3 Reference Solution and Data

Item	Setting
Experiment	NASA LaRC 14×22 ft, Test 513, Run 105 (increasing), corrected to free air, Re 4.6×10^6; Run 106 (decreasing) shown for the hysteresis
Comparison band	95% repeatability interval over three test campaigns ('98, '02, '03)

24.4 Simulation Conditions

Item	Setting
Geometry	NASA Trap Wing, Configuration 1 (slat 30° / flap 25°), half model, free air; the mesh appears to contain no support bracket (not checked directly)
Analysis	Steady, compressible DBNS, RANS, fully turbulent
Mach / Reynolds number	M=0.2, Re_MAC=4.3×10^6, T=288.889 K
Reference quantities	Half-wing reference area 22.028 ft², MAC=39.634 in, moment reference at x=34.342 in (quarter MAC)
Angles of attack	6°, 13°, 21°, 28°, 32°, 34°, 37°



Figure 24.1: Trap Wing geometry: slat, main element, flap, and fuselage

> **Note**
>
> **Differences from the experiment.** The simulation is a free-air half model without a support bracket (as far as could be checked) and with a Reynolds number (`4.3×10^6`) slightly below the tunnel's. The workshop participant band in the force chart below was read from a published figure (AIAA 2011-939, Fig. 2, 37 submissions on the medium mesh) and is an approximation, not the submitted data.

24.5 Mesh

Item	Setting
Mesh	HiLiftPW-1 unstructured mixed mesh, from-tet, node-centered (`Unst-Mixed-FromTet-Nodecentered-A-v1`), Configuration 1, **medium** level — 11,047,965 nodes, 38,665,677 elements (tetrahedra, pyramids, prisms), used as distributed by the workshop

24.6 Boundary and Initial Conditions

N/A: Detailed boundary-condition settings are not documented in this case.

24.6.1 Initial field and procedure

The same input was run in two ways, and the results differ at high angle of attack.

- **Free-stream start.** Every angle started from a uniform free-stream field (=6°, 13°, 21°, and also 28°, 32°, 34°, 37°).
- **Continued start.** For =28°, 32°, 34°, and 37°, the initial field was the converged solution of the previous angle (21° → 28° → 32° → 34° → 37°). Only the flow field was read; iteration count and CFL started from zero.

=6°, 13°, and 21° were run from the free stream. The =13° and 6° runs were extended beyond 10,000 iterations.

24.7 Numerical Methods

Item	Setting
Turbulence model	SA-neg (shat_form: blend2012; ft2, QCR, rotation correction off), Pr_t=0.9, farfield nu_tilde/nu = 3
Convective scheme	Roe, U-MUSCL kappa=0.5, second order
Gradients / limiter	Green–Gauss physical gradient, least-squares reconstruction gradient, edge-based van Albada limiter
Time integration	Euler implicit; FGMRES; adaptive CFL, 2 → 30 (per point); iteration limit 10,000 per angle

24.8 Results

24.8.1 Forces and Moment

The values below are averages over the last 200 iterations, with the experimental 95% band for the same angle. Coefficients are shown to four decimals.

[°]	Start	CL	CD	CMy	CL band	CD band	In band (CL / CD)
6	free stream	1.5069	0.1987	−0.4802	1.4980–1.5540	0.1990–0.2090	yes / on the edge (−0.0003)
13	free stream	1.9949	0.3218	−0.4700	2.0140–2.0700	0.3270–0.3430	no (−0.0191) / no (−0.0052)

[°]	Start	CL	CD	CMy	CL band	CD band	In band (CL / CD)
21	free stream	2.5167	0.5022	−0.4622	2.5380–2.5950	0.5060–0.5420	no (−0.0213) / no (−0.0038)
28	previous angle	2.8920	0.6766	−0.4438	2.8860–2.9420	0.6640–0.7130	yes / yes
32	previous angle	2.9887	0.7552	−0.3964	2.9790–3.0350	0.7380–0.7880	yes / yes
34	previous angle	2.9984	0.7850	−0.3621	2.9740–3.0310	0.7610–0.8100	yes / yes

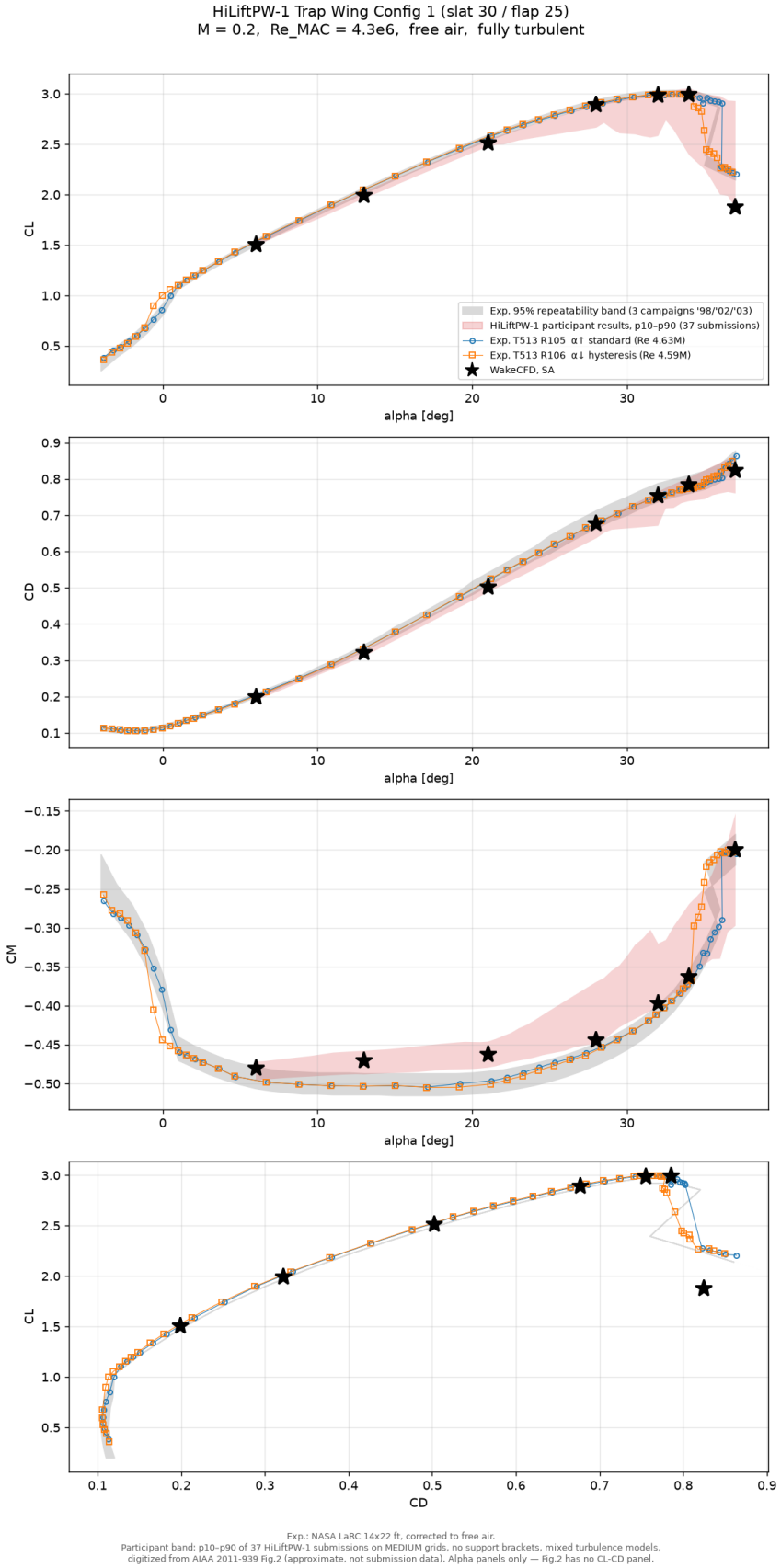


Figure 24.2: Lift, drag, pitching-moment coefficients and polar versus angle of attack — experiment (Run 105 and Run 106), workshop participant band, and Wake CFD. The `=37°` point is not a converged value (see the stall section).

- **Up to maximum lift the forces follow the experiment.** `=28–34°` is inside the band for both `CL` and `CD`, including the maximum-lift region (`CL 2.99–3.00` at `=32–34°`).
- **At `=13°` and `21°` the lift is slightly below the band** (`CL` −0.02, `CD` −0.004 to −0.005). With a single mesh level it is not possible to say whether this is a mesh effect or a model effect.
- **`CMy` is less negative than the experiment at `=6–21°`** by 0.02–0.03; the workshop participant band lies on the same side. It is not a Wake CFD-specific deviation as far as this comparison can tell.

24.8.2 Surface pressure

Spanwise sections at 17%, 50%, 85%, and 95% of the semi-span, against the experimental pressure taps at `=12.99°`, `28.41°`, `31.95°`, and `33.95°`.

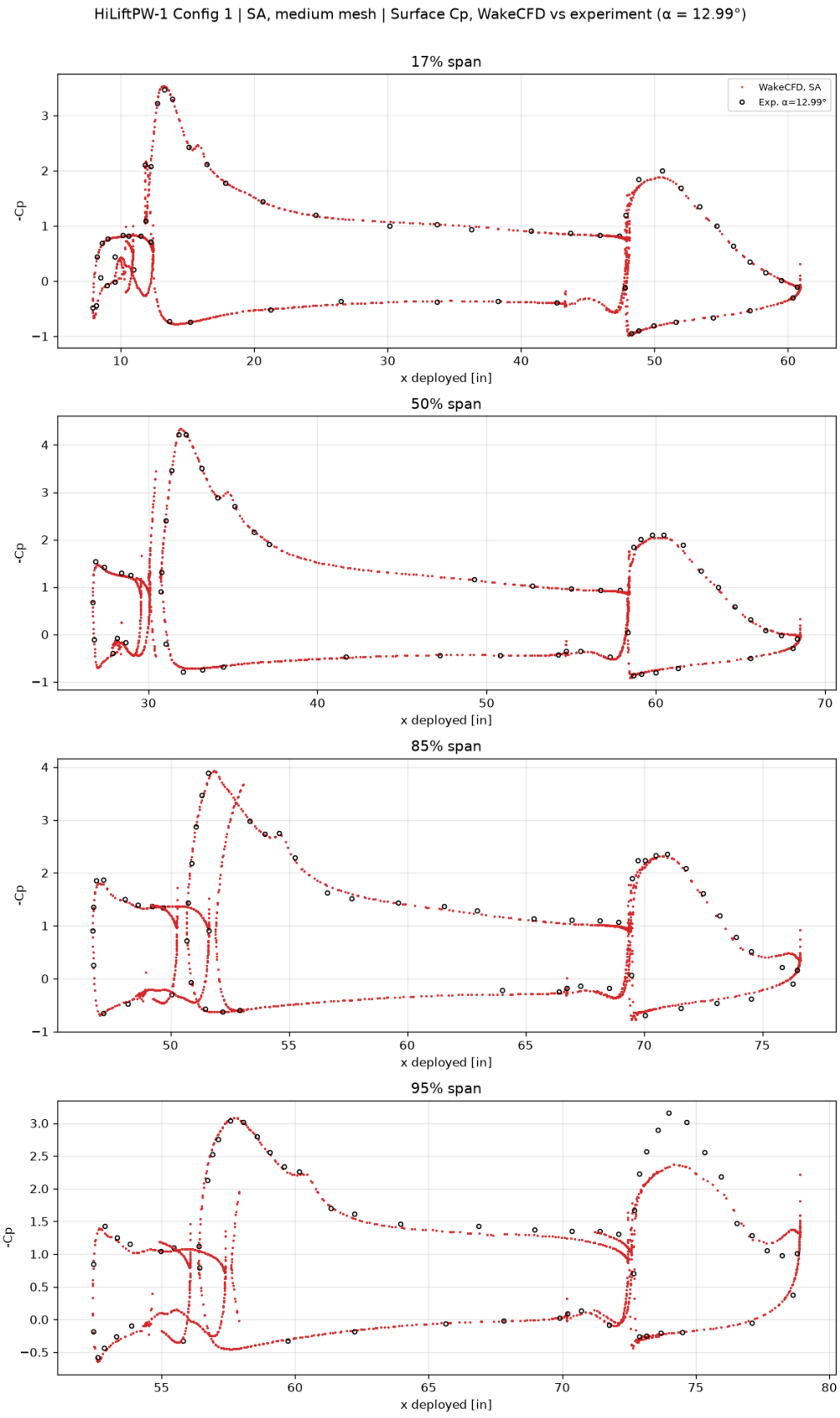


Figure 24.3: Surface pressure coefficient at =13°

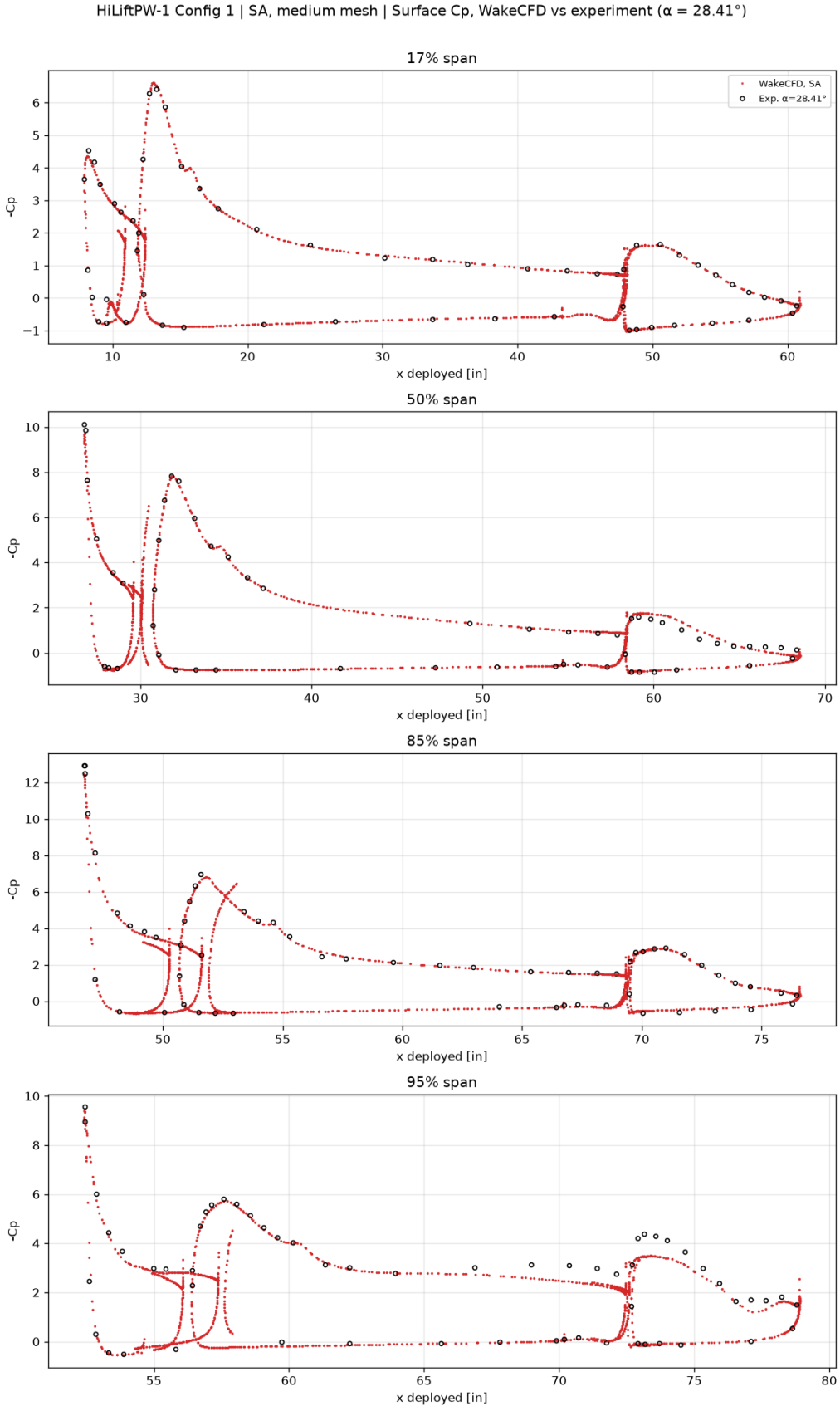


Figure 24.4: Surface pressure coefficient at =28°

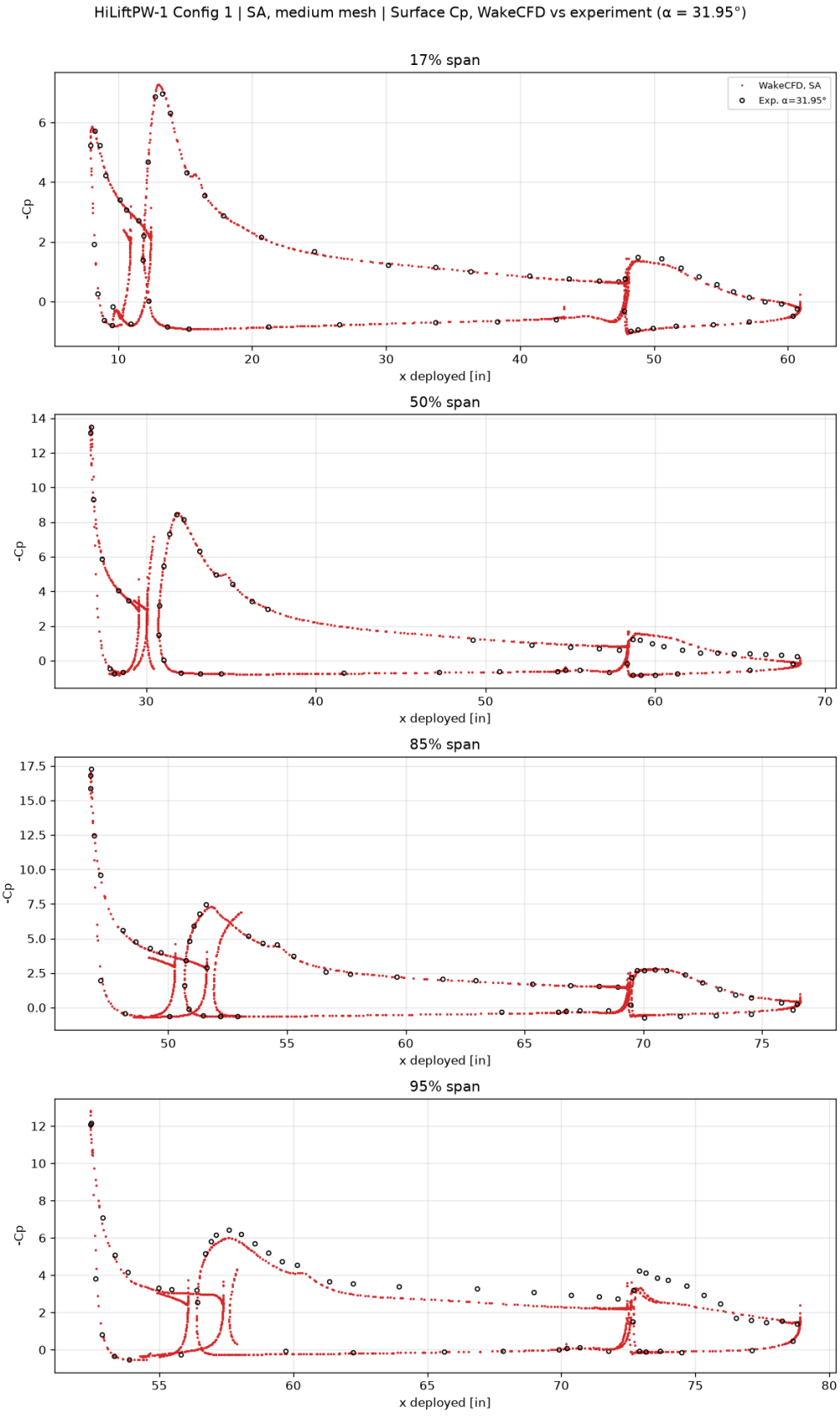


Figure 24.5: Surface pressure coefficient at =32°

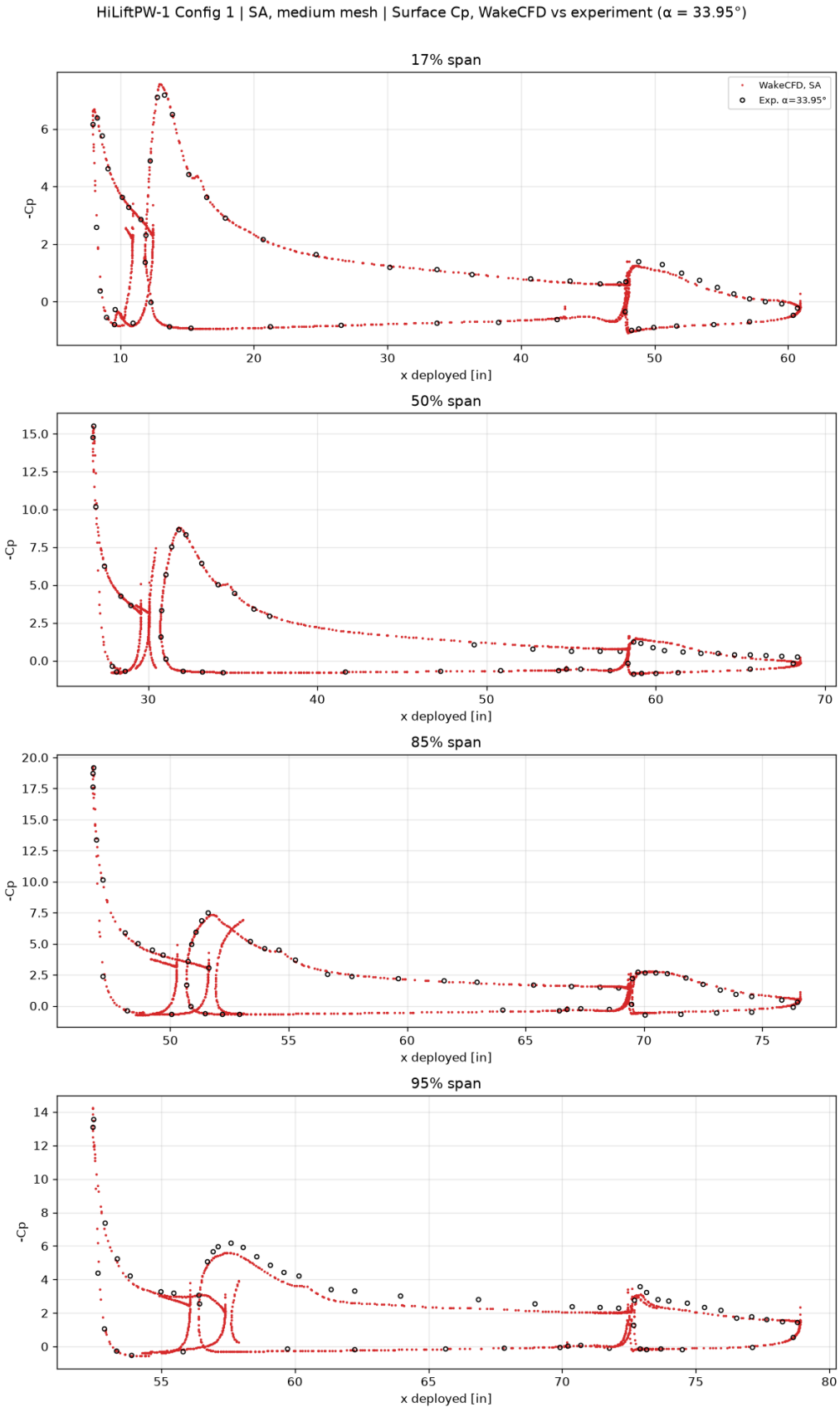


Figure 24.6: Surface pressure coefficient at =34°

At 17%, 50%, and 85% span the slat, main-element, and flap suction peaks overlap the experimental points at all four angles. **At 95% span (near the wing tip) the main-element and flap suction is weaker than in the experiment** — at `=32°` the main-element peak `-Cp` is about 6.0 against 6.4, and the flap peak about 3.2 against 4.2; `=34°` shows the same trend. The wing-tip vortex strength or position may be predicted differently, but this was not investigated. The tangled curves where the slat and main element overlap come from the planar section cutting several elements at once and are a post-processing effect.

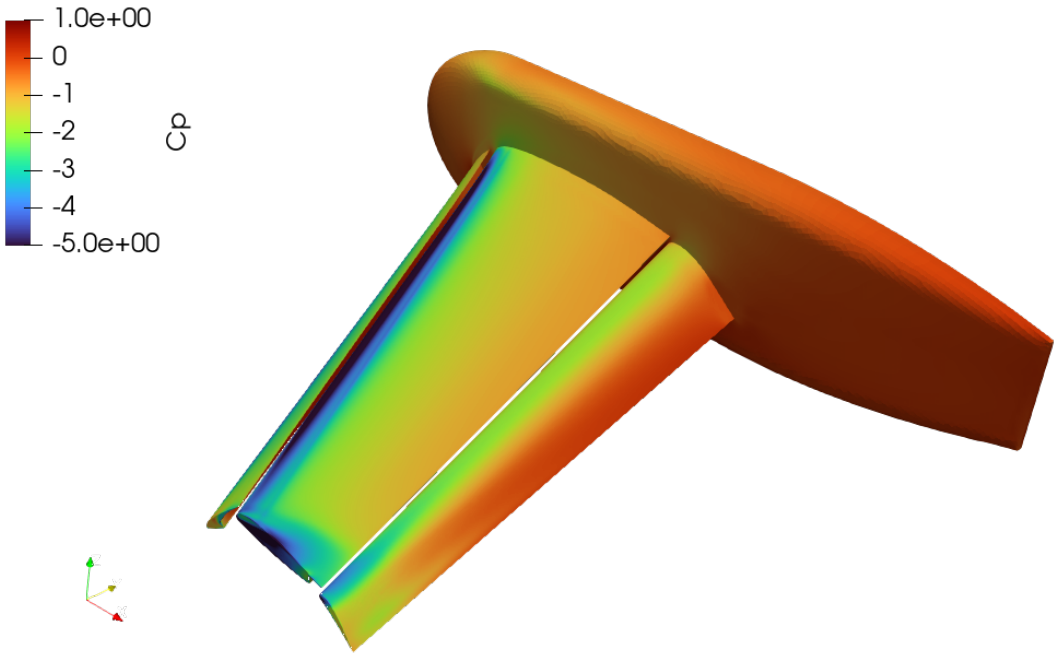


Figure 24.7: Surface `Cp` at `=21°` (color range −5 to 1; stronger suction is saturated)

24.8.3 Is the Stall Found?

In the experiment, the lift stays near its maximum (`CL 3.0`) through `34-35°` and then drops abruptly near `36°` (Run 105: from 2.91 to 2.28). At `=37°` the experiment gives `CL=2.2065`, `CD=0.8637`.

Wake CFD maximum lift is reproduced; the stall is not established.

- **Continued from the previous angle (`=37°` after `34°`).** The solution starts attached (`CL 2.95-2.96`), holds for the first 1,000–2,000 iterations, and from about iteration 3,000 the lift falls: `CL=2.79` (3,000), `2.40` (4,000), `2.25` (5,000), `2.12` (6,000), `1.96` (8,000), `1.87` (10,000). The lift drops through the experimental post-stall value (2.2) and keeps falling; at the end of 10,000 iterations it is still changing by about −0.036 per 1,000 iterations. **This is not a steady state**, so neither the stall angle nor the post-stall level (1.8787 in the chart) can be read from it.
- **Started from the free stream (`28°`).** The solutions settle in a different, separated state with lift far below the experiment at the same angle: `CL=2.0270` at `28°` (band 2.886–2.942), and 1.6162 / 1.6102 / 1.5918 at `32°` / `34°` / `37°`. The same mesh, model, and settings give

a different steady state depending on the initial field at high angle of attack. It was not determined whether the free-stream solution is a non-physical early separation caused by SA-neg and the medium mesh, or a second branch of the steady equations. The experiment shows only the attached branch at =28°.

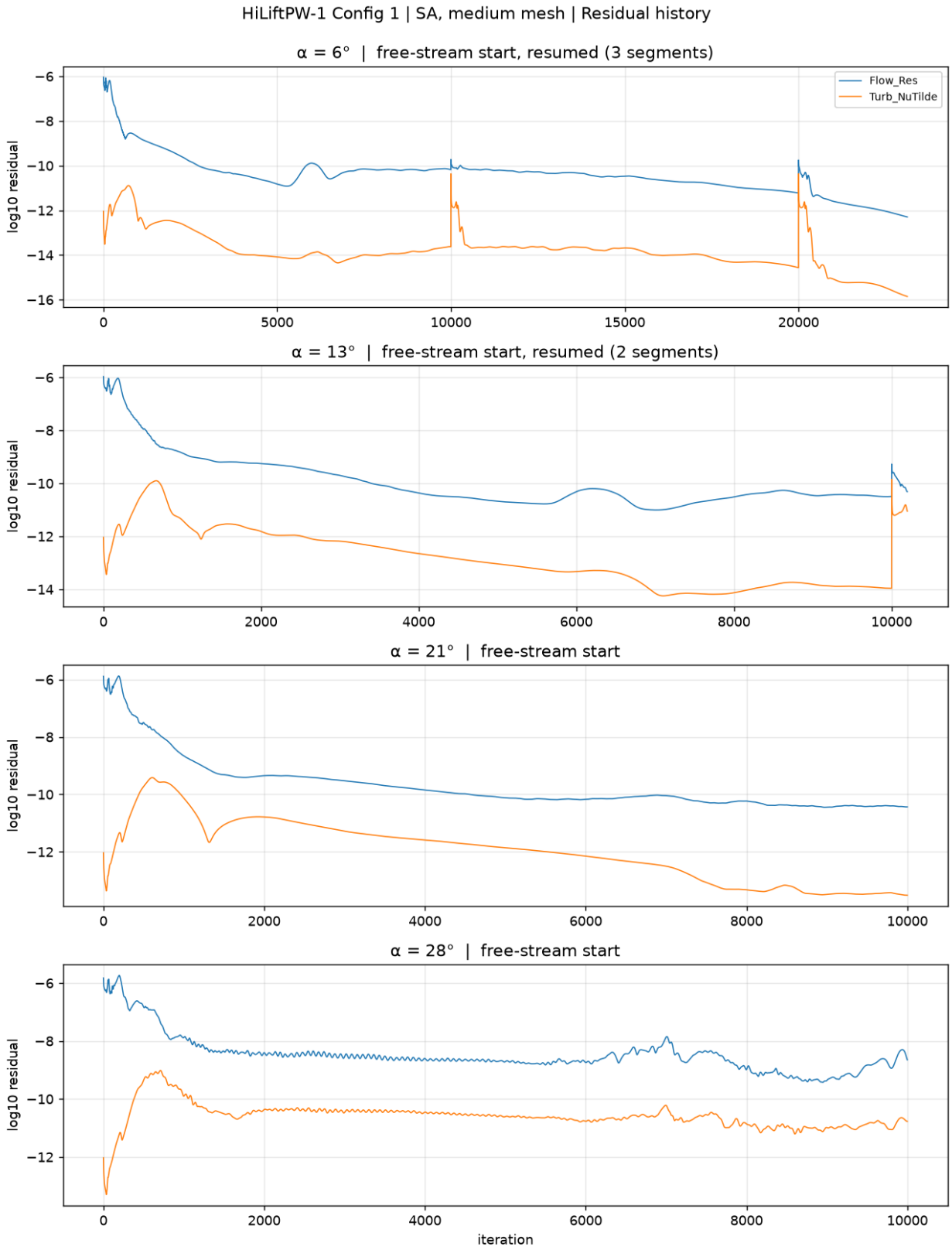


Figure 24.8: Residual history, free-stream start

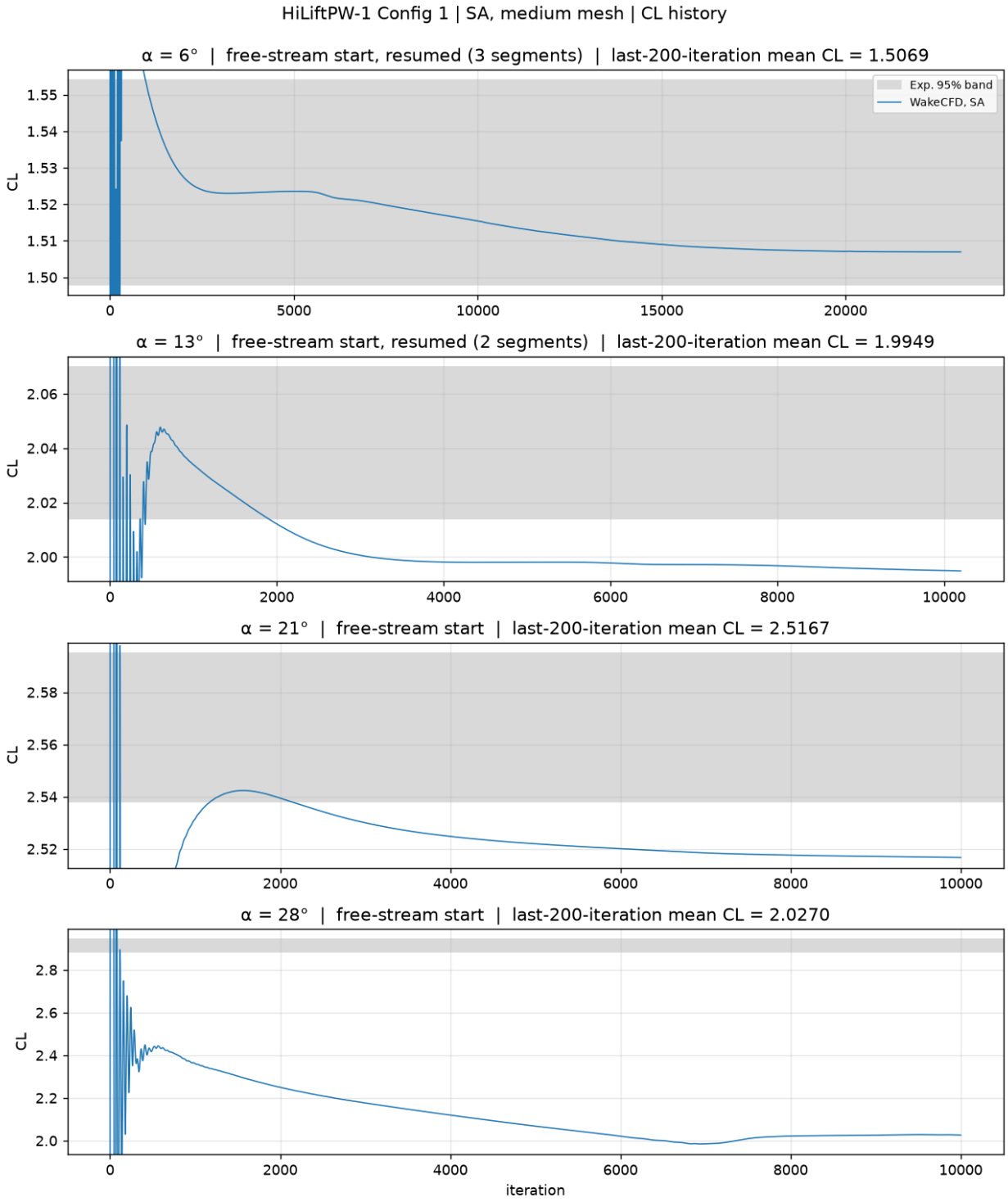


Figure 24.9: `CL` history, free-stream start. At `=28°` the lift decreases steadily from the start and settles near 2.03.

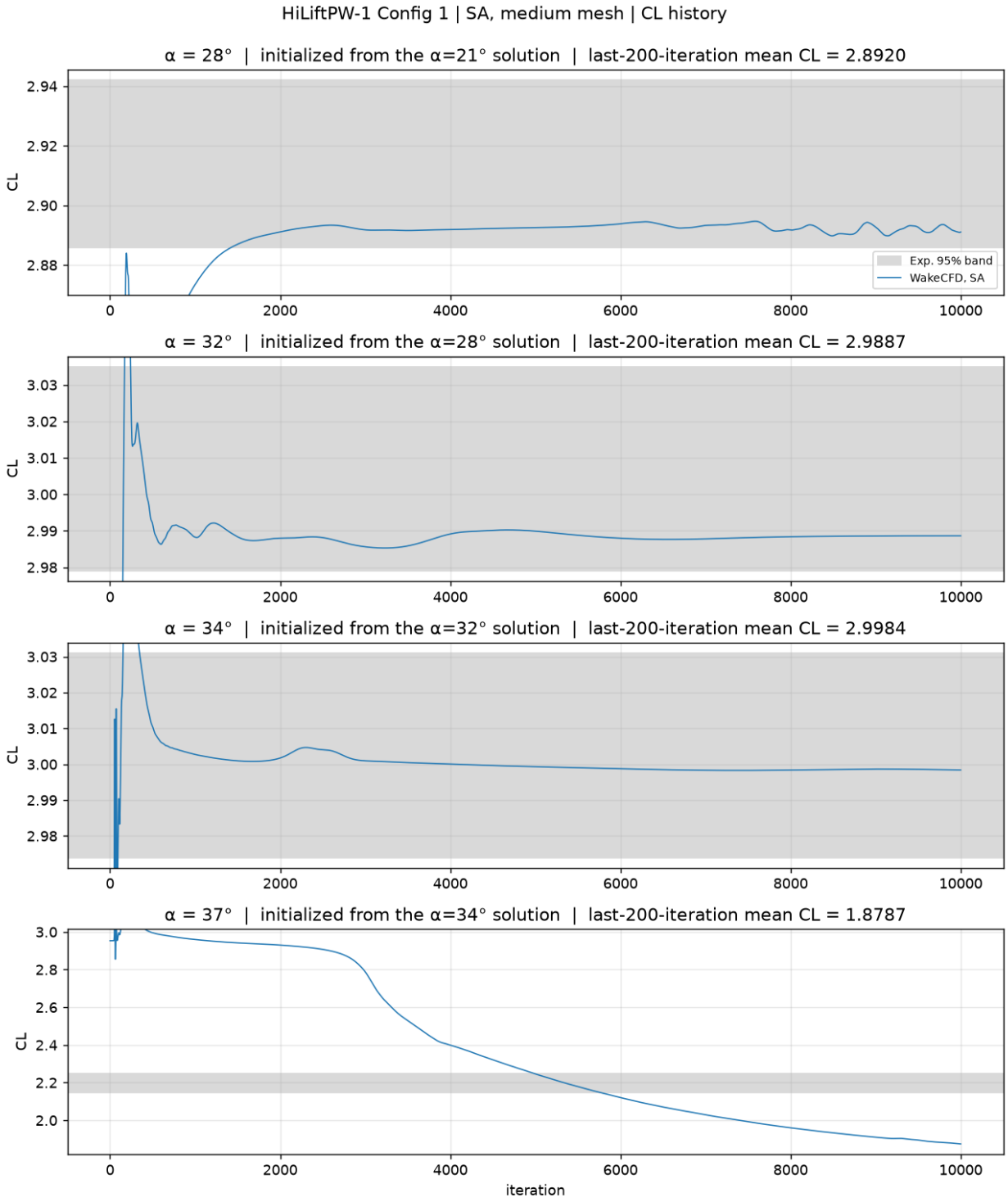


Figure 24.10: `CL` history, continued start. `=37°` falls from about iteration 3,000 and does not settle.

What can be stated. Maximum lift near `=32–34°` is reproduced when the high-angle solutions are continued from the lower angle. A loss of lift does appear at `=37°`, in the direction of the experimental stall, but it does not converge and it is not a prediction of the stall angle or of the

lift after the stall. The experiment also shows a large hysteresis between increasing and decreasing angle near `36°`; only the increasing-angle path was computed.

24.8.4 Convergence History

Iterative convergence was checked on the change of `CL` over the last 1,000 iterations: below 0.002 at `=6-34°` (continued start). The flow residual finished near −10 for `=6-34°` (down to −12.3 at `=6°` after the extension; −8.7 at `=28°` free-stream start). Residual and CFL histories are shown for each way of starting. The adaptive CFL reaches its limit of 30 within about 30–35 iterations and stays there.

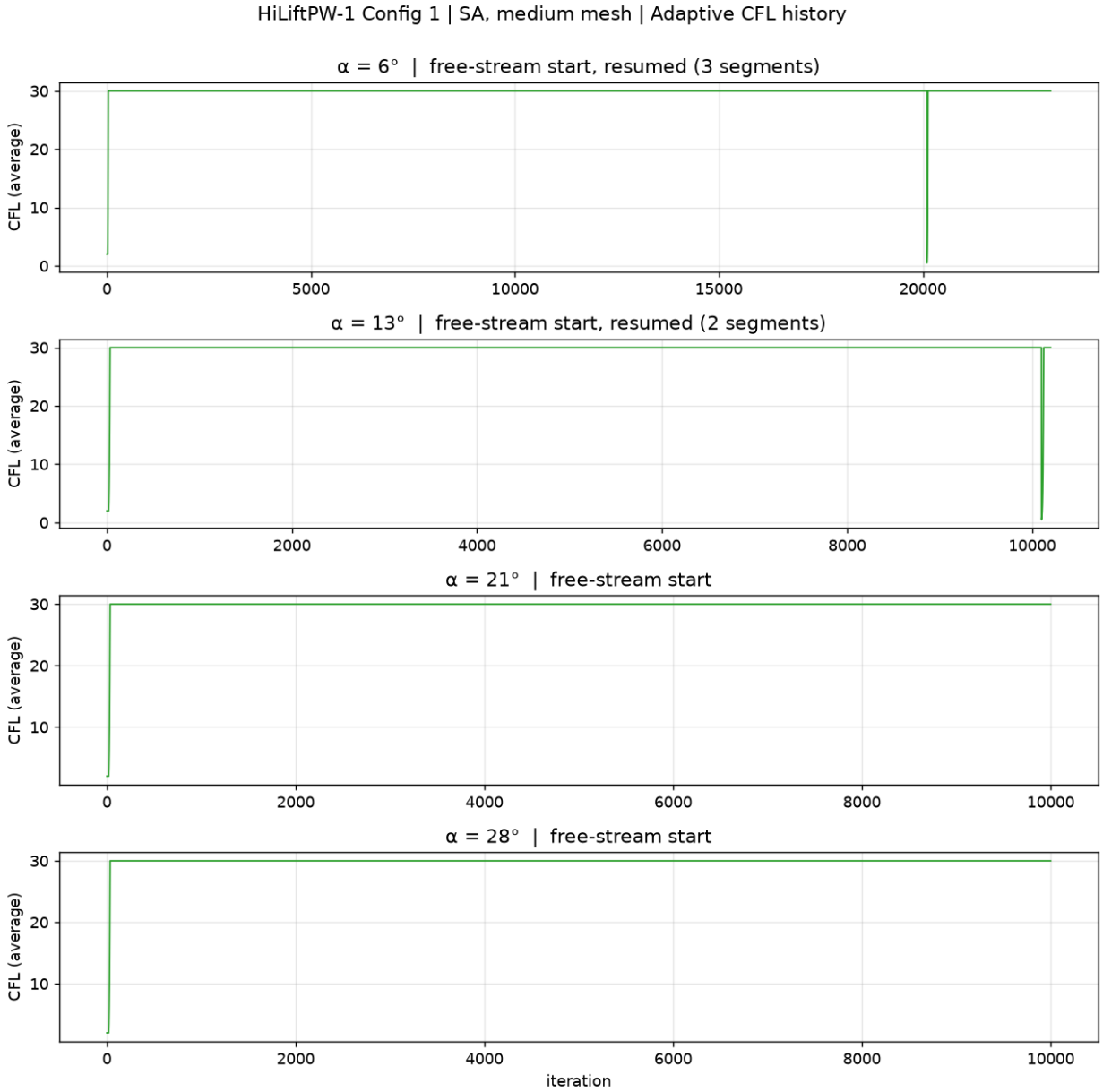


Figure 24.11: Adaptive CFL history, free-stream start

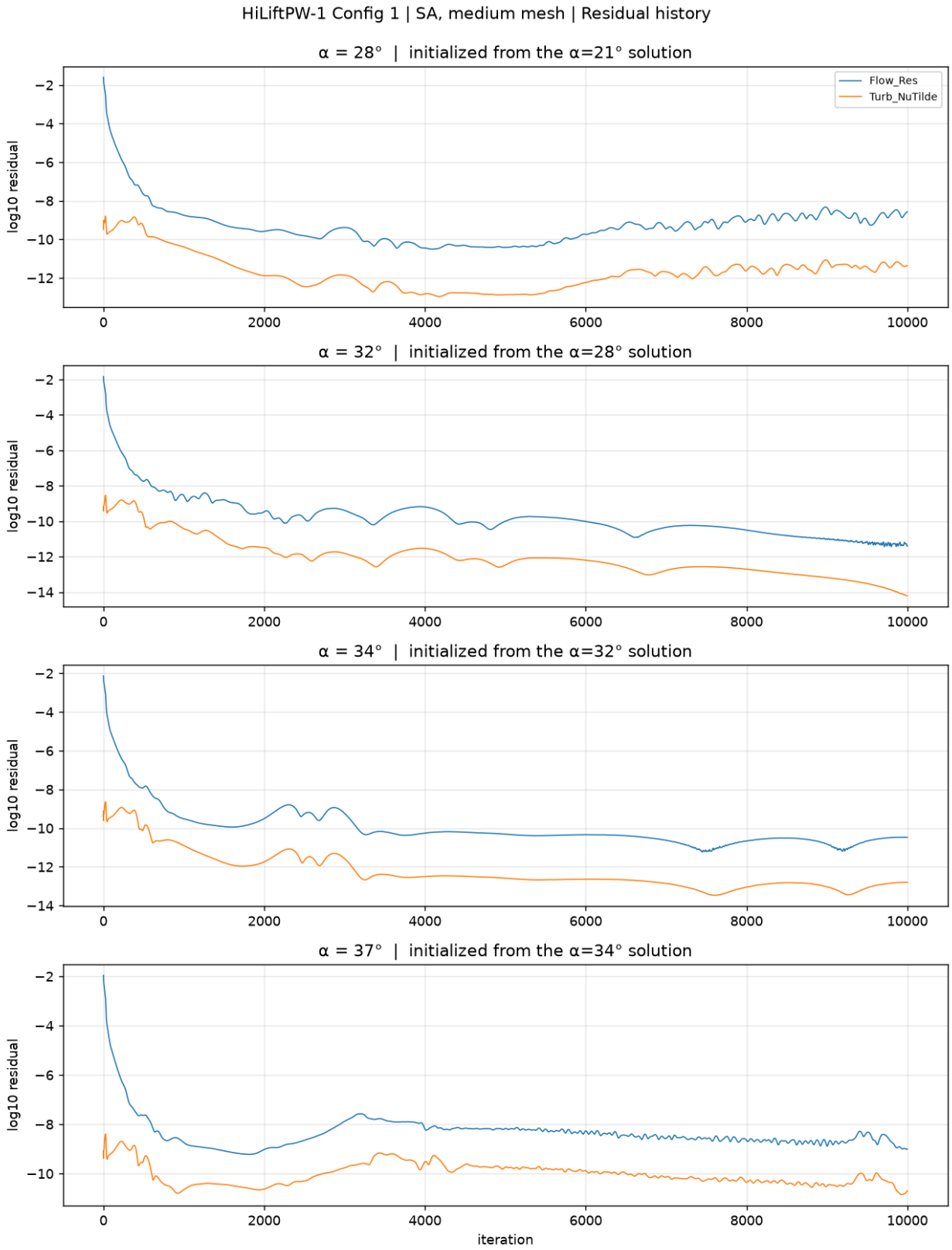


Figure 24.12: Residual history, continued start

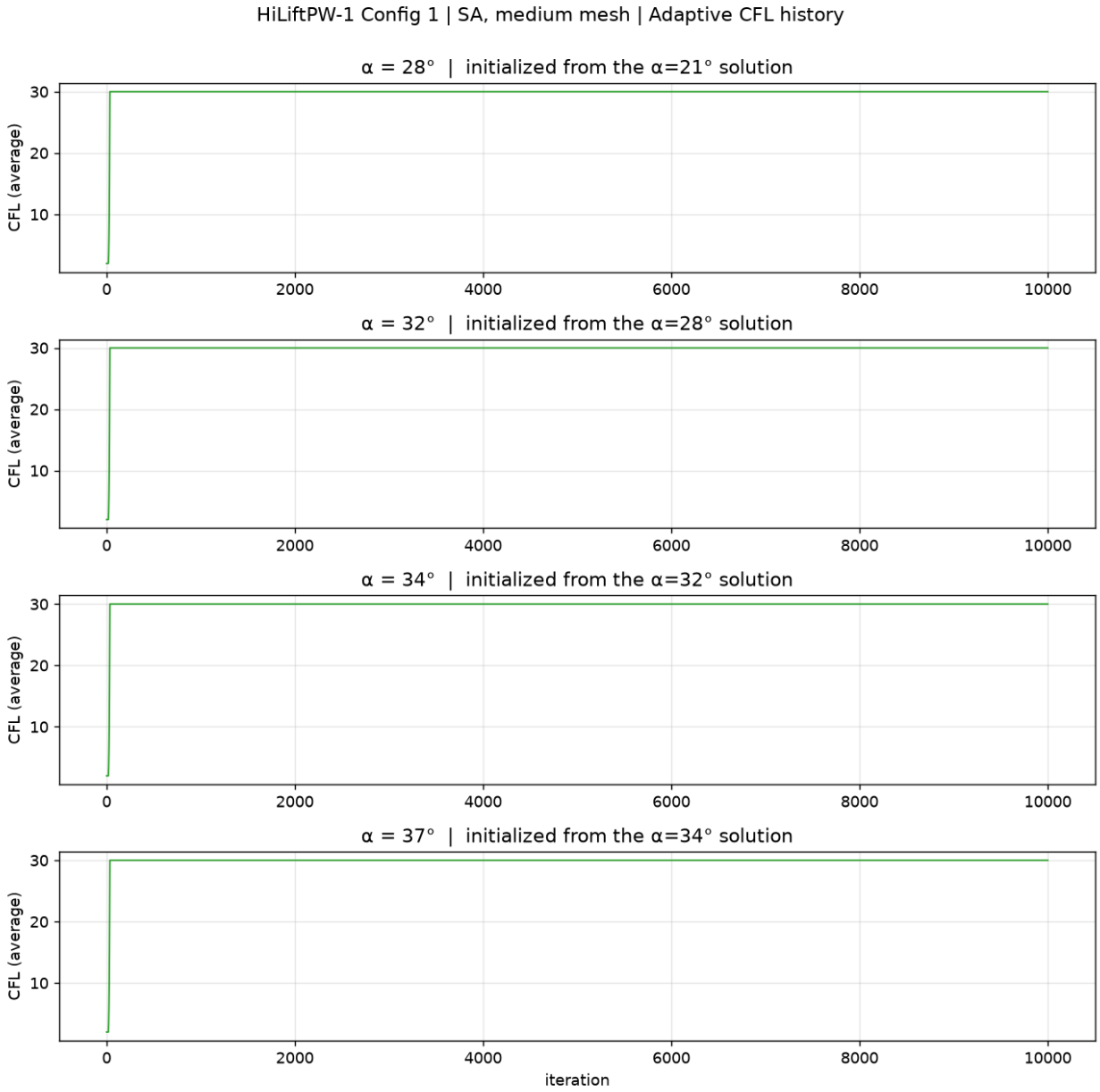


Figure 24.13: Adaptive CFL history, continued start

- Spikes in the `=6°` and `13°` histories mark the points where the run was extended beyond 10,000 iterations; the converged coefficients were not affected.
- **`=28°` shows a weak oscillation** after iteration 6,500: period about 700 iterations, `CL` peak-to-peak 0.0047 (0.16% of the mean). Whether it is physical unsteadiness or an iterative limit cycle was not determined. `=32°` and `34°` show no such oscillation.

24.9 Conclusions and Applicable Scope

- For `=28-34°` — the range around maximum lift — Wake CFD with SA-neg gives `CL` and `CD` inside the experimental 95% band, together with surface pressure that matches the experiment at 17–85% span.
- **The stall is not found in a usable way.** At `=37°` the lift starts to fall but does not settle in 10,000 iterations, and the free-stream-started solutions at `28°` converge to a different, separated state. The results after the stall are not reliable, and no stall angle is claimed.
- The solution at `28°` depends on the initial field. Results at these angles are valid only for the continued-start procedure described above.
- At `=13°` and `21°` the lift and drag are slightly below the band; with one mesh level this cannot be attributed.
- Surface pressure near the wing tip (95% span) is weaker than the experiment; the cause was not investigated.
- **Not done:** mesh-level (coarse, medium, fine) convergence; Configuration 8; the decreasing-angle (hysteresis) path; a converged `=37°` solution.
- These results apply to this mesh, this half-model free-air setting, and `M=0.2`. They cannot be extended to other flap/slat settings, higher Reynolds numbers, or tunnel-wall and support effects.

24.10 References

- NASA HiLiftPW-1: 1st AIAA CFD High Lift Prediction Workshop
- Rumsey et al., "Summary of the First AIAA CFD High-Lift Prediction Workshop," AIAA 2011-939 (also *J. Aircraft* 48(6), 2011)
- NASA LaRC 14×22 ft Trap Wing experiment, Test 513 (Run 105/106)

Part VIII

Axisymmetric Bodies

25 3D Sphere Bow Shock — Stand-off Distance Validation

Shock stand-off distance and stagnation pressure against the Billig (1967) correlation and the Rayleigh-Pitot relation, on a mesh-refinement sequence

25.1 Run Provenance and Artifacts

Item	Value
Wake CFD baseline version	`0.22.0`
Solver	DBNS
Compute device	GPU (NVIDIA RTX A6000)
Parallel execution	1 MPI rank
Arithmetic precision	FP64
Run date	2026-09-22

> **Note**
>
> Results depend on the solver build that produced them. Read every figure in this report together with the version and date above — re-running the same input on a later build may give different numbers.

25.1.1 Downloadable Files

Not available: standalone input decks and solver result files have not yet been published for download.

25.2 Validation Objective

This case checks whether Wake CFD's 3D Euler solver captures the detached bow shock ahead of a sphere in supersonic flow at the correct stand-off distance and stagnation pressure. The reference is the Billig (1967) shock stand-off correlation together with the normal-shock (Rayleigh-Pitot) relation applied along the stagnation streamline — both are correlations fitted to experimental and

computational data, so this is a validation case per this report's classification convention (see Case Directory). Unlike an axisymmetric-stub approach, the mesh here is a genuine unstructured 3D tetrahedral mesh with no axisymmetric simplification.

25.3 Reference Solution and Data

Item	Setting
Reference	Billig (1967) shock stand-off correlation; Rayleigh-Pitot normal-shock relation

25.4 Simulation Conditions

Item	Setting
Geometry	Sphere, radius `R = 0.1 m`; farfield boundary at `0.6 m` (`= 6R`); half-domain (`z 0` symmetry plane)
Analysis	Steady, inviscid (Euler), ideal-gas air (`=1.4`)
Freestream	`M = 3.0`, `p = 101,325 Pa`, `T = 288.15 K`, zero angle of attack

Billig correlation (sphere, ideal gas): `Δ/R = 0.143·exp(3.24/Mω²)`, giving `Δ/R = 0.20497` and `Δ = 20.497 mm` at `Mω=3`.

Stagnation-streamline normal-shock relation gives the post-shock stagnation pressure `p ,` directly comparable to the CFD wall stagnation-point pressure: `p , = 1,222,077 Pa` at `Mω=3`.

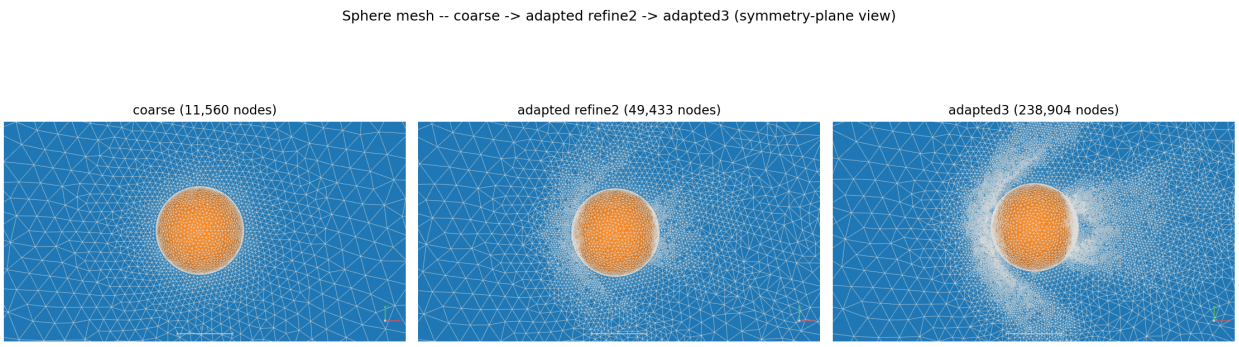


Figure 25.1: Mesh refinement sequence, symmetry-plane view: coarse → adapt3 → adapt4

25.5 Mesh

Item	Setting
Mesh sequence	Unstructured tetrahedral; `coarse` (uniform, `11,560` nodes) refined toward a solution-adaptive, shock-band-targeted sequence: `adapt3` (`238,904` nodes) and `adapt4` (`656,764` nodes)

25.6 Boundary and Initial Conditions

Item	Setting
Wall	Free-slip (inviscid)
Farfield	Single characteristic-based boundary covering both the upstream and downstream (wake) regions

Initial field: Not reported.

25.7 Numerical Methods

Item	Setting
Convective scheme	HLLC
Gradient method	Green–Gauss with Venkatakrishnan limiter
Time integration	Implicit, CFL constant `5.0`

25.8 Results

A clearly detached bow shock is reproduced at every mesh resolution, consistent with the expected qualitative feature of blunt-body supersonic flow:

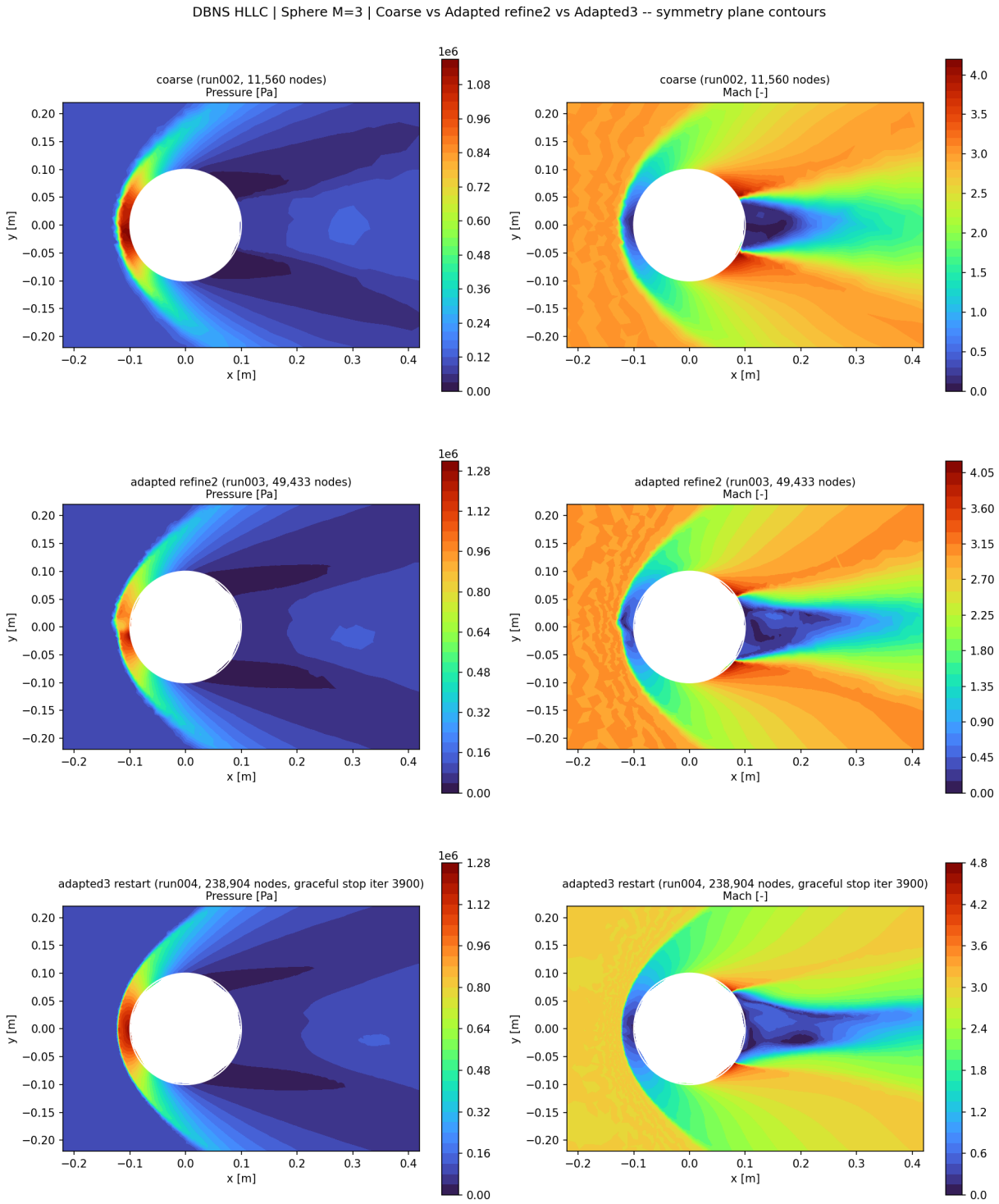


Figure 25.2: Symmetry-plane shock structure across the mesh sequence: coarse, adapt3, adapt4

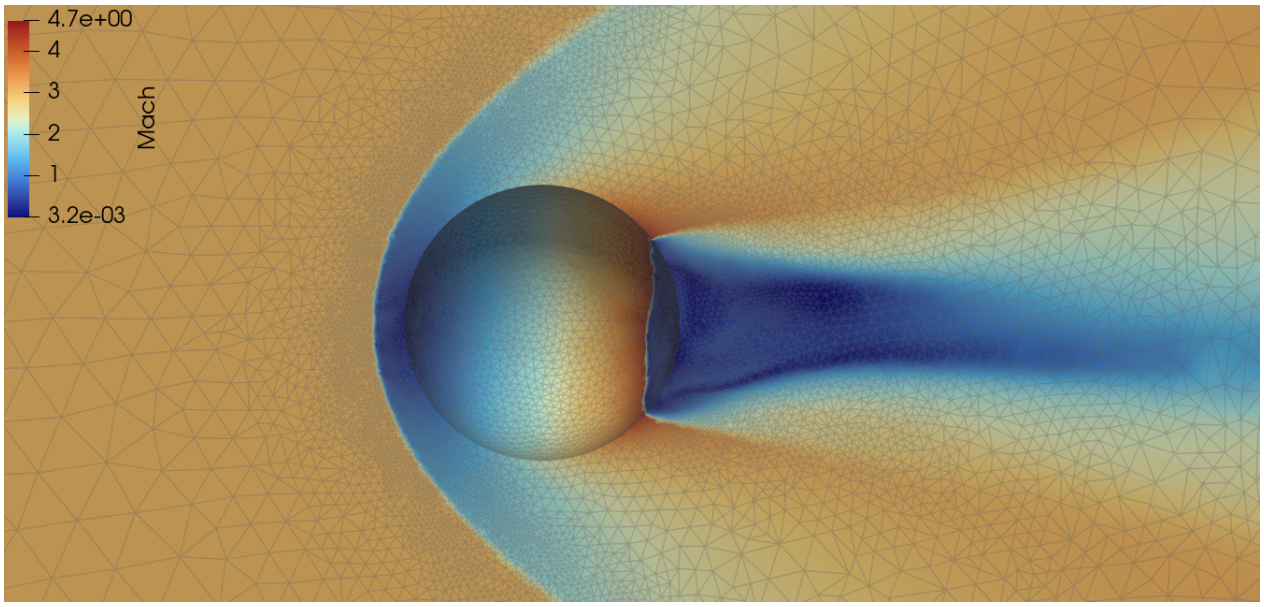


Figure 25.3: Mach-number contour with mesh overlay, finest (adapt3) mesh

Quantitative comparison against the Billig stand-off distance and the Rayleigh-Pitot stagnation pressure, along the stagnation streamline:

Mesh	Nodes	Stand-off distance Δ	Error vs. Billig	Stagnation pressure p_{t_2}	Error vs. Rayleigh-Pitot
coarse	11,560	23.18 mm	+13.1%	1,102,994 Pa	−9.7%
adapt3	238,904	**21.41 mm**	**+4.5%**	**1,222,333 Pa**	**+0.0%**
adapt4	656,764	21.73 mm	+6.0%	1,200,418 Pa	−1.8%

Refining from `coarse` to `adapt3` (shock-band-targeted adaptive refinement) substantially reduces the error in both metrics, with the stagnation pressure converging to the theoretical value. A further refinement step (`adapt3`→`adapt4`) does not continue this trend — the error increases slightly rather than decreasing further, indicating that `adapt3` is close to the practical resolution limit for this particular mesh sequence and quantity of interest, rather than errors decreasing monotonically without bound.

On the finest meshes (`adapt3`, `adapt4`), the density residual settles into a bounded oscillation rather than reaching the fully converged level obtained on the `coarse` mesh; integrated force coefficients and flow-field extrema were confirmed to settle to stationary values well before the run was stopped, and the reported stand-off distance and stagnation pressure are based on these settled states. The stand-off distance itself is resolved over only a few mesh cells (it is comparable in size to the local cell spacing near the shock even on the finest mesh), so its precise numerical value carries a meaningfully larger uncertainty than the stagnation-pressure comparison.

25.9 Conclusions and Applicable Scope

- Wake CFD's 3D Euler solver reproduces a correctly detached bow shock with stand-off distance and stagnation pressure matching established correlations to within a few percent on a refined mesh (`Δ`: +4.5%, `p ,` : +0.0% at the best-resolved point in this sequence).
- Refinement reduces error up to a point (`coarse`→`adapt3`) but does not continue to do so indefinitely in this mesh sequence (`adapt3`→`adapt4` shows a small regression) — this result should be read as validation at the demonstrated resolution, not as evidence of unbounded grid convergence.
- The stand-off distance comparison carries larger relative uncertainty than the stagnation-pressure comparison, because the shock stand-off distance is resolved over only a few mesh cells even on the finest mesh used.
- This result applies to inviscid, supersonic (`M=3`), ideal-gas flow over a sphere at zero angle of attack. It does not establish accuracy for viscous (shock-boundary-layer interaction) effects, other Mach numbers, or non-spherical blunt bodies.

25.10 References

- Billig, F. S., "Shock-Wave Shapes Around Spherical- and Cylindrical-Nosed Bodies," *Journal of Spacecraft and Rockets*, 4(6), 1967, pp. 822–823.

26 Secant-Ogive-Cylinder — Static and Magnus Aerodynamic Coefficients

Static and Magnus (spin-induced side force) coefficients at Mach 3 against BRL supersonic wind-tunnel data

26.1 Run Provenance and Artifacts

Item	Value
Wake CFD baseline version	`0.22.1`
Solver	DBNS
Compute device	GPU (NVIDIA RTX A6000)
Parallel execution	1 MPI rank
Arithmetic precision	FP64
Run date	2026-09-21

> **Note**
>
> Results depend on the solver build that produced them. Read every figure in this report together with the version and date above — re-running the same input on a later build may give different numbers.

26.1.1 Downloadable Files

Not available: standalone input decks and solver result files have not yet been published for download.

26.2 Validation Objective

This case computes both static aerodynamic coefficients (normal force, pitching moment, axial force) and Magnus (spin-induced side force) coefficients for a secant-ogive-cylinder (SOC) projectile shape, and compares both against a single BRL supersonic wind-tunnel dataset that reports both quantities for the same model. It validates Wake CFD's rotating-wall boundary condition (`motion.type:`

rotating) against experimental Magnus data — the first such comparison in this report — using the static-coefficient agreement as a supporting check on mesh and numerical setup.

26.3 Reference Solution and Data

Item	Setting
Reference	Nietubicz and Opalka (1980), BRL Memorandum Report ARBRL-MR-02991

26.4 Simulation Conditions

Item	Setting
Geometry	Secant-ogive-cylinder (SOC), 6 calibers long (3-caliber secant ogive + 3-caliber cylinder), no boat-tail, flat sharp-cornered base; reference diameter `d = 57.15 mm`
Analysis	Steady, compressible DBNS, RANS (Spalart–Allmaras)
Mach	`3.0`
`Re_L` (body length)	`7.22×10` (freestream conditions from isentropic expansion of the tunnel stagnation state)
Angle of attack	`0°` to `10°` (static sweep, 6 points)
Spin rate `Pd/V`	up to `0.4` (Magnus sweep; `2215 rad/s` at `Pd/V=0.2`)
Nose tip	Blunted to `R_n = 0.5 mm` (`0.87%` of caliber) — the experimental model has a mathematically sharp secant-ogive tip, which cannot be meshed directly; this blunting radius is conservative relative to published precedent for similar shapes

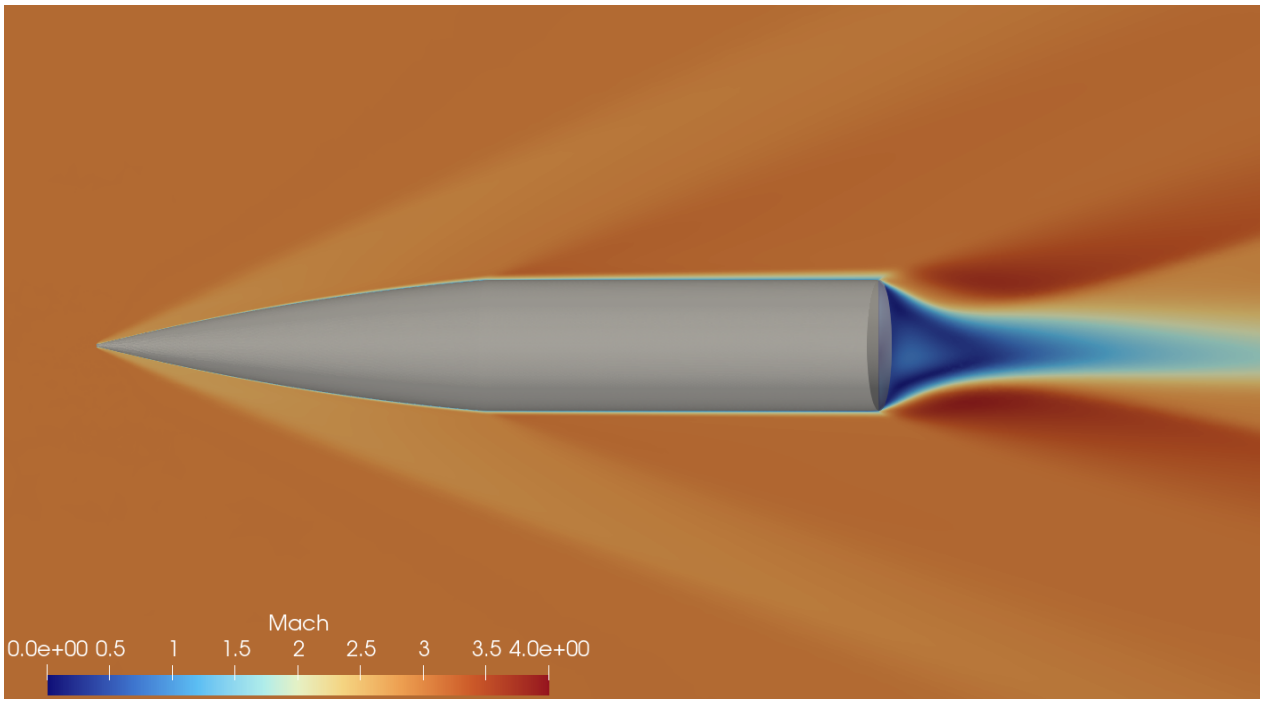


Figure 26.1: Mach-number contour, M=3, =0°: bow shock at the nose, expansion around the ogive-cylinder shoulder, and the base wake

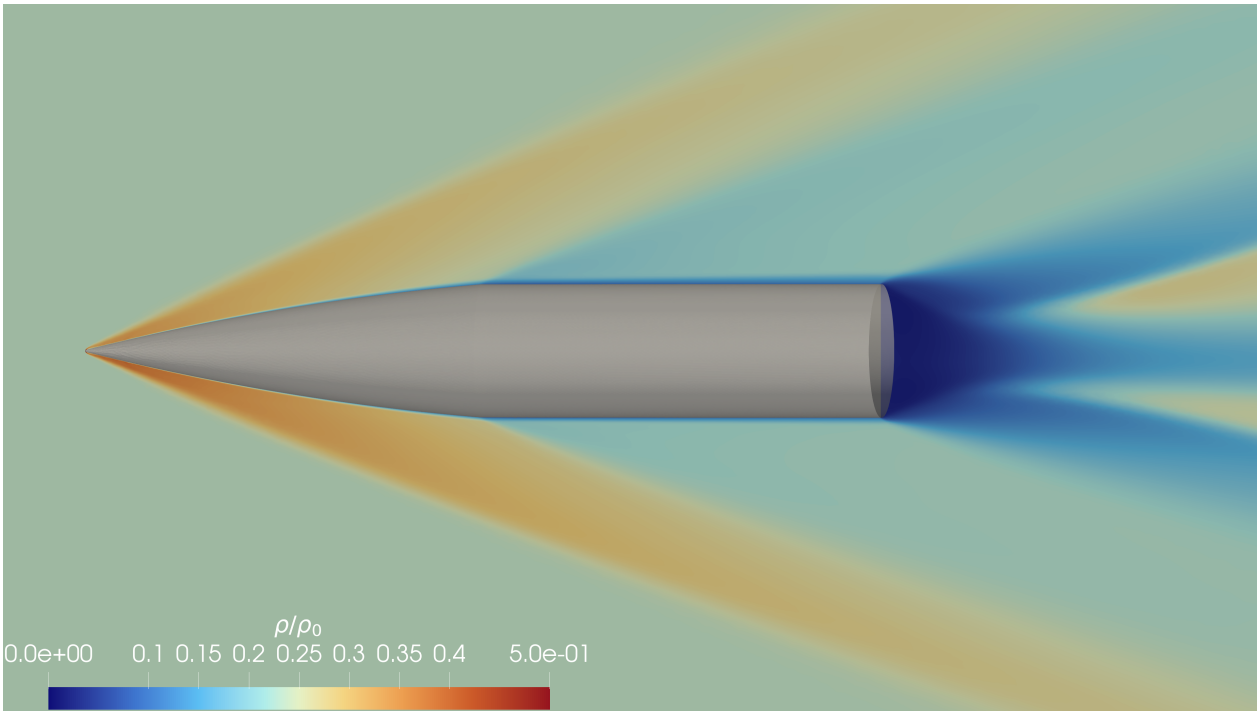


Figure 26.2: Density ratio (/) contour, M=3, =0°: shock and expansion structure along the body and into the base wake

26.5 Mesh

Item	Setting
Mesh	Unstructured tetrahedral + prism boundary layer, 12.9M cells, 2.7 µm first cell height (y 0.4 average on the cylinder)

26.6 Boundary and Initial Conditions

Item	Setting
Wall	No-slip, fully turbulent (no boundary-layer trip modeled)

Initial field: Not reported.

26.7 Numerical Methods

Item	Setting
Convective scheme	AUSM+-up2, 2nd order (Green–Gauss gradients, Venkatakrishnan limiter, coeff=0.01)
Time integration	Implicit, CFL schedule (low-CFL start, ramped)

26.8 Results

26.8.1 Static Coefficients

Mach 3, angle-of-attack sweep, compared against Table III of the reference (linear range) and digitized figure data (4°):

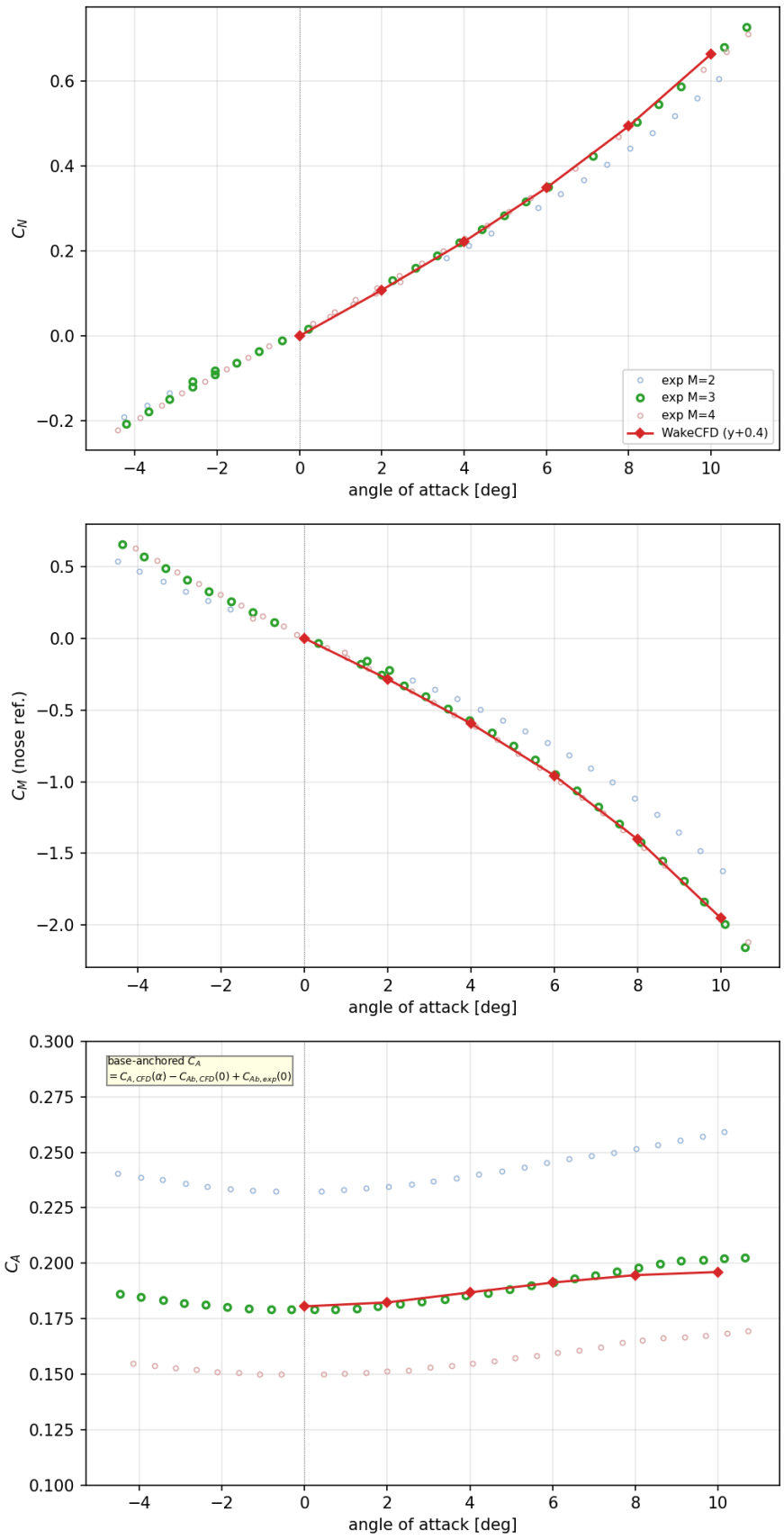


Figure 26.3: Static coefficients (`C_N`, `C_M`) versus angle of attack, CFD versus experiment

	C_N	Error	C_M	Error
0°	0.0000	—	0.0000	—
2°	0.1083	+0.4%	−0.2849	+1.0%
4°	0.2224	−1.9%	−0.5944	+3.1%
6°	0.3490	+0.0%	−0.9572	+1.7%
8°	0.4945	+1.2%	−1.4018	−0.0%
10°	0.6642	+1.9%	−1.9514	−0.7%

Normal force and pitching moment agree with the experiment within 3.1% across the full `0°–10°` range. Axial force comparison is complicated by base-flow contamination in the experimental setup (a balance-strut assembly and spin-drive turbine exhaust are present behind the model, so the reported experimental base pressure is not a free-flight value) — anchoring the CFD forebody-plus-base axial force to the experimental base-pressure level at `=0°` and tracking the CFD's own base-pressure variation with angle of attack gives agreement within 3% across the sweep; comparing against the experiment with a naive constant-base-pressure assumption instead produces a spurious 5.8% error at `=6°`, which is an artifact of that assumption rather than a modeling error.

26.8.2 Magnus Coefficients

Mach 3, `Pd/V = 0.2`, compared against Table IV of the reference (transcribed, not digitized):

	C_Yp error	C_np error	CPY (CFD / experiment)
1°	+8.5%	−1.2%	4.54 / 5.25
2°	+6.0%	−2.4%	4.56 / 4.86
4°	**−1.3%**	−7.3%	4.61 / 4.96
6°	**−1.7%**	−7.3%	4.68 / 5.02
10°	+19.6%	+18.6%	4.73 / 4.77

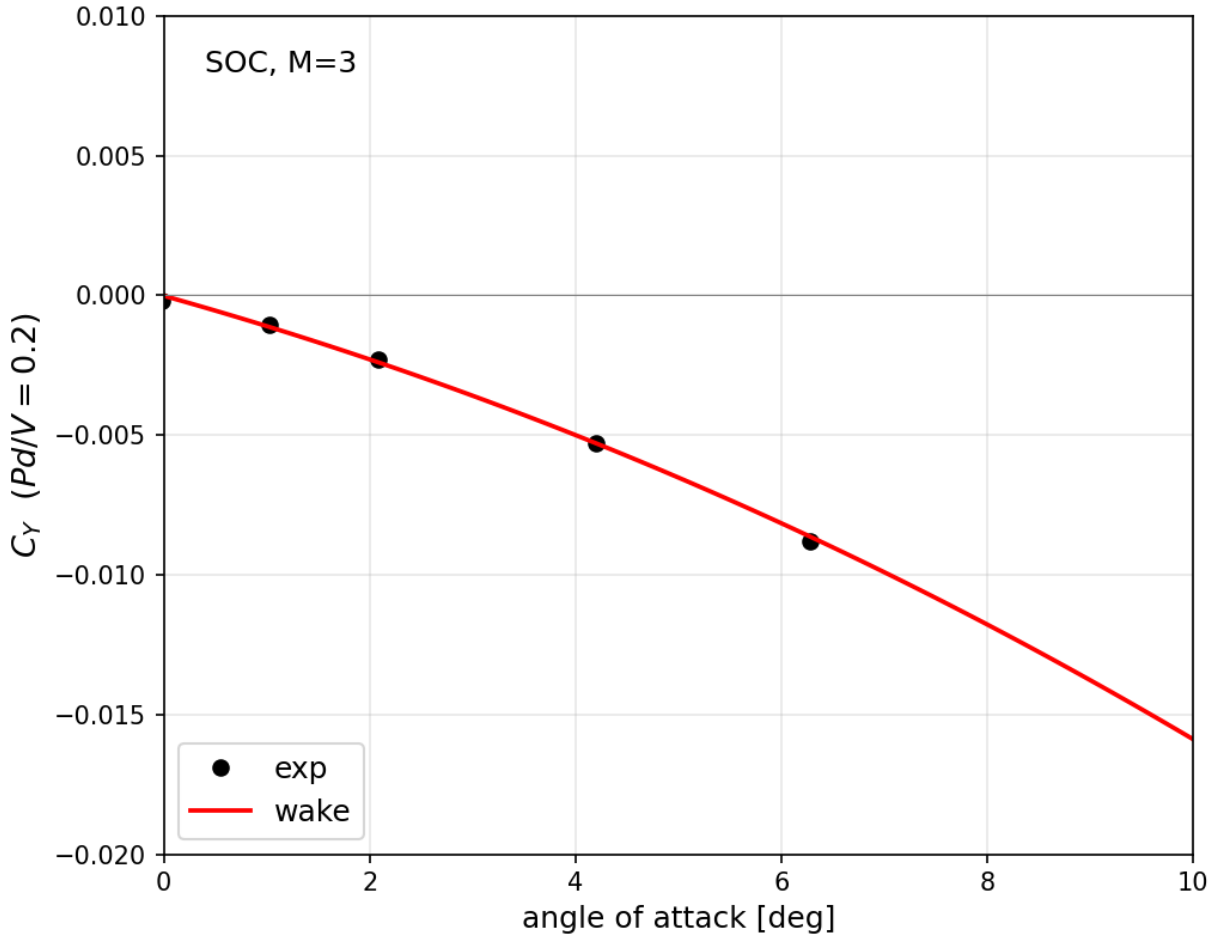


Figure 26.4: Magnus side-force coefficient `C_Yp` versus angle of attack, CFD versus experiment

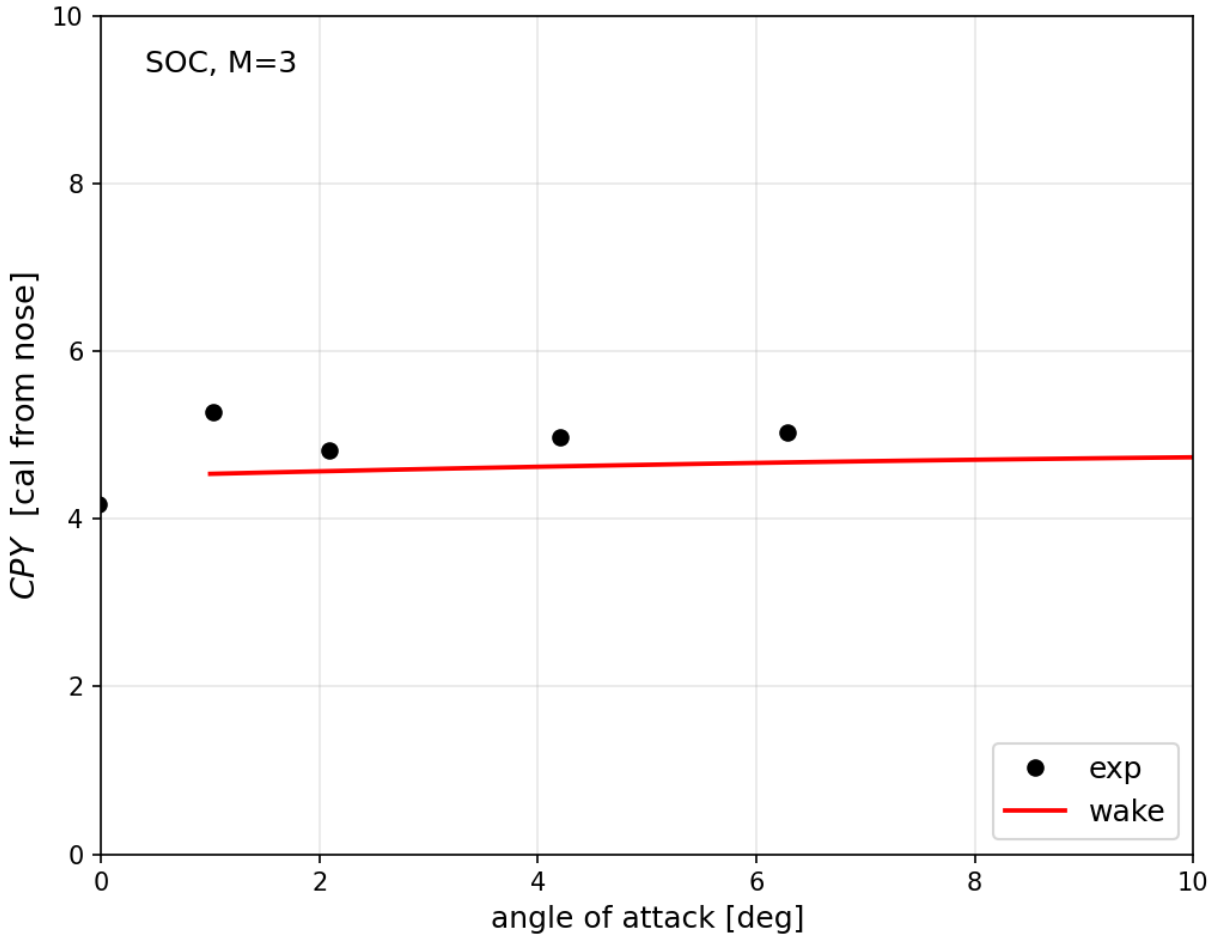


Figure 26.5: Magnus center of pressure `CPY` versus angle of attack, CFD versus experiment

At `= 4°` and `6°`, Magnus side force (`C_Yp`) agrees with experiment within 2%, but Magnus moment (`C_np`) is consistently further off (`-7.3%` at both angles) — the spin-induced side-force *magnitude* is well captured, but its *distribution* along the body is not: `CPY` (center of pressure `= C_np/C_Yp`, roughly) comes out systematically forward of the experimental value because the moment under-predicts by more than the force does. Averaged over `| | 2°`, `CPY = 4.65` calibers (CFD) versus `4.90` calibers (experiment), a 0.25-caliber (−5%) forward offset. At low angle of attack (`=1°-2°`), the experimental Magnus moment itself becomes poorly conditioned (the reference notes large measurement uncertainty in this range), which is the most likely explanation for the larger apparent deviation there. At `=10°`, both Magnus coefficients deviate by about 20% — the experiment shows Magnus force saturating with angle of attack while the CFD continues to grow faster than linearly; this deviation is within the experimental measurement uncertainty band that the reference itself reports as "large" for Magnus data, but it remains the one clearly open physical question in this comparison.

26.9 Conclusions and Applicable Scope

- Wake CFD's rotating-wall boundary condition produces Magnus side-force coefficients within 2% of experiment at =4° and 6°, and the underlying static coefficients (which share the same mesh and numerical setup) agree with experiment within about 3% across =0°–10°.
- The one clear open discrepancy is at =10°, where both Magnus coefficients deviate by about 20% in a way not explained by the rest of the comparison — within the experiment's own reported "large" uncertainty for Magnus measurements, but not yet independently resolved on the CFD side.
- **Grid convergence has not been performed for this case** — only boundary-layer (near-wall spacing) resolution was swept to convergence; a systematic volume-mesh refinement study (independent of boundary-layer spacing) has not been done. The reported agreement therefore reflects model accuracy combined with unquantified remaining discretization error, not model accuracy alone.
- The experimental nose tip is mathematically sharp; the CFD model uses a small blunting radius (0.87% of caliber) to permit meshing. The local pressure field near the tip differs as a result, though the integrated-force contribution of this region is negligible given its small area fraction.
- The experimental model's boundary-layer trip rings (three rings at 0.71 calibers from the nose) are not modeled; the CFD instead assumes a fully turbulent boundary layer from the nose. This is the most likely cause of the Magnus center-of-pressure offset: net Magnus force agrees with experiment within 2%, so the spin-induced side-force mechanism itself is captured correctly, but its distribution along the body depends on boundary-layer history, which differs between the tripped experiment and the untripped CFD. A follow-on run with the trip rings modeled is needed to confirm this and close the gap.
- This result applies to one geometry (SOC, no boat-tail), one Mach number (3.0), and the angle-of-attack and spin-rate ranges tested. It does not establish accuracy at other Mach numbers, for boat-tailed variants, or with the sting/base-flow hardware modeled explicitly.

26.10 References

- Nietubicz, C. J., and Opalka, K. O., *Supersonic Wind Tunnel Measurements of Static and Magnus Aerodynamic Coefficients for Projectile Shapes with Tangent and Secant Ogive Noses*, US Army Ballistic Research Laboratory, ARBRL-MR-02991, February 1980 (AD-A083297).

Part IX

Internal Flow

27 3D Supersonic Square Duct — SA-QCR2000 Secondary-Flow Validation

Confirmation that the Quadratic Constitutive Relation reproduces corner secondary flow, against the Davis-Gessner (1989) experiment and CFL3D/FUN3D reference solutions

27.1 Run Provenance and Artifacts

Item	Value
Wake CFD baseline version	`0.22.0`
Solver	DBNS
Compute device	GPU (NVIDIA RTX A6000)
Parallel execution	1 MPI rank
Arithmetic precision	FP64
Run date	2026-09-09

> **Note**
>
> Results depend on the solver build that produced them. Read every figure in this report together with the version and date above — re-running the same input on a later build may give different numbers.

27.1.1 Downloadable Files

Not available: standalone input decks and solver result files have not yet been published for download.

27.2 Validation Objective

This case checks whether Wake CFD's implementation of the Spalart Quadratic Constitutive Relation (QCR2000, `models.turbulence.sa.qcr2000`) reproduces corner secondary flow of the second kind in a supersonic square duct. A linear Boussinesq turbulence model (SA alone) cannot generate

this secondary flow by construction, so an SA-versus-SA+QCR2000 comparison gives an unambiguous physical pass/fail signal. Results are compared against the NASA Turbulence Modeling Resource (TMR) 3D Supersonic Square Duct case, which provides the Davis and Gessner (1989) experimental data together with CFL3D (SA) and FUN3D (SA-QCR2000) reference solutions on the same grid.

27.3 Reference Solution and Data

Item	Setting
References	Davis and Gessner (1989) experiment; CFL3D (SA) and FUN3D (SA-QCR2000), published by NASA TMR

27.4 Simulation Conditions

Item	Setting
Geometry	Square duct, `D = 25.4 mm`, domain length `52D`; one-quarter model with two symmetry planes and two viscous walls
Analysis	Steady, compressible DBNS, RANS (SA, run with and without QCR2000)
Inflow Mach	`3.9` (uniform inflow; boundary layer develops from the duct entrance)
`Re_D`	`0.508×10`
Freestream temperature	`288.889 K`
Viscosity law	Sutherland
Judgment stations	`x/D = 40, 50` (fully turbulent region only, per the case's own transition-delay caveat for `M>2`)

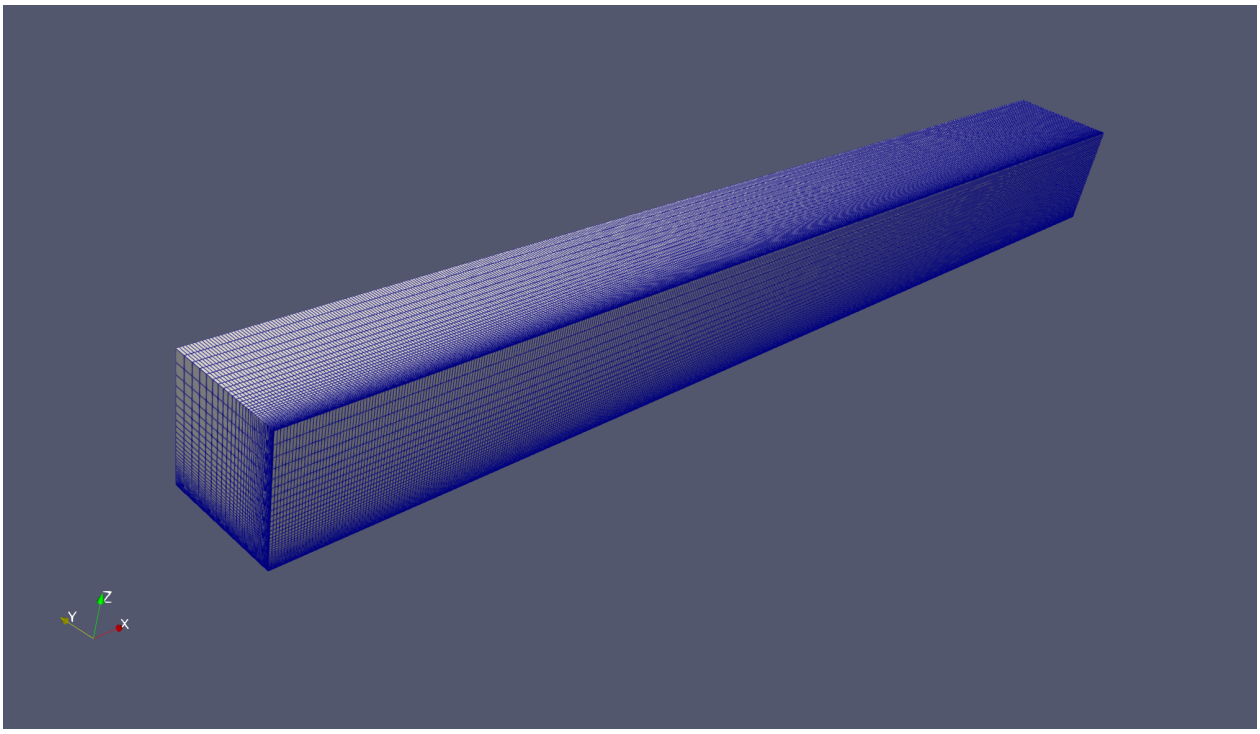


Figure 27.1: Medium-grid (481×81×81) mesh overview, one-quarter domain

The reference solutions are computed on the medium grid, so the comparison grid is fixed at medium to keep the code-to-code comparison free of a grid-resolution variable. A coarse-grid run confirms that the SA result is already grid-converged at coarse resolution; the QCR2000 secondary-flow intensity still shows a modest coarse-to-medium change (see Applicable Scope).

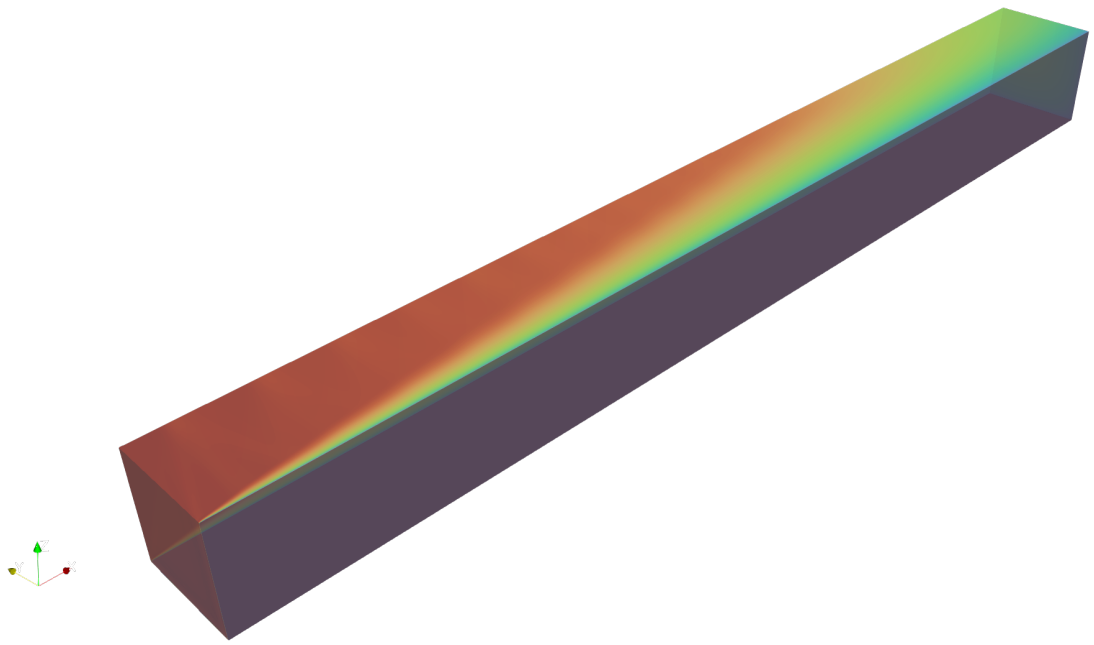


Figure 27.2: Mach-number contours over the duct surface, SA-QCR2000, medium grid

27.5 Mesh

Item	Setting
Mesh	Unstructured hexahedral, nested two-level family used for comparison: `coarse` (`241×41×41`) and `medium` (`481×81×81`, matching the reference solutions' grid)

27.6 Boundary and Initial Conditions

Item	Setting
Wall	Adiabatic, no-slip

Initial field: Not reported.

27.7 Numerical Methods

Item	Setting
Convective scheme	Roe, Green–Gauss gradients, Venkatakrishnan limiter (`K=0.05`, frozen after initial transient)
Time integration	Euler implicit, CFL schedule `0.5 → 5.0`

27.8 Results

27.8.1 Secondary-Flow Signature (SA vs. SA-QCR2000)

In-plane velocity magnitude (relative to centerline axial velocity `u_max`) at the judgment stations, medium grid:

Model	max `|(v,w)|/u_max`	rms
SA	0.09–0.14%	0.02–0.03%
SA-QCR2000	**1.18–1.19%**	0.53%

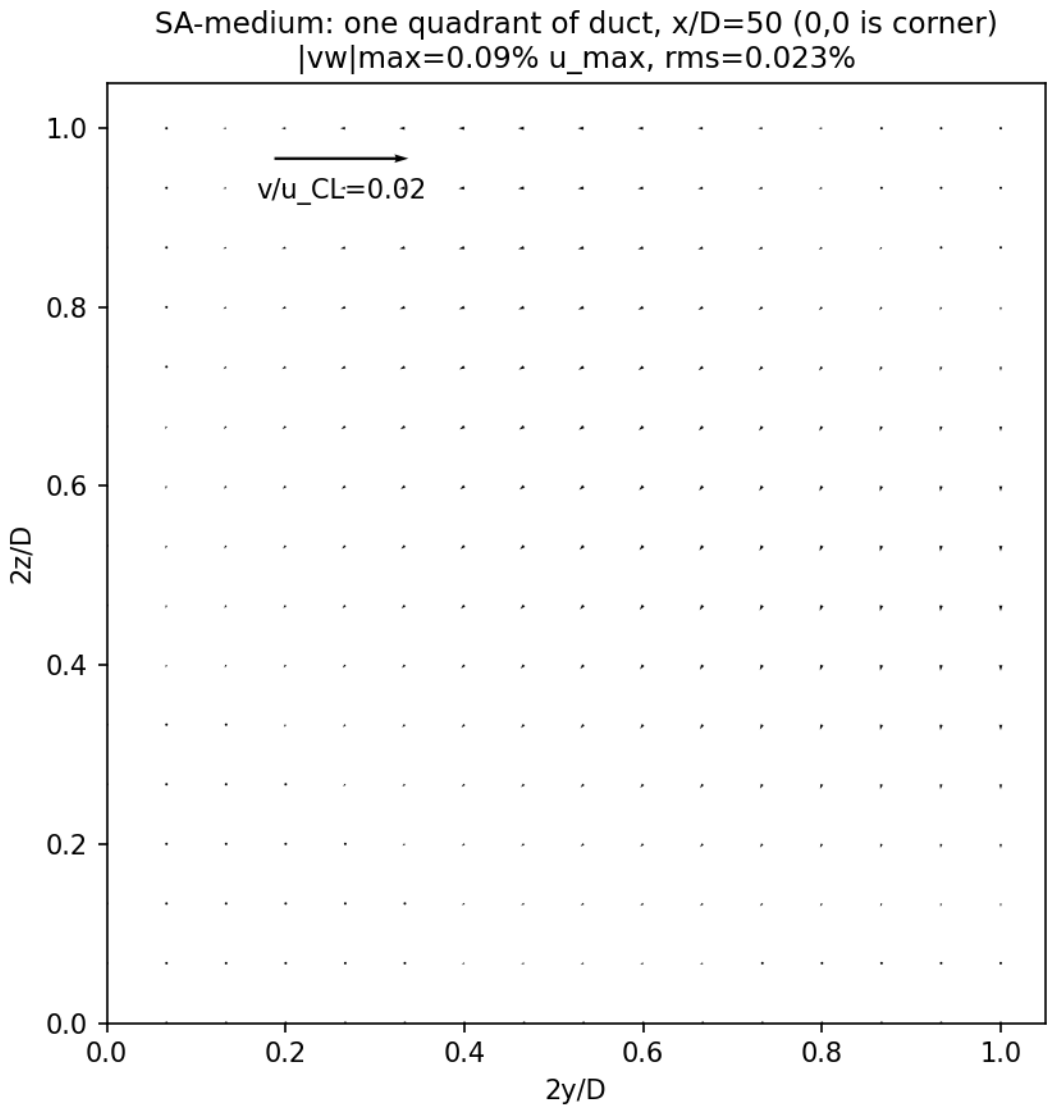


Figure 27.3: In-plane velocity vectors and magnitude at x/D=50, SA (no secondary flow) versus SA-QCR2000 (corner vortex pair), medium grid

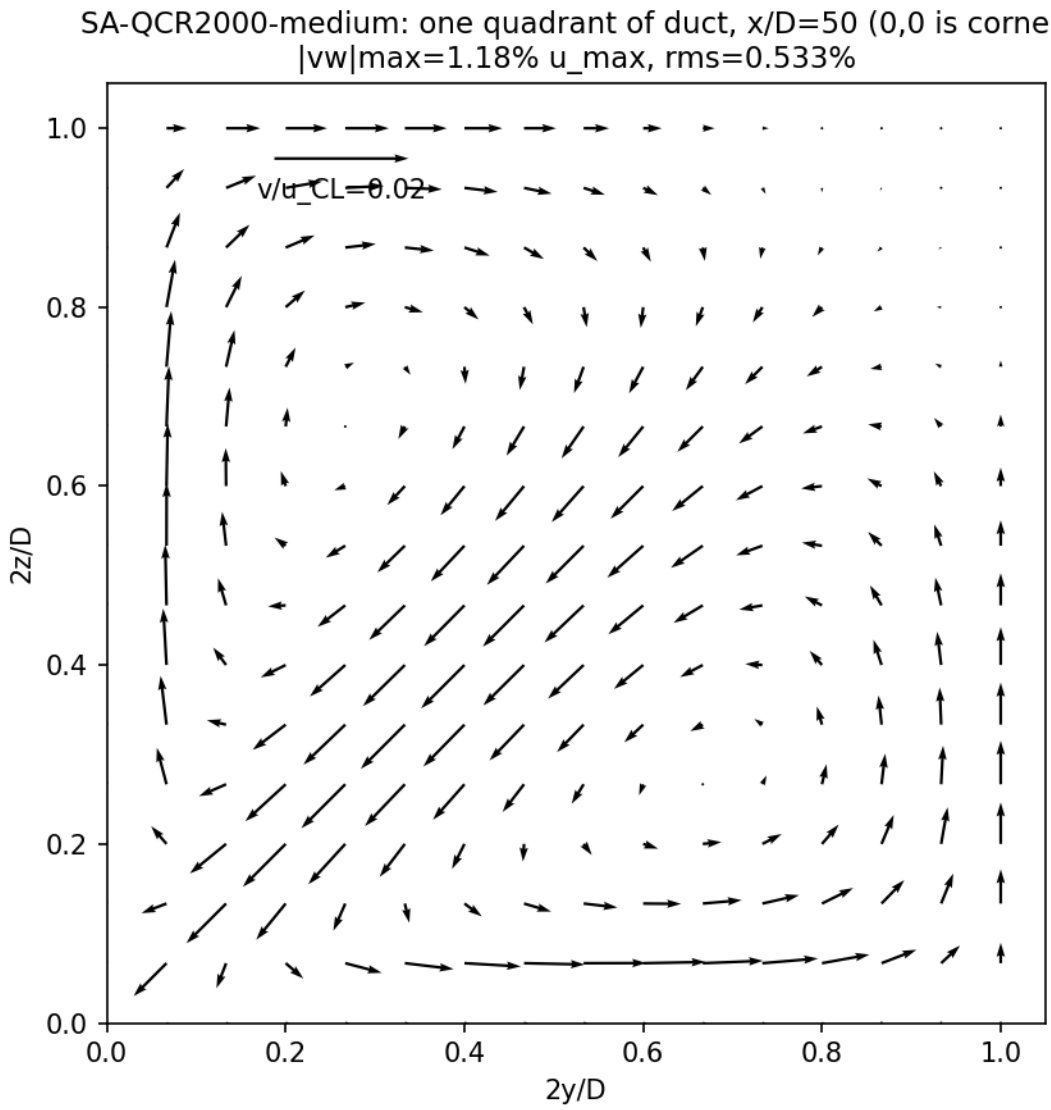


Figure 27.4: In-plane velocity vectors and magnitude at x/D=50, SA-QCR2000, medium grid

SA alone produces in-plane velocity at the noise floor of the discretization (`0.09–0.14%` of `u_max`) — the expected negative-control result for a linear Boussinesq model, which cannot represent stress anisotropy. SA-QCR2000 produces a pair of counter-rotating corner vortices at `1.18–1.19%` of `u_max`, matching the experimentally observed scale (`~1%`) and topology: an inflow jet along the corner bisector and a return flow along both walls.

27.8.2 Comparison Against Experiment and Reference Codes (medium grid)

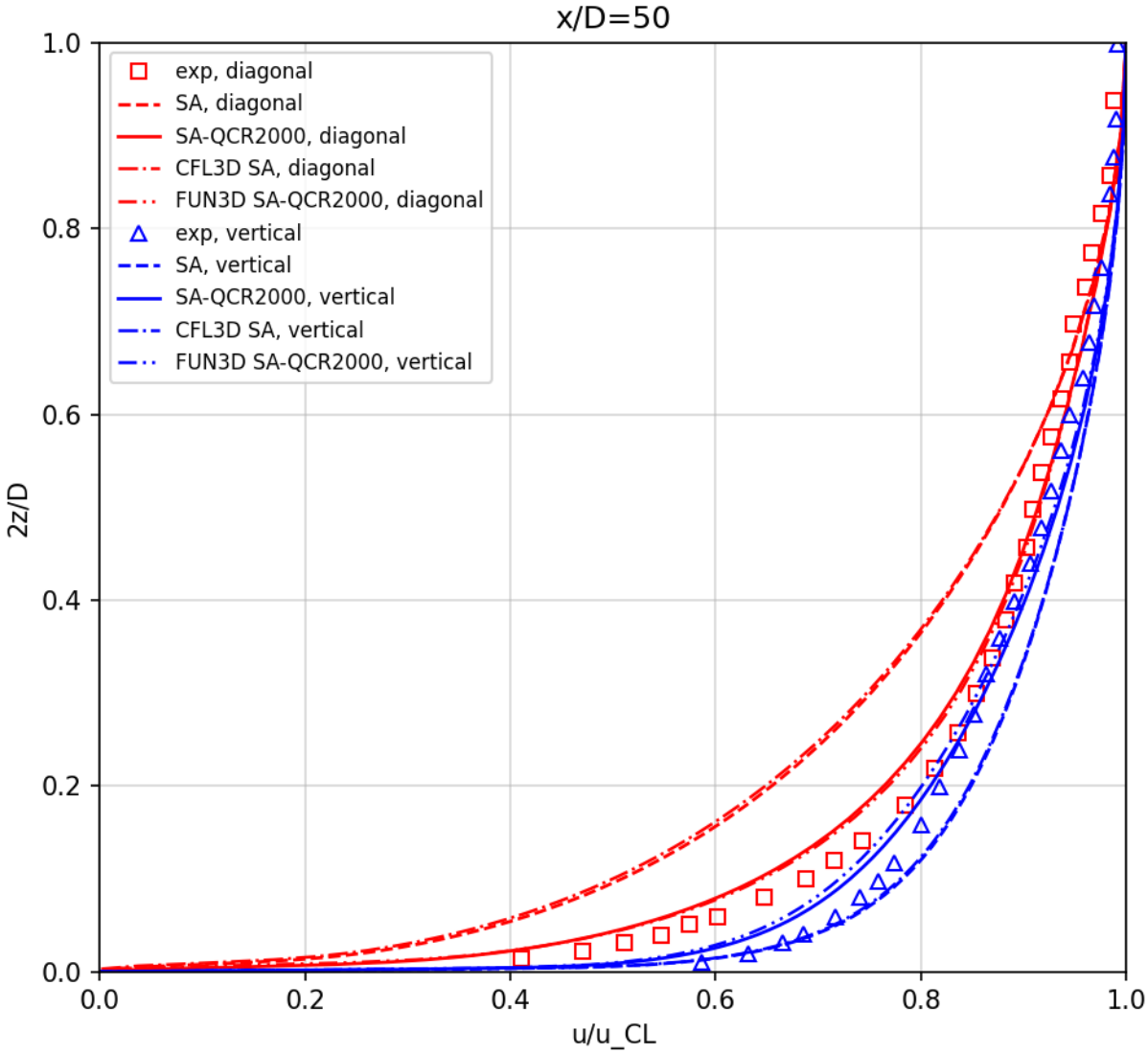


Figure 27.5: Velocity profile comparison at x/D=50: Wake CFD SA and SA-QCR2000 versus experiment, CFL3D SA, and FUN3D SA-QCR2000

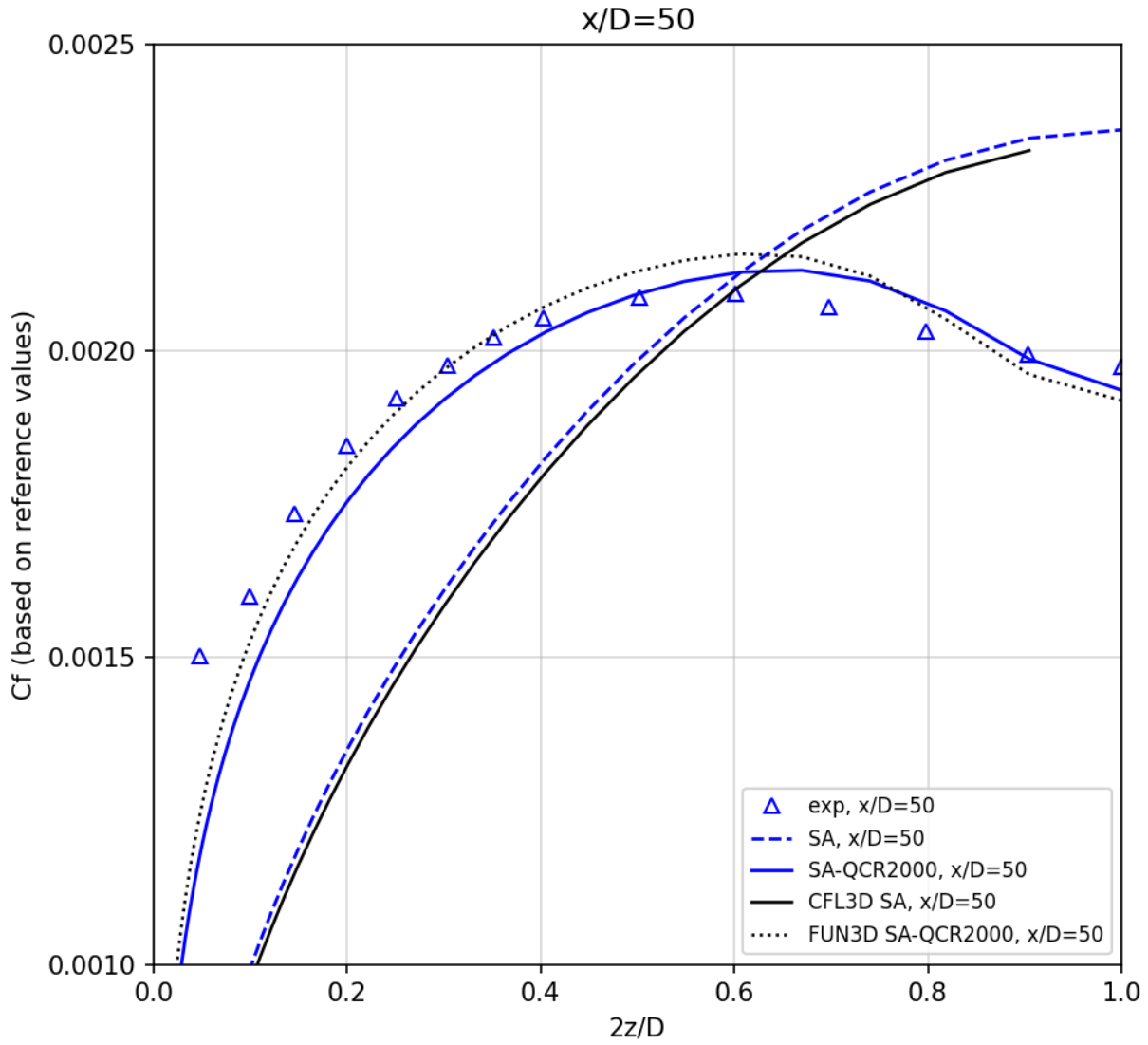


Figure 27.6: Skin-friction comparison at x/D=50: Wake CFD SA and SA-QCR2000 versus experiment, CFL3D SA, and FUN3D SA-QCR2000

- **Wake CFD SA and CFL3D SA agree closely** — the velocity and skin-friction profiles are within the plotted resolution of each other. Both codes show the same gap against the experiment (under-predicted diagonal velocity deficit, missing skin-friction inner peak) — this gap is a known limitation of the linear model, not a code-specific error.
- **Wake CFD SA-QCR2000 and FUN3D SA-QCR2000 agree closely** — velocity profiles overlap; skin friction agrees in peak location and shape, with the reference computation running slightly higher (1–2%) in part of the profile. Against the experiment, SA-QCR2000 reproduces the diagonal-cut velocity deficit and the skin-friction inner peak that SA misses, and matches the experimental data closely at `x/D=40`.

27.9 Conclusions and Applicable Scope

- Wake CFD's SA-QCR2000 implementation generates corner secondary flow at the experimentally observed scale and topology; the SA-only (negative-control) run does not, confirming that the physical mechanism is correctly implemented.
- On the same grid as the reference solutions, Wake CFD SA matches CFL3D SA and Wake CFD SA-QCR2000 matches FUN3D SA-QCR2000 — the residual gap against the experiment is attributable to turbulence-model form error, not to the Wake CFD implementation.
- Grid-convergence was confirmed for SA (coarse and medium agree). For SA-QCR2000, the secondary-flow intensity changes by approximately 13% from coarse to medium; the comparison grid was fixed at medium (matching the reference solutions) rather than extended to a finer grid, so a small residual grid-dependence remains in the absolute magnitude of the QCR2000 secondary flow. This residual uncertainty does not affect the primary pass/fail signal (secondary flow present versus absent), which is an order of magnitude larger than the coarse-to-medium change.
- The inflow boundary layer in this simulation develops from a uniform inlet condition, differing from the experiment's facility-developed inlet boundary layer; this is the case's own documented convention, and the fully turbulent judgment stations (`x/D=40, 50`) are chosen specifically to be outside the region most sensitive to this difference.
- This result applies to a supersonic (`M=3.9`), corner-bounded duct flow. It does not by itself establish QCR2000 accuracy for other corner geometries, other Mach numbers, or subsonic conditions. Linear Boussinesq models (SA, standard SST) should not be expected to reproduce corner secondary flow in any geometry — this is a structural model limitation, not a case-specific result.

27.10 References

- Davis, D. O., and Gessner, F. B., "Further Experiments on Supersonic Turbulent Flow Development in a Square Duct," *AIAA Journal*, 27(8), 1989, pp. 1023–1030, doi:10.2514/3.10216.
- Spalart, P. R., "Strategies for Turbulence Modelling and Simulations," *International Journal of Heat and Fluid Flow*, 21(3), 2000, pp. 252–263.
- NASA Turbulence Modeling Resource, 3D Supersonic Square Duct Validation Case.